Coherent combining of few-cycle pulses for the next generation of Terawatt-class laser sources devoted to attosecond physics

Hermance Jacqmin

THESE DE DOCTORAT
DE
L'UNIVERSITE PARIS-SACLAY
PREPAREE A
"L'ECOLE POLYTECHNIQUE"

ECOLE DOCTORALE N° 572
Ondes et matières

Spécialité de doctorat : Physique

Par

Mme Hermance Jacqmin

Coherent combining of few-cycle pulses for the next generation of Terawatt-class laser sources devoted to attosecond physics

Thèse présentée et soutenue à l'ENSTA, le 07 octobre 2016 :

Composition du Jury :

M. F. Balembois, Professeur, IOGS, Président du Jury
M. C. Durfee, Professeur, Colorado School of Mines, Rapporteur
M. E. Cormier, Professeur, CELIA, Rapporteur
M. M. Hanna, Chargé de recherche, IOGS, Examinateur
Mme A. Jullien, Chercheuse, INLN, Encadrante
M. Rodrigo Lopez-Martens, LOA, Directeur de thèse
M. Christophe Simon Boisson, Thales Optronique, Co-directeur de thèse

Contents

Remerciements

Ces trois années de thèse ont été l'occasion de rencontrer de nombreuses personnes et je souhaite remercier tous ceux qui ont contribué à ce travail.

Je tiens tout d'abord à remercier Rodrigo Lopez Martens et Christophe Simon Boisson, qui ont mis en place le financement de cette thèse, et qui m'ont confié leur projet de développement d'une source laser. Cette thèse a été réalisée dans le cadre d'un contrat CIFRE avec Thales Optronique et a donc été l'occasion de rencontrer Olivier Chalus, que je remercie pour les échanges que nous avons eu, ainsi que Paul Jougla, que je remercie pour sa disponibilité et son aide précieuse alors que j'effectuais mes premières simulations en Zemax en début de thèse.

Je tiens ensuite à remercier Eric Cormier, Charles Durfee, Marc Hanna et François Balembois, qui ont accepté de faire partie de mon jury de thèse, et qui ont pris le temps d'évaluer mon travail.

Ma thèse s'est déroulée au sein du groupe PCO (Physique du Cycle Optique) au Laboratoire d'Optique Appliquée. Un grand merci aux autres thésards de ma génération, Maïmouna Bocoum, Frédérik Boehle, Maxence Thévenet et Benoît Beaurepaire, toujours disponibles pour débattre de sujets divers et variés. Je tiens également à remercier Jean-Philippe Rousseau, qui m'a familiarisé avec les sources lasers femtosecondes en début de thèse, ainsi qu'Olivier Albert, qui était toujours d'excellent conseil. Enfin, je souhaite remercier Magali Lozano, avec qui j'ai eu la chance de travailler lors de ma dernière année de manips, et qui reprend le flambeau de la chaîne laser 3.0.

Au cours de mes deux premières années de thèse, j'ai eu la chance de travailler avec une laseriste hors pair : Aurélie Jullien. Le poids d'un simple 'merci' semble bien trop léger en comparaison de tout ce que tu m'a transmis. Si j'ai pris goût à la femto, c'est bel et bien grâce à toi. J'ai également eu la chance de travailler avec Brigitte Mercier, qui m'a formée sur le logiciel Miro et appris à porter un regard critique, aussi bien sur les résultats expérimentaux que numériques. Grâce à vous, les expériences de combinaison cohérente d'impulsions ultracourtes furent une belle aventure ! Je n'oublierai pas votre soutien sans failles lors de la période de rédaction et de préparation de la soutenance, malgré nos situations géographiques et professionnelles respectives changeantes.

Le groupe PCO travaillant en étroite collaboration avec le groupe APPLI, j'ai interagi quotidiennement ou presque avec Jérôme Faure, Geoffrey Galle, Diégo Guénot, Dominykas Gustas, Davide Boschetto et Aline Vernier. Je tiens à les remercier pour tous les échanges enrichissants que j'ai pu avoir avec les uns et les autres. Je tiens également à remercier Florian Mollica, pour m'avoir dévoilé les subtilités du SID4, mais avant tout pour son soutien indéfectible et ses bons plans de soirées.

J'ai eu la chance de pouvoir effectuer des expériences de filamentation dans l'air avec le groupe ILM. Un grand merci à Yi Liu et Andre Mysyrowicz, pour avoir pris le temps de me faire découvrir une physique riche et pleine de mystères, ainsi qu'à Pengji Ding, pour sa patience alors que la stabilisation de la CEP me donnait du fil à retordre. Je tiens également à remercier Yves-Bernard André, qui est venu à la rescousse en salle Azzurra un certain nombre de fois, que ce soit pour

Résumé

Ce travail de thèse s'inscrit dans le cadre du développement d'une source laser TW, de cadence élevée, stabilisée en phase, et délivrant des impulsions de quelques cycles optiques pour explorer la physique attoseconde. Ce type de source laser permet d'étudier la physique des plasmas à haute intensité, et plus particulièrement la génération d'ondes attosecondes par miroir plasma dont le principe peut être simplifié de la manière suivante : la focalisation d'une source primaire délivrant des impulsions IR femtosecondes sur une cible en verre entraîne la création d'un plasma. Dans le cas où les impulsions délivrées par la source primaire sont suffisamment intenses, le plasma se comporte comme un miroir et réfléchit le champ incident avec une forte distorsion : le champ réfléchi est alors constitué d'ondes attosecondes dont les composantes spectrales sont dans la gamme XUV. Ce type d'expérience est fortement lié aux caractéristiques de la source primaire IR, telles que l'intensité ou la phase des impulsions.

Une manière d'augmenter l'intensité crête des impulsions sur cible consiste à réduire autant que possible la durée des impulsions. Il est aujourd'hui possible de générer des impulsions de 5 fs à mi-hauteur et dont le spectre est centré à 800 nm. De telles impulsions contiennent seulement 4 oscillations du champ électrique ou cycles optiques, la période d'oscillation du champ électrique correspondant étant de 2,67 fs. On peut donc parler de régime du cycle optique. Dans le cadre de la génération d'ondes attosecondes par miroir plasma, le cahier des charges de la source laser peut être résumé comme suit :

- La durée des impulsions doit être de 5 fs pour atteindre un niveau d'intensité crête suffisamment élevé sur cible et explorer un régime d'interaction lumière-matière qualifié de relativiste. Dans un tel régime, la vitesse des électrons atteint la vitesse de la lumière.

- Le contraste des impulsions doit être suffisant pour éviter tout phénomène de pré-ionisation de la cible.

- La phase entre le champ électrique et son enveloppe (Carrier Envelope Phase, CEP) doit être stabilisée tir à tir pour contrôler l'interaction laser-matière sur une échelle sub-femtoseconde.

- Un taux de répétition élevé est souhaitable pour mesurer le rayonnement XUV avec un rapport signal sur bruit élevé.

La contrainte en terme de contraste implique une architecture laser à deux étages d'amplification à dérive de fréquence (Chirped Pulse Amplification, CPA), séparés par un étage de filtrage temporel. D'autre part, la stabilisation de la phase des impulsions contraint les schémas d'étirement et de compression. Une source laser avec ce type d'architecture a déjà été réalisée dans le cadre du projet de la Salle Noire 2.0 (Jullien et al, Opt. Lett., 2014). Mon travail de thèse a consisté à développer la Salle Noire 3.0, source laser délivrant deux fois plus d'énergie que la source précédente (Salle Noire 2.0). L'architecture retenue pour cette nouvelle source laser est la suivante : un oscillateur injecte un premier CPA qui délivre des impulsions de 30 fs avec une énergie de 1,6 mJ. Un étage de filtrage temporel permet alors d'augmenter le contraste des impulsions de plusieurs ordres de grandeur. La transmission de ce filtre étant de l'ordre de 20 %, un second CPA est nécessaire pour atteindre un niveau d'énergie de l'ordre de 25 mJ. A ce stade de la chaîne laser, les impulsions ont une durée de 25 fs. Pour réduire la durée des impulsions et atteindre le régime du cycle optique,

l'ajout d'un étage de post-compression est nécessaire. Il est prévu ainsi de générer des impulsions de 5 fs avec une énergie de 15 mJ.

La première partie de ce manuscrit est consacrée d'une part à la caractérisation expérimentale des premiers modules de cette chaine laser, et d'autre part aux études et simulations nécessaires à la définition et au dimensionnement des modules suivants. La caractérisation du front-end (oscillateur et premier CPA) ainsi que de l'étage de filtrage temporel est détaillée au début de cette partie. Les performances en terme de durée, contraste et stabilisation de la CEP y sont présentées. La problématique de dégradation du contraste cohérent par effet de diffraction temporel non linéaire est abordée. Enfin, l'exploitation et la mise en place d'un diagnostique permettant de quantifier les couplages spatio-temporels de la source laser sont détaillés. Les différents choix technologiques et simulations de la suite de la chaine sont abordés en fin de partie. En particulier, le design de l'étireur et du compresseur du second CPA est discuté, les problèmes liés aux effets thermique dans les étages d'amplification sont mis en évidence au travers de simulations dont les résultats sont confrontés à des mesures expérimentales, et les résultats de simulation du processus d'amplification au sein du second CPA sont présentés.

La deuxième partie de ce manuscrit est consacrée à la post-compression d'impulsions intenses. La réalisation de l'étage de post-compression constitue en effet une réelle difficulté en raison du niveau d'intensité crête des impulsions disponibles à la sortie du second CPA. Deux techniques sont proposées. La première technique consiste à exploiter un effet non linéaire d'ordre trois, la génération de polarisation croisée (Crossed Polarized Wave (XPW) generation), dans des cristaux de BaF2. Le dimensionnement et la mise en oeuvre d'un tel dispositif ont été réalisés dans le cadre de la Salle Noire 2.0. Les résultats de cette campagne d'expérience ont été confrontés à ceux de simulations numériques. Les limites de cette technique, en partie liées au niveau d'intensité élevé des impulsions incidentes et aux caractéristiques de la source laser disponible, sont mises en évidence.

Une autre technique de post-compression efficace pour obtenir des impulsions de quelques cycles optiques consiste à élargir le spectre des impulsions laser par automodulation de phase dans une fibre creuse remplie de gaz, puis à compenser la phase spectrale introduite avec des miroirs chirpés. Cette technique convient à des impulsions dont l'énergie est inférieure au millijoule. Au-delà, la transmission et la stabilité du compresseur chutent fortement à cause d'effets non linéaires tels que l'autofocalisation et l'ionisation. Pour comprimer des impulsions énergétiques et dont la phase de l'enveloppe est stabilisée par rapport à la porteuse (stabilisation de la CEP), il est possible de diviser l'impulsion initiale en plusieurs répliques d'énergie moindre et de réduire ainsi l'intensité crête en entrée de fibre. Le spectre de chaque réplique est alors élargi indépendamment. Dans le cadre de cette thèse, la combinaison cohérente passive d'impulsions de quelques cycles optiques issues d'une fibre creuse remplie de gaz est démontrée pour la première fois. L'utilisation de lames biréfringentes (calcite) dont l'orientation est soigneusement déterminée permet de générer et combiner des répliques avec une efficacité élevée. Ainsi, dans le cas d'une division en deux répliques, des impulsions stabilisées en phase (CEP), de durée 6 fs et d'énergie 0.6 mJ ont été générées de manière fiable et reproductible. L'étude détaillée de cette technique, aussi bien théorique qu'expérimentale, a permis de mettre en évidence les conditions requises pour générer des impulsions de quelques cycles optiques et présentant un bon contraste temporel. Plus précisément, la phase spectrale relative entre les répliques peut être mesurée à l'aide d'une méthode interférométrique permettant de quantifier les déphasages résiduels dus à la lame qui recombine les répliques, ainsi que ceux induits lors de la propagation dans la fibre par d'éventuels effets de modulation de phase croisée ou d'ionisation. Les effets qui affectent le processus de combinaison des répliques, tels que les modifications des états de polarisation des répliques ou bien les interactions non linéaires entre les répliques, sont analysés en détail. Une méthode est proposée pour minimiser ces effets, même dans le cas plus critique de la division et

combinaison d'impulsions à quatre répliques.

Abstract

The framework of this thesis is the design and development of a TW-class, high-repetition rate, CEP-stabilized, few-cycle laser system devoted to attosecond physics. Few-cycle pulses includes only a few oscillations of the carrier wave (duration about 5 fs for 800nm central wavelength) and are not directly available at the output of typical femtosecond sources. One of the most popular techniques used for producing such pulses with high spatial quality is nonlinear spectral broadening in a gas-filled hollow-core fiber followed by temporal compression with chirped mirrors. However, as the input pulse energy approaches the milliJoule level, both the transmission and stability of hollow fiber compressors rapidly drop with the onset of self-focusing and ionization. A way of overcoming this limitation is to divide the input pulse into several lower energy replicas that can be subsequently recombined after independent spectral broadening in the fiber. In this thesis, the passive coherent combining of millijoule energy laser pulses down to few-cycle duration in a gas-filled hollow fiber is demonstrated for the first time. High combining efficiency is achieved by using carefully oriented calcite plates for temporal pulse division and recombination. Carrier-envelope phase (CEP)- stable, 6-fs, 800-nm pulses with more than 0.6 mJ energy were routinely generated in the case of twofold division and recombination. A detailed theoretical and experimental analysis of this temporal multiplexing technique is proposed to explain the conditions required for producing few-cycle pulses with high fidelity. In particular, an interferometric method for measuring the relative spectral phase between two replicas is demonstrated. This gives a measure of the phase mismatch in the combining plate, as well as that induced by eventual cross-phase modulation or ionization during propagation in the fiber. The effects degrading the combining process, as polarization change or nonlinear interactions between pulse replicas are analyzed in details. A method is proposed to overcome these limitations, even in the critical case of fourfold pulse division and combination.

General introduction

Recent developments in ultrafast laser technologies over the two last decades enabled the generation of extremely short laser pulses. Durations of a few femtoseconds can be now achieved (1 fs = 10^{-15} s), with a few optical cycles of the electric field in the visible spectral range. Strongly focusing such pulses allows to spatially and temporally concentrate the laser energy and to reach very high peak intensities, defined by I = E / ($\pi r^2 \tau$) where E is the pulse energy, τ the pulse duration and r the radius of the focal spot.

Femtosecond lasers makes femtochemistry possible

The time feature for atoms motion is on the femtosecond scale. Pulses with similar durations make the vibration states of molecules measurable: femtosecond lasers offer the possibility to study every step of chemical reactions and to discover substances formed along the way from the original chemical product to the final one. A new research field has opened and leads to fruitful discoveries: the Nobel Prize in Chemistry was attributed to Ahmed H. Zewail in 1999 for his studies of the transitions states of chemical reactions using femtosecond spectroscopy. To take our understanding of matter further with the study of electron dynamics, femtosecond pulses are not short enough as the relaxation timescale of the electronic process is the attosecond (1 as = 10^{-18} s).

Laser-matter interaction for attosecond pulse generation

Attosecond durations can be achieved in the XUV spectral range thanks to the High Harmonic Generation (HHG) process occurring via laser-atoms interactions. When a highly intense laser pulse is focused in a gas target (see Fig. 1), its electric field induces potential barrier curvature of atoms and leads to tunnel ionization of electronic wavepackets. Electrons bunches are accelerated by the laser electric field and acquire significant kinetic energies. The process is brief (a fraction one cycle of the electric field) and repeated every half-cycle of the driving pulse. Some electrons can recombine and convert their kinetic energy into coherent XUV photons. In the early 2000s, such a technique led to the generation of attosecond pulse trains [1, 2] and opened a new attractive research domain [3, 4]. Attosecond pulses can indeed bring answers to the time removal of an electron from an atom or a molecule, the molecular orbitals rearrangement after an electron leaving, the electrons movement during chemical reactions, etc.

The femtosecond laser source intensity and the target properties determine the physical process involved in the laser-matter interaction. The HHG process does not occur in atomic gas targets for laser intensities higher than 10^{14} W.cm^{-2}, when the ionization rate inside the gas is too significant. Besides, the process efficiency is very low (10^{-6}-10^{-5}). As an alternative, plasma mirrors are very promising because they allow HHG with laser intensities largely higher than 10^{14} W.cm^{-2}. Their reflective surface is made of a dense plasma generated by an intense laser field via an ionization process of a solid target. This technology will permit to study ultra-intensity physics and to explore the relativistic regime achieved for laser intensities higher than 10^{18} W.cm^{-2}. In this regime, the electric field makes a blanket of electrons on the mirror surface which oscillates at the laser frequency, with speeds close to the speed of light. This relativistic movement of the mirror surface induces HHG via Doppler effect. The reflected beam is made of not only the incident laser frequency but also of high order harmonics of the laser frequency. The highest harmonic
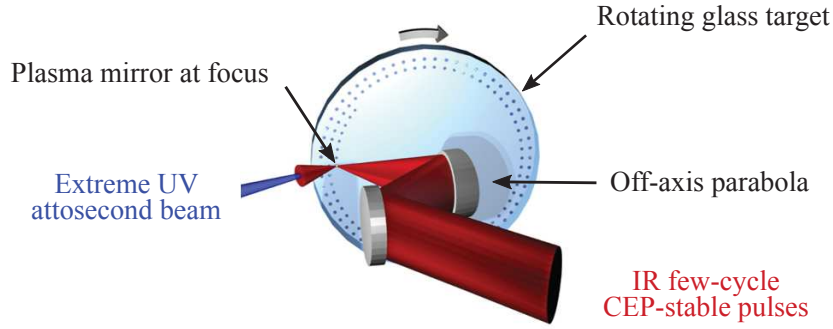
Figure 1 – Experimental setup for attosecond pulses generation (adapted from [5]). The IR beam is focused at a 1 kHz repetition rate onto a rotating glass target. The plasma created at the target surface emits a coherent XUV radiation.

order that could be achieved is unknown but there is hope for generation of X rays. This regime is named relativistic because the electrons speed is about the light one, meaning that the mass variation of electrons must be taken into account, and that the magnetic force [-e $\mathbf{v} \wedge \mathbf{B}$] cannot be neglected. To date, the laws of linear and nonlinear optics are unknown in this regime. For all these reasons, plasma mirrors are considered as the second generation of attosecond sources [6]. They are able to provide attosecond sources with more intensity, lower pulse duration and shorter wavelengths than gas targets for instance. This considerably broadens the range of applications of attosecond sources, in addition to enabling the study of the behavior of matter under extreme light intensities. This last basic research project requires the development of laser sources delivering pulses with enough intensity to reach the relativistic regime. Such laser systems are usually called relativistic laser sources.

Relativistic laser source specifications

The relativistic laser source specifications are very constraining. As explained previously, the pulse energy (resp. duration) must be high (resp. low) enough to reach relativistic intensities on target, always maintaining a good spatial and temporal pulse quality. Compromises must be done and there are two options. The pulse energy can be increased, but this implies a reduced laser repetition rate [7]. It is also possible to decrease the pulse duration down to a few optical cycles, reduce the spot size on target and increase the laser repetition rate. In this case, the pulse energy is limited. The PCO group chose this last option.

Attosecond pulse generation via plasma mirrors requires laser pulses with a high temporal contrast. Titanium Sapphire laser systems generate pulses which are surrounded by a pedestal of incoherent light on a nanosecond timescale (with a typical relative intensity between 10^{-6} and 10^{-9}) and by coherent parasitic pulses on a picosecond timescale (with a typical relative intensity between 10^{-3} and 10^{-4}). The incoherent temporal pedestal can be a limitation when focusing intense laser pulses on a solid target. If its intensity is high enough to pre-ionize the target before the main pulse arrival, the plasma mirror cannot be created. The plasma induced by the laser pedestal spreads out before the interaction of the main pulse with the target. In the end, the main laser pulse interacts with a low density plasma, which is not of interest.

Working with few-cycle laser pulses necessitates that the phase between the electric field and its envelope, called Carrier Envelope Phase (CEP), be stabilized. The intensity of a pulse made of only two optical cycles is indeed strongly affected by a CEP shift. The variations of the CEP are influenced by environment fluctuations (temperature, mechanical and acoustic vibrations, etc) and undesirable nonlinear effects experienced by pulses all along the laser chain. As a consequence, the CEP must be stabilized as close as possible to the target.

Finally, a repetition rate of 1 kHz is desirable to achieve significant XUV photon flux and to perform statistics. As a consequence, the thermal effects must be controlled in the amplification

stages, as well as in the compressor. A constant refreshment of the target consistent with the laser repetition rate is also required.

Motivation and outlines of the thesis

This thesis falls within the development of unique few-cycle laser sources by the PCO group. The first Salle Noire laser demonstrated for the first time HHG from solid targets at 1 kHz repetition rate in the few-cycle regime [8, 5]. The role of the CEP was specially highlighted.

An upgrade of this laser (Salle Noire 2.0) was aimed at increasing the available energy to 10 mJ, while implementing contrast enhancement in a double-CPA, CEP-stabilized system [9]. Some of the first associated results demonstrated the anti-correlated emission of HHG and electrons [10] and the role of the laser wavefront in the emission of fast electrons [11]. The reliable few-cycle pulse production from this laser source is still under process.

Based on these developments, the project presented here is devoted to further increase the energy on target. In this framework, this thesis aimed to conceive and develop a new high contrast few-cycle CEP-stabilized Terawatt-class 1 kHz laser, which will be dedicated to attosecond pulses generation in the relativistic regime on solid target. This project draws its dynamism from the ELI project in Hungary, called ELI-ALPS (Extreme Light Infrastructure - Attosecond Light Pulse Source). Financial support was provided by Conseil Régional d'Ile-de-France and Thales Optronique.

The thesis manuscript is divided into two parts. The first part is dedicated to the dimensioning calculations I performed to design the entire laser chain. This involves optical design simulations of the key optical systems of the laser chain (stretcher and compressor), the amplification calculations and a preliminary study on thermal issues. Some critical technological choices were made at the light of these calculations and the discussions with some suppliers. The experimental characterization of the front-end is also presented through temporal measurement, CEP stabilization and spatio-temporal coupling estimation.

The second part deals with the post-compression experiments performed in the framework of a research project founded by ELI-ALPS. This project was dedicated to the study of several options to post-compress multi-mJ pulses down to the few-cycle regime (< 10 fs). In this thesis, two different options were explored. I first present a post-compression technique based on Cross-polarized wave generation (XPW) which was tested with a 10 mJ, 25 fs, 1 kHz laser source (Salle Noire 2.0). Another technique consisting in implementing a pulse dividing and combining setup in a hollow-core fiber post-compressor is then introduced and analyzed in details. This last setup was used to perform filamentation experiments with the ILM group, as shown in the last chapter.

Part I

Towards a high contrast few-cycle CEP-stabilized Terawatt-class laser at high repetition rate

Chapter 1

Introduction

The first femtosecond technology appeared in the 1970s with passively mode-locked dye lasers, delivering sub-1 ps pulses [12]. The dye laser principle is based on the use of organic molecules which are diluted in a solvent. The specificity of these molecules is their manifold energy levels. Their continuous emission in the spectral visible range allows the generation of short pulses via the use of mode-locking methods. In this way, a colliding-pulse mode-locking technique allowed the 100-fs barrier to be broken in the 1980s [13]. A few years later, 27 fs pulses were obtained thanks to a precise intracavity group-delay dispersion (GDD) management [14]. The shortest pulse duration obtained with a dye laser was 6 fs for energies about the nanojoule [15]. In this case, an extracavity pulse compression technique was used. The peak power upgrade of dye lasers could be then achieved thanks to kHz pump lasers. This is how tens of megawatts could be generated [16]. However, these laser sources require a constant dye circulation to avoid molecules breaking by the pumping process. This complicated implementation, in addition to the increasing demand for energies higher than the microjoule level, made this technology progressively outdated.

At the end of the 1980s, titanium-doped sapphire (Ti:Sa) crystals were identified as excellent candidates for broadband solid-state lasers [17]. The main reasons are listed below:

- These crystals can support a high thermal charge thanks to the excellent thermal conductivity of sapphire.

- The very large gain bandwidth of Ti^{3+} ions ($\approx$ 650-1100 nm) is suited to ultrashort pulses generation.

- Ti:Sa exhibits a high saturation fluence so that significant energy can be extracted.

- High peak power can be achieved with this material, as it can be grown as large size crystals.

The boundaries of Ti:Sa crystal-growth technology were pushed by the increasing demand for high peak power lasers, especially Petawatt lasers. As an example, the company Crystal Systems is now able to produce 170 mm diameter crystal boules with excellent properties. Further developments are needed to meet the demand of the ELI platforms, consisting in 250 mm boules. In the end, Ti:Sa crystals are still at the front of the femtosecond lasers research area, although it became a proven technology a long time ago.

The successful career of Ti:Sa started in 1991, at the time of the first demonstration of a Kerr-lens mode-locked Ti:Sa laser oscillator [18], delivering 45 fs pulses thanks to extra-cavity dispersion compensation with bulk. The advantage of these oscillators is their very fast response and the absence of saturable absorber medium. Further experimental work lead to a better understanding of the Kerr-lens mode-locking process [19], showing that high spatial modes are not required to start and sustain mode-locking which is entirely due to self-focusing effect in the Ti:Sa rod.

In the first Kerr-lens mode-locked oscillators, pulse compression was managed with a pair of prisms. However, this compression device induces uncompensated high order dispersion. This is not the case of chirped multilayer mirrors, which introduce a constant negative dispersion over a

large frequency range. Such coatings were proposed by [20, 21] and exhibit negative dispersion on a 80 THz spectral bandwidth. Thanks to these innovative coatings, few-cycle pulses were routinely produced at the nanoJoule level, as demonstrated in [22]. Femtosecond Kerr-lens mode-locked Ti:Sa lasers became then a worldwide reference technology.

The amplification of pulses beyond the nanoJoule level is limited by the onset of self-focusing. The chirped-pulse amplification technique (CPA) proposed by [23] overcomes this limitation. Its principle relies on pulse temporal stretching before performing pulse amplification. The pulse peak power is thus strongly decreased in the amplifiers, avoiding the deleterious effects of self-focusing. At the end, high peak power is recovered via temporal compression. This is how picosecond pulses were amplified from the NanoJoule to the Joule level [24]. Otherwise, 350 μJ, 55 fs compressed pulses were produced by implementing this technique with regenerative amplifiers operating at 1 kHz repetition rate [25].

The next purpose is dedicated to the progress of kHz laser systems. A recent paper overviews laser technologies with a similar repetition rate [26]. A survey of this state of the art with some additional references is summarized in Tab. 1.1. The best performance achieved with a dye laser, as well as performances of Ti:Sa rod kHz lasers, are gathered on Fig. 1.1. The Salle Noire 3.0 project follows on from the Salle Noire 2.0 one (10 mJ, 22 fs, 1 kHz) [9] and plans to deliver 25 mJ, 20 fs, pulses at 1 kHz repetition rate. These specifications correspond to a slight increase of both peak power and mean average power compared to the sources previously developed and based on the same technology (see Fig. 1.1). There are also additional constraints related to the contrast and CEP stability.
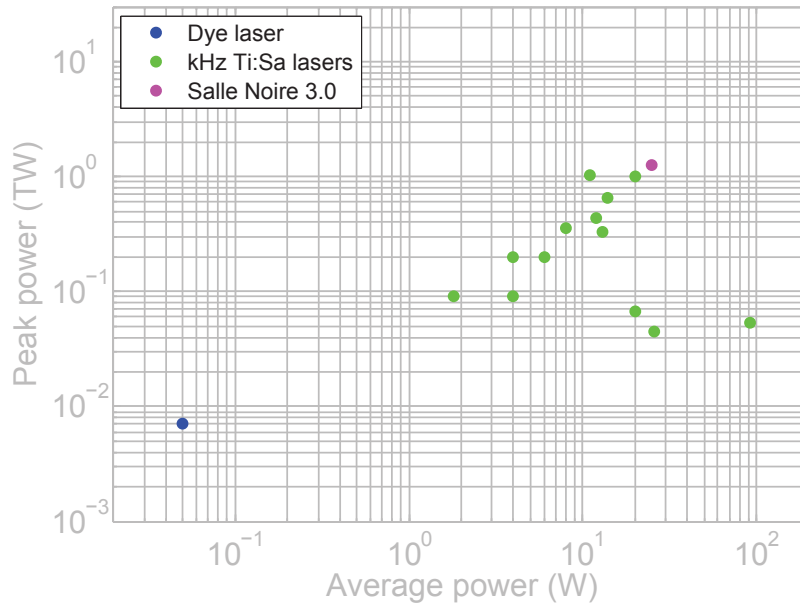
Figure 1.1 – Summary of the key results in terms of average and peak power, obtained with dye lasers and Ti:Sa lasers these last decades.

The minimum pulse duration that can be obtained with a Ti:Sa-based laser system is about 20 fs. This is due to the limited spectral bandwidth of the gain in Ti:Sa crystals. To achieve the few-cycle regime, the femtosecond laser source must be completed by a post-compression stage. Nowadays, the most widespread method to spectrally broaden and temporally compress amplified femtosecond laser pulses down to few-cycle duration is via self-phase modulation (SPM) in noble gas-filled hollow-fibers followed by chirped mirror compression. This technique was successfully implemented for the first time in 1996 [39]. A detailed overview of the main post-compression techniques is presented in Part 2.

To end this introduction, I should mention an another emerging technology suited to attosecond generation based on the OPCPA concept (Optical Parametric Chirped-pulse Amplification)

Ref.	Year	f	E	τ	P_{peak}	P_{mean}	Remark
[27]	1997	1 kHz	4 mJ	20 fs	0.2 TW	4 W	Thermal lens managed through Ti:Sa crystal cooling to 125 K.
[28]	1998	1 kHz	14 mJ	21 fs	0.66 TW	14 W	Pulse compression managed through a pair of prisms inserted in the regenerative amplifier.
[29]	2000	1 kHz	1.8 mJ	20 fs	0.09 TW	1.8 W	Single multipass amplifier stage. Chirped mirrors provide compensation for gain narrowing and high-order dispersion.
[30]	2000	1 kHz	20 mJ	20 fs	1 TW	20 W	A thermal lens imaging technique is preferred to Ti:Sa cryogenic cooling.
[31]	2001	1 kHz	4 mJ	45 fs	0.09 TW	4 W	
[32]	2001	7 kHz	1.3 mJ	24 fs	0.05 TW	9.1 W	Single-stage laser amplifier. Ti:Sa crystal cryogenically cooled (77 K).
[33]	2004	10 kHz	1.1 mJ	28 fs	TW	11 W	Single-stage amplifier with cryogenic cooling (73 K). The seed is negatively chirped so that compression is achieved through bulk.
[34]	2006	10 kHz	2.6 mJ	58 fs	0.045 TW	26 W	
[35]	2009	1 kHz	6 mJ	30 fs	0.2 TW	6 W	CEP noise = 90 mrad.
[36]	2010	1 kHz	12 mJ	27 fs	0.44 TW	12 W	
[37]	2011	1 kHz	13 mJ	40 fs	0.33 TW	13 W	Cryo-cooling, CEP noise = 440 mrad.
[38]	2013	10 kHz	2 mJ	30 fs	0.067 TW	20 W	Cryo-cooling, CEP noise = 320 mrad.
[9]	2014	1 kHz	8 mJ	22 fs	0.36 TW	8 W	High contrast, CEP noise = 240 mrad.

Table 1.1 – State of the art of Ti:Sa rod lasers operating at kHz repetition rates and exhibiting 20-30 fs pulse durations. The last reference (2014) corresponds to the Salle Noire 2.0 performances.

[26]. In this case, the CPA technique is implemented together with optical parametric amplifiers. This technology is very attractive because there are no thermal issues unlike the Ti:Sa-based amplifiers. Besides, the contrast requirement is easily achieved as the parametric gain occurs only within the duration of the pump pulse. The main disadvantages of OPCPA systems are: the limited aperture of the available nonlinear crystals, the synchronization issues between the pump and the signal, as well as the phase-matching issues. In general, many disadvantages of the Ti:Sa-based

14

systems are translated to the OPCPA pump (thermal management, footprint).

Chapter 2

General view of a relativistic laser source

Contents

In this chapter, I present the general concepts used to define and design the relativistic laser source. In a first step, I introduce the main characteristics of femtosecond laser pulses, restricted to the definitions extensively used in the manuscript. Next, I will present how the required laser specifications determine its architecture and the technical challenges that need to be overtaken.

2.1 Main concepts of ultrashort pulses

2.1.1 Description of an ultrashort pulse

Temporal domain

The electric field of a light pulse can be described as the product between a carrier wave, oscillating at the fundamental frequency of the laser ω_0, and an envelope function. The oscillation period of the electric field is determined by the central wavelength of the laser and is $\frac{2\pi}{\omega_0} = 2.7\,\text{fs}$ for a 800 nm centered pulse. Assuming a Gaussian shape and neglecting the spatial dependance, the electric field can be written as:

$$\text{E}(t) = \text{E}_0 \exp\left[-\frac{t^2}{\tau^2}\right] \exp\left[j\left(\omega_0 t + \Phi_0 + \Phi_{\text{NL}}(t)\right)\right] \tag{2.1}$$

where Φ_0 is the phase-shift between the carrier wave and the envelope function and $\Phi_{\text{NL}}(t)$ the nonlinear temporal phase of the pulse. The quantity Φ_0 is usually called 'Carrier Envelope Phase' (CEP) and is represented on Fig. 2.1(a). For pulses exhibiting ultrashort duration (typically $\leq 10\,\text{fs}$), the value of the electric fied at $t = 0$ is strongly affected by the value of Φ_0. CEP control is thus necessary, as highlighted in [40]. The $1/e^2$ width of the pulse intensity is 2τ and is defined as:

$$\text{I}(t) \propto |\text{E}(t)^2| = |\text{E}_0^2| \exp\left[-\frac{2\,t^2}{\tau^2}\right] \tag{2.2}$$
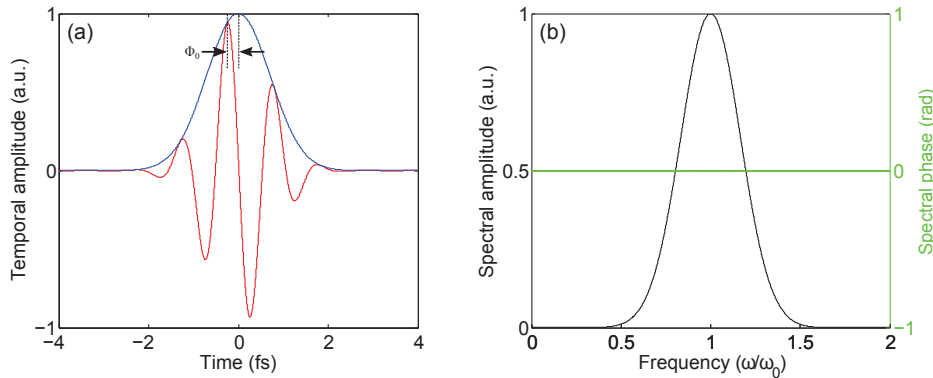
Figure 2.1 – Fourier Transform limited pulse in temporal (a) and spectral (b) domain.

Spectral domain

The electric field can be expressed in the spectral domain via a Fourier Transform (FT) and is written as:

$$\text{E}(\omega) = \text{A}(\omega) \exp\left[j\,\phi(\omega)\right] \tag{2.3}$$

where $\text{A}(\omega)$ is the spectral amplitude of the field and $\Phi(\omega)$ its spectral phase. In the ideal case, $\Phi(\omega) = 0$ and the pulse is considered as Fourier Transform Limited (FTL) (see Fig. 2.1(b)), meaning that it has the shortest pulse duration for a given spectrum. When a pulse propagates through a dispersive medium, $\Phi(\omega) \neq 0$ and the temporal shape of the pulse is affected. In this case, $\phi(\omega)$ can be decomposed into a Taylor series around the fundamental frequency of the laser ω_0:

$$\phi(z,\omega) = k(\omega)\, z = \phi(\omega_0) + \phi^{(1)}(\omega_0)(\omega - \omega_0) + \frac{1}{2}\phi^{(2)}(\omega_0)(\omega - \omega_0)^2 + \frac{1}{6}\phi^{(3)}(\omega_0)(\omega - \omega_0)^3 + ... \quad (2.4)$$

The first term $\phi(\omega_0)$ corresponds to a CEP change. The first order is related to the temporal shift of the pulse, without any deformation. $\phi^{(1)}(\omega_0)$ is defined as the group delay of the pulse. The second order, called Group Delay Dispersion (GDD), is responsible for the linear temporal spreading of the pulse frequencies (chirp). The effect of a quadratic spectral phase is detailed in appendix A: the amplitude and CEP of the chirped pulse electric field are analytically calculated, as well as the chirped pulse duration. The temporal chirp parameter, named b in the following, is also defined.

Notions of pulse front and wavefront

The spectral phase can be expressed at different transverse locations **r** within the beam:

$$\phi(\mathbf{r},\omega) = \phi(\mathbf{r},\omega_0) + \phi^{(1)}(\mathbf{r},\omega_0)(\omega - \omega_0) + \frac{1}{2}\phi^{(2)}(\mathbf{r},\omega_0)(\omega - \omega_0)^2 + \frac{1}{6}\phi^{(3)}(\mathbf{r},\omega_0)(\omega - \omega_0)^3 + ... \quad (2.5)$$

- The first term of the spatio-temporal phase, $\phi(\mathbf{r},\omega)$, characterizes the **wavefront**, which is the surface defined by $\left(\mathbf{r}, z = c \cdot \frac{\phi(\mathbf{r},\omega_0)}{\omega_0}\right)$. The wavefront propagates at the phase velocity $v_\phi = \omega/k$ where k is the wave vector.

- The second term characterizes the **pulse front**, which is the surface defined by $\left(\mathbf{r}, z = c \cdot \phi^{(1)}(\mathbf{r},\omega_0)\right)$. The pulse front propagates at the group velocity $v_g = 1/k^{(1)}(\omega)$. $\phi^{(1)}(\mathbf{r},\omega_0)$ can be defined as a local group delay.

When these two surfaces are not coincident, the pulse is distorted, meaning that the arrival time of the pulse depends on the transverse coordinate, with respect to the wavefront taken as a reference. In other words, the CEP of the pulse varies spatially. The nature of the differences between the pulse front and the wavefront defines the nature of the spatio-temporal distortions.

2.1.2 Temporal contrast

Attosecond generation on a solid target requires a high temporal quality. Any parasitic pulse prior to the main pulse with an intensity higher than the ionization threshold of the target (typically 10^{10} W.cm^{-2}) will be detrimental to the laser-matter interaction. If the parasitic pulse creates a plasma with a density close to the critical density, the ionized target behaves like a mirror and reflects the main pulse, preventing its interaction with the target. In practice, the temporal profile of a pulse is characterized on tens of picoseconds timescale thanks to a high dynamic range ($> 10^{10}$) correlator.

The coherent contrast is defined on a picosecond timescale and reflects the imperfect pulse compression due to uncompensated residual high order terms in the spectral phase, as well as eventual spectral modulations or spectral cutoff. The pedestal surrounding the pulse on a nanosecond timescale is due to the Amplified Spontaneous Emission (ASE). The pump laser duration ($\approx$ 150 ns) is indeed larger than the pulse one, allowing the amplification of the forward fluorescence emitted by the Ti:Sa crystal. The incoherent contrast, named $\mathcal{C}_{ASE}$, is defined as the ratio between the maximum intensity of the pulse and the ASE intensity level.

2.2 Salle Noire 3.0 laser specifications

The laser specifications are summarized in Tab. 2.1:

- The intended energy level is 25 mJ, which is 2.5 times higher than the energy reached in Salle Noire 2.0. This energy level together with the high repetition rate will cause thermal issues, especially in the amplification stages. This makes also the post-compression stage development very challenging.

- The compressed pulse duration should be 20 fs, meaning that the pulse spectral bandwidth should be carefully managed all along the laser chain. The pulse duration can be then reduced to 5 fs using a post-compression stage.

- To achieve an incoherent contrast better than 10^{12}, a double CPA architecture is required [41]. The insertion of a nonlinear temporal filter between the two CPA can improve the contrast by several orders of magnitude.

- Finally, the CEP drift of the final 5 fs pulses should be about 200 mrad RMS for several hours. This is one of the most constraining specifications. The CEP noise is indeed not only degraded by the environment (air flow, mechanical and acoustic vibrations, thermal fluctuations), but also by the nonlinear effects occurring in the amplification and compression stages. This CEP stability requirement dictates the stretcher and compressor design.

Physical quantity	Before PCS	After PCS	Requirement
Energy	25 mJ	15 mJ	Thermal effects management
Repetition rate	1 kHz		
Pulse duration	20 fs	5 fs	20 fs pulses will be achieved after the compressor if a large spectral bandwidth is maintained in the amplification stages and if the spectral phase is kept as smooth as possible. 5 fs pulses will be achieved via a post-compression stage.
Incoherent contrast	$\mathscr{C}_{\mathrm{ASE}} > 10^{12}$		A double CPA architecture with a nonlinear filtering stage are required.
CEP drift	200 mrad RMS		The nonlinear effects in the amplification and compression stages must be minimal. The stretcher and compressor devices must be free from fluctuations (thermal drift, air flow) and from mechanical and acoustic vibrations.

Table 2.1 – Salle Noire 3.0: Laser source specifications. PCS: Post-Compression Stage.

To summarize, the energy level aimed in Salle Noire 3.0 necessitates new developments compared to the current design of the Salle Noire 2.0 laser: a specific stretcher-compressor design, the thermal issues management and a post-compression setup suited to highly intense pulses. The first two issues are addressed in part 1, whereas the last one is studied in part 2.

2.3 Layout of the laser

The future Salle Noire 3.0 will be set up in the Bâtiment P, according to the scheme given on Fig. 2.2. This building was not available during my PhD, so that the beginning of the laser chain was installed in the Salle Azzurra.

The first CPA (Rainbow CEP 4 + FemtoPower Pro HE CEP) was bought from the company FemtoLasers GmbH. This system delivers 1,6 mJ, 30 fs, CEP-stable pulses. Its description and performance are presented in detail in the next chapter. To enhance the temporal contrast of pulses

from the first CPA, an XPW (Crossed polarized wave generation) setup is inserted before the second CPA. This temporal filter allows a contrast enhancement of 3 to 4 orders of magnitude and is based on a third order nonlinear process in BaF_2 crystals. LOA (Laboratoire d'Optique Appliquée) has a strong know-how with this device which was developed by Olivier Albert and Aurélie Jullien a decade ago [42].

The second CPA is composed of an Öffner-type stretcher [43], a Dazzler for dispersion management, a Booster which will be manufactured by FemtoLasers GmbH, a home made Power Amplifier (PA) and a Transmission Grating Compressor (TGC). This architecture choice will be justified in chapter 4. The post-compression stage, including a Hollow-Core Fiber (HCF) and chirped mirrors, is supposed to provide 5 fs pulses. Based on our experience in Salle Noire 2.0, we want to totally avoid air propagation of the 25 mJ, 20 fs pulses. Vacuum chambers will be thus installed to house the compressor as well as the post-compression stage. The dashed grey line on Fig. 2.2 indicates the laser chain stages that should be under vacuum.

During my PhD, I have implemented the first CPA in the Salle Azzurra and worked on its extensive characterization. The XPW stage and Öffner stretcher were also installed in the framework of this thesis. Because of the undergone delay in other equipments delivery, this is the current status of the construction of the laser. However, I have prepared the implementation of the second CPA by dimensioning calculations and making the technological choices for the key elements of the laser system.
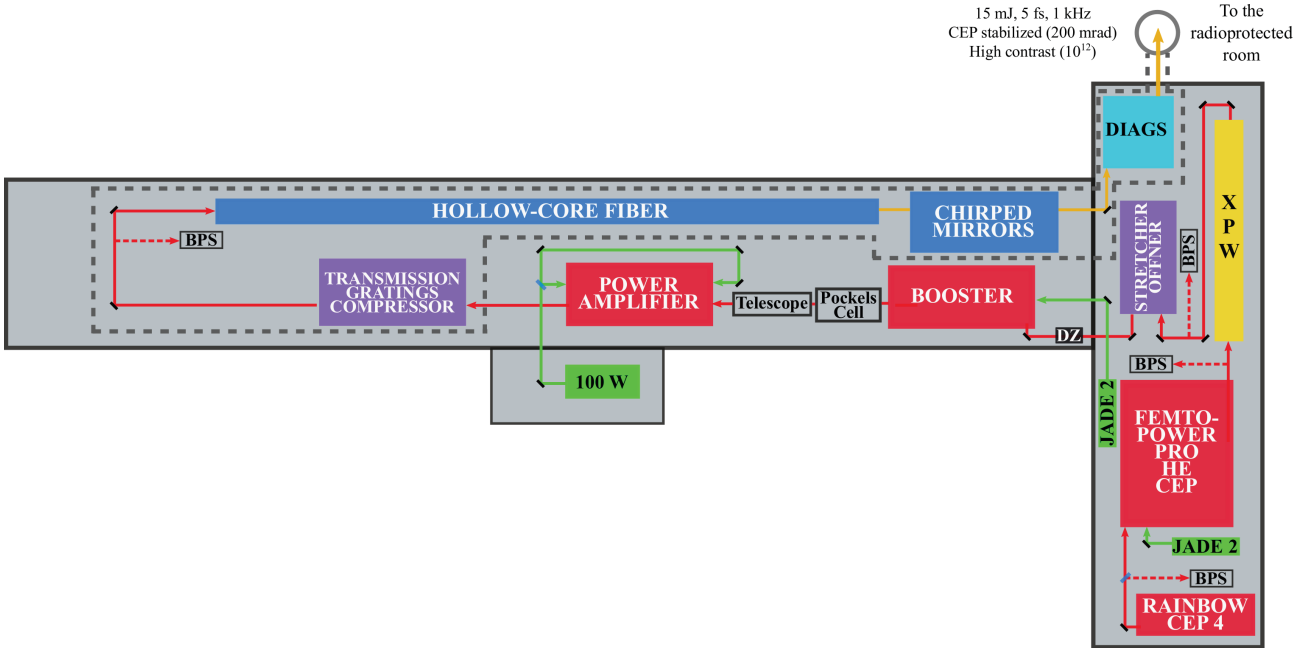
Figure 2.2 – Overview of the future Salle Noire 3.0 in the Bâtiment P. Grey dashed lines mark out the stages under vacuum. BPS: Beam Pointing Stabilization. XPW: Cross-polarized wave generation setup. DZ: Dazzler.

Chapter 3

Front-end performance and characterization

Contents

This chapter is dedicated to the front-end description and characterization. I first describe the oscillator and its CEP stabilization scheme before showing the CPA 1 performances. The differences between the CEP stabilization schemes of the Salle Noire 2.0 and 3.0 are highlighted. Otherwise, results from a spatio-temporal coupling characterization of the front-end are presented. To end this chapter, I mention some preliminary results obtained by implementing a nonlinear temporal filter to enhance the front-end contrast.

3.1 Front-end description

The oscillator together with the first CPA form the front-end. This section aims to give a general description of the front-end of the Salle Noire 3.0, which was bought from the company Femtolasers GmbH. The oscillator model is a Rainbow CEP 4, a Kerr-lens mode-locked oscillator including a CEP stabilization device. The first CPA is integrated in a FemtoPower Pro High Energy CEP, including a stretcher, a multi-pass amplifier and a compressor. A scheme of the front-end is given on Fig. 3.1.
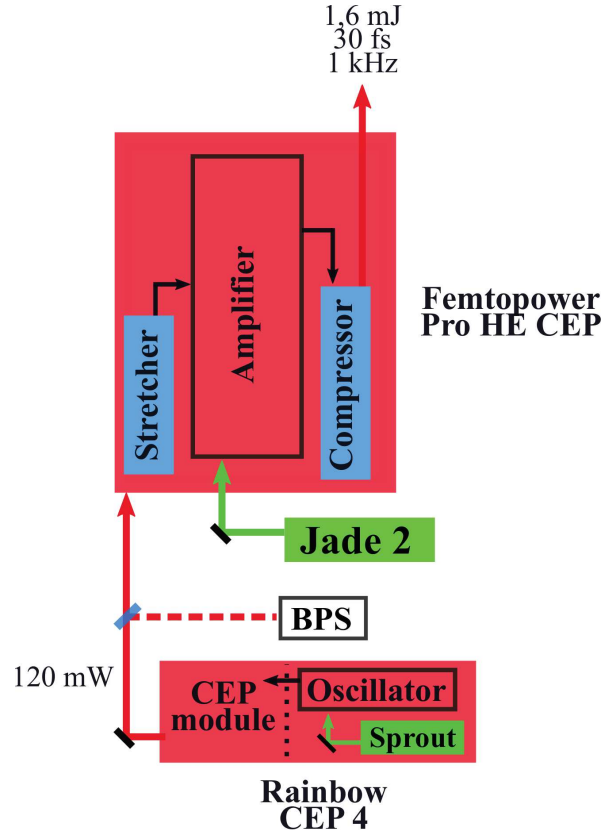
Figure 3.1 – Scheme of the front-end. BPS: Beam Pointing Stabilization.

3.1.1 Oscillator

The oscillator delivers pulses with an energy of 3.7 nJ at 75 MHz repetition rate. Mode-locking is achieved by moving quickly an end-cavity mirror so that the continuous mode experiences high losses and the pulsed mode is favored. The oscillator output spectrum is shown on Fig. 3.2(a). The significant spectral modulations are the consequence of amplitude-to-phase coupling in the Ti:Sa crystal due to SPM (Spectral Phase Modulation) processes. Assuming that pulses are FTL, their duration can be estimated via a Fourier Transform, as illustrated on Fig. 3.2(b). The FWHM pulse duration is found to be about 4.6 fs, which is less than 2 optical cycles as the electric field period at 800 nm is 2.6 fs. A CEP measurement and control module follows the oscillator and is part of

the laser. The paragraph below explains in details how works this CEP module and highlights the differences with the conventional CEP stabilization scheme.
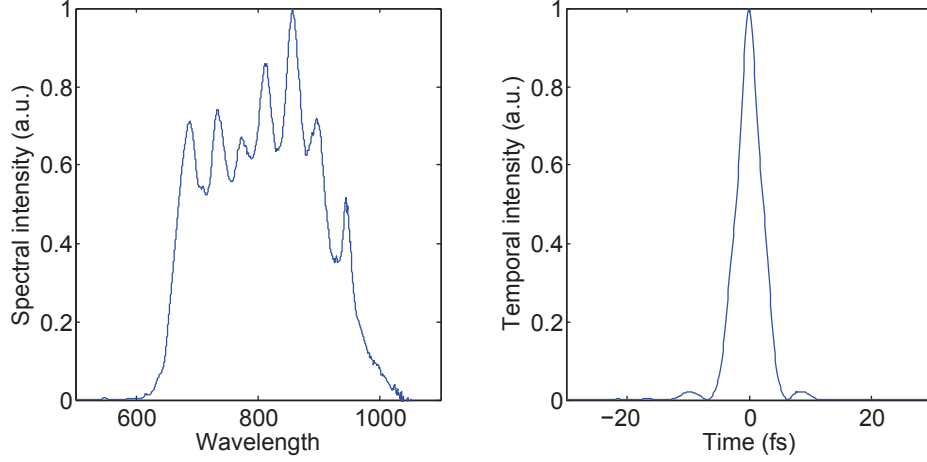
Figure 3.2 – Typical oscillator output spectrum (a) and corresponding temporal profile calculated via a Fourier Transform (b). The intensity FWHM is 4.6 fs assuming FTL pulses.

3.1.2 CEP module

In a dispersive medium, the carrier wave and the pulses envelope propagate at different velocities. As a result, pulses are CEP-shifted. In a laser cavity, thermal, nonlinear and mechanical instabilities in the various dispersive components induce pulse-to-pulse CEP changes, meaning that the resulting pulse train is formed by pulses with different electric field structures. A significant contribution to the pulse-to-pulse CEP change is related to the intensity fluctuations of the pump laser. The CEP is indeed directly affected by the Kerr-induced nonlinear phase in the Ti:Sa crystal, meaning that the pump intensity fluctuations translate into CEP noise.

Carrier Envelope Frequency

A pulses train from an oscillator is described by a frequency comb in spectral domain, with an inter-frequency gap equal to the repetition frequency of the laser, f_{rep}. The phase noise translates into a frequency offset according to:

$$f_{CE} = f_{rep} \frac{\Phi_{CE}}{2\pi} \tag{3.1}$$

where Φ_{CE} is the CEP shift per round-trip and f_{CE} the carrier envelope frequency. The absolute frequency of the spectral line n of the comb is given by:

$$f_n = n f_{rep} + f_{CE} \tag{3.2}$$

A CEP-shift in the temporal domain reflects thus in a shifted frequency comb in the spectral domain. CEP stabilization can be achieved via f_{CE} measurement and stabilization.

CEP measurement in the Rainbow CEP 4

In practice, the CEP drift measurement is achieved in the spectral domain. Among the various existing methods to measure the CEP drift [44], second order nonlinear frequency mixing (Second Harmonic Generation (SHG) or Difference Frequency Generation (DFG)) is usually used. This method requires an octave spanning spectrum and the broadband spectrum from a Ti:Sa based oscillator can be easily extended to a full octave by SPM.

The second harmonic generation of a low-frequency n component of the broadened oscillator spectrum beats with the $2n$ high-frequency component of the oscillator spectrum. The beating frequency is f_{CE}:

$$f_{beating} = 2f_n - f_{2n} = 2[nf_{rep} + f_{CE}] - [2nf_{rep} + f_{CE}] = f_{CE} \qquad (3.3)$$

The same information can be obtained with a DFG process. The only difference is the spectral range of the beat note: a SHG process produces a high-frequency beat note whereas a DFG process produces a low-frequency beat note. The choice between the two processes is driven by the highest quantum efficiency of the photo-detector in the considered spectral range [44].

The question of the optical implementation of the CEP measurement device is now discussed. Usually, the beam is split into two arms: one arm allows to measure the CEP drift and the other arm seeds the following of the laser chain or the experiment. However, any reliable phase-locking device will not compensate the phase jitter experienced by the laser pulses after the beam sample for the CEP measurement. A monolithic In-Loop (IL) interferometer scheme was proposed by [45] and has the main advantage of a unique common beam path. In this approach, the CEP measurement and control are performed directly in the beam which is used in the following of the laser chain (or for applications). Besides, using the full power of the oscillator makes the nonlinear process easier.

In the Rainbow CEP 4, the DFG process is achieved in a PPLN crystal inserted in a monolithic IL interferometer, as described above. The full power is used, meaning that the intensity on the PPLN is very close to its damage threshold. The oscillator delivers on a routinely basis between 270 and 290 mW and the maximum acceptable power on the PPLN is about 300 mW so that the seed power of the CEP module should be checked carefully. After the nonlinear wave mixing process, a dichroic mirror selects the infrared beam at the beating frequency f_{CE} which is then coupled in a photodiode.

Conventional stabilization scheme (Salle Noire 2.0 case)

In a conventional scheme, the CEP stabilization process is based on a Phase-Locked Loop (PLL) between f_{CE} and a reference signal given by the oscillator itself. An Acousto-Optic Modulator (AOM) allows the CEP adjustment via the modulation of the oscillator pump power [46]. This modulation induces indeed a variation of the nonlinear phase-shift experienced by the femtosecond pulses and consequently their CEP. The PLL allows the f_{CE} extraction and frequency-to-voltage conversion, which is constrained by a maximum error margin and a minimum voltage step [47]. The first constrain makes the PLL not robust (a significant CEP drift will be translated into a voltage higher than the fixed margin, interrupting the PLL). The second constrain limits the PLL sensitivity. A compromise must be found between precision and robustness. Moreover, performing a feedback on the pump laser degrades the oscillator performances in terms of output power, pulse duration and round-trip time. Finally, the PLL technique does not allow to achieve $f_{CE} = 0$ as it requires non-zero frequencies for phase comparison.

Feed-forward scheme (Salle Noire 3.0 case)

The feed-forward CEP stabilization scheme was proposed in [48] and leads to the generation of a frequency comb at an arbitrary offset frequency f_{CE} with extremely weak residual phase jitter. To do so, the free-running oscillator is focused in an Acousto-Optic Frequency Shifter (AOFS) of which the driving frequency corresponds to the amplified CE frequency, $f_{CE}(t)$. As a result, the 1st order diffracted beam at the AOFS output corresponds to a frequency comb down-shifted to exactly zero offset, which is a pulse train exhibiting identical electric field structures. Note that no servo-loop control is involved and the pulse train generation is totally decoupled from the stabilization process.

The advantages of this stabilization scheme are numerous, as highlighted in [48, 47] :

- The oscillator runs free, without any intervention on the intra-cavity power.

- The final frequency comb can be synthesized with an arbitrary offset. A zero offset is achieved feeding the AOFS with f_{CE} from the IL interferometer.

- The achievable correction bandwidth is determined by the acoustic delay and is higher than the one in the conventional scheme.

The CEP stabilization of the Rainbow CEP 4 relies on a feed-forward scheme. As explained before, the infrared beam at the beating frequency f_{CE} from the IL monolithic interferometer is measured with a photodiode. Then the beat frequency signal experiences successive filtering and amplification electronic stages before being mixed with a fixed frequency from a RF generator, f_{RF}. The signal is frequency-shifted to decrease the 1/f noise (the CEP noise is close to zero frequency) and to make the detection easier. Finally, the driving frequency of the AOFS is given by:

$$f_{AOFS}(t) = f_{CE}(t) + f_{RF} \tag{3.4}$$

f_{AOFS} is centered at 85 MHz and comprised in a 2 MHz band. A zero offset frequency comb will be achieved if f_{RF} is a multiple of the repetition frequency of the laser. To keep f_{CE} in the bandwidth acceptance of the AOFS, a slow feedback is performed by playing on the Ti:Sa crystal temperature. Finally, another slow feedback rectifies any significant CEP drop by playing on intra-cavity wedges.

Because of this stabilization scheme, the beam pointing at the CEP module output fluctuates permanently, according to the fluctuations of $f_{CE}(t)$. The 1st order diffracted beam after the AOFS is indeed orientated by the driving frequency of the AOFS. Therefore, a beam pointing stabilization (BPS) is required at the CEP module output. The front-end was bought without beam pointing stabilization in a first step and the beam deviation made the output power of the amplifier drop from day to day. Realignment was often necessary and the system was unreliable. The integration of a BPS solved this issue. Note that the output power of the CEP module is 120 mW.

3.1.3 First CPA - description

A FemtoPower Pro High Energy CEP is the first CPA, including a bulk stretcher, a 10-pass amplifier and a Transmission Gratings Compressor (TGC) (see Fig. 3.1). A detailed scheme is given in Appendix B. Pulses are amplified at 75 MHz repetition rate during the four first passes. Between the 4th and the 5th pass, a Pockels cell reduces the recurrence to 1 kHz. The pulse slicer is located inside the amplifier for contrast issues: seeding the amplifier with the full pulse train for the first passes leads to a more complete extraction of stored energy and so to a reduced ASE level. After the pulse slicer, the average power is reduced so that the Dazzler can be inserted for dispersion management.

The amplifier is pumped by a Nd:YLF-type laser (Jade 2, Thales) delivering 25 W at 1 kHz repetition rate. The typical spatial profile of the pump laser within the Ti:Sa crystal has a diameter about 700 µm ($1/e^2$) (see Fig. 3.3). The pump power prior to the crystal chamber is 22 W.
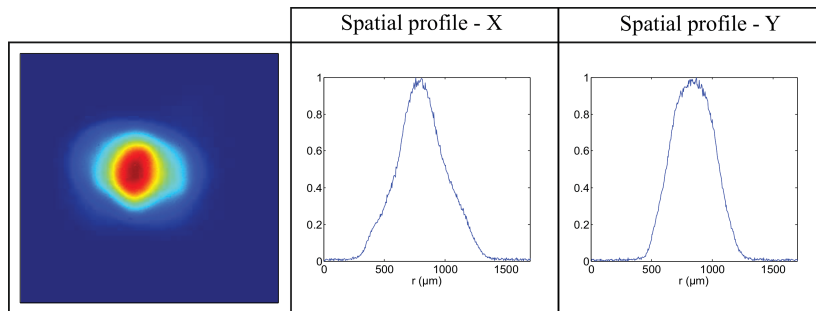
Figure 3.3 – Spatial profile of the pump laser in the Ti:Sa crystal.

Femtosecond CEP-stable lasers require specific stretcher and compressor designs. Both devices are composed of open-space dispersive components, making the propagation of each spectral component very sensitive to environment fluctuations. The optical path through both devices must be reduced as far as possible, by limiting the stretching ratio and improving their compactness. Although their low stretching ratio, bulk stretchers are stable against environmental variations and can efficiently transmit large spectral bandwidths. The GDD introduced by a bulk stretcher can be compensated by a Transmission Grating Compressor (TGC). However, the third order dispersion introduced by the TGC is added to the one introduced by the bulk stretcher, so that a Dazzler is required to manage the third order dispersion. In the FemtoPower, pulses are stretched in bulk to a ten of ps (see the schematic given in Appendix B) and compressed with a TGC. Pulse compression is achieved when the Dazzler settings are typically: 6709 fs, 10000 fs^2, -261000 fs^3 and 290000 fs^4. The separation distance between the gratings (1280 gr/mm, Littrow incidence) is 16 mm so that the TGC introduces -75000 fs^2 and 160000 fs^3. In the last pass of the amplifier, the pulse duration is thus about 7 ps. The beam diameter is set to 10 mm before the TGC to avoid nonlinear effects in the gratings bulk. The typical energy of the 30 fs pulses at the FemtoPower output is 1.6 mJ and can be adjusted playing on the amplitude of the Dazzler acoustic wave. The energy stability is about 2 %RMS and is limited by the pump laser fluctuations (the amplifier is not saturated).

The far field beam profile at the FemtoPower output is shown on Fig. 3.4. A 1 m focal length mirror was used and lead to a beam diameter about 160 µm ($1/e^2$) and an ellipticity of 0,9. This typical beam profile seeded the post-compression setup described in Part 2.
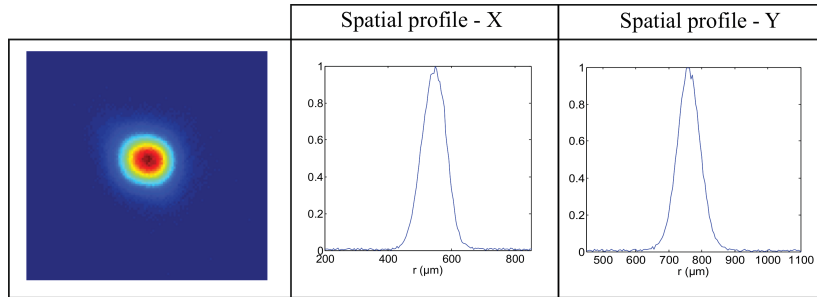
Figure 3.4 – Far-field beam profile at the FemtoPower output.

Finally, the CEP stabilization of the amplified pulses is ensured by the bulk stretcher of which one prism is mounted on piezo-motors (a scheme is given in Appendix A). A commercial f-2f interferometer and software (APS) supplied by MenloSystems enabled the CEP noise measurement and stabilization via a slow feedback on the bulk stretcher.

3.2 CEP stabilization performances

To confirm that CEP stability is preserved at the first CPA output, we measured the CEP noise at the FemtoPower output. Data obtained for an integration time of 1 ms and a slow feedback period on the bulk stretcher of 21 ms are shown on Fig. 3.5 and 3.6. The slow loop efficiency is highlighted: the phase noise is decreased by more than 1 order of magnitude for frequencies below 0.1 Hz. The CEP drift is about 190 mrad RMS and is related to the intensity fluctuations of the pump laser and probably also to the temporary thin optical tables.

The CEP stabilization process of the Salle Noire 3.0 laser should be more robust than the Salle Noire 2.0 one. The fast loop (responsible for the oscillator stabilization) provides a feedback on the AOFS which is external to the oscillator cavity, whereas the slow loop (responsible for the laser system stabilization) provides a feedback on the bulk stretcher in the pre-amplifier. The fast and slow feedback are thus decoupled.

This is not the case in Salle Noire 2.0 were both loops control over the oscillator pump power. Such a stabilization system works for limited CEP noises. When upgrading the laser output energy
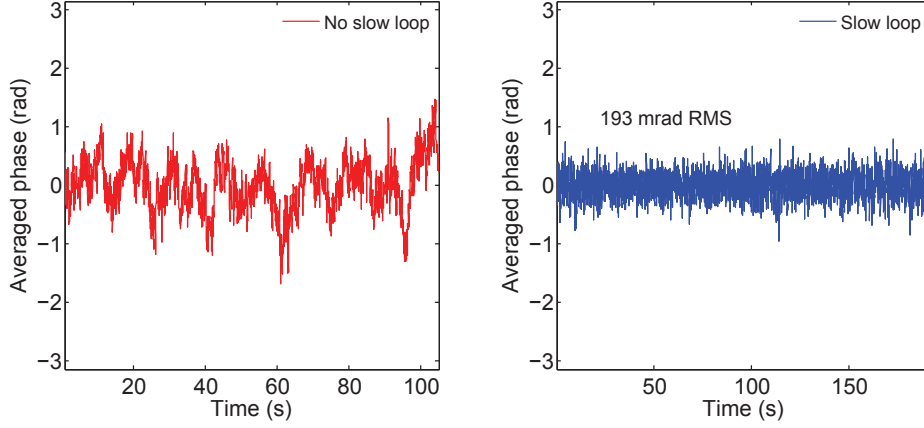
Figure 3.5 – CEP drift at the FemtoPower output when no loop is activated (left, red) and when a slow loop controls the bulk stretcher (right, blue).
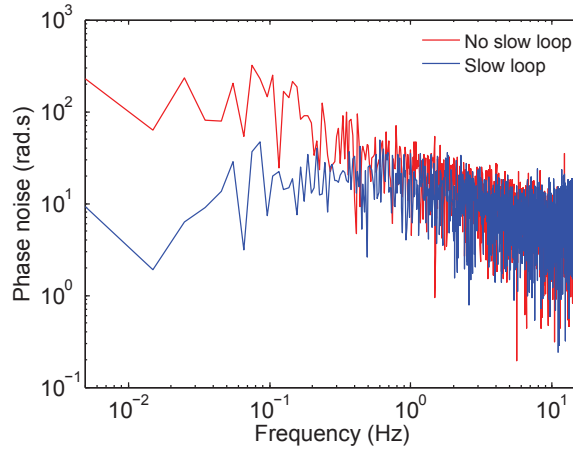
Figure 3.6 – Phase noise when the slow loop is activated or not.

with an additional power amplifier, the CEP noise due to the increased B integral may become too strong to be managed by such a feedback design. This was confirmed by systematic CEP measurements at different stages of the laser in Salle Noire 2.0 (this laser system is described in detail in [9]). The results of this CEP campaign are presented in Appendix C and underline the necessity to move to a new CEP stabilization scheme for the Salle Noire 3.0.

In the following, it is shown that B integral is also detrimental to the laser contrast and more generally to the pulse temporal quality, via the experimental spectro- and spatio-temporal characterizations of the front-end of the Salle Noire 3.0.

3.3 Spectro-temporal characterization

3.3.1 Best performance in terms of coherent contrast

The FemtoPower output pulses were daily measured with a Wizzler device (Fastlite). One of the best performances in terms of coherent contrast is shown on Fig. 3.7: the contrast is 10^{-4} beyond 100 fs. The spectrum measured by the Wizzler device is smooth. A Wizzler-Dazzler loop made the spectral phase flat. In this case, the pulse duration is 33,5 fs.

The spectra recorded before and after the TGC are shown on Fig. 3.8. Both spectra have very similar shape, meaning that negligible nonlinear effects happen in the gratings bulk. Two reflective polarizers were inserted after the compressor to improve the polarization quality of the laser.
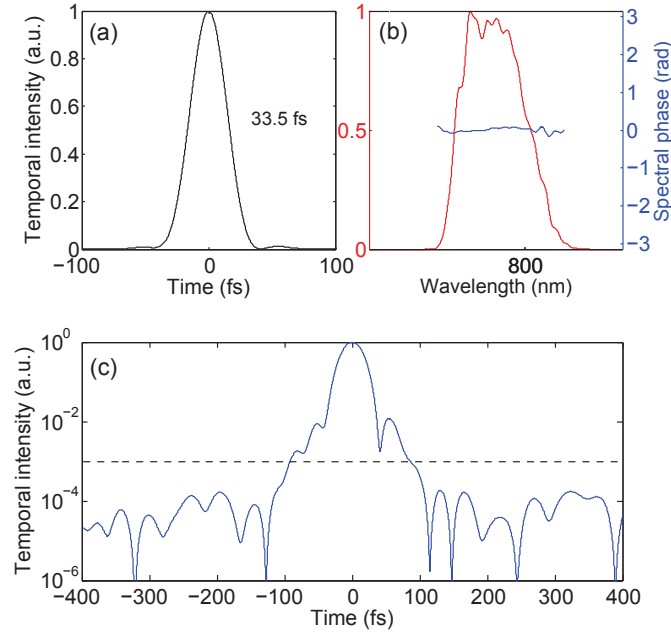
Figure 3.7 – Wizzler measurement after the first CPA. The pump power is 22 W (the measurement was performed just before the crystal chamber).
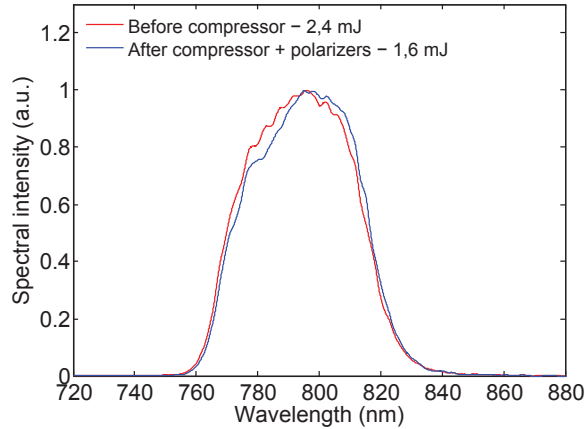
Figure 3.8 – Spectra before and after compressor.

3.3.2 Coherent contrast issues

The Wizzler measurements highlighted sometimes the presence of a parasitic pulse delayed by 212 fs from the main pulse, as shown on Fig. 3.9. This post-pulse might be caused by polarization changes within the amplifier, as explained below.

A contribution to the laser pedestals might be related to the birefringence of the Ti:Sa crystals and is strongly dependent on the beam path. Amplifiers are usually designed so that the pulses polarization is parallel to the extraordinary axis of the Ti:Sa crystal. The emission cross section is indeed inversely proportional to the square of the refractive index. As the Ti:Sa crystal is a negative uniaxial medium, the ordinary index (n_o = 1.7601 at 800 nm [49, 50]) is higher than the extraordinary one (n_e = 1.7522 at 800 nm [49, 50]), meaning that the stimulated emission cross sections is higher when the incident pulse polarization is parallel to n_e [51]. When the pulses to be amplified are P-polarized, the Ti:Sa crystal is thus mounted so that its extraordinary axis is horizontal.

A slight mismatch between the incident polarization and the extraordinary axis of the Ti:Sa
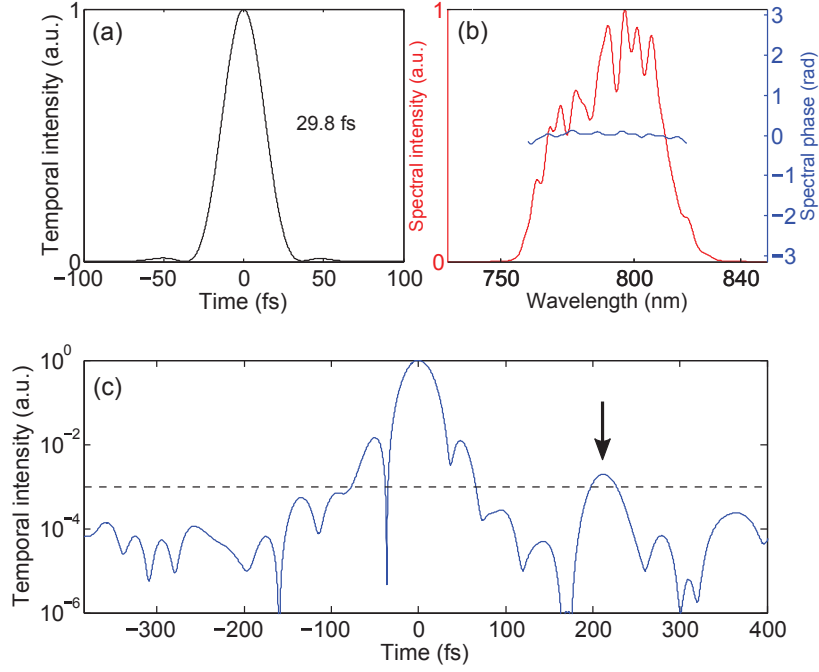
Figure 3.9 – Wizzler measurement after the first CPA. A parasitic pulse appears at 212 fs from the main pulse.

crystal is responsible for the creation of a small S-polarized component delayed from the main P-polarized pulse by the quantity:

$$\tau = \frac{L}{c}(n_o - n_e) \tag{3.5}$$

where L is the Ti:Sa crystal length, n_o and n_e the ordinary and extraordinary indices of the medium. In the case of the 8 mm-long crystal inside the Femtopower, τ is found to be about 210 fs. The post-pulse intensity depends on the incident polarization orientation with respect to the extraordinary axis of the Ti:Sa crystal. If the post-pulse observed on the Wizzler measurement is due to the birefringence of the Ti:Sa crystal, its polarization should be S. However, the polarization of the post-pulse could not be clearly determined.

To conclude, it seems that the laser pedestal is degraded by polarization changes in the bire-fringent amplifier medium. If this hypothesis is true, the coherent contrast cannot be controlled easily as it is related to the amplifier alignment which is driven by two pierced plates (one hole for one pass at each side of the crystal). Furthermore, the crystal mount is fixed and cannot be rotated. The fluctuations of the coherent contrast can affect the good operation of any nonlin-ear stage afterwards the amplifier, even more so when nonlinear temporal diffraction phenomena occur in addition to polarization changes in the amplifier.

3.3.3 Degradation of the coherent contrast by nonlinear temporal diffraction

Non-linearities experienced by the stretched pulses in the laser chain materials, and especially in the amplification media, can turn post-pulses into pre-pulses. The pre-pulse amplitude depends on the accumulated B integral in the material. This phenomenon is usually called 'nonlinear tem-poral diffraction'.

Theoretical overview

The nonlinear temporal diffraction phenomenon is explained in detail in [52]. In this paper, it is shown that the propagation of two identically polarized stretched pulses partially overlapped in

a laser gain medium leads to the generation of new pre- and post-pulses once the pulse is compressed, even though the B integral is low (0.3 rad). This can be explained by a Four Wave Mixing (FWM) process occurring between the frequencies of the main pulse and the post-pulse.

The instantaneous frequencies of the main pulse and the post-pulse can be expressed as follows:

$$\omega_M(t) = \omega_0 + 2b\,t \tag{3.6}$$

$$\omega_P(t) = \omega_0 + 2b\,(t - \tau) \tag{3.7}$$

where b is the temporal chirp parameter and τ the delay between the main pulse and the post-pulse. The FWM process is governed by the third order nonlinear susceptibility and creates instantaneously new frequencies, like:

$$2\omega_M - \omega_P = \omega_0 + 2b\,t + 2b\,\tau \qquad\qquad \text{blue-shift} \tag{3.8}$$

$$2\omega_P - \omega_M = \omega_0 + 2b\,t - 4b\,\tau \qquad\qquad \text{red-shift} \tag{3.9}$$

When the chirped pulses are re-compressed, the newly created frequencies '$2\omega_M$-ω_P' (resp. '$2\omega_P$-ω_M') are advanced (resp. postponed) by τ relative to ω_M. A pre-pulse appears at t = -τ (Eq. 3.8) and another post-pulse at t = +2τ (Eq. 3.9). More generally, the FWM process generates many pre- and post-pulses shifted from the main pulse by a multiple of the initial delay between the post-pulse and the main pulse. This explains the designation 'temporal diffraction'. It is also interesting to notice that the spectral content of the newly created N-order pulses is shifted by a the product 2N b τ. Pre-pulses are blue-shifted whereas post-pulses are red-shifted.

The FWM process was described above in the case of identically polarized pulses. However, such a process occurs no matter the polarization orientation of the post-pulse with respect to the main pulse. Only the efficiency of the process can be affected by the initial polarization states of the pulses. Besides, the numerical simulations presented below will specify the polarization states of the newly created pulses in the case of incident cross-polarized pulses.

Nonlinear temporal diffraction within the FemtoPower

Some Wizzler measurements evidenced the presence of not only a post-pulse at t $\approx$ 200 fs, but also of a pre-pulse at t $\approx$ -200 fs (see Fig. 3.10). The laser spectrum measured by the Wizzler device becomes strongly modulated. The flat spectral phase confirms that the parasitic pulses are not related to uncompensated phase terms. The appearance of a pre-pulse at a delay similar to that one of the initial post-pulse suggests that nonlinear temporal diffraction occurs within the amplifier. The B integral is indeed not negligible because of the limited stretching ratio. Moreover, the presence of these parasitic pulses was experimentally confirmed by the spatio-temporal characterization of the laser (see section 3.4).

To go further, I performed numerical simulations with MIRO [53]. The post-pulse relative intensity is set to 10^{-3} and delayed from the main pulse by 200 fs. Both pulses are cross-polarized. The stretched pulse duration is 10 ps and the B integral is about 1,8 rad. The compressor compensates strictly the stretcher dispersion so that the phase of the output pulses corresponds to the nonlinear phase.

Fig. 3.11 shows the temporal intensity of compressed pulses along X (P polarization) and Y (S polarization). In case I (resp. case II), the polarization directions of the post-pulse and the main pulse are parallel (resp. crossed). When B = 0, no pre-pulse is created, whereas when B = 1,8, pre- and post-pulses are generated on either side of the main pulse in both cases. In case II, odd order pulses are polarized parallel to the initial post-pulse whereas even order pulses are polarized parallel to the main pulse. Otherwise, the process is more efficient in case I as the relative intensity of the 1st order pre-pulse is 10^{-3}, compared to 10^{-4} in case II.

The spectral shift of the pre-pulse can be evaluated via the product 2b$\times\tau$ (see Eq. 3.8). In the case of a 30 fs pulse stretched up to 10 ps, the temporal chirp parameter is about $4,62.10^{24}\,\text{s}^{-2}$. If
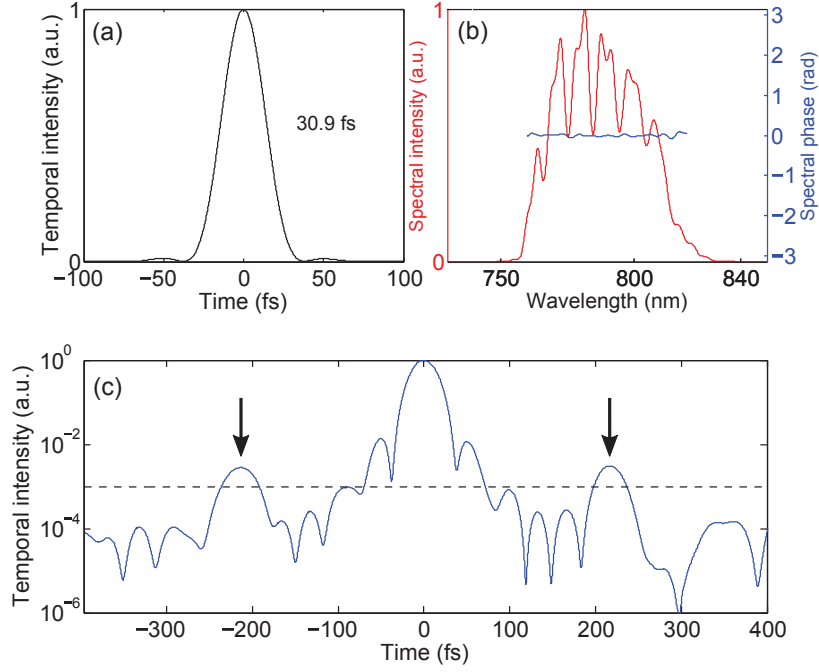
Figure 3.10 – Wizzler measurement after the first CPA. Two parasitic pulses appear at -212 fs and +217 fs from the main pulse.
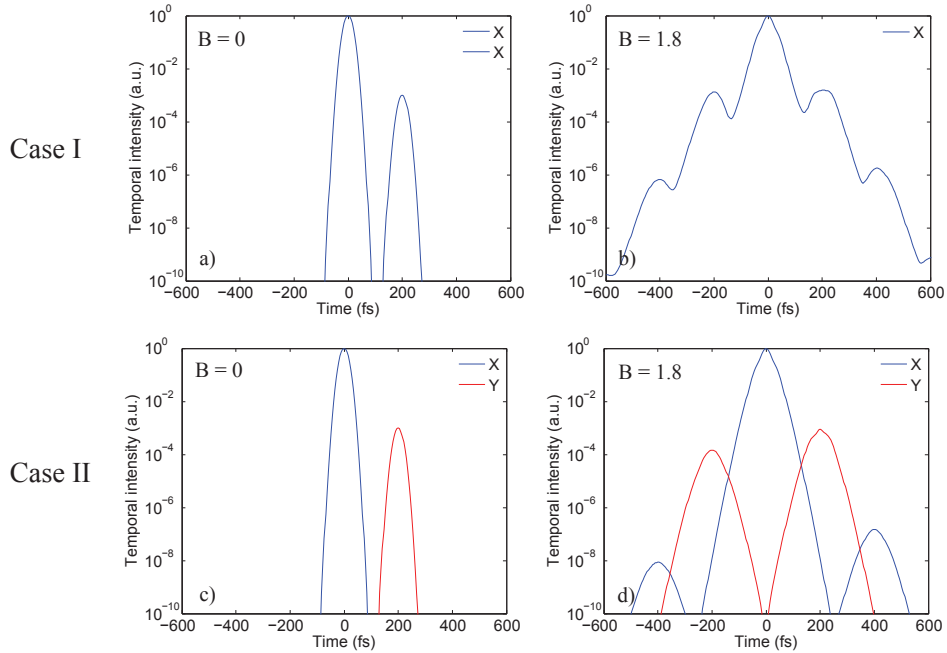
Figure 3.11 – Temporal intensity of the compressed pulse ahead (a,c) and afterwards (b,d) the nonlinear medium for B = 0 and B = 1,8. In case I (a,b) (resp. case II (c,d)), the polarization directions of the main pulse and the post-pulse are parallel (resp. crossed).

the initial post-pulse is delayed from the main pulse by 200 fs, the product $2b \times \tau$ is $18,48.10^{11}$ s^{-1}, corresponding to a spectral shift from 800 nm about 0,6 nm. In this case, the product $2b \times \tau$ is too small to induce a significant spectral shift. Another case of nonlinear temporal diffraction with significant spectral shift will be presented in section 4.3.

To conclude, the Wizzler device evidenced the presence of pre- and post-pulses. During the first passes in the amplifier, a mismatch between the laser polarization and the extraordinary axis

of the Ti:Sa crystal can induce a post-pulse delayed from the main pulse by τ = 200 fs according to the birefringence properties of Ti:Sa. Because of B integral issues in the following passes, nonlinear temporal diffraction occurs. In this way, many post- and pre-pulses are created and delayed from the main pulse by a multiple of τ. Otherwise, numerical simulations underlined that when the main pulse and the initial post-pulse are cross-polarized, the newly created replicas are alternatively S and P-polarized. This study aimed to characterize and understand the origin of the coherent contrast degradation on a timescale of only 1 ps. In the following, the temporal characterization of the laser is completed by a contrast measurement on several hundreds of ps.

3.3.4 Incoherent contrast measurement

The laser pedestal is limited by ASE (Amplified Spontaneous Emission) on a nanosecond timescale. In this way, a complete temporal characterization of the front-end output pulses will be achieved by measuring their temporal profile on several hundreds of ps.

A high dynamic 3rd order correlator (Sequoia, Amplitude Technologies) was used to quantify the incoherent contrast of the front-end. Two measurements were performed: one on a long delay range with low resolution (Fig. 3.12) and another one on a short delay range with higher resolution (Fig. 3.13). As announced by the laser supplier, the incoherent contrast is well 10^{-8}. Such a high contrast is achieved thanks to the clever location of the Dazzler inside the amplifier, as mentioned above. The pierced plates allow also to maximize the contrast, spatially filtering the beam before and after each pass in the crystal.
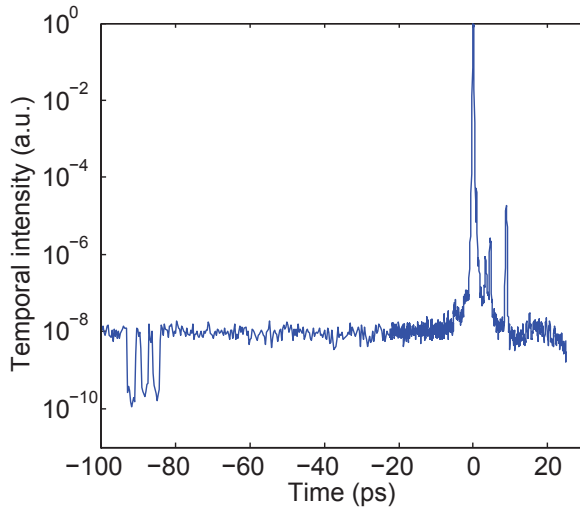
Figure 3.12 – Contrast measurement of the first CPA output on a long delay range.
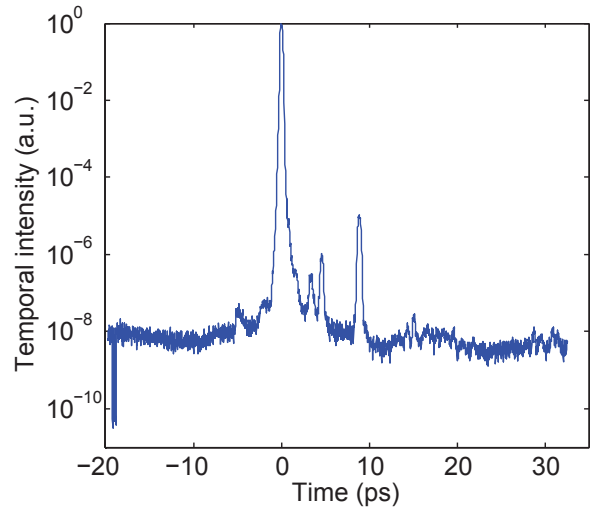
Figure 3.13 – Contrast measurement of the first CPA output on a shorter delay range with a reduced time step.

To conclude, this section proposed a spectro-temporal characterization of the front-end. Both coherent and incoherent contrast were measured. The experimental and theoretical analysis of the coherent contrast issues suggested that polarization changes and nonlinear temporal diffraction effects happen during the amplification process. Finally, the pre- and post-pulses evidenced by the Wizzler device were confirmed by the spatio-temporal characterization shown in the next section.

3.4 Spatio-temporal coupling

The Spatio-Temporal Coupling (STC) is defined as a spatial variation of a temporal property of the pulse or a temporal variation of the beam spatial properties. STC translates into an increased pulse duration [54] and an increased focus spot, strongly reducing the laser peak intensity [55, 56].

The STC characterization is very interesting to know the actual peak intensity and deduce the nature of the interaction regime when investigating ultrafast phenomena as plasma dynamics. It is also interesting to use STC diagnostics at various stages of the laser system to understand the different contributions to the overall STC or to simply achieve a better understanding of the physical processes involved in the laser system.
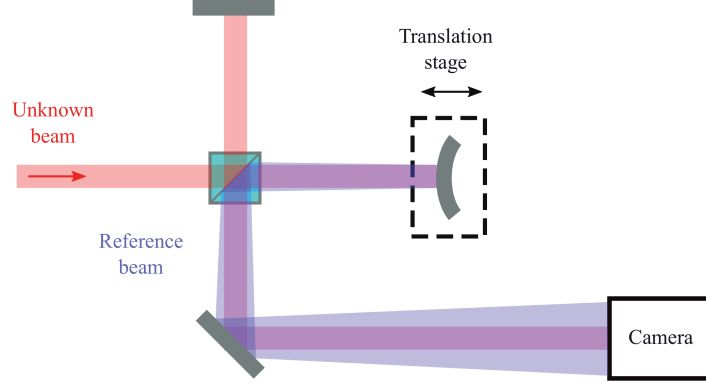
Figure 3.14 – Principle of a STC diagnostic based on the TERMITES technique.

Recently, a STC diagnostic based on the TERMITES technique ("**T**otal **E**-field **R**econstruction using a **M**ichelson **I**nterferometer **TE**mporal **S**can"), was developed in CEA [57, 58]. This diagnostic consists in a Michelson interferometer where one of the arms contains a convex mirror which makes the beam diverge to produce a reference beam. An illustration of the setup is given on Fig. 3.14. At the interferometer output, the splitting optics recombines spatially the unknown beam and the reference beam so that spatial interferences occur. The detection plane location is determined by the ratio between the diameters of the collimated beam (unknown beam) and the divergent beam (reference beam). This ratio should be large enough to assume that the divergent beam exhibits no STC in the area delimited by the collimated beam. This also ensures that interferences occur over the entire diameter of the unknown beam. The interference pattern is recorded as a function of the delay between the two beams. The resulting set of images (one scan generates 45 Gb of data!) can be then Fourier-analyzed with an iterative algorithm to recover the spatio-spectral laser electric field. The algorithm steps are described in detail in [58].

In the framework of a collaboration with the CEA, a TERMITES-based diagnostic was built for the front-end of the Salle Noire 3.0. In the previously proposed setup [58], a plate was used as a beam splitter. A compensation plate was inserted in the reference arm to balance the GDD experienced by both beams and thus maximize the fringes contrast. This solution requires that both plates have the same thickness, especially when working with few-cycle pulses. Another elegant solution is to use a cube as a beam-splitter. In this way, the GDD is the same for both beams and the setup is simplified. A picture of the setup is shown in Fig. 3.15.

Experimental setup parameters

The ratio $\gamma = d/D$ between the diameters of the collimated beam and the reference beam in the detection plane should be first determined. This ratio should be as small as possible to achieve a precise electric field reconstruction with negligible distortion effects. At the same time, a small γ value makes the fringes contrast too low and the fringes width too small to be correctly resolved. As a compromise, γ was set to 0,5. The diameter of the beam to characterize is here ≈ 10 mm.

$$f' = \frac{L}{\gamma^{-1} - 1} \tag{3.10}$$

The device must be as compact as possible to limit the influence of environmental fluctuations. In the experiment, the camera was located at 50 cm from the divergent mirror. The focal length of the divergent mirror is then given by Eq. 3.10 (see on Fig. 3.16) and is found to be -50 cm.
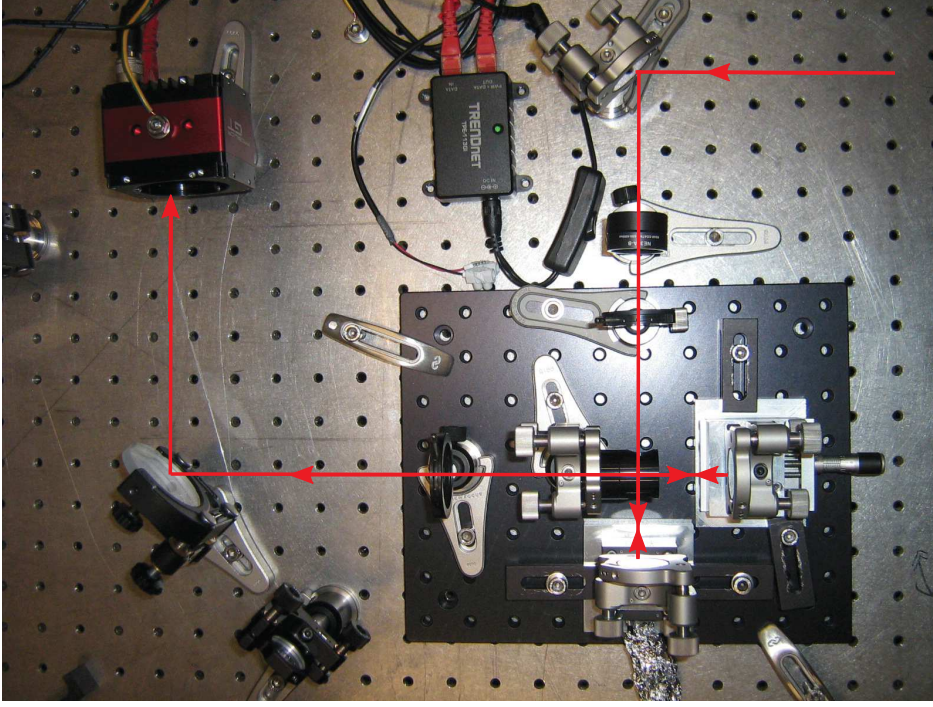
Figure 3.15 – Experimental setup of a STC diagnostic based on the TERMITES technique.

The fringe contrast can be optimized by replacing the plane mirror of the interferometer by a partially reflective optics, as suggested in [58]. However, the contrast we obtained was largely enough to perform a good quality measurement and electric field reconstruction. Silver mirrors were used in both arms (UltraFast Innovations).
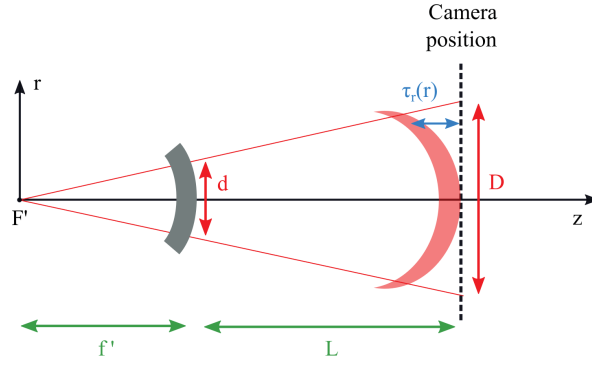
Figure 3.16 – Parameters of the reference beam. f' is the focal length of the divergent mirror, L the distance between the divergent mirror and the camera. d and D are the reference beam diameters respectively on the divergent mirror and in the camera plane.

Translation stage parameters

The delay-scan has to be performed on a range $\Delta\tau$ to get fringes on the whole unknown beam diameter. $\Delta\tau$ can be estimated by the sum of the radial delay $\tau_r(r = D/2)$, corresponding to the curvature of the reference beam (see Fig. 3.16), and the coherence time of the laser source. According to [58], $\Delta\tau$ can be expressed as:

$$\Delta\tau \approx \frac{D^2}{8\,(L+f)\,c} + \frac{2.4\,\lambda_0^2}{c\,\Delta\lambda} \tag{3.11}$$

The travel range of the translation stage can be determined with Eq. 3.12 and is about 34 µm. In practice, the delay scan is started a few microns before the delay position at which the first fringes

appear and is ended a few microns after the last fringes disappear. It is also interesting to explore a larger delay range to measure eventual pre- and post-pulses on either side of the main pulse.

$$\Delta z = \frac{c \, \Delta \tau}{2} \tag{3.12}$$

Then, the scan step size in delay, $\delta \tau$, has to be determined to achieve a good quality electric field reconstruction. The periodic signal will be properly sampled if the sampling step is two times smaller than the oscillation period of the electric field. Therefore, $\delta \tau_{max}$ is given by:

$$\delta \tau_{max} = \frac{T}{2} = \frac{\lambda_0}{2 \, c} \tag{3.13}$$

In practice, the maximum mechanical step of the translation stage is calculated as follows:

$$\delta z_{max} = \frac{c \, \delta \tau_{max}}{2} = \frac{\lambda_0}{4} \tag{3.14}$$

and is about 187 nm.

A translation stage from Physik Instrumente (P621) featuring a travel range of 100 µm and a resolution better than 0.5 nm was used. The mechanical step during the scans was set to ≈ 150 nm and the total delay range was 666 fs.

Camera requirement

The interference pattern was recorded with a highly resolved camera featuring a large dynamic range (Prosilica GT 6600, Allied Vision). The pixel size is 5.5 µm, which is small enough to resolve the fringes at the edges of the beam with our experimental setup. According to [58], the fringe spacing on the beam edges can be approximated by:

$$i_{min} \approx 2 \frac{\lambda_0 (L + f)}{D} \tag{3.15}$$

and is about 80 µm. The minimum number of pixels can be deduced according to: $N_{min} = 2D/i_{min}$ [58]. In practice, one fringe should be as large as 5 pixels to ensure a correct reconstruction. In this case, the smallest fringes are as large as a ten of pixels.

The sensor of the camera we used is composed of 6576×4384 pixels. One interferogram is thus made of 29 millions of points, which considerably limits the acquisition rate. The laser repetition rate is here 1 kHz and does not limit the acquisition speed. The duration of a scan was about 20 min. The measurement is thus influenced by the fluctuations of the laser and of the environmental conditions.

Experimental results - Data processed by Gustave Pariente (CEA, High intensity physics group)

The compressor influence was investigated. Doing so, we performed two STC characterizations at the FemtoPower output: one when the compressor is included in the beam path and another one when the compressor is bypassed. The integration time of the camera was set to 5.5 ms. The pulse energy after compression was 1.8 mJ. The energy was attenuated prior to the TERMITES device using wedges.

Fig. 3.17 and Fig. 3.18 show respectively interferograms at various delays when the compressor is bypassed and when it is included in the beam path. When scanning the delay, the fringes move radially. The travel range of the translation stage is 100 µm which corresponds to a delay excursion of 666 fs. At a delay about 324 fs, circular fringes can be observed almost on the whole area of interest because of the temporal overlap between the reference beam and the unknown beam. In both cases, we noticed the appearance of fringes at 131 fs and 507 fs, meaning that a pre and a post-pulse are observed at $\approx \pm 200$ fs from the main pulse. This confirms the observations made previously with the Wizzler device. Otherwise, the beam intensity is uniform and radially symmetrical when the compressor is bypassed. The fringes at $\approx \pm 200$ fs from the main pulse are

also spatially homogeneous. It is not the case any more when the compressor is included in the beam path: the radial symmetry is lost and the beam is spatially distorted.
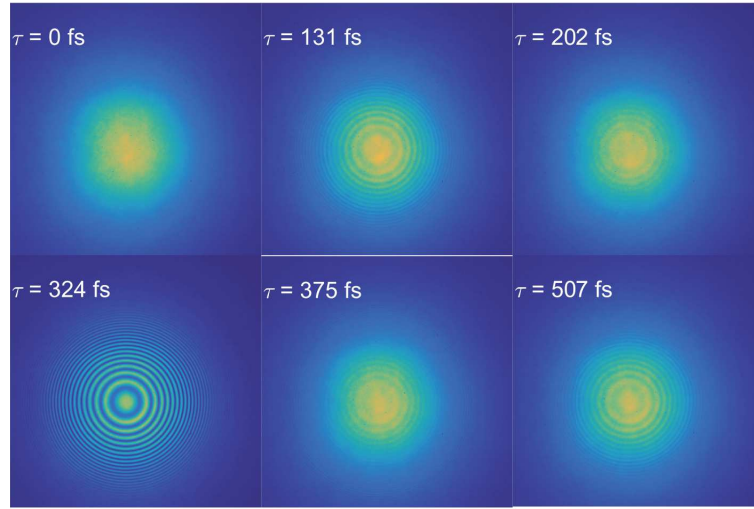
Figure 3.17 – CCD images at various delays when the compressor is bypassed.
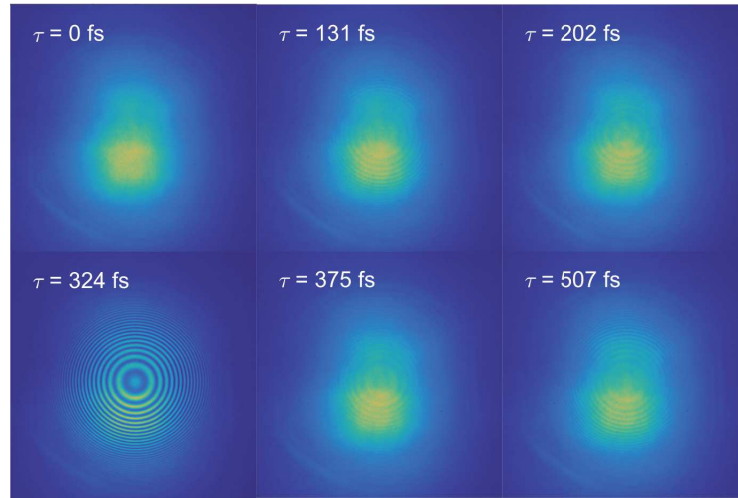
Figure 3.18 – CCD images at various delays when the compressor is included in the beam path.

Fig. 3.19 shows the amplitude and phase of the electric field in both configurations (compressor bypassed and compressor included in the beam path) at three different wavelengths (777 nm, 783 nm and 793 nm). Intensity profiles (Fig. 3.19a,b,c) are uniform and similar for the three wavelengths when the compressor is bypassed. However, when the compressor is included in the beam path, the intensity profiles are asymmetrical and very different from wavelength to wavelength. An intense lobe appears progressively for positive values of Y with the decreasing wavelength. It seems that the compressor introduces angular dispersion. When a laser pulse experiences angular dispersion, its different spectral components have slightly different propagation directions. Therefore, angular dispersion induces another STC: spatial chirp. Each spectral component has a spatial distribution different from the other ones.

The phase profiles (Fig. 3.19d,e,f) highlight the presence of angular dispersion due to the gratings of the compressor. Note that the rings and straight lines observed on the phase profiles are artifacts. When the compressor is bypassed, the phase profiles are globally uniform and flat. This

is clearly visible on the phase profiles along Y=0 (Fig. 3.19g,h,i). When the compressor is included, the phase profiles along Y=0 feature different behaviors. In particular, the edge wavelengths exhibit two opposite slopes whereas the phase profile along Y=0 of the middle wavelength evolves continuously and linearly with the X coordinate.
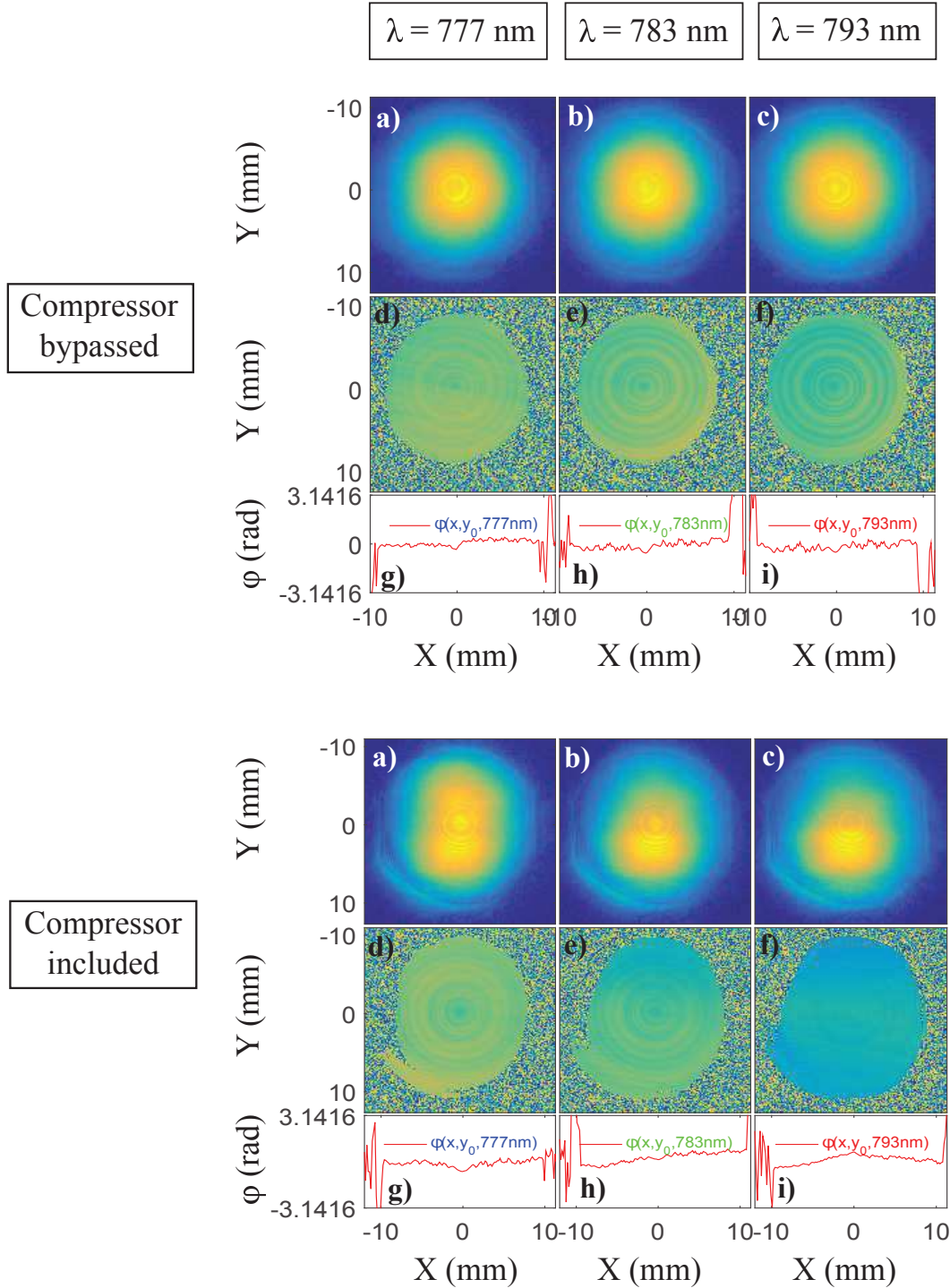
Figure 3.19 – Projections of the completely reconstructed E-field, when the compressor is bypassed or not, at three different wavelengths. (a,b,c) 2D amplitude of the beam. (d,e,f) Phase profile. (g,h,i) Phase profile along Y=0. *Circles and straight lines on the 2D spectral phase and amplitude profiles are artifacts.*

Because of a misalignment of one of the gratings in the compressor, angular dispersion makes the pulse spectral components propagate in different directions. As a consequence, a spectral phase shift is created and leads to a linear phase chirp which depends on the spatial coordinates. In other words, a group delay is introduced and varies transversely within the beam. The laser

37

pulse front is thus tilted with respect to the phase fronts.

The laser beam at focus was calculated with a 2D Fourier Transform with respect to the transverse coordinate **r**, assuming a perfect focusing optics with a focal length of 100 mm. An illustration of the spectrally-resolved focal spot intensity profiles is given in both cases (without and with compressor) on Fig. 3.20. In the case where the compressor is bypassed, no spatial chirp can be noticed. Some modulations are visible on the pulse intensity and are due to the pre and post-pulses. When the compressor is included, a spatial chirp can be noticed in both directions but is more pronounced in the Y direction. This is related to the deliberate misalignment of the first grating of the compressor, as explained in the below paragraph.

The gratings lines are vertical but a crossed periscope on the beam path reverses the coordinates: the gratings lines are thus parallel to the X direction. One of the grating was deliberately misaligned by Femtolasers: it was tilted in the neutral direction, which is the vertical direction, to avoid back reflection in the amplifier. It was indeed observed that when the TGC alignment was optimal (ie, exactly at Littrow incidence), a leak went back in the amplifier and oscillated between retro-reflectors so that the gain medium could be depleted by the parasitic pulse. In this case, the output energy of the amplifier dropped to almost zero. Some other times, the leak did not deplete the gain medium but was amplified enough to damage some optical components. The misalignment of the first grating was thus recommended by the laser supplier. It should be noted that the significant sensitivity of the amplifier to low energy back reflection is due to the strong pumping regime.
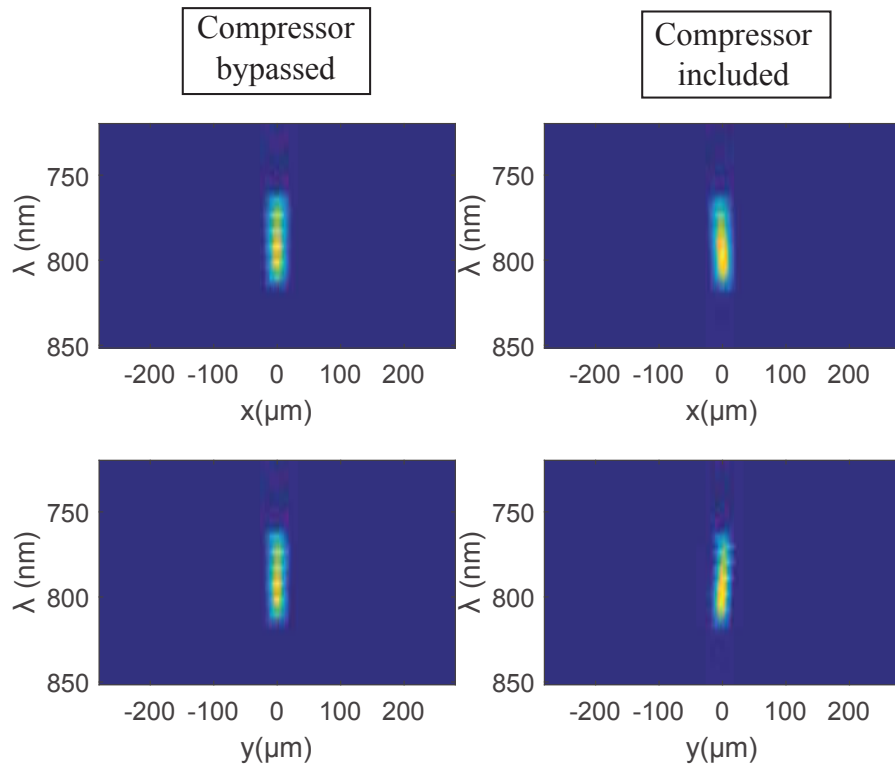
Figure 3.20 – Spectrally-resolved focal spot intensity profiles (calculated), with and without compressor in the beam path.

To conclude, a STC diagnostic based on the TERMITES technique was built. This device can support a 10 mm beam. Its compactness makes it few sensitive to the environmental conditions fluctuations and easy to move from a laser system to another one (footprint: 20×30 cm). The use of a cube as a beam-splitter reduces the number of optics and so the potential STC sources introduced by the device itself. The compressor contribution to STC was investigated at the FemtoPower output. When the compressor is bypassed, the beam presents negligible STC: the 2D amplitude and phase profiles are homogeneous, meaning that the amplifier provides good qual-

ity pulses although the limited stretching ratio and the presence of numerous optics. The main measured default was the presence of significant pre and post-pulses at ± 200 fs from the main pulse, as measured previously with the Wizzler device. The intensity modulations observed on the laser beam focus spot are related to the presence of these parasitic pulses. The compressor clearly degrades the pulses quality, introducing angular dispersion which translates into spatial chirp. These data are still being processed in CEA to achieve a better understanding of the compressor contribution to the observed STC.

In the previous sections, a detailed characterization of the front-end in terms of CEP performances, spectro-and spatio temporal quality was performed. The next stage of the laser chain consists of a nonlinear filter for contrast enhancement and was implemented, as explained in the paragraph below.

3.5 Contrast enhancement of the front-end

To enhance the temporal contrast of pulses from the first CPA, an XPW (Crossed polarized wave generation) setup is required before the second CPA. XPW generation is a third order nonlinear process, meaning that there is a cubic dependance between the final and initial intensities. This provides an improvement of the pulses temporal contrast (3 to 4 orders of magnitude), as well as pulse shortening (the minimum duration ratio is $\sqrt{3}$) [42, 59]. More details are given in Part 2. Here, I present the technical implementation of the XPW setup, which is an improved version of the setup used in Salle Noire 2.0.

3.5.1 Setup description
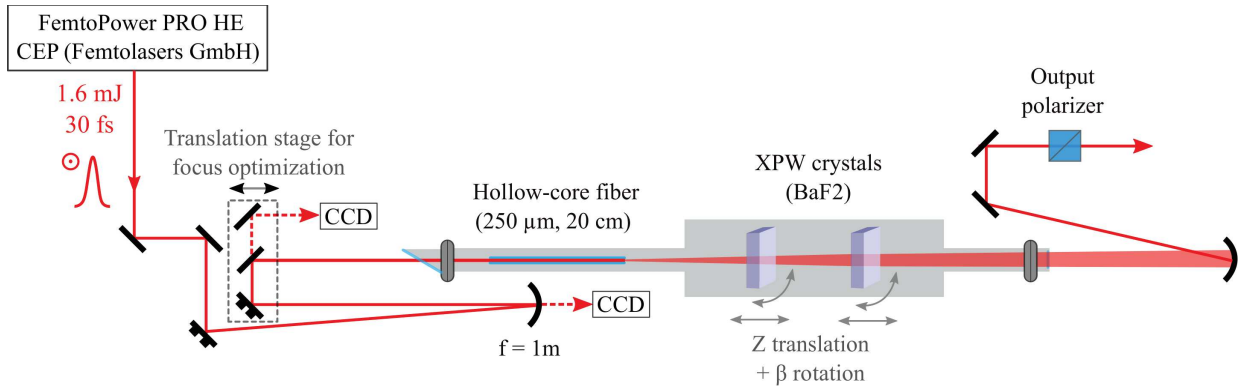
Figure 3.21 – XPW setup for contrast enhancement between the two CPA. The orientation of each crystal is defined by β, the angle between the input polarization direction (P) and the crystallographic axis of the crystal.

The XPW setup of the Salle Noire 3.0 was elaborated in the framework of a collaboration with Sourcelab. The prototype is illustrated on Fig. 3.21. A four axes Beam Pointing Stabilization ensures efficient and stable coupling in a 20 cm long hollow-core fiber with an inner diameter of 250 µm. The spatial filtering stage prior to XPW generation is indeed crucial to achieve significant conversion homogeneously [60]. The three 45° mirrors prior to the vacuum setup are placed on a single translation stage so that the focus position can be adjusted from day to day. The vacuum setup entrance window is placed at Brewster incidence for two reasons: (i) it cleans the incident polarization. (ii) eventual back reflection in the amplifier are avoided. However, the output window was at normal incidence in a first step to characterize the XPW efficiency easily.

The fiber is followed by two 1.5 mm-thick XPW crystals (BaF$_2$) placed in the divergent beam under vacuum. Their mounts allow two degrees of freedom: a Z translation and a rotation in the plane perpendicular to the laser propagation direction. The intensity on each crystal can be adjusted playing on the Z positions of the crystals, whereas the crystallographic axis orientation of
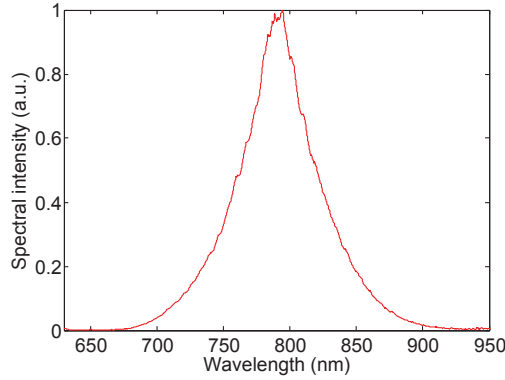
Figure 3.22 – XPW spectrum obtained at the output of the Sourcelab prototype. A Glan polarizer was used. Efficiency conversion is 30 %.
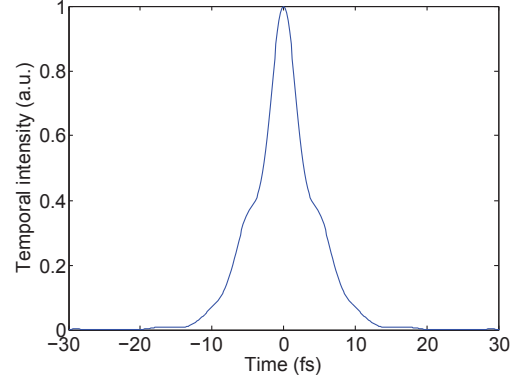
Figure 3.23 – Fourier Transform of the XPW spectrum measured after the Glan polarizer. The FTL FWHM duration is 5 fs but the pulse pedestal is larger.

each crystal relative to the incident polarization direction can be tuned by rotating the crystals mounts. The advantage of using two crystals rather than a single one is that intensity can be relaxed on the first crystal to avoid damaging issues. Additional conversion in the second crystal enables a high XPW efficiency, which is defined as the energy ratio before and after the output polarizer. This component is placed in the output collimated beam and allows to discriminate the XPW along the S direction as the incident beam is P-polarized. The quality of the incident polarization is thus crucial and the contrast enhancement is limited by the extinction ratio of the polarizer.

3.5.2 Preliminary experimental results

The XPW spectrum and its Fourier Transform are shown on Fig. 3.22 and 3.23. The XPW spectrum exhibits a triangular shape. Adjusting the input spectral phase with the Dazzler settings or the intensity on crystals did not help to make the XPW spectrum shape closer to a Gaussian. This phenomenon may be related to the thickness of the crystal: if it is too long, the input pulse is dispersed and XPW conversion leads to a narrow XPW pulse spectrum. Otherwise, the significant Self-Phase Modulation (SPM) observed in the Glan polarizer worsened the XPW spectrum shape. The purchase of a custom Glan polarizer with a wider aperture will solve this last issue. The conversion efficiency, defined as the energy ratio before and after the output Glan polarizer, was > 30 %, corresponding to an available XPW energy of 300 μJ.

The energy stability of the XPW pulses was measured with a photodiode and compared to the amplifier output one. The laser stability is increased by a factor 1.7 after the XPW setup. This good performance was attributed to the four axes Beam Pointing Stabilization at the setup entrance.

Finally, the far field spatial profile was characterized at the XPW setup output using a 50 cm focal length mirror (see Fig. 3.24). The XPW pointing was recorded for one hour and the deviation was about 15 μm RMS.

3.5.3 Conclusion

This chapter described in details the front-end composed of an oscillator and a first CPA, both from Femtolasers. The front-end performances in terms of CEP stability, spectro- and spatio-temporal quality were shown and analyzed. I explained how some polarization changes can degrade the contrast during the amplification process. The STC characterization highlighted that pulses exhibit excellent spatio-temporal properties at the amplifier output. However, the compression stage degrades the pulses quality with spatial chirp. This issue cannot be solved easily because of the amplifier sensitivity to back reflection. Finally, I set out the XPW setup implemented after the front-end to enhance the incoherent contrast of several orders of magnitude.
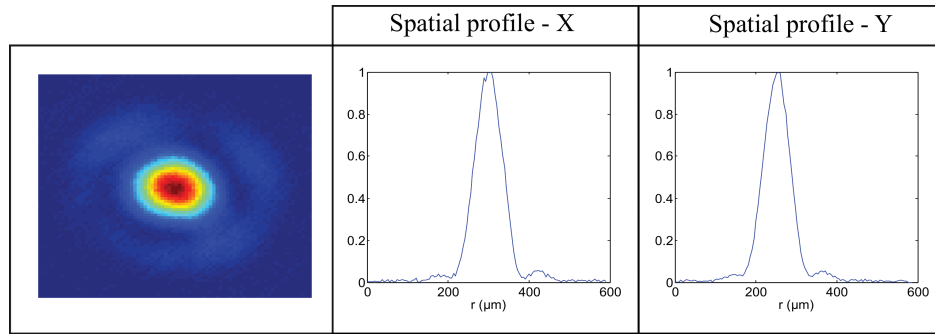
Figure 3.24 – Far field profile at the XPW setup output. A 50 cm focal length mirror was used. Beam diameter $(1/e^2)$ is about 125 µm.

Some preliminary results are shown but some in-depth work still needs to be done to improve and understand the XPW spectro-temporal performances, in light of the results of the spatio-temporal characterization.

In the next chapters, I present the technological developments required for the design of a second CPA to meet the energy specification of the Salle Noire 3.0.

Chapter 4

Technological challenges of the 2nd CPA

Contents

The second CPA is described on Fig. 2.2 and aims to deliver an energy of 25 mJ at 1 kHz repetition rate. The first part explains how the stretcher-compressor scheme must be carefully determined, according to the CEP stability specification and the need of limiting non-linearities. The second part deals with thermal issues within the last power amplifier which is subjected to a high average pump power level. Two experimental protocols are proposed to characterize the considered cryogenic cooling system. Finally, the amplification calculations in the last amplifier are presented in a third part and allow to set the number of passes to achieve at the same time the aimed energy level and a minimum amount of non-linearities.

4.1 Stretcher-compressor design

Performing the CEP stabilization of multimillijoule energy CPA systems remains challenging. The stretcher and compressor devices are particularly sensitive to the environmental conditions and to the laser beam pointing fluctuations because of their open-space dispersive components. A way to limit this sensitivity is to minimize the optical pathway in these devices, by reducing the stretching ratio and improving their compactness and stability.

4.1.1 Technological choice for CEP stable operation

The association of a bulk-base stretcher with a Transmission Gratings Compressor (TGC) demonstrated its ability to preserve the CEP stability [61]. However, the Third Order Dispersion (TOD) introduced by the bulk stretcher and the TGC is positive for both. The stretching factor is thus limited by the maximum amount of TOD which the Dazzler is able to correct. Usually, this pulse stretching compression design allows a stretched pulse duration of a few ps to tens of ps and is thus restricted to lasers with an energy lower than ≈ 3 mJ. This design is not suited to higher energy laser systems because of the accumulated nonlinear phase which tends to degrade the pulse quality.

A compressor based on the combination of gratings and prisms (GRISM) [62] adds a negative TOD so that it matches the positive TOD of a bulk stretcher. A two passes GRISMS compressor in a unfolded configuration was implemented in Salle Noire 2.0, confirming that this design is suited to CEP stable lasers [63], even until 10 W average power [9]. However, the GRISM compressor adds a non negligible positive Fourth Order Dispersion (FOD) to that of the bulk stretcher. Two passes in the Dazzler device were thus required to correct the FOD. In this scheme, the significant amount of FOD limits the stretched pulse duration (46 ps in Salle Noire 2.0) and restrains the correction factor of the Dazzler device on the other dispersion orders, as well as its efficiency on the whole pulse spectral width. Furthermore, a strong thermal lens was observed in the compressor prisms at 10 W average power. As a result, the spatial profile of the compressed pulses was strongly degraded. Although these disadvantages, this compression scheme is attractive for the Salle Noire 3.0 because of its capability to maintain CEP stability.

To achieve high stretching ratios, Öffner stretchers and associated gratings compressors are usually employed in high power laser chain. These schemes are usually avoided in CEP-stable lasers because of the requirements on the mechanical design stability [64]. Nevertheless, such designs have demonstrated their ability to preserve CEP stability [65, 37].

A low aberration Öffner triplet [43] enables pulse stretching up to hundreds of ps [66] in a compact package. It is composed of two spherical concentric mirrors: one is concave, one is convex (see Fig. 4.1c). The magnification of the telescope is -1 so that the radius of curvature ratio is two. This combination is completely symmetric, meaning that only spherical aberration and astigmatism can appear. These aberrations are partly canceled because of the opposite sign of the two radii of curvature. As demonstrated in [66], the use of a single grating located out of the plane of the center of curvature still enables weak spherical aberration and is favorable compared to the use of two distinct gratings which are hard to maintain exactly parallel each other. A transmission grating is preferable to a reflective one as it can be used in a compact in-line configuration, which

is crucial to preserve CEP stability.

In the next paragraph, I discuss the advantages and disadvantages of both possible designs ("Bulk stretcher - GRISM compressor", called design 1 or "Öffner stretcher - TGC", called design 2).

4.1.2   Necessity to move from the scheme "Bulk stretcher - GRISM compressor" to "Öffner stretcher - TGC"
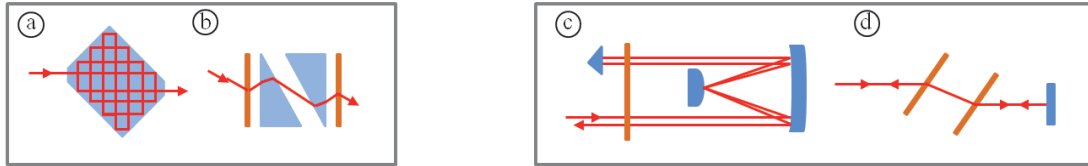
Figure 4.1 – Scheme of the two possible stretching-compression designs: "Bulk stretcher (a) - GRISM compressor (a)", or "Öffner-type stretcher (c) - TGC (d)".

The design 1 (Fig. 4.1a,b) was simulated by Fastlite. The calculations highlighted that the maximum Stretching Factor (SF) available with such a design is 3 ps/nm, meaning that the SF57 bulk length should be 4.5 m. A higher SF would involve a GRISM compressor with large dimensions (and so a considerable price). A propagation beam path of 4.5 m can be achieved in a compact snooker-type bulk stretcher (Fig. 4.1a) through manifold total internal reflexions. Although SF57 material is not produced any more by Schott because of new environmental directives, another material produced by Ohara suits our need: PBH56. This material exhibits similar dispersion properties and a lower absorption of low wavelengths than SF57. The thermal effects in bulk will be thus avoided. Two double-passed PBH56 blocks measuring 12 per 15 cm are required to achieve a SF of 3 ps/nm.

The GRISM compressor design was then broached. Fig. 4.1b shows the considered GRISM setup [67]: two anti-parallel right angle prisms are between two parallel transmission gratings used at Littrow incidence for optimal efficiency. The GDD compensation is driven by the distance between the two gratings, whereas the ratio TOD/GDD is controlled by the prisms position. The Salle Noire 3.0 laser specifications require stringent constraints on the compressor in terms of FOD correction. The simulations performed by Fastlite systematically converged to a solution where the gratings are not parallel to prisms and almost in touch with a prism edge. This result is the consequence of the FOD compensation specification. The large amount of FOD cannot be managed by only the Dazzler which would be highly constrained in terms of transmitted spectral bandwidth and efficiency. A last critical point concerns the thermal effects in the prisms. In Salle Noire 2.0, the thermal lens is so strong at 10 W average power that the beam profile is highly deteriorated, degrading the post-compression setup performances, and even damaging it. The thermal issues could be solved by increasing the aperture of the GRISM compressor. However Fastlite cannot provide the device with an aperture larger than 5 mm, because of the tilted GRISM design for FOD compensation.

To conclude, the FOD requirement leads to an impracticable solution. Thermal and nonlinearities issues won't be managed with a larger aperture. A water cooling could be considered but may not be compatible with CEP stable operation because of eventual flow related vibrations and inhomogeneous cooling. A SF of 3 ps/nm is also too small, leading to a high B integral value as highlighted in the following. Considering an upgrade of the Salle Noire 3.0 up to 100 mJ before compression, the SF sould be about 6 ps/nm [37]. For all these reasons (see Tab. 4.1), our choice shifted to design 2: "Öffner stretcher - TGC".

Now the the design of the stretching-compression device is set, the SF has to be determined. This parameter is driven by a compromise between minimizing the nonlinear effects through the whole laser chain (B integral) and maintaining the CEP stability with a limited optical path in the stretcher. A stretched pulse duration of 200 ps brings about an accumulated B integral less than 2 rad in the power amplification stages, taking into account an eventual energy upgrade until

Issue	Bulk stretcher - GRISM compressor	Öffner stretcher - TGC
Stretching factor	3 ps/nm maximum	5 ps/nm
B integral in PA stages	2,9 rad	1,7 rad
Spectral phase high orders	Significant FOD. Its compensation leads to an impracticable design with limited aperture.	Stretcher and compressor are phase-matched. Compression can be achieved with a single pass through the Dazzler.
Thermal effects	A strong thermal lens was observed in the GRISM compressor of the Salle Noire 2.0 at 10 W average power.	Few thermal effects in the transmission gratings.
CEP stable operation	CEP stability is guaranteed.	CEP stability is maintained provided that highly stable mechanical mounts are used and the stretcher is free from fluctuations.

Table 4.1 – Summary of the main advantages and disadvantages of design 1 and design 2. B integral was calculated using the 3D propagation code CommodPro. This code is the commercially available version of the MIRO code developed in CEA [53]. I performed calculations assuming a potential upgrade of the Salle Noire 3.0 up to 100 mJ energy before compression and considering pulses with a spectral width of 47 nm (FWHM). Only B integral in the Power Amplifier (PA) is considered.

100 mJ level before compression. Considering a 47 nm FWHM spectrum (that is a 20 fs FTL pulse), the corresponding SF is 4,3 ps/nm and is still compatible with CEP stable operation [65, 37]. However, precautions must be considered. In [37], the mechanical mount of the Öffner stretcher was designed with special care to be free from vibrations. Otherwise, the CEP noise was mainly attributed to beam pointing instabilities. In [65], various tests were performed to understand the main CEP noise sources. It appeared that floor vibrations considerably amplified the CEP noise in the Öffner stretcher because of the open-space dispersive propagation in this device. The use of rubber sheets under the table legs and the cryocooler tripod solved this issue.

As a conclusion, the SF of the Öffner stretcher is set to 4,3 ps/nm. Previous results in literature proved that such a device is compatible with CEP stable operation, provided that precautions are taken to stabilize the beam pointing and to make the stretcher vibrations-free.

4.1.3 Matlab calculations for devices setting

The stretcher and compressor gratings groove density was fixed to 1200 gr/mm, because it corresponds to a standard product among many gratings suppliers. Standard components are preferred because of their attractive price and their ability to be manufactured quickly. In case any damage occurs, it can be replaced easily. We acquired a standard transmission grating from Wasatch Photonics (1200 gr/mm) for the stretcher. A groove density of 1200 gr/mm is standard for Horiba which can provide large size transmission gratings for the compressor. All these transmission gratings are optimized for the Littrow incidence to achieve an optimal diffraction efficiency.

In the following, the incidence angles on the stretcher grating (resp. the compressor gratings) are named θ_s (resp. θ_c). The distance between the grating of the Öffner and its image is d_s (see Fig. 4.2). The distance between the compressor gratings is d_c (see Fig. 4.2). I detail below the analytical calculations to set the devices parameters (θ_s, θ_c, d_s and d_c) so that the final pulse duration at the TGC output is 500 fs. This allows to limit the B integral in the compressor gratings bulk. Compression can then be ended with chirped mirrors.
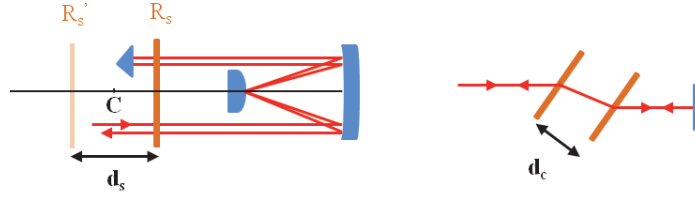
Figure 4.2 – Definition of the stretcher and compressor inter-gratings distances, d_s and d_c.

Evaluation of the inter-gratings distances

A 200 ps stretched pulse with a spectral bandwidth of 47 nm (FWHM) is considered. According to Eq. A.25, the temporal chirp parameter at 795 nm is b = $3{,}46.10^7$ fs^{-2}. The equivalent chirp, determined via Eq. A.20, is $\phi_s^{(2)}(\omega_0) = 144{,}36.10^4$ fs^2 and corresponds to the GDD introduced by the stretcher.

The dispersive components in CPA 2 are gathered in Tab. 4.2. Taking into account the GDD introduced by the Dazzler (5000 fs^2), the total GDD due to materials in CPA 2 is about: $\phi_{mat}^{(2)}(\omega_0) = 18\,244$ fs^2. Finally, the compressor has to compensate a total GDD of $\phi_c^{(2)}(\omega_0) = \phi_s^{(2)}(\omega_0) + \phi_{mat}^{(2)}(\omega_0) = 146{,}18.10^4$ fs^2. In this case, the pulse duration at the TGC output is 20 fs. However, we rather plan to achieve 500 fs pulses at the TGC output to limit the B integral in the gratings bulk. In this way, the total GDD compensated by the compressor is relaxed by 3600 fs^2 and $\phi_c^{(2)}(\omega_0) = 145{,}82.10^4$ fs^2.

Material	Refractive index	Type and number of components	Total length (cm)
Ti:Sa	1,76 (n$_o$)	Booster: 6 passes in a 8 mm long crystal Power Amplifier 1: two passes in a 10 mm-long crystal Power Amplifier 2: two passes in a 15 mm-long crystal	9,8
Fused silica	1,45	Ten 3 mm-thick lenses Twenty 1,5 mm-thick windows 4 passes in a 6 mm-thick transmission grating (Stretcher) 4 passes in a 15 mm-thick transmission grating (TGC)	14,4
KDP	1,5	Pockels Cell	3,5
Calcite	1,48 (n$_e$)	Glan polarizer	3

Table 4.2 – List of the considered material in CPA 2 to calculate the GDD that needs to be compensated by the compressor in addition to $\phi_s^{(2)}$. Refractive indices are given at 800 nm in the table but dispersion calculation were performed using the Sellmeier coefficients [50].

Phase introduced by materials (Dazzler included)	
GDD	18 244 fs^2
TOD	10 296 fs^3

Table 4.3 – Phase introduced by materials in CPA 2. Calculation was performed at 795 nm.

The next step consists in calculating the inter-gratings distance of the TGC (d_c) which compensates the laser chain dispersion. The TGC is composed of two parallel gratings and a folding dihedral to ensure two passes. The spectral phase introduced by a TGC in a two passes configuration is given by [68]:

$$\phi(\omega) = 2\frac{\omega}{c}\frac{d_c}{\cos\alpha}\cos(\alpha - \beta(\omega)) \tag{4.1}$$

were α is the incidence angle and β the diffracted angle:

$$\beta(\omega) = \arcsin\left(\frac{2\pi N_c c}{\omega} - \sin\alpha\right) \tag{4.2}$$

N_c is the groove density of the compressor and c the light velocity. To achieve a high diffraction efficiency, Littrow incidence is considered:

$$\alpha_{\text{Littrow}}(\lambda) = \arcsin\left(\frac{N_c\lambda}{2}\right) \tag{4.3}$$

For a standard groove density of 1200 gr/mm, $\alpha_{\text{Littrow}} = 28,49°$ at 795 nm. For any incidence angle, the second order term of the spectral phase introduced by the TGC is expressed as:

$$\frac{\partial^2 \Phi}{\partial\omega^2} = -2\frac{(2\pi N_c)^2 d_c c}{\omega^3 \cos^3\beta(\omega)} \tag{4.4}$$

Fig. 4.3 shows the GDD introduced by the compressor as a function of the grating separation, d_c. A grating separation of 385 mm compensates the GDD introduced by the stretcher whereas a grating separation of 389 mm compensates the total GDD of CPA 2 (stretcher + material) considering that the pulse duration at the TGC output is 500 fs. Results are gathered in Tab. 4.3. The compressor parameters can be then optimized to minimize the total amount of GDD and TOD introduced by the whole CPA 2.
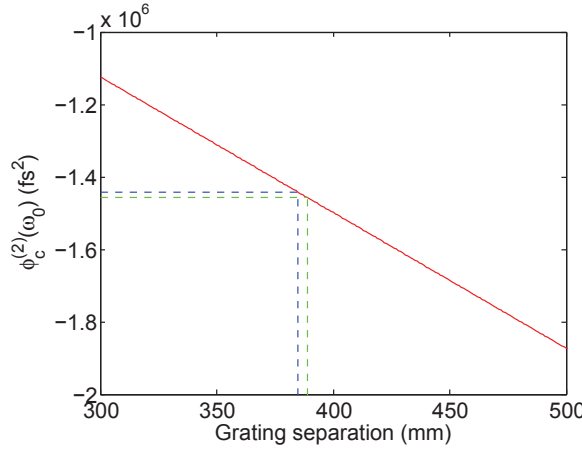
Figure 4.3 – GDD introduced by the compressor as a function of the grating separation. Calculation was performed at 795 nm for N_c = 1200 gr/mm. The blue (resp. green) dashed lines indicates the GDD introduced by the stretcher (resp. the stretcher and material in CPA 2).

Quantity	Stretcher	Compressor
N	1200 gr/mm	
Littrow incidence	28,49°	
Chirp	144,36.10^4 fs^2	-145,82.10^4 fs^2
d_{ini}	-385 mm	389 mm

Table 4.4 – Stretcher and compressor inter-gratings distances to cancel the total amount of GDD. Calculation are performed at 795 nm and for Littrow incidence.

Optimization of the compressor parameters to minimize the total GDD and TOD

The total GDD (resp. TOD) introduced by CPA 2 is calculated using Eq. 4.4 (resp. Eq. 4.5).

$$\frac{\partial^3 \Phi}{\partial \omega^3} = 6 \left(2\pi N\right)^2 dc \frac{1}{\omega^4 \cos^3 \beta(\omega)} + 6 \left(2\pi N\right)^3 dc^2 \frac{\sin\beta(\omega)}{\omega^5 \cos^5 \beta(\omega)} \tag{4.5}$$

The minimization of the functions:

$$\Phi_{\text{tot}}^{(2)}(d_s, d_c) = \left| \Phi_s^{(2)}(d_s) + \Phi_{\text{mat}}^{(2)} + \Phi_c^{(2)}(d_c) \right| \tag{4.6}$$

$$\Phi_{\text{tot}}^{(3)}(\theta_s, \theta_c) = \left| \Phi_s^{(3)}(\theta_s) + \Phi_{\text{mat}}^{(3)} + \Phi_c^{(3)}(\theta_c) \right| \tag{4.7}$$

using d_c and θ_c as variables set the optimal compressor parameters. An inter-gratings distance about 396 mm and an incidence angle about 29.15° lead to residual GDD, TOD and FOD respectively of 386 fs^2, 2842 fs^3 and 128 470 fs^4 (see Tab. 4.5). The Fourth Order Dispersion (FOD) was calculated thanks to the following equation:

$$\frac{\partial^4 \Phi}{\partial \omega^4} = -24 \left(2\pi N\right)^2 dc \frac{1}{\omega^5 \cos^3 \beta(\omega)} - 48 \left(2\pi N\right)^3 dc^2 \frac{\sin\beta(\omega)}{\omega^6 \cos^5 \beta(\omega)} - 6 \left(2\pi N\right)^4 dc^3 \frac{1}{\omega^7 \cos^5 \beta(\omega)}$$
$$- 30 \left(2\pi N\right)^4 dc^3 \frac{\sin^2 \beta(\omega)}{\omega^7 \cos^7 \beta(\omega)} \tag{4.8}$$

The calculated residual phase orders can be managed by the Dazzler without any difficulty. Otherwise, the angle incidence on the compressor gratings is still very close to the Littrow incidence so that a high diffraction efficiency is guaranteed.

Quantity	Stretcher	Compressor
N	1200 gr/mm	
Littrow incidence	28,49°	
Incidence angle	28,49°	29,15°
d$_{\text{opt}}$	-385 mm	396 mm
Phase term	**Residual spectral phase at 795 nm - After optimization**	
GDD	386 fs^2	
TOD	2842 fs^3	
FOD	128 470 fs^4	

Table 4.5 – Results of the compressor parameters optimization and residual GDD, TOD and FOD. Calculation are performed at 795 nm.

To conclude, calculations allowed to set the optimal inter-gratings distance that minimize the residual GDD, as well as the incidence angle on the compressor that minimize the residual TOD, all taking into account the material dispersion in CPA 2. Now the incidence angles and the inter-grating distances are known for both stretcher and compressor, their optical design (mirrors curvature, mirrors diameters, gratings dimensions) needs to be established.

4.1.4 Optical design of the Öffner-type stretcher

Incident beam size

The beam size definition is driven by 4 physical quantities: peak intensity, thermal load, maximal fluence and B integral. Specifications are gathered in Tab. 4.8 and partly related to the grating

specifications purchased from Wasatch Photonics (1200 gr/mm, 130 × 100 mm, 6 mm-thick, 700-900 nm, λ/10).

At the stretcher input, the pulses exhibit a duration about 100 fs and an energy about 300 μJ. The calculations highlight that a 3 mm beam diameter (FWHM) fulfills the required specifications.

Physical quantity	Specifications	Actual value considering 300 μJ, 100 fs pulses with a 3 mm beam diameter (FWHM)
Peak intensity	< 1.1.10^{11} W/cm^2	2,1.10^{10} W/cm^2
Thermal load	3 kW/cm^2	3 W/cm^2
Maximal fluence	100 mJ/cm^2	3 mJ/cm^2
B integral	< 2 rad	0,4 rad

Table 4.6 – Specifications of the Öffner-type stretcher. A incident beam diameter of 3 mm FWHM satisfies all the criteria. Calculation were performed with CommodPro.

Zemax simulations for optics definition

Although an Öffner-type stretcher exhibits few aberrations, it is not completely aberration-free as the considered design is based on the use of a single grating which is not located in the center of curvature plane. The amount of aberrations is determined by the radii of curvature of the mirrors: short focal lengths increase aberrations. Long focal lengths would be thus preferable. However, the stretcher has to maintain CEP stability, meaning that a limited optical pathway is required. A compromise between the amount of aberrations and the optical pathway has to be found.

I performed simulations with Zemax, an optical design software which allows ray tracing and aberration calculation. I describe below how I proceeded.

- Calculation mode

  Two calculation modes are available. In sequential mode, trajectories of light rays are calculated from an object surface to an image surface, according to a predefined sequence of surfaces. This calculation mode gives access to aberrations evaluation. In non-sequential mode, no ordered sequence of surfaces is defined. The objects that the rays hit are determined by the physical positions and properties of the objects as well as the propagation directions of the rays. Rays may hit a surface several times. This calculation mode is particularly adapted to stray-light analysis in optical systems with multiple passes. However, aberration evaluation is not available in this mode. Besides, a sequential treatment of a multiple-pass system is not conceivable when rays hit a surface because a minimum of 3 lines of code are necessary to manage the reference changes (the optical axes of the components are not the same and there are some non-zero incidence angles) and each optics must be defined k times in a k passes system. The inter-dependance relations between each surface (including the reference changes) have to be established and are a source of possible error.

  Performing simulations in a hybrid ray tracing mode (mixed sequential/non-sequential) enables to calculate aberrations introduced by a multiple passes system with few lines of code. To do so, the non-sequential objects are inserted in a set of sequential objects.

- Reference for wavefront error calculation

  Aberrations calculations are performed with respect to a reference. Usually, it is recommended to choose the exit pupil as a calculation reference. The position and diameter of the exit pupil is calculated by Zemax according to the entrance pupil properties. Aberrations are then evaluated in the plane of the exit pupil. The reference wavefront, defined as

the sphere transmitted by the non-aberrant system, intercepts the real wavefront at the center of the exit pupil. The gap between the two considered wavefronts quantifies the amount of aberrations.

In the case of an Öffner-type stretcher, the determination of the exit pupil is difficult because of the off-axis beam propagation and the afocal property of the system. An absolute reference is preferred, meaning that the wavefront error is calculated with respect to a plane wavefront located in the image surface plane and perpendicular to the ray propagating through the center of the system pupil. In this way, a non perfectly collimated output beam makes the aberration calculation dependent on the image surface position. This applies to the stretcher because the mirrors positions are fixed and the optical pathway varies from pass to pass. I still chose the absolute reference as the exit pupil position cannot be determined precisely by Zemax and the output beam collimation is not so bad. Note that "Spot Diagram" is the only diagnostic which does not depend on the wavefront reference and the image surface position.
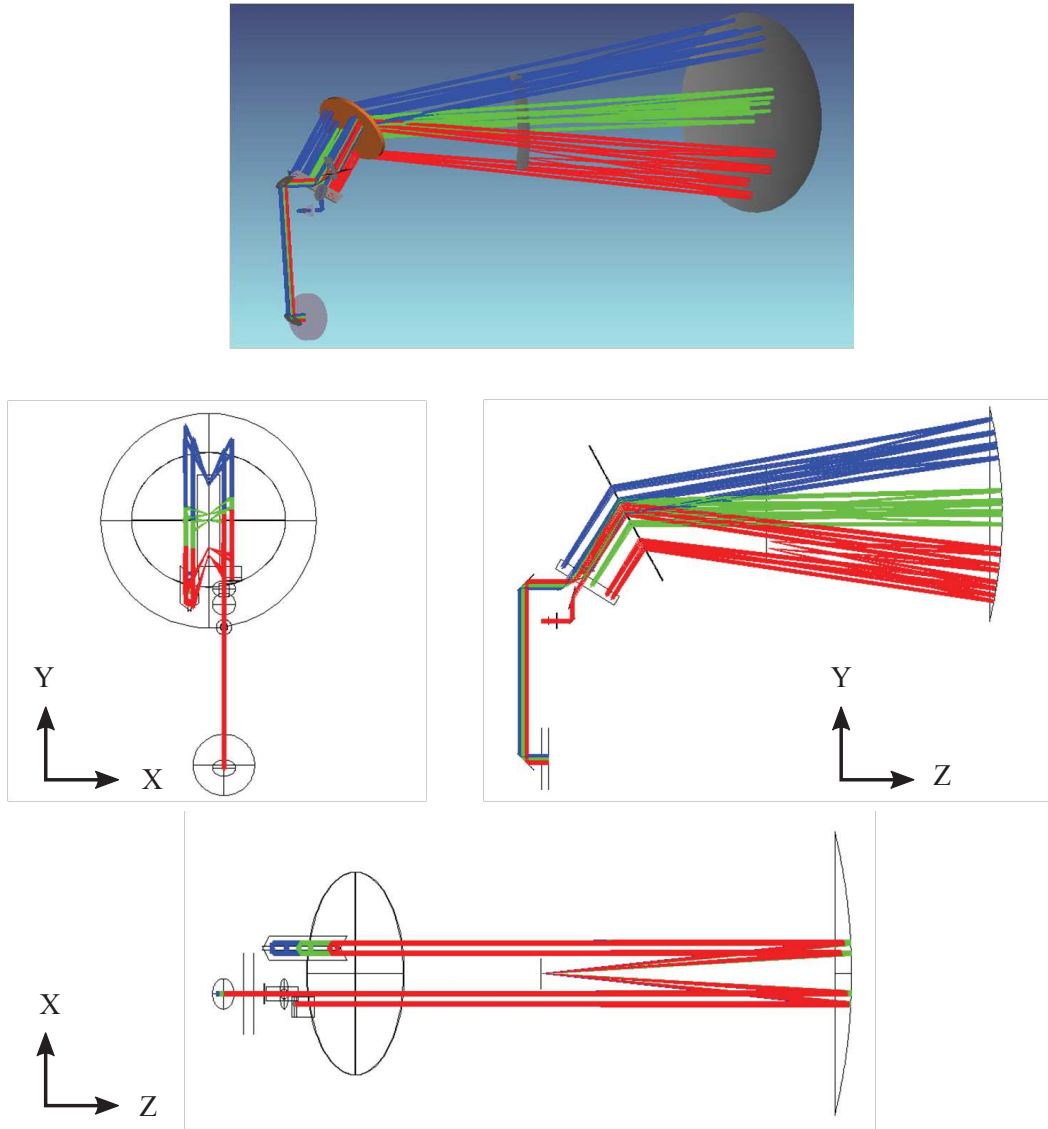
Figure 4.4 – 3D and 2D schemes of the Öffner-type stretcher in a double pass configuration. The blue, green and red rays correspond respectively to 680 nm, 795 nm and 900 nm.

Zemax simulations were performed to determine not only the optical components dimensions but also the focal lengths of the concave and convex mirrors.

Optics dimensioning is driven by the stretching factor as well as the required transmitted spectral bandwidth. Simulations were performed considering a stretched pulse duration of 200 ps (SF = 4,3 ps/nm). The corresponding optimal inter-gratings distances are d_s = 385 mm and d_c = 396 mm. The optical components dimension should be large enough to transmit the entire spectral bandwidth of the pulses at the XPW setup output, that is [680-900] nm.

The focal lengths choice is driven by the amount of aberrations. I compared two couples of concave/convex mirrors with the following radii of curvature: [+600 mm/-300 mm] (Case 1) and [+800 mm/-400 mm] (Case 2).

	Rcc = 600 mm Rcx = -300 mm	Rcc = 800 mm Rcx = -400 mm
PSF		
Spot Diagram	680 nm 795 nm 900 nm Airy disk	680 nm 795 nm 900 nm Airy disk
Wavefront (795 nm)	0.30 λ PV 0.07 λ RMS	0.15 λ PV 0.03 λ RMS
Zernike coefficients	Z 1 0.10793644 : 1 Z 2 0.00123641 : 4^(1/2) (p) * COS (A) Z 3 -0.00168563 : 4^(1/2) (p) * SIN (A) Z 4 0.06236002 : 3^(1/2) (2p^2 - 1) Z 5 -0.00477425 : 6^(1/2) (p^2) * SIN (2A) Z 6 0.03139597 : 6^(1/2) (p^2) * COS (2A) Z 7 -0.00059591 : 8^(1/2) (3p^3 - 2p) * SIN (A) Z 8 0.00043710 : 8^(1/2) (3p^3 - 2p) * COS (A)	Z 1 0.04962186 : 1 Z 2 0.00053309 : 4^(1/2) (p) * COS (A) Z 3 -0.00072422 : 4^(1/2) (p) * SIN (A) Z 4 0.02866791 : 3^(1/2) (2p^2 - 1) Z 5 -0.00202748 : 6^(1/2) (p^2) * SIN (2A) Z 6 0.01189885 : 6^(1/2) (p^2) * COS (2A) Z 7 -0.00025604 : 8^(1/2) (3p^3 - 2p) * SIN (A) Z 8 0.00018847 : 8^(1/2) (3p^3 - 2p) * COS (A)

Figure 4.5 – Results of the Zemax simulations performed with an entrance pupil diameter of 3 mm. The grating is at Littrow incidence. PSF: Point Spread Function.

A layout of the simulated device is illustrated on Fig. 4.4. The grating position is given by:

$$D_s = 4 \left[R_{cc} - L_{g-cc} \right] \tag{4.9}$$

were D_s is the slant inter-gratings distance of the stretcher, R_{cc} the radius of curvature of the concave mirror and L_{g-cc} the distance between the grating and the concave mirror. Results are summarized on Fig. 4.5. The Point Spread Function (PSF), which is the irradiance distribution that results from a single point source in object space, highlights that the device is aberrant in case 1 whereas it is diffraction-limited in case 2. The spot diagram shows that the output beam exhibits a spatial chirp related to chromaticism effects in the transmission grating. The wavefront function amplitude (Peak to Valley) is about 0,30 λ in case 1 and 0,15 λ in case 2. The Zernike coefficients underline that 0° and 90° astigmatism is preponderant in both cases (defocus is not considered as a disturbing aberration for our application). Finally, case 2 is the most preferable in terms of aberrations and still offers the possibility of a compact design suited to CEP stability.

I also measured the optical components dimensions to transmit the required spectral bandwidth (680-900 nm) and a 10 mm-large beam (1/e^2 diameter). The grating should be 120 mm-height and 50 mm-large. The concave (resp. convexe) mirror diameter should be 340 mm (resp. 160 mm). The convex mirror width should be 20 mm.

Mechanical design

As demonstrated in [65], an Öffner-type stretcher is very sensitive to mechanical vibrations and has to be isolated from any source of vibrations to be compatible with CEP-stable operation. In this way, we bought four mechanical vibration isolators to make the 100 kg-weighted stretcher vibrations-free (Newport). Their frequency transmission in both horizontal and vertical directions is illustrated on Fig. 4.6. The isolators feature a 7 Hz vertical resonance frequency, meaning that vertical vibrations are attenuated from 10 Hz. The horizontal resonance frequency is 6.5 Hz, meaning that horizontal vibrations are attenuated from 9,3 Hz. Some preliminary tests demonstrated the efficiency of those isolators, looking at the focused beam after propagation through the stretcher, when the isolators are locked or not. However, we cannot confirm yet that the isolators integration is sufficient to maintain a low phase noise as CEP stability could not be tested (a Dazzler was missing and pulse compression could not be achieved).
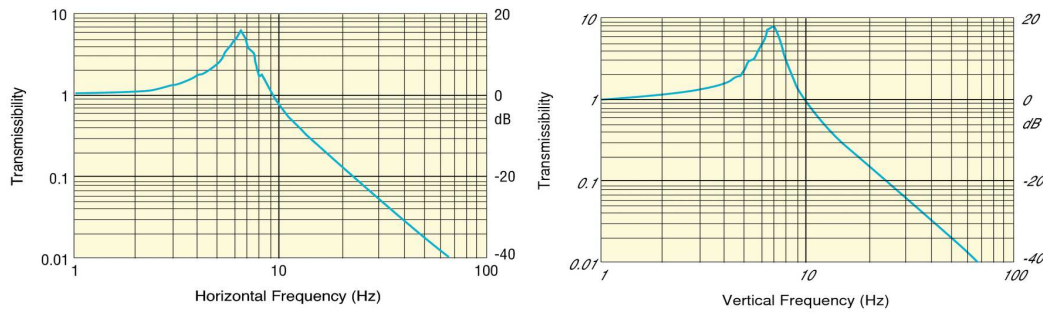
Figure 4.6 – Frequency transmission of mechanical vibration isolators from Newport in both horizontal and vertical directions. Reprinted from *Newport.com*.

4.1.5 First experimental tests with the Öffner-type stretcher

The calculations and measurements presented in [69] show that the optical quality of the components included in the stretcher (and the compressor) should be better than $\lambda/30$ RMS (and $\lambda/5$ PtV) to yield high-quality sub-20-fs pulses from CPA laser systems.

The surface quality of the grating from Wasatch Photonics is indicated as $\lambda/10$ PtV. All mirrors inside the stretcher were purchased from Fichou with the following surface quality requirements: $\lambda/10$ PtV and $\lambda/40$ RMS.
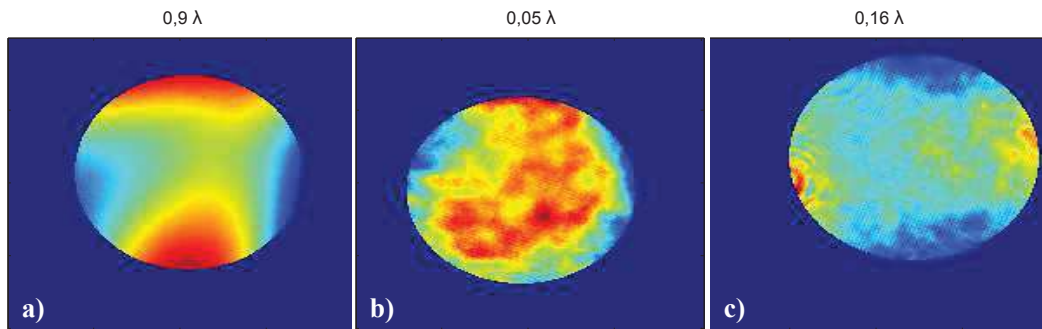
Figure 4.7 – Wavefront characterization using a SID4 device (Phasics): a) XPW output without optimization. b) XPW output after 0° astigmatism correction. c) Stretcher output when seeded by the optimized XPW pulses. *Beam diameter (1/e^2) was 5 mm. Aberrations were calculated using a 4 mm-large circular mask. The Peak to Valley wavefront amplitudes are indicated in each case.*

We performed wavefront measurements using a SID4 device (Phasics). This wavefront sensor is based on quadriwave lateral shearing interferometry: a modified Hartmann mask creates four beamlets which interfere on a camera. The wavefront distortions are recovered thanks to a Fourier

analysis of the interferogram. As several pixels are involved in the measurement of one phase pixel, the resolution is increased compared to other wavefront sensors (Shack-Hartmann).

The results are shown on Fig. 4.7. The stretcher was seeded by the XPW beam. A first measurement was performed to characterize the wavefront at the XPW setup output. Significant 0° astigmatism was observed (see Fig. 4.7a) with a wavefront amplitude about 0,9λ Peak to Valley. This is probably related to the Brewster window at the XPW setup entrance. Astigmatism was corrected using a tilted lens in the collimated beam. The resulting wavefront exhibited an amplitude about 0,05λ PtV, as seen on Fig. 4.7b and was used to seed the stretcher. A third measurement was performed at the stretcher output (Fig. 4.7c) and shows that optical components included in the stretcher introduce a phase-shift of 0,16 λ PtV (0,019 λ RMS). The corresponding PtV phase distortion is 1 rad and the wavefront appearance show the signature of astigmatism, confirming the predictions of the Zemax simulations. Note that the entrance pupil diameter in Zemax was 3 mm. In the experiment, the beam size was 5 mm (1/e^2) and aberrations were characterized using a 4 mm large circular mask. Tab. 4.7 gathered the radii of curvature measured by the Phasics device before and after the stretcher.

Measurement	PtV	R$_x$ (m)	R$_y$ (m)
Stretcher seed	0,05 λ	-1,5.10^2	-1,5.10^2
Stretcher output	0,16 λ	100	50

Table 4.7 – Results of the wavefront measurements performed before and after the stretcher.

Finally, the spectral bandwidth transmitted by the stretcher was measured seeding the device with broadband pulses from the post-compression setup (this setup will be described in Part 2). The incident P-polarized pulses featured a spectral full-width about [520-940] nm. At the stretcher output, their spectral full-width was reduced to [684-917] nm, as expected. A similar transmission is obtained with incident S-polarized pulses.

To conclude, the Öffner-type stretcher we built exhibits the expected performances in terms of transmitted spectral bandwidth and amount of aberrations. A good agreement is found between the calculations performed with Zemax and the measurements.

4.1.6   Optical design of the TGC

Incident beam size

At the TGC output, the pulse duration is about 500 fs to relax the nonlinear effects in the compressor. Complete pulse compression can be then achieved with a set of chirped mirrors (-3600 fs^2 still needs to be compensated). Taking into account an eventual energy upgrade up to 100 mJ, a beam size of 20 mm FWHM suits the specifications reminded in Tab. 4.8. The grating thickness is 15 mm.

Physical quantity	Specifications	Actual value considering 100 mJ, 500 fs pulses with a 20 mm beam diameter (FWHM)
Peak intensity	< 1.1.10^{11} W/cm^2	4.10^{10} W/cm^2
Thermal load	3 kW/cm^2	20 W/cm^2
Maximal fluence	100 mJ/cm^2	20 mJ/cm^2
B integral	< 2 rad	1,5 rad

Table 4.8 – Specifications of the TGC. A incident beam diameter of 20 mm FWHM satisfies all the criteria. The calculations were performed with CommodPro.

Zemax simulations for optics sizing

I performed Zemax simulations to determine the size of the required gratings. The 3D view of the simulated TGC is given on Fig. 4.8. The TGC is centered at 810 nm because of the red-shifting caused by amplification. Considering an entrance pupil diameter of 65 mm and a spectral bandwidth of [720-880] nm, the first (resp.second) grating dimensions should be 110 mm × 180 mm (resp. 180 mm × 210 mm).
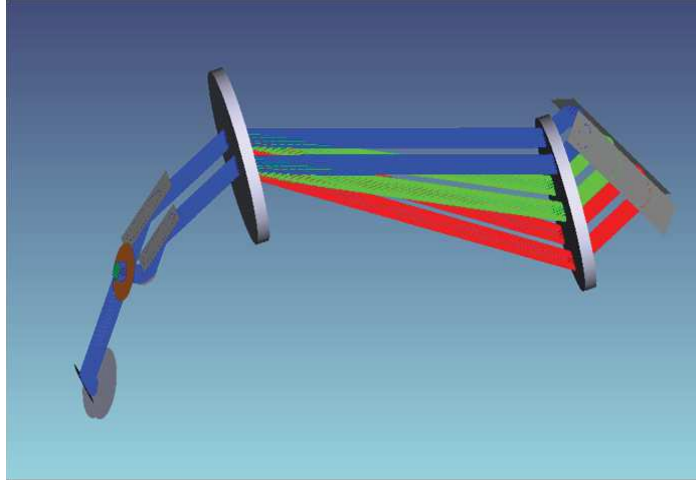
Figure 4.8 – 3D view of the TGC simulated with Zemax. The inter-gratings distance is 396 mm, the groove density of both gratings is 1200 gr/mm. The blue, green and red rays correspond respectively to 720 nm, 810 nm and 880 nm.

Horiba Scientific can provide 1200 gr/mm gratings with the required dimensions thanks to their engraving holographic method. The gratings could feature 96 % efficiency at 800 nm for P-polarized pulses. The anti-reflective coating of the 15 mm-thick substrates can be managed by Fichou.

4.1.7 Conclusion

In this section, I presented the two considered stretcher-compressor designs: Bulk- GRISM and Öffner-TGC. I explained how the various constraints related to the laser chain specifications required the design Öffner-TGC. The numerical calculations for devices setting were reported, as well as the aberrations calculations for the Öffner sizing. The preliminary tests performed on the Öffner-type stretcher gave results close to the Matlab and Zemax simulations in terms of transmitted spectral bandwidth and amount of aberrations.

Now the stretching ratio is set, one can perform simulations of the amplification process in the home-made power amplifier. To do so, one first needs to evaluate the crystal dimensions thanks to temperature gradient calculations within the crystal.

4.2 Thermal issues and diagnostics

Thermal management in the power amplification stage (see Fig. 2.2) is challenging because of the high average power level (100 W). The heat caused by crystal pumping must be evacuated efficiently in order to avoid deleterious effects on the beam quality and even material damage. The main contribution to thermal effects in a pumped crystal comes from the non radiative transitions. The heat rise in the crystal results in an heterogeneous temperature distribution which affects the material properties (dimensions, refractive indices, conductivity, heat capacity, etc). When pumped with significant power, the crystal behaves as a lens with a certain amount of aberrations. Therefore, propagation through the crystal deteriorates the laser wavefront as well as beam properties in terms of divergence and polarization.

In this section, I estimate the heat rise in a pumped crystal using the theoretical model proposed by Chénais [70]. Then, the thermal lens value is deduced from the temperature map within the crystal. These calculations allow to set the amplifier design of the Salle Noire 3.0. Finally, I propose two experimental protocols to characterize the thermal lens in any amplifier or optical device that undergoes thermal effects. Both methods were experimentally verified on a test bench and compared each other. The convergence of the two methods with the theoretical model is also underlined.

4.2.1 Analytical calculation of the heat rise in a pumped Ti:Sa crystal

Heat source

Thermal effects originate in the non radiative processes occurring during population level dynamics. The main contribution to the heat rise in a pumped crystal is related to the quantum defect. It corresponds to the ratio between the emitted radiation energy and the energy absorbed by the amplification medium: $\eta_q = \lambda_p/\lambda_l$. At 800 nm, η_q=66.5 % in a Ti:Sa crystal pumped at 532 nm. As a first approximation, 34.5 % of the absorbed energy translates into thermal energy. Another significant heat source comes from non radiative transitions occurring between the excited states of the material. It is described by the quantum efficiency and reflects the fact that only a part of the pump photons generates radiative emissions. It can be expressed according to the temperature-dependent upper-state lifetime τ and the radiative lifetime of the excited electronic state τ_r [71]: $\eta_c = \tau(T)/\tau_r$. According to [72], τ can be written as:

$$\tau(T) = \left\{ \frac{1}{\tau_r} + \frac{1}{\tau_{nr}} \exp\left[-\frac{\Delta E}{k_b T} \right] \right\}^{-1} \tag{4.10}$$

τ_{nr} in the non radiative lifetime (2,93 ns), ΔE is the transition energy ($3,56.10^{-20}$ J) and k_b the Boltzmann constant. At 300 K, η_c=80 %. Finally, the energy converted into heat can be calculated as follows:

$$E_{th} = \left[1 - \eta_c \eta_q \right] E_{abs} = \eta_h E_{abs} \tag{4.11}$$

At 300 K (resp. 180 K), 46.7 % (33.6 %) of the absorbed energy is converted into heat within the crystal and limits the energy extraction in the amplification medium. Some other non radiative processes happen but are negligible in Ti:Sa [73].

Solving the heat equation

The heat transfer within a pumped crystal can be described by the following equation:

$$\rho C_p \frac{\partial T}{\partial t} - \nabla(K_c . \nabla T) = Q \tag{4.12}$$

ρ is the material density, C_p the heat capacity for constant pressure in J.kg^{-1}.K^{-1}, K_c the thermal conductivity in W.m^{-1}.K^{-1}, Q the heat source or thermal load in W.m^{-3} (thermal power dissipated per unit of volume) and T(r,z) the temperature field to be determined. This equation can be simplified thanks to the following hypotheses:

- Steady state modeling is considered because the thermal relaxation time, expressed as a function of the crystal half width r_0, is long enough compared to the time between two successive pulses:

$$\tau_{th} = \frac{\rho \, C_p \, r_0^2}{K_c} \approx 1 \, \text{to} \, 2 \, \text{s} \, >> 1 \, \text{ms} \tag{4.13}$$

- K_c is constant within the entire crystal. In practice, this is not the case as the crystal is uniaxial and features a different conductivity along each axis. However, few data are available.

- The temperature of the crystal mount is assumed constant and the contacts crystal-mount and crystal-cold finger are assumed perfect.

- The cooling process has a radial symmetry, meaning that heat transport is not advantaged in a specific direction. This makes sense as the crystal is placed under vacuum so that air convection cooling on both sides is negligible. This hypothesis is valid even if the crystal is square-shaped because the pumped area is small compared to the crystal dimensions and cooling is ensured on each side of the crystal [74].

- The pump beam has a top-hat shape.

- The thermal conductivity, which is temperature-dependent, is taken at the crystal mount temperature.

In the framework of these hypotheses, the heat equation becomes:

$$\nabla^2 T(r,z) = \frac{-Q(r,z)}{K_c} \tag{4.14}$$

r (resp. z) is the radial (resp. longitudinal) coordinate. The solution was given by [75] for L-long medium when absorption is not saturated:

$$\Delta T(r,z) = T(r,z) - T(r_0, z) \tag{4.15}$$

$$\Delta T(r,z) = \frac{\eta_h P_{abs}}{4\pi K_c} \frac{\alpha}{1 - e^{(-\alpha L)}} e^{(-\alpha z)} \left\{ \left[1 - \frac{r^2}{\omega_p^2(z)} + \ln\left(\frac{r^2}{\omega_p^2(z)}\right) \right] \cdot \Theta(\omega_p^2(z) - r^2) + \ln\left(\frac{r_0^2}{r^2}\right) \cdot \Theta(r^2 - \omega_p^2(z)) \right\} \tag{4.16}$$

$\Delta T(r,z)$ is the temperature within the crystal relative to the crystal edge temperature. α is the non saturated absorption coefficient, Θ the Heaviside function and $\omega_p(z)$ the pump radius, expressed as [70]:

$$\omega_p(z) = \omega_{p0} \sqrt{1 + \left(\frac{M^2 \lambda (z - z_0)}{\pi \omega_{p0}^2}\right)^2} \tag{4.17}$$

ω_{p0} is the waist radius of the pump beam and z_0 the z-position of the pump waist relative to the incident side of the crystal. In all calculation, $z_0 = L/2$ is assumed and M^2 is set to 30, according to the DM50/100 (Photonics Industries) specifications.

Eq. 4.16 underlines that the temperature profile is parabolic within the pumping area and logarithmic outside. The incident laser mode should be thus smaller than the pump mode to avoid high order aberrations in the pump mode-free area, due to the non quadratic terms in the relative temperature expression.

In the above heat equation solution, the absorption saturation is not taken into account so that the absorbed energy and consequently the gradient temperature within the crystal are overvalued. In [70], the heat equation is solved taking into account the saturation absorption and leads to the following solution:

$$\Delta T(r,z) = \frac{\eta_h \frac{dP_p(z)}{dz}}{4\pi K_c} \left\{ \left[1 - \frac{r^2}{\omega_p^2(z)} + \ln\left(\frac{r^2}{\omega_p^2(z)}\right) \right] \cdot \Theta(\omega_p^2(z) - r^2) + \ln\left(\frac{r_0^2}{r^2}\right) \cdot \Theta(r^2 - \omega_p^2(z)) \right\} \tag{4.18}$$

where $dP_p(z)$ corresponds to the absorbed power in the dz-long crystal slice. Assuming that the pump profile is close to a top-hat, the pump intensity can be written as:

$$I_p(z) = \frac{P_p(z)}{\pi \omega_p^2(z)} \tag{4.19}$$

and the term $dP_p(z)/dz$ becomes [76]:

$$\frac{dP_p(z)}{dz} = \frac{-\alpha\, P_p(z)\, I_{psat}\, \pi\, \omega_p^2(z)}{P_p(z) + I_{psat}\, \pi\, \omega_p^2(z)} \qquad (4.20)$$

with I_{psat} the saturation intensity and α the absorption coefficient expressed according to the crystal absorption factor, A:

$$I_{psat} = \frac{h\,c}{\lambda_p\, \tau(T)\left[\sigma_{abs}^p + \sigma_{em}^p\right]} \qquad (4.21)$$

$$\alpha = -\frac{1}{L}\ln(1-A) \qquad (4.22)$$

σ_{abs}^p and σ_{em}^p are respectively the absorption and emission cross sections at the pump wavelength ($\sigma_{abs}^p = 5.10^{-24}\,\text{m}^{-2}$, $\sigma_{em}^p \approx 3.10^{-28}\,\text{m}^{-2}$). h is the Planck constant.

Application to the home-made power amplifier of the Salle Noire 3.0

The above theoretical model can be now applied to a concrete case: the power amplifier of the Salle Noire 3.0. Calculating the temperature profile allows to set the pumping geometry and the crystal length so that the maximum temperature gradient is about 10°C. The general crystal geometry is first discussed.

A plane-parallel crystal geometry is preferred to a cylindrical one in order to maintain an homogeneous contact between the crystal and its mount. It was indeed demonstrated in [73] that the radii of curvature-match between the cylindrical crystal and the crystal mount is hard to carry out because of the opposite thermal constraints experienced by the components: the pumped crystal is warm whereas the mount is cooled at low temperature. As a result, the bad contact between the crystal and the mount does not allow uniform heat extraction and translates into strong thermal constraints within the crystal. Significant wavefront deformations were observed with such a crystal geometry [73]. As mentioned previously, the theoretical model presented above is still valid with a plane-parallel crystal. The pumped area is indeed small compared to the crystal dimensions and every side face of the crystal is in contact with the copper mount.

Then, the incident side orientation of the crystal should be determined. A Brewster-cut crystal is preferred as it supports a fluence about 8 J/cm^2, enabling high gain values. The maximum fluence on a crystal placed at normal incidence is two times less (4 J/cm^2). A fluence about 7-8 J/cm^2 is obtained for a pump power of 100 W and a pump diameter of 1.2 mm (1/e^2). The Brewster angle for a Ti:Sa crystal is $\theta_B = 60°$ so that $\cos(\theta_B) = 1/2$. The pump beam dimensions will be thus 1.2 mm in the vertical direction and 2.4 mm in the horizontal direction (case of P-polarized pulses). As the theoretical model is valid for a crystal placed at normal incidence, the calculated thermal lens should be close to the thermal lens measured along the vertical direction, where the pump diameter is 1.2 mm.

For practical reasons, the crystal absorption is set to 95%. Re-injection of the unabsorbed pump power in the crystal is thus avoided.

I calculated the temperature gradient within the crystal for three cooling temperatures: 110 K, 180 K and 300 K. The respective conductivity values are 360 W.m^{-1}.K^{-1}, 98 W.m^{-1}.K^{-1} and 44 W.m^{-1}.K^{-1} [73]. The Ti:Sa conductivity was assumed equal to the one of undoped sapphire because of the small Ti^{3+} ions concentration.

The temperature gradient map is illustrated on Fig. 4.9 for a cooling temperature of 110 K. The transverse and longitudinal crystal dimensions are respectively 8 mm and 10 mm. Fig. 4.10 shows the maximum temperature gradient for the three considered cooling temperatures. The gradient reaches 10.6°C, 38.9°C and 120.1°C respectively for T = 110 K, 180 K and 300 K. Fig. 4.10 highlights that a 10 mm-long 8 mm-large crystal cooled at 110 K fulfills our requirement as the maximum temperature gradient is about 10°C.
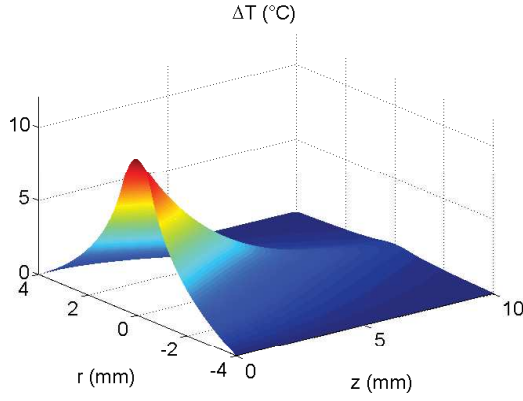
Figure 4.9 – 3D view of the temperature gradient profile in a pumped Ti:Sa crystal (single-side pumping).
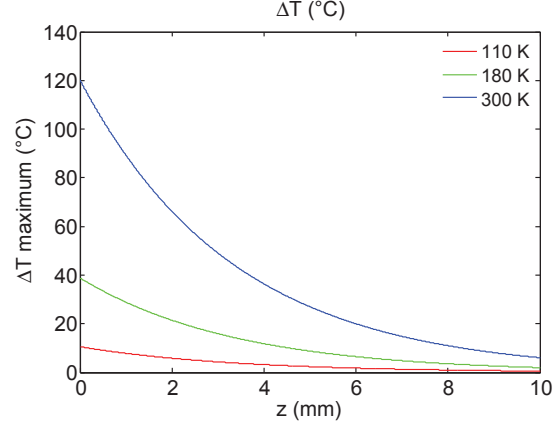
Figure 4.10 – Temperature gradient within the center of the crystal in the case of single-side pumping.

Parameters that could be used to decrease the temperature gradient

To conclude, decreasing the cooling temperature makes the conductivity of the sapphire higher and so the temperature gradient lower. The cooling parameter is not the only parameter that has an influence on the temperature map within the crystal. The thermal gradient could be reduced using a longer crystal with a similar absorption (A = 95 %). The α coefficient (see Eq. 4.22) will be indeed smaller and the heat will be deposited within a bigger volume. For instance, a 20 mm-long 180 K-cooled crystal exhibits a gradient of 19.4°C in the same pumping conditions. However, the B integral should be limited as far as possible and a 10 mm-long crystal is a good compromise, as highlighted in the following by the amplification simulations. A shorter transverse dimension would also reduce the temperature gradient, as underlined in [77]. However, it is hard to make small crystals with good surface quality. Otherwise, a bad thermal contact is all the more so detrimental for crystal dimensions in the same range than the pump diameter.

4.2.2 Thermal lens calculation from the heat rise map

The thermal lens can be deduced from the temperature gradient map. Assuming a perfect contact between the crystal and its mount, T(r,z) is given by:

$$T(r,z) = T_c + \Delta T(r,z) \tag{4.23}$$

where T_c is the cooling temperature. The phase-shift induced by thermal effects in the crystal, or Optical Path Difference (OPD) is given by [78]:

$$OPD(r) = \underbrace{\int_0^L \frac{dn}{dT} T(r,z)\,dz}_{\text{Refractive index change}} + \underbrace{(n_o - 1)\,\alpha_T \int_0^L T(r,z)\,dz}_{\text{Bulging of the end faces}} \tag{4.24}$$

The first contribution to the OPD is related to the refractive index change with temperature. The dn/dT measurements performed by [79] for the spectral range [475-701] nm were fitted by [73] according to the following law:

$$\frac{dn}{dT} = 4,11.10^{-6} - 1,565.10^{-10} \cdot T + 6,449.10^{-11} \cdot T^2 \tag{4.25}$$

dn/dT is expressed in K^{-1} and corresponds to extraordinary index at the wavelength 701 nm. The second term accounts the longitudinal elongation of the crystal. α_T is the thermal expansion coefficient associated with the change of crystal length. The value of α_T at ambient temperature was considered ($6.10^{-6}\,K^{-1}$) because no other value could be found. A third contribution related to the

photo-elastic effect can be taken into account. However, this effect is negligible compared to the other contributions [80] and the low availability of the photo-elastic coefficients of Ti:Sa makes this contribution imprecise.

Fig. 4.11 shows the OPD for the three considered temperatures. The maximum OPD is about 0,37 μm, 1,94 μm and 11,47 μm at T = 110 K, 180 K and 300 K respectively. A parabolic fit of the OPD over the pump beam area is performed to extract the averaged focal length, according to [78]:

$$\text{OPD}(r) = \text{OPD}_0 - \frac{r^2}{2 f_{th}} \tag{4.26}$$

where f_{th} is the thermal lens. The crystal under thermal load behaves as a convergent lens. In the case of the considered power amplifier, the corresponding focal lengths are 3.49 m, 66.1 cm and 10.7 cm at respectively 110 K, 180 K and 300 K. Note that Eq. 4.26 does not take into account the lens aberrations.
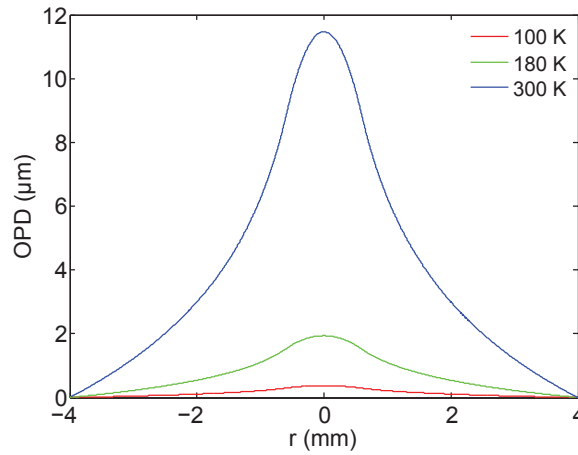
Figure 4.11 – Optical Path Difference (OPD) induced by thermal effects in the crystal for three cooling temperatures. Single-side pumping.

Tab. 4.9 sums up the results of the analytical calculations. To conclude, a 8 mm-large and 10 mm-long Ti:Sa crystal fulfills our requirements. The thermal gradient is about 10°C and makes the 110 K-cooled crystal behaves as a 3,5 m focal length lens that can be compensated by well-chosen optical components. A good thermal contact between the crystal and its mount should be guaranteed by the large crystal dimensions. Besides, silver layers should be used to ensure a good thermal contact crystal-mount at such a cooling temperature. The softness property of indium at ambient temperature is indeed not valid any more at very low temperature. The use of silver requires that the crystal sides are polished.

Cooling temperature	Maximum temperature gradient	Maximum OPD	Thermal lens
110 K	10.58°C	0.37 μm	3.49 m
180 K	38.91°C	1.94 μm	66.1 cm
300 K	120.14°C	11.47 μm	10.7 cm

Table 4.9 – Results of the analytical calculations performed with a 8 mm-large, 10 mm-long crystal with an absorption of 95 %. Thermal load is due to a 100 W, 1,2 mm-sized pump beam. The thermal contact between the Ti:Sa crystal and its mount is assumed perfect.

We have been in discussions with CryoSpectra which is able to provide a 110 K-150 W cryogenic cooling system. This system could not be validated via thermal lens measurements because of the lack of the 100 W pump laser. Performing experimental characterizations is crucial because theoretical calculations make many assumptions and do not take into account the thermal contact defaults. A complete 3D thermal modeling can be performed using a finite elements-based software like Comsol. However, even with such a performing software, the thermal and mechanical

behaviors of the layer sandwiched between the crystal and the mount remains hard to simulate. The low availability of the thermo-optic and mechanical Ti:Sa coefficients for a significant range of temperatures makes also the simulations imprecise.

4.2.3 Thermal diagnostics

To go further and compare the results given by the theoretical model with the experimental ones, I performed thermal lens measurements using a pump laser (DM30, Photonics Industries) delivering 16 W at maximum current intensity. I used a 5 mm-long Brewster-cut Ti:Sa crystal mounted in a copper mount cooled by circulating water at 18°C. The measurement of the optical path length variation of a probe beam, when passed through the Ti:Sa crystal under pumping, reveals the temperature change within the material. I compared two methods: one is based on the use of a Mach-Zehnder interferometer whereas the other one relies on the use of a wavefront sensor.

Thermal lens measurement with a Mach-Zehnder interferometer

The Mach-Zehnder setup is illustrated on Fig. 4.12. The pump laser delivers 1 to 16 mJ, P-polarized pulses at 1 kHz repetition rate and is focused in the TiSa crystal using a 400 mm focal length lens. The corresponding pump beam profile at focus has a diameter about 1040 µm at $1/e^2$, as shown on Fig. 4.13. The intensity profile is top-hat along the X direction whereas it is sharp in the Y direction. The pump power variation is ensured by a half-waveplate associated with a polarizer.
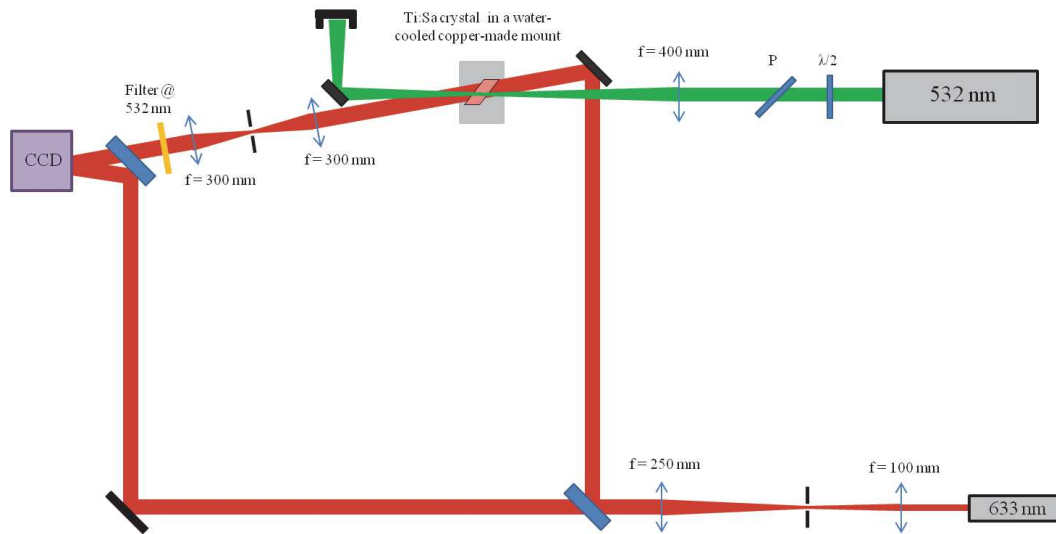
Figure 4.12 – Setup for thermal measurement using interferometry.

An Helium-Neon laser is used as a probe beam. After being spatially filtered, the 633 nm beam is collimated so that its diameter covers the entire crystal transverse dimension (≈ 4 mm). After propagation through the Ti:Sa crystal, spatial and spectral filtering are both required to eliminate a maximum of pump photons. The output face of the crystal is imaged on a CCD camera. The aberrant wavefront and the reference wavefront are thus size-matched.

The fringes pattern are given on Fig. 4.14 for various pump powers. As expected, fringes curve progressively with the increasing power. The phase-shift induced by thermal load is deduced from the interferogram thanks to a wavelet analysis and 2D unwrapping techniques. To do so, I used an open-source software, called 'Neutrino', which was developed by Alessandro Flacco and Tommaso Vinci (*https://github.com/aflux/neutrino*). The steps of data processing are shown on Fig.4.15: the wavelet analysis enables the extraction of the $\pm\pi$-limited phase from the interferogram. 2D unwrapping techniques [81, 82] allow continuous phase recovering. Finally, the thermal-induced
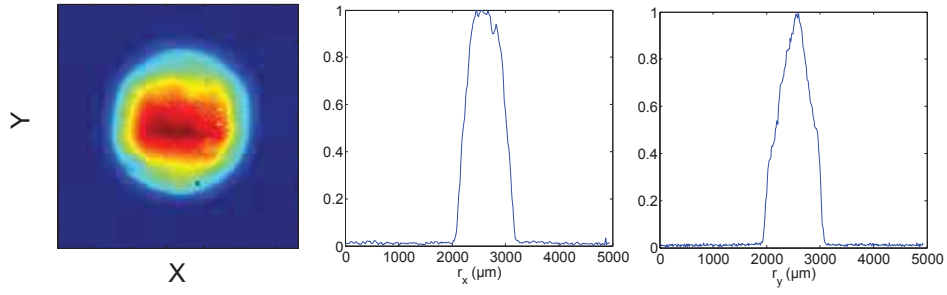
Figure 4.13 – Pump beam profile at focus.

phase-shift is obtained subtracting a reference phase measured when no pump beam propagates through the Ti:Sa crystal.
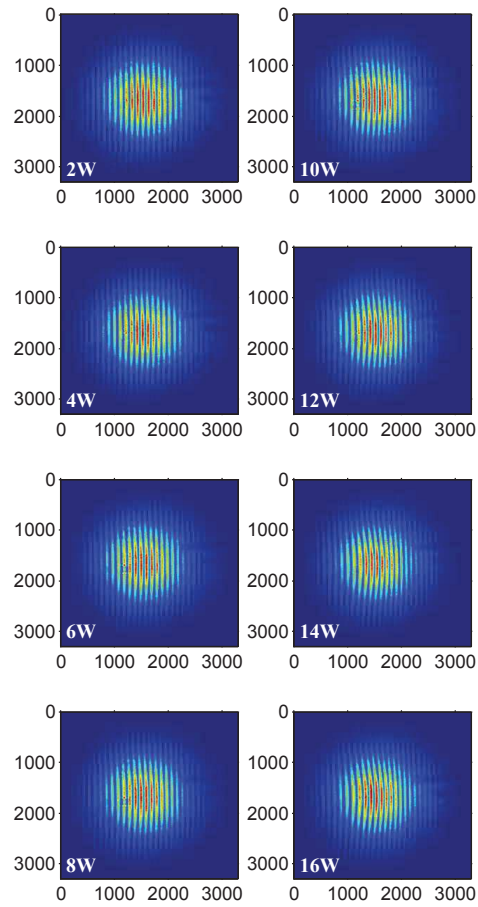
Figure 4.14 – Interferograms given for several pump powers. The axes are given in µm. The fringes curve progressively with the increasing pump power.

Comment on wavelet analysis

The Wavelet Transform (WT) can be considered as a generalized form of Fourier Transform (FT) and windowed FT. A WT uses generalized local base functions called wavelets, that can be stretched and translated in both frequency and time. Detailed explanations about wavelet analysis can be found in [83]. The quality of the phase reconstruction strongly depends on the parameters chosen to generate the 2D wavelets packets. A wavelets packet is defined by four parameters:

- the wavelet wavelength, corresponding to the wavelet stretching factor. This parameter is defined according to the fringes width (broad fringes require high wavelet wavelengths).

- the wavelet rotation angle, defined according to the curvature of the fringes: the more fringes are curved, the more the angle range should be significant.

- the wavelet thickness: Considering the 2D wavelets as small ellipses, their minor axis is called the wavelet thickness. This parameter should be at least 2 pixels and depends on the measured phase gradients (strong gradients require short wavelet thicknesses).

- the damp factor, defined as the wavelet length in terms of oscillations number. A low damp factor makes the code less robust.

The algorithm can calculate a quality map defined as the spanning integral between wavelets and interferogram. The wavelets parameters are well defined when the quality map is smooth.
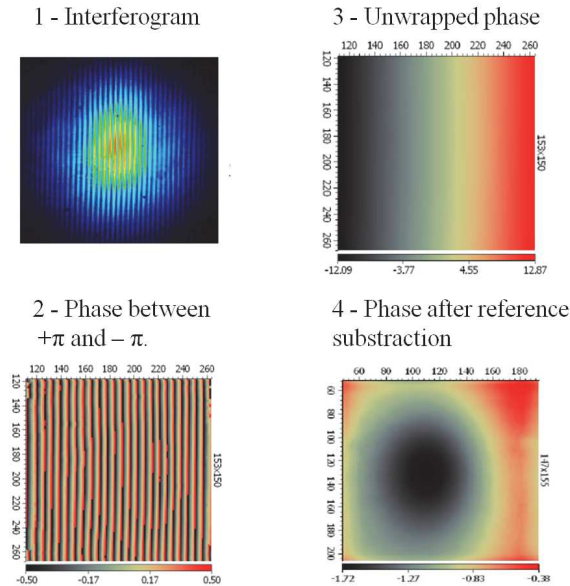
Figure 4.15 – Principle of the algorithm used for phase extraction.

The phase maps are shown on Fig. 4.16 for each pump power. The color scale is given in µm. The thermal-induced phase-shift gets stronger with the increasing pump power. I performed horizontal and vertical cross-sections of these phase maps (see Fig. 4.17 and 4.18). The OPD is less sharp along the horizontal direction because the pump radius is spread on the Brewster-cut crystal in this direction. The maximum Y-OPD is indeed higher than the maximum X-OPD at equivalent pump power. For instance, the X-OPD (resp. Y-OPD) maximum is 0.48 µm (resp. 0.65 µm). The thermal lens in both planes can be determined via a parabolic fit of the OPD cross-sections in the

pump beam area (1040 µm), as illustrated on Fig. 4.19 and 4.20. The focal length of the thermal lens can be deduced using Eq. 4.26 (see Fig. 4.21).

The measurement uncertainty was determined considering two sources of errors:

- the uncertainty of the pump power measurement, estimated as 5 % according to the power-meter supplier (Thorlabs).

- the uncertainty related to the location of the OPD cross-section. I evaluated the corresponding standard-deviation by measuring the thermal lens on ten of pixels in the area where the OPD is maximum.

Finally, the error on the focal length measurement is given by:

$$\sigma = \sqrt{0.05^2 + \sigma_{\text{cross-section}}(P)^2} \qquad (4.27)$$
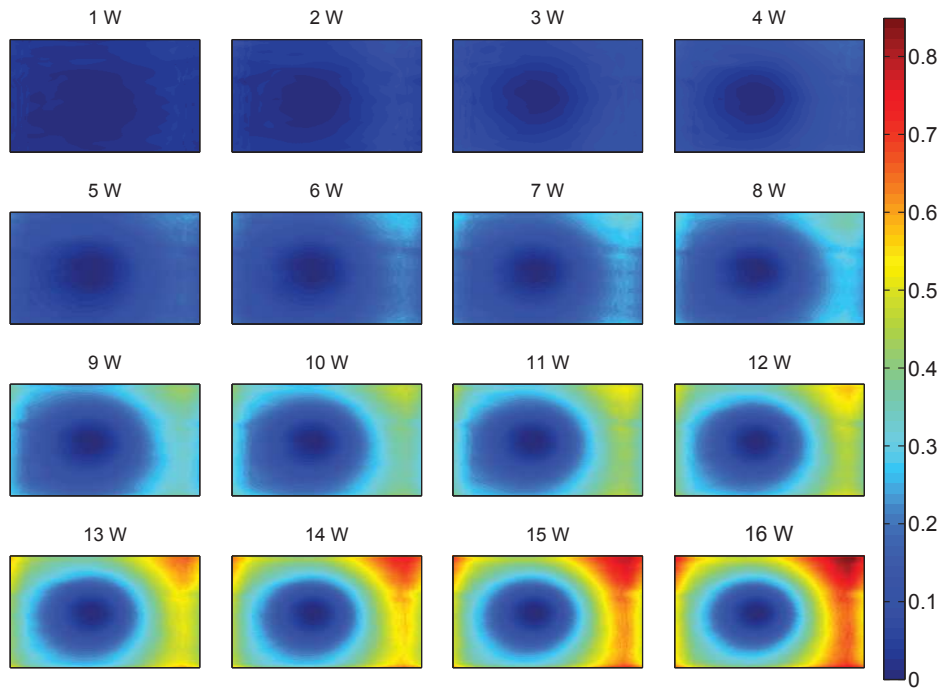
Figure 4.16 – Thermal-induced phase maps for various pump power. The scale is given in µm.

As expected, the focal length of the thermal lens is higher in the horizontal plane because of the Brewster incidence. These experimental data can be compared to the theoretical model. To do so, the crystal absorption should be first measured. The incident power was limited so that saturation absorption does not occur. The crystal absorption was measured and found to be 70 %.

For comparison with the experiment, I run the theoretical model presented above with the following parameters: T = 300 K, L = 5 mm, r_0 = 2.5 mm, A = 0.7, ω_{p0} = 520 µm. The results are shown in green on Fig. 4.21. The theoretical values should match the experimental focal lengths in the vertical plane, where the pump radius is 520 µm as well. However, they are higher and closer to the experimental data obtained in the horizontal plane. The theoretical model assumed a perfect
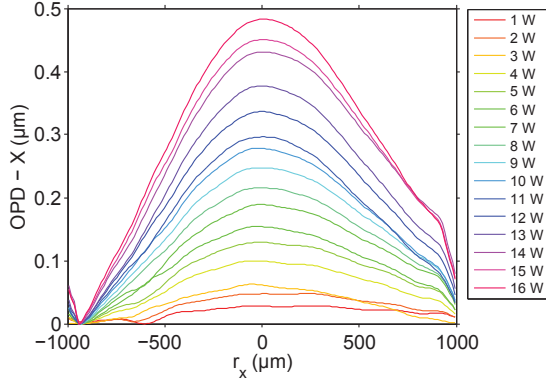
Figure 4.17 – Horizontal cross-sections of the phase maps. Phase is converted into Optical Path Difference (OPD).
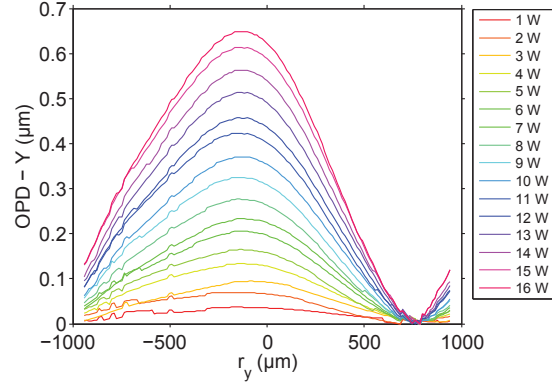
Figure 4.18 – Vertical cross-sections of the phase maps. Phase is converted into Optical Path Difference (OPD).
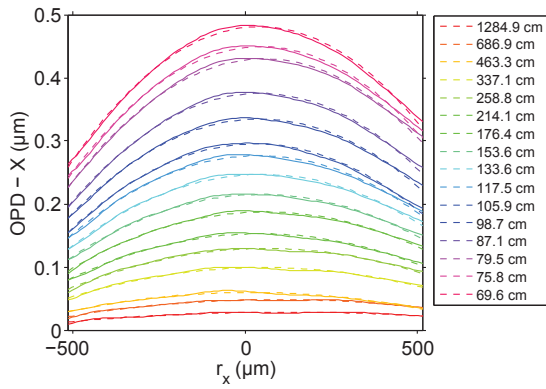
Figure 4.19 – Fit of the OPD curves along the horizontal direction.
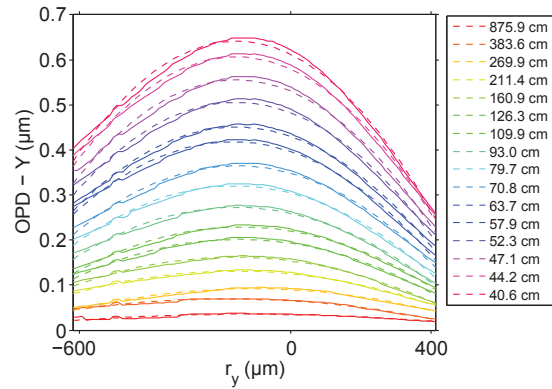
Figure 4.20 – Fit of the OPD curves along the vertical direction.

contact between the crystal and its mount, which is not the case in real life. This explains why the theoretical focal lengths are longer than the experimental ones. Then, the pump laser beam profile is sharp in the vertical direction. This could explain why the experimental values of thermal lens focal length are shorter than the ones given by the theoretical model, which assumes a top-hat pumping beam. However, this last issue should have a negligible influence compared to the contact quality issue: it is demonstrated in [80] that a super-Gaussian pumping beam (n=m=10) leads to temperatures within the crystal only 1.5 K less than with a Gaussian pumping beam (n=m=1).

Thermal lens measurement with a wavefront sensor

I performed the same experiment using another diagnostic: a wavefront sensor (Sid4, Phasics). The setup is illustrated on Fig. 4.22. As in the case of the interferometer, the crystal output face is conjugated with the detection plane. However, the magnification is not anymore 1. A theoretical magnification of 2.3 enables to cover a maximum of the detector surface. The pumping beam parameters are the same than in the case of the previous experiment. In particular, the pumping beam profile is top-hat in the horizontal direction and sharp in the vertical direction. The major difficulty with this setup is to isolate the wavefront sensor from the pump photons. Spatial and spectral filtering of the probe beam allows to preserve the CDD from the 527 nm photons.

The reference measurement is performed when no pumping beam propagates through the crystal. As in the case of the previous experiments with the Mach-Zehnder setup, I measured the thermal-induced phase-shift for various pump powers (see Fig 4.23). The same data processing is applied: the horizontal and vertical cross-sections are extracted (see Fig. 4.24 and 4.25) and fitted with a parabolic function in the pumping beam area (see Fig. 4.26 and 4.27) to deduce the
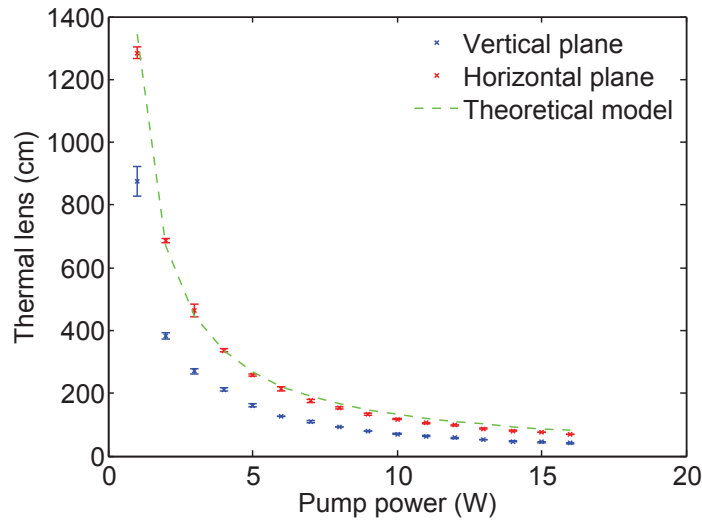
Figure 4.21 – Thermal lens in the horizontal and vertical planes, obtained with the Mach-Zehnder setup and comparison to the theoretical model presented above [70].
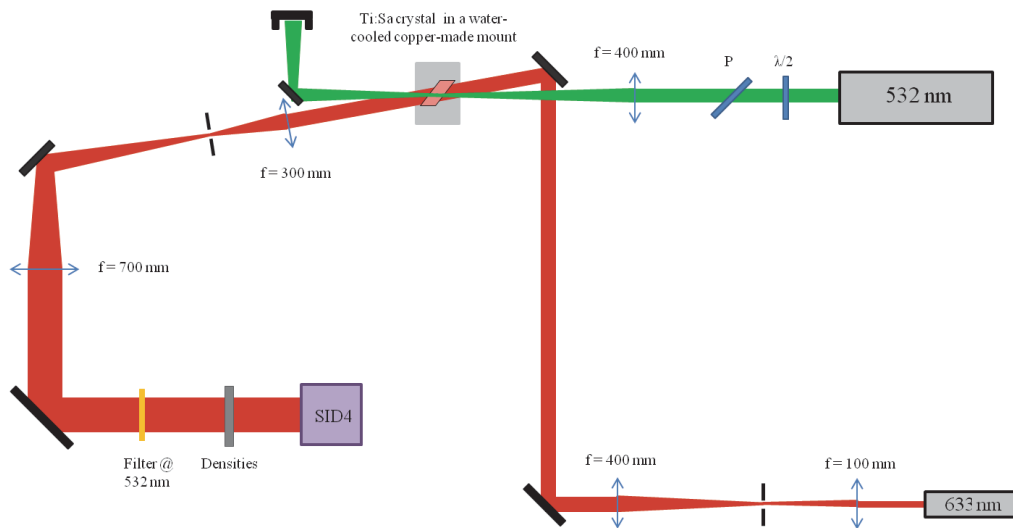
Figure 4.22 – Setup for thermal measurement using a wavefront sensor.

thermal lens focal length according to Eq. 4.26. The results are shown on Fig. 4.28. The error bars are calculated according to Eq. 4.27. The wavefront sensor error itself is not taken into account. It should be negligible compared to error made on the pump power measurement, as the Sid4 accuracy is 10 nm RMS and the OPD amplitude is a few µm. As previously, the experimental data are compared to theory (Fig. 4.28). The focal lengths given by the theoretical model are longer than the experimental value obtained in the vertical plane, mainly because of the perfect thermal contact assumption.

Comparison between the two thermal diagnostics

Finally, I gathered all the experimental data on a single graph (see Fig. 4.29). The very good agreement between the two diagnostics confirms the correctness of the thermal lens characterization, all the more so the two experiments runs were not performed the same day. A small gap is even observed between the two methods and can be related to the reference making. With the wavefront sensor, I performed a reference measurement before each measuring point, whereas I performed
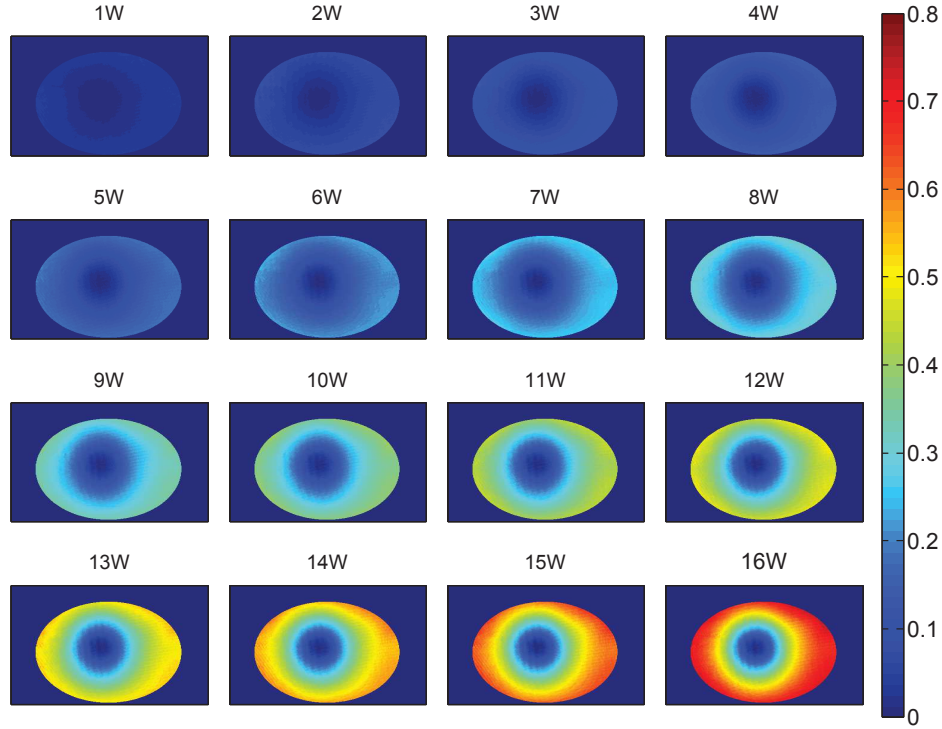
Figure 4.23 – Thermal-induced phase maps measured with a wavefront sensor (Sid4, Phasics) for various pump power. The scale is given in µm.
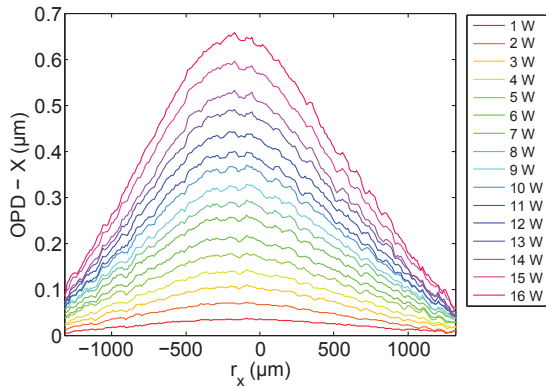
Figure 4.24 – Horizontal cross-sections of the phase maps measured with a wavefront sensor (Sid4, Phasics). The phase is converted into Optical Path Difference (OPD).
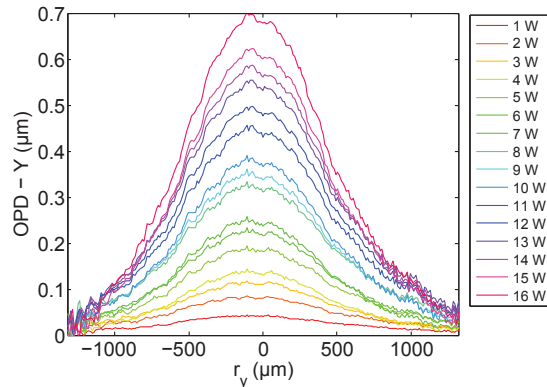
Figure 4.25 – Vertical cross-sections of the phase maps measured with a wavefront sensor (Sid4, Phasics). The phase is converted into Optical Path Difference (OPD).

a single reference for all the measuring points in the case of the Mach-Zehnder experiment.

From the practical point of view, the wavefront sensor is advantageous because the results are directly available and no data post-processing is required. Although many reliable algorithms performing wavelet analysis and 2D phase unwrapping are available, the interferograms processing is heavy going.
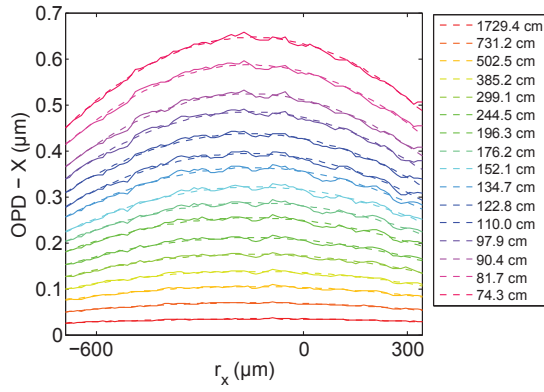
Figure 4.26 – Fit of the OPD curves along the horizontal direction.
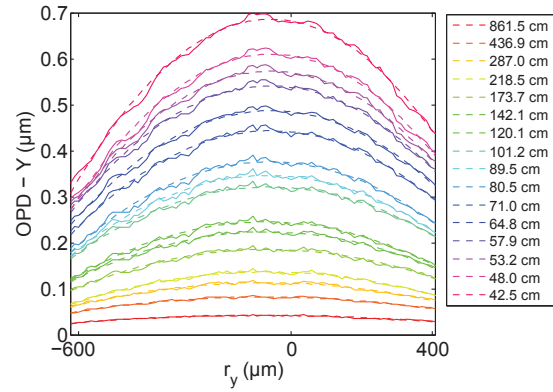
Figure 4.27 – Fit of the OPD curves along the vertical direction.
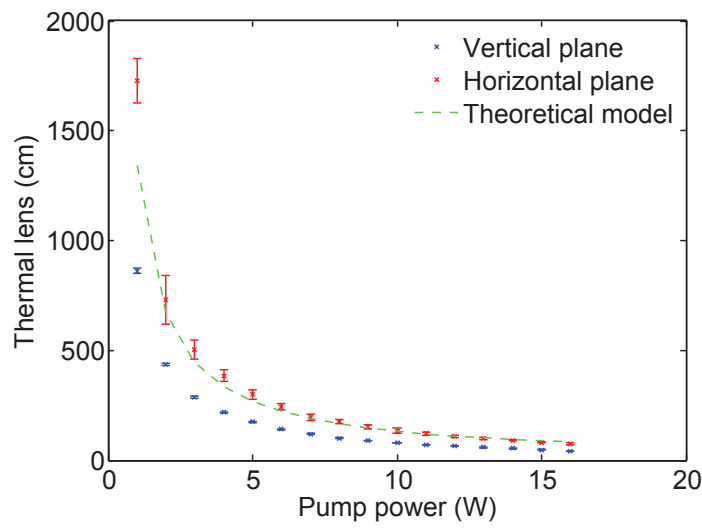
Figure 4.28 – Thermal lens in the horizontal and vertical planes, obtained with the wavefront measurement setup - Comparison to theory [70].
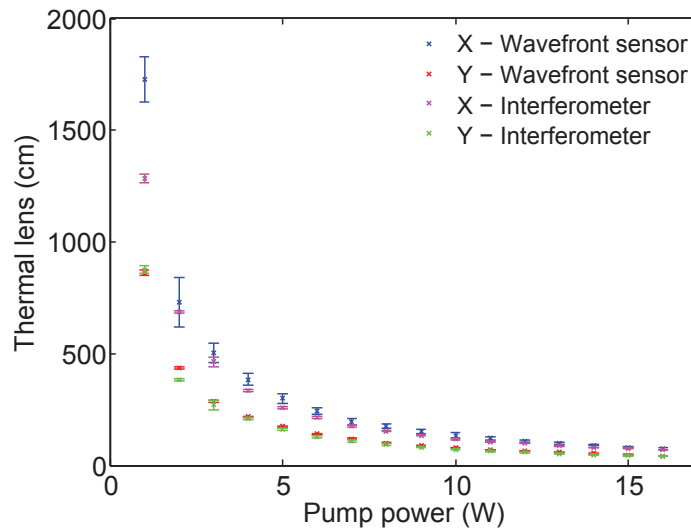
Figure 4.29 – Comparaison between the experimental results obtained with the two setups: the Mach-Zehnder interferometer and the wavefront sensor.

Conclusion to the theoretical and experimental thermal analysis

To conclude, I made theoretical calculations to evaluate the thermal lens focal length in a Ti:Sa crystal under pumping. To do so, I based on the model proposed by Chénais, which takes into

account the absorption saturation. I applied this model for sizing the Ti:Sa crystal of the power amplifier of the Salle Noire 3.0 laser and to determine a cooling temperature leading to a limited temperature gradient within the crystal. Cooling the 10 mm-long, 8 mm-wide crystal at 110 K limits the gradient temperature to $\approx 10°C$ and leads to a focal length about 3.5 m which can be easily compensated in a two passes amplifier.

Then, I compared the theoretical model to the results given by two experimental setups: a Mach-Zehnder interferometer and a setup including a wavefront sensor. Both setups give similar results, confirming the correctness of the proposed experimental protocol which will be useful for the characterization of the thermal effects within the power amplifier in the near future.

4.3   Simulation of the amplification process in the power amplifier

The crystal dimensions are now set (L = 10 mm, r = 8 mm), and the simulation of the amplification process can be performed. To do so, I used CommodPro, a MIRO-based code developed by CEA [53]. This code allows to solve the coupled equations governing the amplification process and the nonlinear Schrödinger equation governing the propagation of the broadband laser pulses. Diffraction, optical Kerr effect and material dispersion are taken into account.

4.3.1   CommodPro Simulations

In a first step, the 2D gain map is calculated. The pumping beam parameters are gathered in Tab. 4.10 with the main Ti:Sa characteristics. The population of the bottom level is set so that the non-saturated absorption coefficient of the crystal, α, is equal to 95 %. The maximum gain is 22.4.

Pumping beam parameters		Ti:Sa crystal parameters	
Energy	100 mJ	Dimensions	10 mm-long 8 mm-wide
Diameter ($1/e^2$)	1.2 mm	Cut	Brewster ($\theta_B = 60°$)
Pulse duration	150 ns	Saturation fluence	$8.44.10^3$ J.m^{-2}
Maximum pump fluence	$7.67.10^4$ J.m^{-2}	End face transmission	98 % for each face
Temporal pump profile	Super-Gaussian (order 2)	Population of the bottom level	$5.15.10^{25}$ m^{-3}
Spatial pump profile	Super-Gaussian (order 3)	Coherence time	5.10^{-14} s

Table 4.10 – Parameters used for gain calculation with CommodPro.

The energy and duration of the 805 nm-centered initial pulses are respectively 5 mJ and 200 ps. The temporal chirp parameter is b = $3.27.10^{23}$ s^{-2}, considering that the spectral bandwidth of the incident pulses is 45 nm (FWHM). All parameters used in the simulation are gathered in Tab. 4.11. The energy reached at each pass is given on Fig. 4.30 and the results are summarized in Tab. 4.12. Two passes enable to achieve an energy of 42.6 mJ with an accumulated B integral of 0.58 rad.

The spectra and temporal phases are shown for each pass on Fig. 4.31 and 4.32. A red-shift about 10 nm is observed on the amplified pulse spectra. The pulse leading edge contains indeed the highest wavelengths and is more amplified than the pulse trailing edge. This phenomenon is called 'gain shifting' and translates here into a red-shift amplified pulse spectrum. This can be also observed on the pulse temporal phase, which is shifted towards negative times corresponding to the pulse leading edge.

After two passes, the energy reaches 42.6 mJ. Considering a TGC transmission about 65 %, the energy of the compressed pulses will be 27.7 mJ. In this way, two passes meet the laser specifications. However, a third pass could improve the laser stability thanks to the amplification saturation
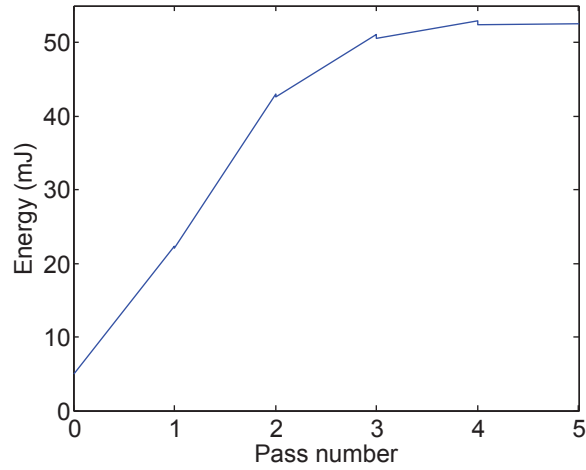
Figure 4.30 – Energy as a function of the pass number in the amplification medium.

Seed parameters		Ti:Sa crystal parameters	
Energy	5 mJ	Refractive index	1.76
Diameter ($1/e^2$)	1.1 mm	n_2	$5.2.10^{-20}$ m^2.W^{-1}
Pulse duration	200 ps	Saturation fluence	$8.44.10^3$ J.m^{-2}
b	$3.27.10^{23}$ s^{-2}	Group Velocity Dispersion (GVD)	$-5.82.10^{-26}$ s^{-2}.m^{-1}
Temporal and spatial profile	Super-Gaussian (order 2)	Coherence time	2.73 fs

Table 4.11 – Parameters used for the amplification simulation.

Pass	Energy (mJ)	B integral (rad)
P1	21.9	0.15
P2	42.6	0.58
P3	50.3	1.13
P4	52.2	1.70

Table 4.12 – Results of the amplification simulation.
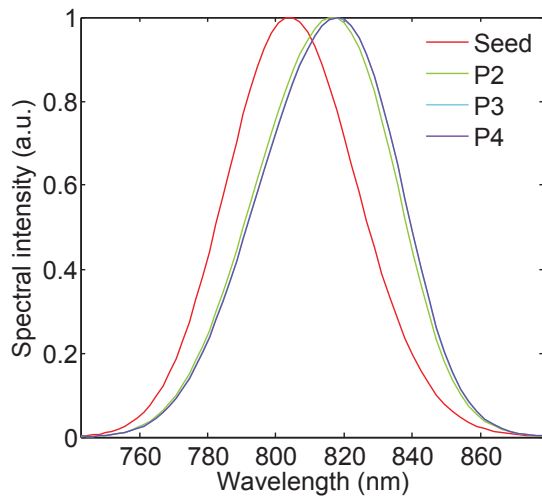
Figure 4.31 – Seed spectrum and spectrum for each pass in the amplification medium.
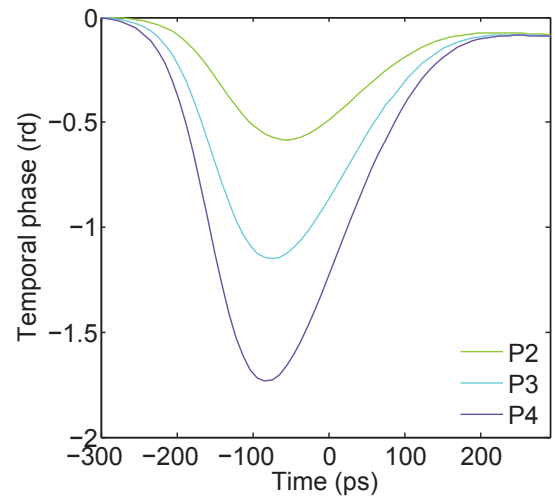
Figure 4.32 – Temporal phase after each pass in the amplification medium.

process. At the same time, a third pass implies a higher accumulated B integral which can degrade the laser contrast, as demonstrated in the next paragraph. A compromise should be found between energy stability and contrast.

4.3.2 Nonlinear temporal diffraction implies a compromise between contrast and energy stability

Post-pulses originate in the manifold internal reflections occurring in optical components with imperfect anti-reflective coatings. These post-pulses are not an issue as they do not disturb the laser-target interaction. However, as explained in section 3.3, the non-linearities experienced by overlapped stretched pulses in the laser chain materials, and especially in the amplification media, can turn post-pulses into pre-pulses [52].
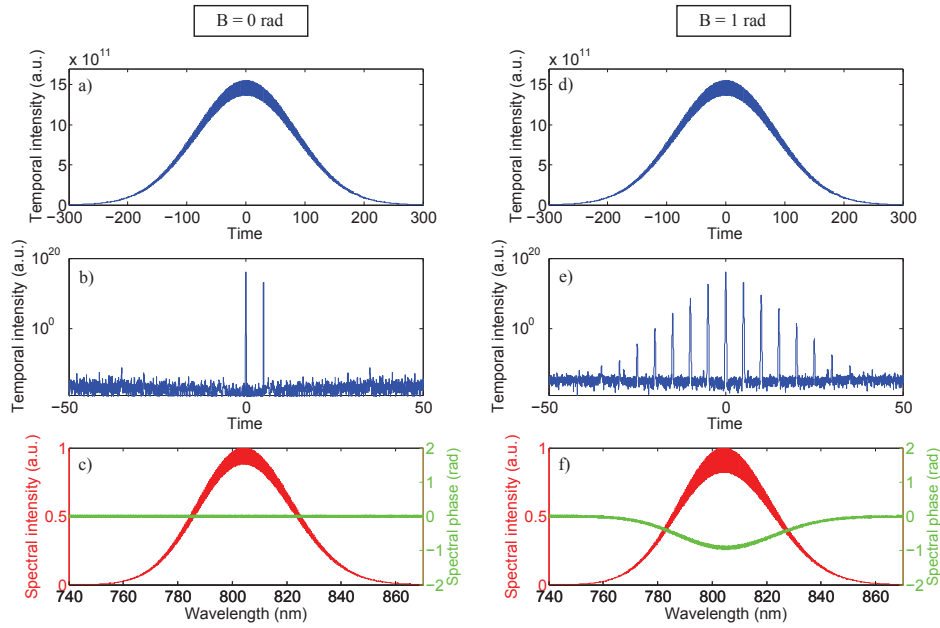
Figure 4.33 – Simulation of the nonlinear temporal diffraction effect under B integral. The initial post-pulse delay is $\tau = 5\,\text{ps}$ and B = 0 or 1 rad. a,d) Pulse temporal intensity prior to compression. b,e) Pulse temporal intensity after compression. c,f) Pulse spectral intensity after compression and corresponding spectral phase.

To quantify this phenomenon according to the B integral value, I performed simulations with MIRO [53]. I defined analytically an initial pulse and a post-pulse at 10^{-3} relative intensity delayed from the main pulse by τ. Both 25 fs pulses are stretched to 200 ps and undergo non-linearities in a plate. The B integral is set via the nonlinear index of the plate, which is the only source of non-linearities. The pulses are finally compressed and analyzed. Fig. 4.33 shows the temporal intensity before (a,d) and after (b,e) compression in the case where B = 0 or 1 rad. As expected, when the B integral is different from zero, the compressed pulse exhibits new pre- and post-pulses with decreasing intensities around the main pulse. Each Nth pre-pulse is delayed from the main pulse by $\tau_N = N\tau$ where τ is the initial delay between main pulse and post-pulse.

To go further, I used the apodizer component in MIRO to isolate only the pre- or the post-pulse after compression. Fig. 4.34 shows the spectra of each pulse for two different values of the initial delay ($\tau = 5\,\text{ps}$ and $\tau = 50\,\text{ps}$). As highlighted by [52] and explained in section 3.3, the spectra of the created pulses are narrower and shifted from the initial pulse: the pre-pulse is blue-shifted whereas the post-pulse is red-shifted. The spectral shift depends on the product $b \times \tau$. This is clearly visible on Fig. 4.34 where a higher τ value for a given b provides a more pronounced spectral-shift of the pre- and post-pulses. Finally, I isolated the first (N = 1) and the third (N = 3) pre- and post-pulses when the initial delay is 50 ps (see Fig. 4.35). The higher the pulse order is, the larger the spectral shift is.
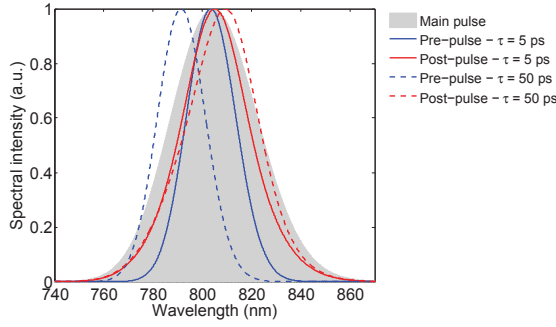
Figure 4.34 – Spectra of the pre and post-pulses the closest to the main pulse for B = 1 rad. The spectrum of the main pulse is also indicated (grey area). The initial post-pulse delay are 5 ps or 50 ps.
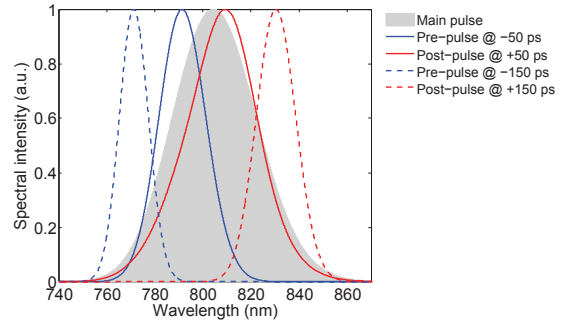
Figure 4.35 – Spectra of the pre and post-pulses at 50 ps or 150 ps from the main pulse for B = 1 rad. The spectrum of the main pulse is also indicated (grey area). The initial post-pulse delay is 50 ps.
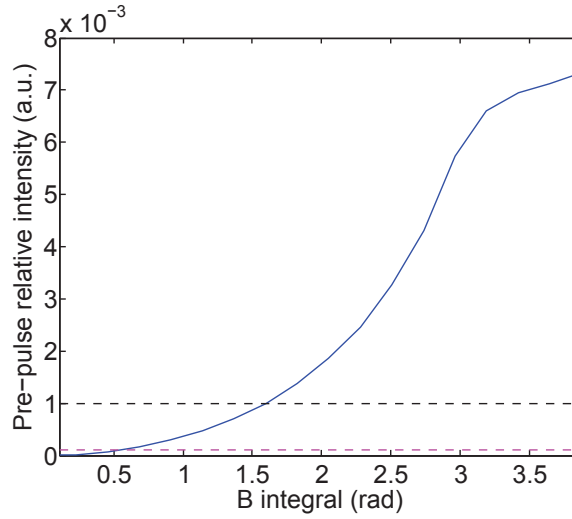
Figure 4.36 – Pre-pulse intensity relative to that of the main pulse, as a function of B integral.

Finally, one can explore the B integral influence on the pre-pulse intensity. I consider only the pre-pulse with the maximum intensity (N = 1). I assumed an initial post-pulse relative intensity of 10^{-3}. Fig. 4.36 shows the pre-pulse relative intensity as a function of the accumulated B integral in the plate. The pre-pulse intensity is below 10^{-4} as long as B is below 0.5 rad. It reaches 10^{-3} when B is equal to 1.6 rad. For B values higher than 3 rad, a saturation effect appears. Note that the pre-pulse intensity gets higher than 10^{-3} but the pre-pulse is not more intense than the initial post-pulse. This is because the maximum intensity of the main pulse slightly decreases when B increases.

To conclude, performing only two passes in the power amplifier (B = 0.58 rad) makes sure that any eventual post-pulse at 10^{-3} relative intensity will be turned to a pre-pulse with a relative intensity only about 10^{-4}. A third pass (B = 1.13 rad) will lead to a pre-pulse with a relative intensity about 5.10^{-4}, still below 10^{-3}. Two passes are preferable from a contrast standpoint, all the more so that additional B integral will deteriorate the contrast in the TGC. Three passes allows a lower contrast (always assuming the presence of an hypothetical post-pulse at 10^{-3} relative intensity) but guarantees a better energy stability. The gain saturation effect was not considered here and leads also to a nonlinear temporal diffraction process [52]. However, the resulting pre- and post-pulses have in this case an intensity smaller by several orders of magnitude compared to the ones induced by the B integral.

4.4 Conclusion

In this chapter, the main technological challenges of the second CPA were discussed. The stretcher-compressor design results from a compromise between a low B integral (guaranteed by a large stretching factor) and its ability to preserve CEP stability (guaranteed by a minimal optical pathway in the stretcher and compressor devices). A full design is proposed, with dispersion and aberration calculations. Otherwise, the thermal lens calculations allowed to set the Ti:Sa crystal dimensions in the power amplifier. Finally, the energy and B integral were determined for each pass of the power amplifier via numerical simulations. I highlighted how some nonlinear temporal diffraction phenomena can occur in the amplifier. The contrast degradation was quantified according to the amount of non-linearities.

The last chapter of this part addresses the post-compression stage of the laser system to achieve few-cycle pulses starting from the 20 fs pulses at the TGC output. Two diagnostics for ultra-short pulses are also investigated.

Chapter 5

Towards Terawatt-class few-cycle pulses

Contents

CPA-based laser systems cannot deliver pulses with durations lower than 15 fs because of the gain limited spectral bandwidth in Ti:Sa crystals. To get shorter pulses, a post-compression stage is required. The most widespread method for producing high quality few-cycle pulses is via self-phase modulation (SPM) broadening of amplified femtosecond pulses in noble gas-filled hollow-core fibers (HCF) followed by temporal compression with chirped mirrors [39]. Such a technique was used in Salle Noire 2.0 where 8 mJ, 23 fs pulses were compressed down to 4 fs with a final energy of 4 mJ [84]. We can wonder if this technique is suitable to the Salle Noire 3.0 which will deliver more energetic pulses. Another issue is the temporal characterization of the resulting few-cycle pulses. In this chapter, I first present two diagnostic tools commercially available for few-cycle pulses temporal measurement. The post-compression challenge in Salle Noire 3.0 is then briefly discussed.

5.1 Testing two metrology devices for ultra-short pulse measurement

A complete review details the various techniques that can be used to characterize temporally ultra-short pulses [85]. During my PhD, I got the opportunity to use in particular two diagnostics: a Wizzler-USP (Fastlite) and a D-scan (Sphere Photonics).

5.1.1 Wizzler-USP (Fastlite)

The Wizzler-USP is a single-shot diagnostic tool which relies on spectral interferences between the pulse to measure and a reference pulse with a flat spectral phase and a broad spectrum [86]. A birefringent plate creates a small replica, which is the pulse to measure. The main replica is used to generate the reference pulse via XPW generation. A Fourier-Transform Spectral Interferometry treatment of the interferogram enables to recover the complete profile of the pulse (intensity and phase) [87].

In the Wizzler-USP, dispersion prior to XPW generation is minimized compared to the classical Wizzler device. The first polarizer is reflective and the only dispersive component prior to the 200 µm-thick XPW crystal is a 100 µm-thick plate used to create the small replica.

5.1.2 D-scan (Sphere Photonics)

The 'D' of 'D-scan' means 'Dispersion'. This technique relies indeed on a dispersion scan around the optimum compression value, while recording simultaneously the SHG spectrum [88]. Silica wedges usually enables to finely tune the dispersion of few-cycle pulses. In the D-scan technique, those wedges also allows the continuous dispersion scan needed for the measurement. The resulting trace of the SHG spectra can be analyzed to retrieve the pulse profile (intensity and phase).

The main advantage of the D-scan technique compared to the Wizzler one is that chirped pulses can be characterized. Because the Wizzler-USP relies on XPW generation, only close-to-compression pulses can be measured. The Wizzler-USP provides indeed a measurement as long as the initial chirp of the 5 fs pulses is between $\approx \pm 10 \, \text{fs}^2$. On the contrary, the D-scan trace is very visual and help appreciating the amount of phase required to achieve pulse compression.

5.1.3 Experimental results with sub-4 fs pulses

The setup is shown on Fig. 5.1. The FemtoPower delivers 30 fs, 1.5 mJ pulses. A 1 m focal length mirror ensures beam coupling in a 1 m-long, statically Neon-filled Hollow-Core Fiber (HCF) with an inner diameter of 250 µm. An iris located prior to the HCF enables to minimize the coupling losses. At the HCF output, the beam collimation is ensured by a 1 m focal length mirror so that the beam diameter is about 10 mm. The compression is achieved with a set of 10 chirped mirrors (-400 fs^2, UltraFast Innovations GmbH). Then, a telescope reduces the beam diameter down to 4 mm to match the entrance aperture of the Wizzler-USP device. A first wedge attenuates the pulse energy and is followed by the D-scan wedges, both mounted on a motorized translation
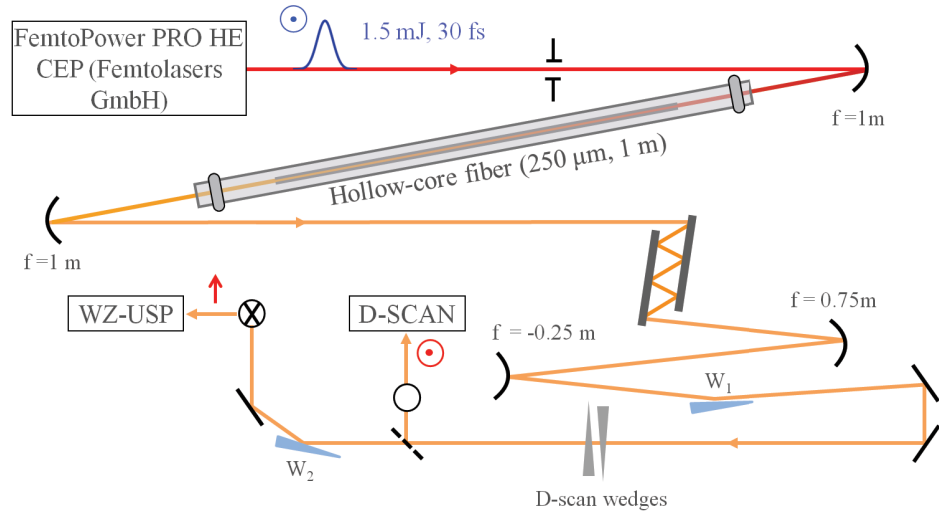
Figure 5.1 – Post-compression setup for comparison between two ultra-short diagnostics: Wizzler-USP and D-scan.

stage. The pulse compression is achieved when the beam is centered on both wedges. A flip mirror sends the beam to the D-scan device which requires P-polarized pulses with an energy about 40 µJ. The Wizzler-USP line requires another wedge for attenuation down to 4 µJ and a periscope with crossed mirrors to turn the pulse polarization into S. Note that the number of mirrors is the same in both lines (2 mirrors in the periscopes + 1 transport mirror). The 6 silver mirrors are from the same coating run so that dispersion should be the same on both lines, making the measurements comparable. The main difficulty in this setup was to find the optimal energy for both devices, playing with the incident angle of the two wedges W_1 and W_2. The use of neutral densities for beam attenuation is absolutely forbidden here because it affects the pulses spectral bandwidth (blue wavelengths < 590 nm are completely absorbed by the available densities).
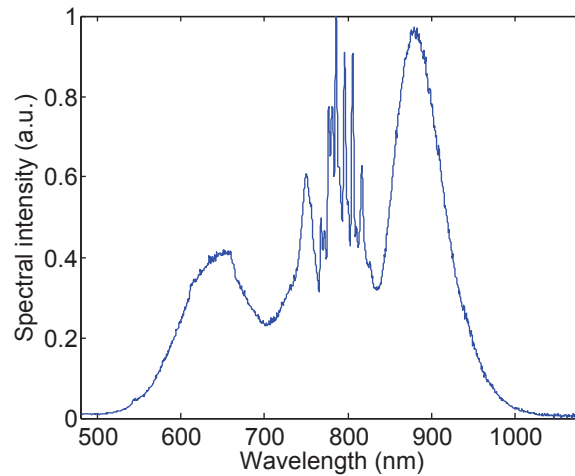
Figure 5.2 – Spectrum at the Hollow-Core Fiber output.

The HCF output spectrum is shown on Fig. 5.2. The barycenter and the bandwidth (FWHM) of the spectrum are respectively 791 nm and 215 nm. The Wizzler-USP measurement is shown on Fig. 5.3. The spectral phase is globally flat with residual oscillations due to the chirped mirrors. The pulse duration indicated by the device is 4.3 fs, which is longer than the actual one because of the limited spectral bandwidth managed by the spectrometer inside the Wizzler device. A sharp

spectral cut-off is indeed observed at 950 nm and corresponds to an edge of the spectrometer gratings.
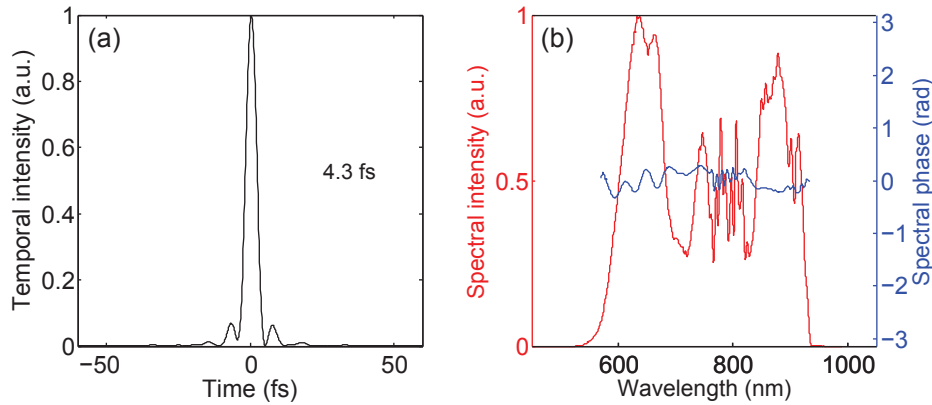
Figure 5.3 – Wizzler measurement. a) Temporal intensity. b) Spectral intensity and phase.

The D-scan measurement and retrieval are shown on Fig. 5.4. The device indicates a pulse duration of 3.7 fs with a retrieval error about 1.74 %. The pulse spectrum is entirely measured (no cut-off are observed) so that the actual pulse duration is obtained. The spectral phase is also globally flat with residual oscillations due to the chirped mirrors.
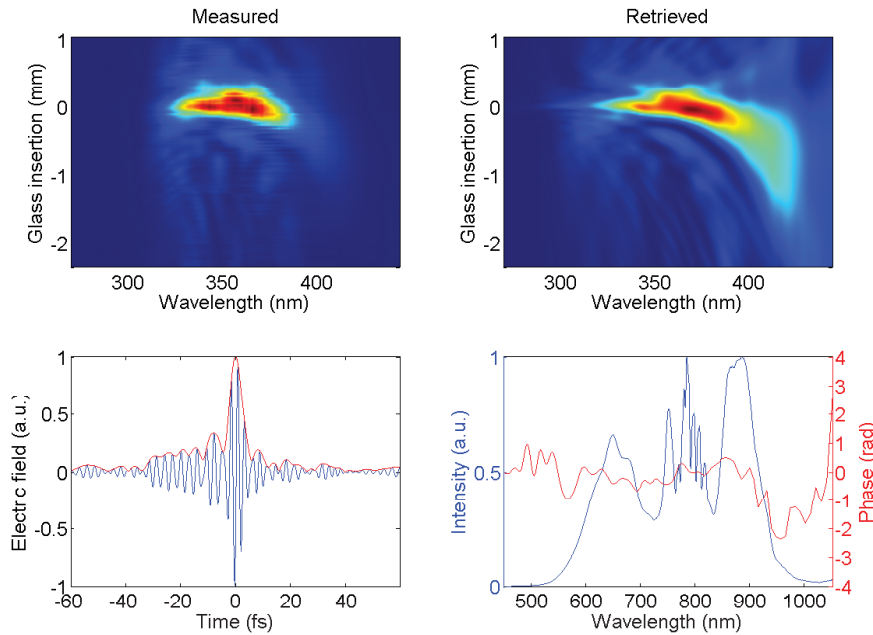
Figure 5.4 – D-scan measurement.

To make the comparison easier, I superimposed both measurements on single graphs. Fig. 5.5 shows the temporal profile of the pulses whereas Fig. 5.6 compares the spectral profile of the pulses (intensity and phase). Even though both phases seem to be opposite, a strong similarity can be observed, as the phase oscillations occur at the same wavelengths. Comparing the reconstructed spectra to the HCF output spectrum (Fig. 5.2), the calibration of the d-scan looks better than the Wizzler-USP one.

To conclude, two ultra-short diagnostic tools were tested: the Wizzler-USP (Fastlite) and the D-Scan (Sphere Photonics). The post-compression setup allowed the production of 3.7 fs pulses, which highlighted the limitation of the Wizzler-USP device in terms of spectral bandwidth acceptance. The implementation of another spectrometer in the device should solve this issue. Both
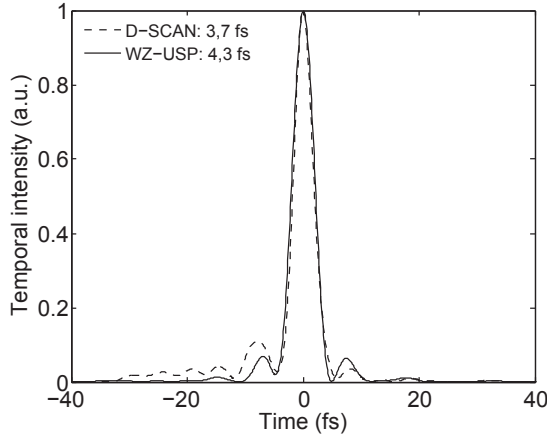
Figure 5.5 – Seed spectrum and spectrum for each pass in the amplification medium.
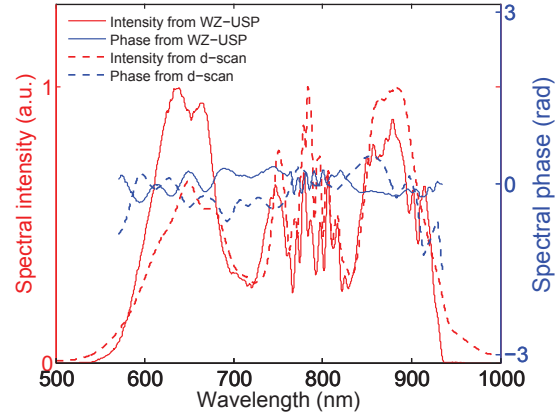
Figure 5.6 – Temporal phase after each pass in the amplification medium.

devices were easy to align but it should be noticed that the need of a crossed periscope for the Wizzler-USP is constraining when working with P-polarized pulses. Finally, the large energy and beam diameter acceptance range of the D-scan makes life easier. In the Wizzler-USP, the energy range acceptance is very limited: a high energy generates continuum in the XPW crystal whereas a too low energy does not allow the generation of a broad enough XPW spectrum. The energy gap between these two limits is roughly 4 μJ with sub-4 fs pulses and the only tool for energy balance is a rough aperture (for the specific comparison experiment presented in this chapter, special care was taken to avoid the use of the aperture, implementing wedges at specific incidence. In this way, both devices measured the entire beam). Besides, the incident beam diameter should be 4 mm maximum, which obliges to build a telescope for a full beam characterization. For comparison, the D-scan can manage a 10 mm beam. Apart from these practical considerations, both devices work pretty well and are in good agreement. It should be noticed that the purpose of these two devices is different. The D-scan technique allows to find and optimize the pulses compression. The Wizzler device offers a large temporal dynamic range and is single shot, allowing direct optimizations.

5.2   The post-compression challenge

The post-compression campaign performed in Salle Noire 2.0 [84] highlighted that the energy at the HCF setup entrance was limited to 8 mJ because of the deleterious nonlinear effects due to propagation in the air and in the post-compression setup windows. The energy upgrade of the Salle Noire 2.0 up to 10 mJ after the GRISM compressor required a new design of the post-compression stage to get free from these nonlinearities. In this way, two vacuum chambers were designed in the framework of a collaboration with Dr. Tamas Naguy, from the Laser-Laboratory in Göttingen. The two vacuum chambers were installed at each side of the hollow core-fiber. There is hope to achieve 5 mJ, 4 fs pulses with this setup.

The Salle Noire 2.0 experience highlighted that the design of post-compression setups suited to high energies is hard, time-consuming and very expensive. A lot of research still needs to be done to find other ways to compress energetic pulses down to 4-5 fs. This issue is all the more so important because the ELI projects plan to achieve unprecedented energies. The next part deals with the experiments founded by ELI-ALPS to explore two options to post-compress multi-mJ pulses down to the few-cycle regime (< 10 fs).

Part II

Investigation into new post-compression techniques adapted to highly intense pulses

Chapter 6

Introduction

Electron dynamic inside atoms and molecules occurs at the attosecond time scale. A way to generate attosecond pulses and to accurately study this dynamic consists in focusing few-cycle CEP-stable laser pulses with high peak intensities on a solid target [3]. The laser-plasma interaction generates a secondary attosecond XUV radiation which provides a unique tool for investigating the electronic processes in matter. To reach the relativistic laser-plasma interaction regime, the peak intensity on target should be at least 10^{18} W.cm^{-2}. However, the generation of highly energetic few-cycle pulses still remains challenging.

To achieve few-cycle pulses, a post-compression stage is required at the output of the CPA-based laser system. Spectral broadening of amplified femtosecond laser pulses can be achieved through self-phase modulation (SPM) or filamentation in noble gas.

Laser filamentation

The filamentation technique is very attractive to post-compress high energetic pulses because no waveguide is required. The damaging issues and coupling losses related to the use of a waveguide are thus avoided. During the filamentation process, pulses generate their own guiding channel, thanks to a balance between self-focusing and ionization. A high peak intensity is maintained over a given length of the channel, enabling significant spectral broadening by SPM. The use of two successive gas cells lead to the generation of 5.1 fs, 180 μJ pulses with a high spatial quality and a good beam pointing stability [89]. The overall compression factor was about 6.8 and the total energy efficiency about 26 %. In another study performed in the same energy range, a single gas cell was used to generate 4.8 fs pulses from 25 fs pulses [90]. Then, this technique was demonstrated with higher energy pulses: 5 fs, 700 μJ pulses were produced with a two gas cells setup [91]. Finally, the highly efficient self-compression of 45 fs, 5 mJ pulses down to 8 fs was demonstrated in [92]. These results show that laser filamentation is a reliable process to achieve short pulse durations with high efficiencies and simple setups (no waveguide is required). However, this technique induces a strong spatial chirp compared to other techniques like compression through a gas-filled hollow-core fiber, as demonstrated in [90]. Furthermore, multi-filamentation must absolutely be avoided as it provides uneven and unstable beam profiles. The input energy is thus limited, depending also on the gas parameters.

Hollow planar waveguide

To face with this energy limitation, it was proposed to propagate pulses through a gas-filled planar dielectric waveguide [93]. The mode spreading in one direction allows a higher coupled energy than in a hollow fiber. The simulations predict that this technique is compatible with energies up to the 100 mJ level [94]. The planar waveguides proved their ability to compress pulses with

high input energies: it led to 12 fs, 2 mJ pulses in [95], 11.5 fs, 7.6 mJ pulses in [96], and 10.1 fs, 10.6 mJ pulses in [94]. To date, it seems that the highest energy obtained with this technique is 20 mJ [97], with a pulse duration of 15 fs. However, the focusability of the output beam in the free waveguide dimension is limited by the asymmetric mode guidance [94], and the wavefront deformation during propagation in the waveguide induces an heterogeneous spectral broadening. Finally, it seems that this technique did not allow the generation of sub-10 fs pulses.

Cross-polarized wave generation

Many applications require a high temporal contrast. For instance, the use of solid targets to generate high order harmonics requires high temporal contrast laser pulses because any pre-ionization process prevents the laser-plasma interaction. The temporal filtering ability of the XPW generation process is attractive as it features a contrast enhancement of 4 orders of magnitude [42]. The XPW technique enables also spectral broadening and smoothing so that the final pulses exhibit a high temporal quality. For these reasons, implementing an XPW setup as a post-compression stage seems to be very suited to applications demanding clean pulses. To date, the highest energy used to seed a XPW post-compressor setup was 10 mJ at a 100 Hz repetition rate. It led to the generation of 1.6 mJ, 15 fs pulses with a high temporal contrast [60]. I show in chapter 7 our effort to generate sub-10 fs pulses at 1 kHz repetition rate from 10 mJ pulses, using such a post-compression technique.

Hollow-core fiber

The gas-filled hollow-core fibers have proven over the years to be quite robust and adapted to the generation of sub-10 fs pulses with an excellent spatial quality. Such a device guarantees an uniform spatial mode, allowing to exploit the SPM process homogeneously.

Different broadening regimes were explored. Short pulse durations can be achieved via a strong ionization regime in short capillaries filled with low gas pressures, as demonstrated in [98, 99, 100] where 10 fs pulses were generated. Here, a significant ionization rate was reached, even with a low gas pressure and moderate interaction lengths, because the optical-field-ionization process is very fast and highly nonlinear. However, the compression can be hard to manage because of the strong spectral phase acquired by the blue wavelengths. The ionization process induces also high losses so that the energy efficiency is not higher than 20 %.

Another more efficient regime consists in avoiding ionization and using longer interaction lengths with higher gas pressures to broaden pulses via Kerr effect. In this case, the fiber diameter and gas parameters are constrained so that the multiphotonic ionization threshold is not reached [101]. Besides, an optimal fiber length can be determined, balancing dispersion and SPM [101]. A basic setup including a statically filled fiber, seeded by linearly polarized pulses produced > 1 mJ, 4 fs pulses [102] with a transmission > 60 %. Working with circularly polarized pulses allows a better transmission, broader and more stable spectra [103, 104]. The ionization rate is indeed lower for circularly polarized pulses, which restrains the nonlinear interactions between the first two fiber modes [105]. To extend the energy limit encountered with HCF compressors and related to the ionization issue, another solution is to implement differential pumping [106]: the front side of the fiber is evacuated and noble gas is applied to the end of the capillary. This technique reduces self-focusing inside the fiber. Both transmission and spatial phase are thus significantly improved. This technique demonstrated its relevance in [107, 108, 109, 36]. The best experimental result was achieved in [36], with the generation of 5 fs, 5 mJ pulses at 1 kHz repetition rate. Here, the pressure gradient and the initial chirp played a crucial role on the quality of the output pulses.

To enhance the spectral broadening ability of HCF, the interaction length should be increased. However, the rigid fibers with high guiding qualities are not longer than 1 m for technological reasons. Recently, the manufacturing of stretched flexible capillaries was proposed [110]. This technology is also adapted to the production of fiber with large inner diameter, which is convenient to decrease the losses. The linear losses coefficient is indeed inversely proportional to the fiber inner

diameter [111]. This type of fibers proved their high spectral broadening and transmission ability: in [111], 4.5 fs pulses were produced thanks to a 3 m-long fiber starting from 71 fs pulses.

The additional use of circularly polarized pulses, differential pumping and long fiber (> 1 m) seems to be promising, as demonstrated in [84] with the generation of 4 fs, 3 mJ pulses. These experiments highlighted also that coupling 10 mJ, 25 fs pulses at 1 kHz repetition rate in a fiber remains challenging for two reasons. First, the 10 W average power damages progressively the fiber entrance, even if a coupling taper was implemented. This depends of course on the spatial quality of the input beam. Second, the nonlinear amplitude and phase distortions occurring in the windows setup are detrimental to the post-compression process. This last mentioned point is valid for all the setup including a vacuum chamber.

An elegant way to solve this limitation is to implement pulse dividing before the post-compression setup, allowing to decrease the peak intensity by a factor 2^N where N is the number of dividers. The nonlinear effects in the windows setup, the ionization threshold, and the peak intensity at the fiber entrance are thus relaxed. A high peak intensity can be recovered after the post-compression setup via pulse combining. We demonstrated the relevance of this technique in a HCF post-compressor (chapter 8). This is the first experimental demonstration of coherent combining in the few-cycle regime (< 10 fs).

Chapter 7

Exploring the high energy XPW setup

Contents

The post-compressors based on the cross-polarized wave (XPW) generation process seem to be very attractive, enabling not only pulse shortening but also pulse temporal cleaning. Many applications require ultrashort pulses with a high coherent and incoherent contrast, like high harmonic generation on solid target. However, implementing such a filter as a post-compressor of a CPA-based laser system remains challenging because it must withstand highly energetic pulses and even a high average power when the repetition rate is significant. In this chapter, I report the data we obtained implementing a XPW setup as a postcompressor of a 10 mJ laser source delivering 22 fs pulses at 1 kHz repetition rate (Salle Noire 2.0).

7.1 Theoretical background and state-of-the-art

In the past ten years, at LOA, a nonlinear filtering device based on cross-polarized wave (XPW) generation was developed [42]. XPW generation is a third order nonlinear process which is frequency degenerated, meaning that the XPW spectral content is in the same range as the incident wave. The XPW generation process is governed by the $\chi^{(3)}$ tensor anisotropy in isotropic crystals with respect to refraction index (the Fundamental and XPW waves have both the same group velocity in the crystal). When the linearly polarized incident wave illuminates such a crystal placed between crossed polarizers, it gives rise to the XPW wave, as shown on Fig. 7.1. The wave with the same polarization than the incident one is called Fundamental. The XPW generation process is considered to be instantaneous since the response time of the nonlinear susceptibility is below one femtosecond. The cubic dependance between the output and input intensities provides an improvement of the temporal contrast but also pulse shortening.
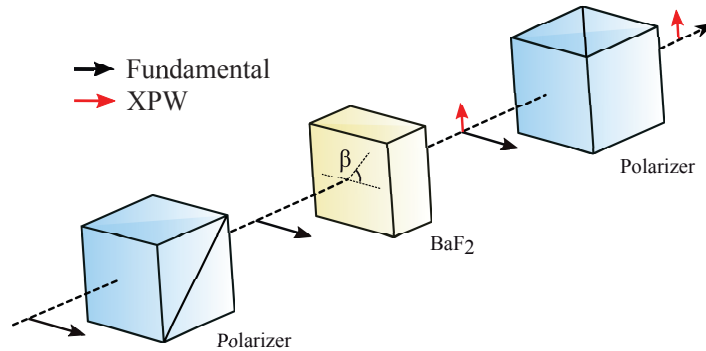
Figure 7.1 – Experimental implementation of XPW generation. β is the orientation of the crystal in the plane perpendicular to the beam propagation direction. In other words, β is the angle between the input polarization direction and the crystallographic axis of the crystal.

The pulse shortening ability of this device was already demonstrated in Salle Noire 2.0 at the mJ level with a two crystals setup [59]. In this case, sub-10 fs XPW pulses were generated with an efficiency around 33 % in a regime close to saturation. The spatial profile of the input beam was filtered in a hollow-core fiber to avoid a non homogeneous conversion, as well as eventual crystal damage due to hot spots. The divergence of the incident beam counterbalances the Kerr focusing effect in the nonlinear medium, enabling a high conversion efficiency even in a single crystal configuration. In a two crystals configuration, the self-focusing effect in the first crystal makes the Fundamental wave collimated. The spatial profile of the Fundamental wave is then improved by propagation between the two crystals. The conversion process is thus enhanced in the second crystal and close to saturation, improving the stability of the XPW pulses. Although the conversion regime is high, the XPW spectrum keeps a smooth and homogeneous shape, meaning that the XPW is not significantly affected by the SPM process. The CEP stability of the XPW pulses was confirmed, demonstrating that this setup can be considered as a post-compressor of laser sources dedicated to HHG on solid targets. Another XPW-based setup enabled to generate 10 fs XPW pulses with 25 % efficiency from 1 mJ, 25 fs pulses [112]. A two crystals configuration is also used but with a different implementation than in [59], as the spatial filter is located between the

two crystals. The idea here is to relax the intensity on the first crystal and to avoid crystal damage or darkening. Finally, a single crystal setup including spatial filtering was implemented with a 10 mJ laser source delivering 50 fs pulses at 100 Hz repetition rate [113]. 1.6 mJ, 15 fs FTL pulses were obtained. The corresponding XPW efficiency was $\approx$ 25%. All these results underline that the XPW filter is a good candidate to post-compress pulses at the end of a CPA laser system.

The XPW generation process applied to femtosecond pulse shortening is not trivial and strongly depends on the incident spectral phase, as demonstrated in [114] in the case of a low conversion regime. For an input pulse with a second order phase $\phi^{(2)}$ equal to zero, the ratio between the spectral bandwidth of the XPW spectrum and the incident one is $\sqrt{3}$. If $\phi^{(2)} \neq 0$, the spectral bandwidth of the XPW wave decreases and can even be smaller than the incident one by a factor $\frac{1}{\sqrt{3}}$.

The XPW energy varies with the initial chirp according to a Lorentzian law. In a low conversion regime, the efficiency and the spectral bandwidth of the XPW pulses are optimal for the same incident chirp, which is slightly negative (about -25 fs^2). The Fundamental wave is thus compressed in the crystal center. If the incident spectral phase exhibits high order terms, the maximum XPW efficiency and spectral broadening are achieved when the incident spectral phase is the flattest. In a high conversion regime, the maximum XPW spectral bandwidth is achieved for an incident positive chirp (about 40 fs^2) whereas the XPW efficiency is optimal for an incident negative chirp (about -25 fs^2) [115]. In this regime, a XPW spectrum 2.5 times broader than the incident one can be achieved, meaning that the generation of 10 fs pulses is possible when starting from 25 fs pulses.

In a first approach, numerical simulations are performed in the ideal case of a Gaussian pulse with a flat spectral phase so that to give an order of magnitude of what can be expected in the experiment. The 1D code I used was previously developed within the PCO group and adapted by Aurélien Ricci to the XPW generation process [115]. The results from the experiment are then presented and compared to the numerical simulations to explain the limitations we encountered.

7.2 Numerical calculation with a 10 mJ, 25 fs Gaussian pulse

I first performed 1D simulation using CommodPro, a MIRO-based propagation code [53]. An XPW component is available. One needs to specify its crystallographic orientation, the coefficient $\chi^{(3)}_{xxxx}$, the $\chi^{(3)}$ anisotropy named σ, the group velocity dispersion of the crystal and its refraction index. All these parameters are summed up in Tab. 7.1 in the case of BaF_2 [116]. This material is indeed the best candidate for XPW generation: it has an appropriate cubic symmetry, with isotropic planes so that the two orthogonally polarized waves propagate with the same group velocity. Besides, BaF_2 is transparent from UV to IR and presents a strong $\chi^{(3)}$ anisotropy. Its weak nonlinear index limits the SPM processes, which should be limited to minimize the phase difference between the Fundamental and the XPW, and also to get a smooth and Gaussian XPW spectrum.

	Index (800 nm)	GVD (800 nm)	$\chi^{(3)}_{xxxx}$	n_2	σ
BaF_2	1.47	-3,6.10^{-26} $s^2.m^{-1}$	1,59.10^{-22} $m^2.V^{-2}$	2.10^{-20} $m^2.W^{-1}$	-1,2

Table 7.1 – BaF_2 properties [116].

The XPW efficiency depends on σ and β (see Fig. 7.1) [117]. As explained in [118], it is preferable to work with holographic-cut crystals ([011]). For these crystals, the optimum β value with respect to the XPW efficiency is indeed not sensitive to the input intensity changes, for the whole reasonable range of input intensities. This is because the optimum phase-shift between the Fundamental and the XPW is maintained on a large intensities range. Besides, the XPW conversion is 26% higher with h-cut crystals than with z-cut ones. For a h-cut crystal, β_{opt} = 64,5° [118].

The XPW efficiency depends also on the term $I_0 L$, where I_0 is the intensity of the incident wave and L the crystal length. The relevant term for the simulations is called S and is given by:

$$S = \frac{\omega_0}{c} n_2 I_0 L \qquad (7.1)$$

where c the light velocity, ω_0 the central pulse frequency of the incident wave and n_2 the non-linear index of the crystal (see Tab. 7.1). The quantity S corresponds to the nonlinear phase accumulated by the wave during propagation through the crystal.

The simulations were performed in only one dimension. As explained in [59], the XPW experiences strong spatio-temporal coupling during the nonlinear process, especially when the conversion rate is significant. Because of the optical Kerr effect, the Fundamental is subject to a significant spectral broadening in the center of the beam, but not on the beam edges. This broadening is transferred to the XPW with the same inhomogeneities. As a consequence, the spectral bandwidth of the final XPW is spatially heterogeneous, making the processing of the 3D simulations data not trivial. A good spatial homogeneity can be obtained after a given propagation distance of the XPW. However, such simulations are time consuming. The idea here is just to give orders of magnitude. The values obtained with these calculations are an over-estimation and corresponds to the maximum spectral broadening and efficiency, obtained at the center of the beam where the intensity is maximum.

A laser source delivering 25 fs, 800 nm-centered pulses with a flat spectral phase is simulated. In the high conversion regime (typically S = 4), the maximum XPW efficiency is reached for a negative pre-chirp whereas the spectral bandwidth is maximum for a positive pre-chirp. In these simulations, I chose to optimize the XPW efficiency and to introduce a negative pre-chirp so that the Fundamental is compressed in the center of the 1.5 mm-long crystal. The S variation is in the range [0.5-5.6] and is achieved via the incident intensity (the crystal length is fixed).

The calculations are performed using the most general mode called 'Broad spectrum' because the considered pulses are not significantly stretched. This calculation mode completely solves the nonlinear Schrödinger equation and requires a high number of points for the temporal dimension. The spatial transverse dimensions are not taken into account to avoid any memory problem. Note that 3D simulations should be achieved with the mode 'Phase modulation' for computer memory reasons. In this mode, the temporal window changes of size during the calculation to limit the calculation time. A last point to mention is that the calculation accuracy is set via the maximum permitted phase-shift accumulated on the step Δz. It is set to 5 mrad. For S = 5 rad, 1000 steps will be thus necessary.

Fig. 7.2 shows the evolution of the Fundamental spectrum (top) and the XPW spectrum (bottom) at the crystal output, as a function of S. In this case, the crystal length is set to 1.5 mm and S varies because the incident pulse intensity varies. The progressive spectral broadening of both waves can be observed. Fig. 7.3 shows the spectral width of both waves as a function of S. The spectral widths are calculated according to:

$$\text{FWHM}^2 = \frac{\int (\omega - \omega_0)^2 \, \text{I}(\omega) \, d\omega}{\int \text{I}(\omega) \, d\omega} \tag{7.2}$$

with:

$$\omega_0 = \frac{\int \omega \, \text{I}(\omega) \, d\omega}{\int \text{I}(\omega) \, d\omega} \tag{7.3}$$

Two regimes are evidenced: for S ≤ 2.5, the XPW process is preponderant while for S ≥ 2.5, the SPM process takes the advantage. The Fundamental and the XPW spectra broaden progressively with S increasing. For S ≤ 3, the XPW pulses are shorter than the incident wave by a factor $\sqrt{3}$ as the XPW process is a third order nonlinear effect and the XPW intensity is proportional to the cube of the incident intensity. From S ≈ 3, the XPW spectrum is broader by a factor $\geq\sqrt{3}$ times compared to the incident spectrum, because of significant self-phase modulation (SPM).

The main advantage of the XPW process over pure SPM for pulse shortening is the excellent output spectral and temporal quality. From the beginning of the propagation in the crystal, the XPW exhibits a large spectral bandwidth ($\sqrt{3}$ factor). Then, SPM broadens significantly the XPW spectrum which is already larger compared to the incident one. The final pulse spectrum is thus smoother than the one obtained via pure SPM.
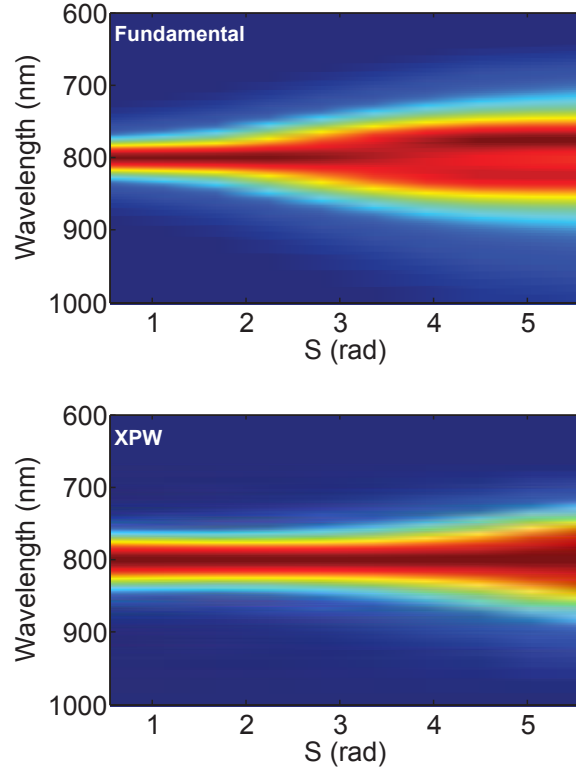
Figure 7.2 – Spectral evolution of the fundamental (top) and XPW (bottom) waves as a function of S. This calculation is performed with a 25 fs input pulse with flat spectral phase and L = 1,5 mm.

The results of the simulations indicate that a S factor of 4 enables to produce sub-10 fs pulses (Fig. 7.4) with a reasonable intensity on the crystal ($< 2.10^{16}$ W.m^{-2}), as shown on Fig. 7.5. I perform these calculations assuming that the spectral phase of the incident pulses is flat. In practice, the input spectral phase should be as smooth as possible to guarantee a significant XPW efficiency. This requirement is even more critical given that the conversion regime is high. The control of the incident spatial profile and divergence is also crucial.
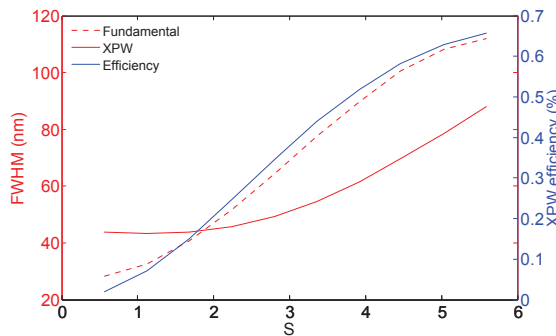
Figure 7.3 – XPW and fundamental spectral broadening as a function of S with a 1,5 mm long crystal. The XPW efficiency is also plotted.
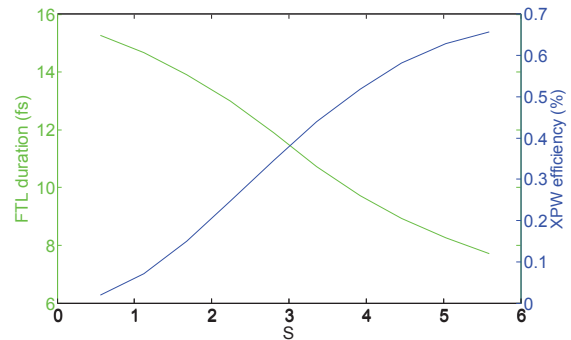
Figure 7.4 – Expected XPW pulse duration and conversion efficiency as a function of S with a 1.5 mm long crystal.
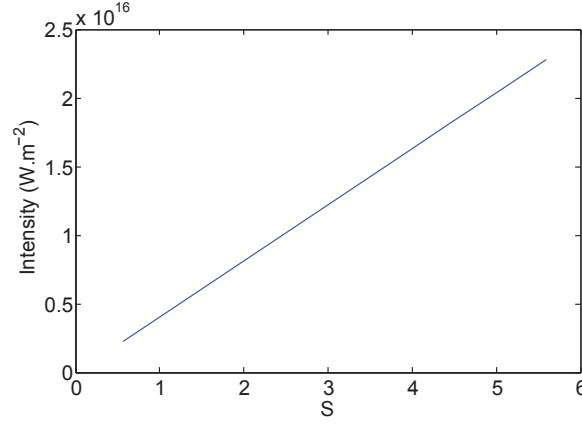
Figure 7.5 – Intensity on the XPW crystal as a function of S. This calculation is performed with a 25 fs input pulse with flat spectral phase and L = 1.5 mm.

7.3 Experimental implementation (10 mJ, 22 fs, 1 kHz)

The laser source is a CEP-stable double CPA system (Salle Noire 2.0), already including an XPW filter at the 1 mJ stage [9]. At the beginning of my PhD, I worked on the development of the last amplifier of this laser source. This upgrade enabled to produce 10 mJ compressed pulses.
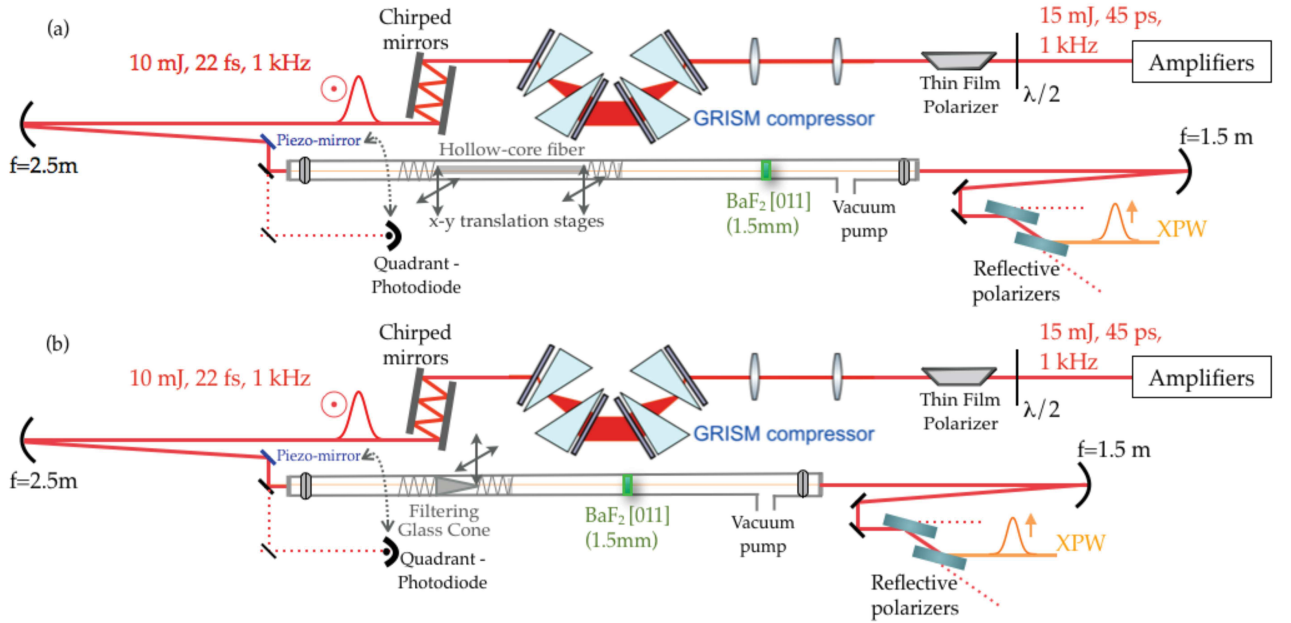
Figure 7.6 – Experimental implementation of high-energy XPW filtering, including a hollow-core fiber (a) or a glass cone filter (b).

The experimental layout is shown on Fig. 7.6. The amplified stretched 15 mJ laser pulses are compressed down to 22 fs through a GRISM compressor and a set of chirped mirrors (UltraFast Innovations GmbH, 8 bounds, design HD58, -250 fs^2 per bounce). The pulse energy can be decreased thanks to a variable attenuator located before the compressor. A Dazzler device (Fastlite) is included in the second CPA for fine tuning of the dispersion. To reach a significant spectral broadening and a high spectral quality with thin nonlinear BaF2 crystals, the accurate spectral phase control of the incident wave is indeed required: as mentioned in section 7.1, any spectral phase distortion will affect the XPW spectrum and will limit the spectral broadening [114]. Such control is achieved thanks to the Dazzler, coupled with a Wizzler to perform optimization loops. A

Wizzler measurement of the compressed 10 mJ pulses is shown on Fig. 7.7.
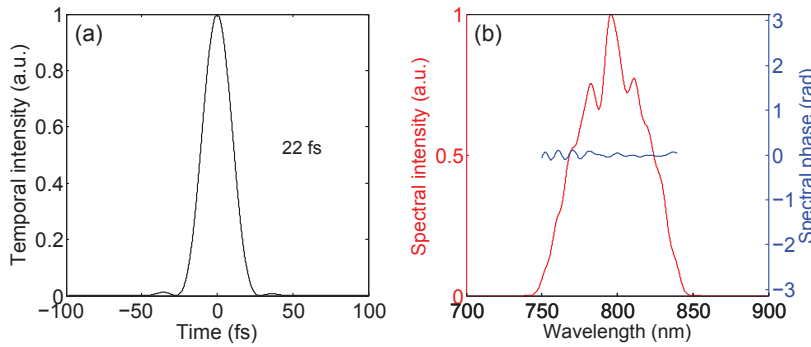
Figure 7.7 – Wizzler measurement of the compressed 10 mJ pulses.

The compressed pulses are focused into the XPW setup with a 2.5 m focal length spherical mirror. As illustrated in Fig. 7.6, the focusing beam is intercepted by two mirrors for active beam pointing stabilization. The first one is mounted on a piezo-mount while the leakage through the second one is sent to a quadrant-photodiode. The fast electronic stabilization is provided by FemtoLasers GmbH and ensured a beam pointing stability around 2 μrad.

The experimental conditions to reach high efficiencies with thin nonlinear medium requires a fine control of the spatial amplitude of the incident beam. This can be achieved through efficient spatial filtering [119, 60]. The XPW setup included thus a waveguide for spatial filtering, placed at the laser focus. The output beam divergence enables to keep the required intensity ($\approx$ 2.10^{-16} W.m^{-2}) for any input energy by simply adjusting the crystal position. During these experiments, we tested and qualified two types of spatial filters: a hollow-core fiber and a glass-cone whose respective advantages will be presented in the following subsections. The spatial filter is followed by one or two nonlinear crystals, all under vacuum. The 1 mm-thick input window has a clear aperture of 15 mm and the beam diameter on this window is around 10 mm. The output window has a thickness of 0.5 mm and a clear aperture of 12 mm. The nonlinear crystals (BaF$_2$, [011], 10*10*1.5 mm^3, EKSMA) are held in magnetic mounts for convenient orientation and z-positioning tunability. The overall length of the setup is comprised between 1.5 m and 2 m.

A critical point concerns XPW pulse selection. Glan polarizers typically ensure low losses together with an extinction ratio of 3-4 orders of magnitude. However, these polarizers introduce significant dispersion and are not suited to pulses with an energy higher than 1 or 2 mJ because of nonlinearities. At the considered level of energy, reflective polarizers are preferred. A set of reflective polarizers from UltraFast Innovations GmbH was used and characterized. The reflective coating is optimized on the [600-900] nm spectral bandwidth. We checked that only minor distortions are introduced on the considered spectral range with a broad spectrum. The surface quality is guaranteed to $\lambda/10$. These 38 mm-large and 3 mm-thick polarizers allow a maximum beam diameter of 9.7 mm (AOI = 75°). We measured a transmission of 90 % and an extinction ratio of 10^{-2} for 2 successive polarizers. Otherwise, it should be mentioned that the good quality of the beam polarization at the GRISM output did not require the use of an input polarizer.

Finally, the encountered limitations due to the imperfect beam profile of the considered laser source should be mentioned. They are specific to this laser source, but generally concern high average power lasers. The beam profile is measured in the focus position. As the average power before compression is 15 W, strong thermal effects in the last amplifier and in the GRISM compressor lead to a deformed and fluctuating beam profile from day to day. As shown on Fig. 7.8, some shoulders might appear in the beam profile, which can be detrimental to the experiment. However, the beam profile could be optimized by adjusting the last prism of the GRISM compressor. Most remaining high frequencies were removed by the spatial filter at the cost of the overall transmission. Finally, the strong thermal lens in the GRISM made necessary to adjust the focus position for each energy level. The typical beam profile had a $1/e^2$ diameter of 220 μm.
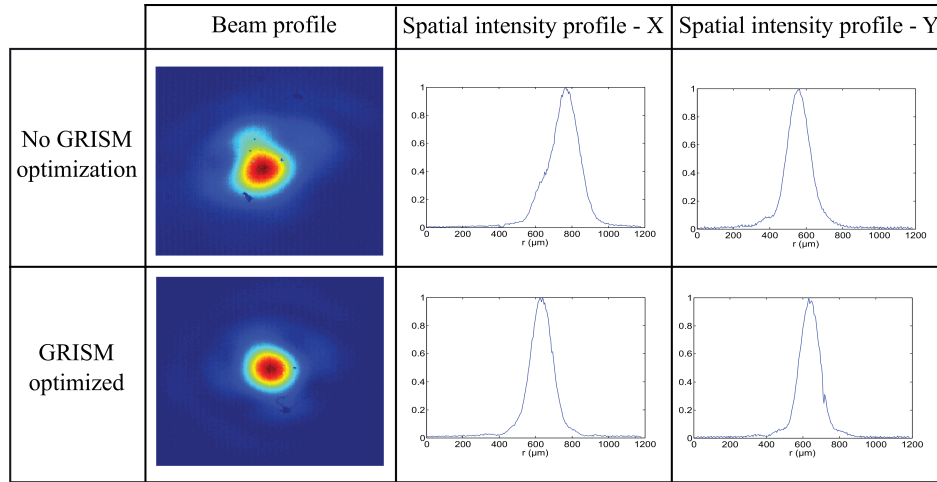
Figure 7.8 – GRISM tuning influence on the beam profile at the laser focus.

7.4   XPW generation with a hollow-fiber spatial filtering

The previously validated waveguided XPW setups feature a short (20 cm) rigid fused-silica hollow-core fiber with an inner-diameter of 250 μm [60, 112], producing a typical LP01 mode. This type of waveguide allows not only high spatial frequencies filtering (occurring at the input of the hollow fiber), but also modal filtering because of the mode-dependent attenuation in the hollow fiber [120]. The beam wavefront quality as well as the beam intensity distribution are thus strongly improved at the fiber output.

Here, a 47 cm-long fiber (FemtoLasers GmbH) lying on a straight metallic home-made V-groove was tested. It appeared that handling the fiber at 10 W average power remains challenging, as the occasional thermal shoulders in the focus (see Fig. 7.8), as well as a small misalignment, irremediably caused the melting of the fiber entrance. Furthermore, the coupling losses caused thermal bending of the V-groove. Lifetime issues of the hollow-fiber at only 3 W average power were also noted in [120]. This arrangement was anyway used for this experiment, but with extra-care for a day-to-day use. A better solution would be to use stretched flexible fibers (no V-groove) with a few cm long solid fused silica taper co-axially adjusted to the fiber, as proposed in [110]. However, even with such a design, the lifetime of the taper remains an issue, all the more so that this complete fiber setup is costly and not re-usable (the taper cannot be changed independently).
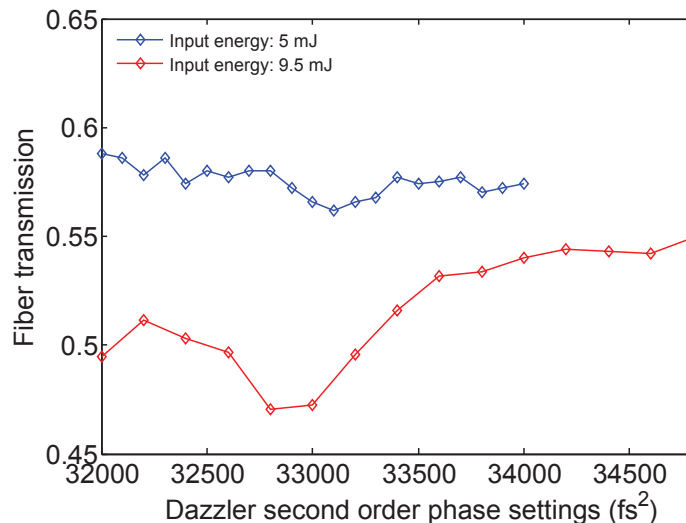
Figure 7.9 – Vacuum transmission of the fiber as a function of input chirp for two input energy levels.

The setup was first characterized without any crystals. The vacuum transmission was recorded as a function of the input chirp at two energy levels: 5 mJ and 9.5 mJ (Fig. 7.9). The Dazzler setting $32800\,\text{fs}^2$ corresponds to the optimum compression. A change of transmission can be observed between the two energy levels. Besides, the input chirp has a stronger influence at 9.5 mJ than at 5 mJ, making the transmission drop when the pulse compression is achieved. This result suggests that the high intensity in the entrance window is responsible for significant nonlinear spatial phase distortions. Propagation in air prior to the vacuum setup generates also some distortions, visible as hot spots on the entrance window. The waveguide transmission is not higher than 47 % at high energy (9.5 mJ) for an input compressed pulse. For a lower energy (5 mJ), it is about 57 %. For an input energy < 4 mJ, the transmission reaches 70 %.

The bad quality of both beam profile and wavefront of the laser source induces strong spatio-temporal couplings in air and in the windows setup, which are detrimental to the setup transmission. For now, the input energy is limited to 5 mJ so that the waveguide transmission is about 57 %.

To highlight the strong distortions through the setup (without any crystals), the transmitted incident spectrum was recorded as a function of the input chirp, as seen on the first column of Fig. 7.10. The shaded area is the spectrum measured at the output of the GRISM compressor for the input chirp leading to the best compression. The transmitted incident spectra shape shows that significant spectral modulations occur, especially when the input pulse is closed to the best compression (Dazzler setting: $32800\,\text{fs}^2$). A Wizzler measurement of the transmitted pulse was performed for each input chirp value (there is no XPW crystal), as shown on Fig. 7.10 (columns 2 and 3). The spectral modulations are more pronounced because this device measures the central part of the beam, which is the most intense and so the most affected by nonlinearities. It can be seen that the edges of the spectrum are not phase-matched (Fig. 7.10, columns 2). The nonlinear nature of the disturbing process becomes clear as a small change of the input chirp changes dramatically the spectral phase and amplitude of the transmitted wave. We tried phase compensation with the Dazzler but this has revealed to be detrimental to the temporal profile.

As explained previously, the condition for efficient pulse shortening, consisting in a flat input spectral phase, is not fulfilled here. This will unavoidably affect the XPW generation process. A 1.5 mm-thick BaF_2 crystal is now added at 45 cm from the fiber output. The beam divergence was already characterized and is about 4 mrad. The beam diameter is thus estimated to be around 2.3 mm in this plane. The crystal is orientated in the plane perpendicular to beam propagation to achieve an optimal XPW efficiency. Fig. 7.11 shows the XPW efficiency for each value of the input chirp. The corresponding XPW spectra are shown on Fig. 7.10 (columns 4). No significant spectral broadening occurs, preventing from reaching the sub-10 fs pulses frontier. The minimum XPW duration (FT limited) is indeed around 14 fs, which is not impressive compared to the input pulse duration (22 fs). This is due to the strong phase distortions undergone by the incident wave. However, considering the effective spectral bandwidth of the transmitted wave measured with the Wizzler (50 nm), the pulse shortening is consistent with what could be expected for 20% efficiency. One can also notice the reduction of the spectral modulations during the XPW process, as a result of the temporal cleaning. The strong spectral intensity peak in the XPW spectra, is probably due to a spectral hole filled via SPM. To illustrate this phenomenon described in details in [121], I performed numerical simulations with MIRO. To do so, the 22 fs pulse spectrum is shaped so that a spectral hole appears at 800 nm, as shown in blue on Fig. 7.12. After propagation through a nonlinear medium (B = 4.2 rad), the initially removed frequencies are regenerated and even enhanced via SPM, as illustrated in red on Fig. 7.12. In the present experiments, a spectral hole can be observed at 782 nm on the Wizzler measurement (Fig. 7.7). This spectral modulation may be worsened by non-linearities in the entrance window of the setup as well as during the XPW generation process, and be responsible for the peak observed at 788 nm on the XPW spectrum. The 6 nm gap between the considered spectral modulations could be related to the XPW blue-shift property.

To conclude, the post-compression mechanism during the XPW process is inhibited by phase and amplitude distortions prior to the nonlinear interaction.
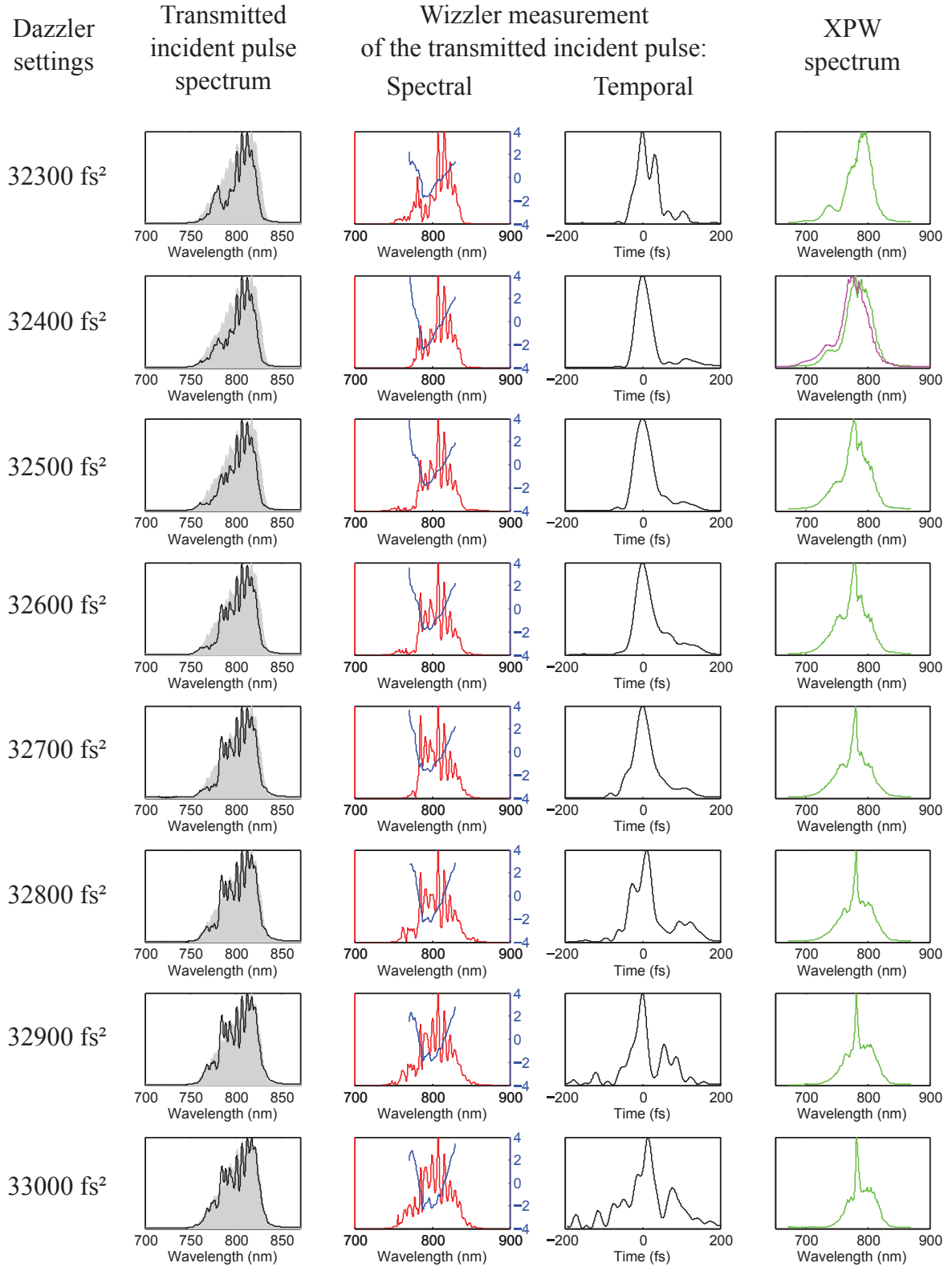
Figure 7.10 – Chirp scan: characterization of the incident pulse transmitted through the fiber (spectrum and Wizzler measurement) and XPW spectrum. The shaded area (column 1) is the spectrum measured at the output of the GRISM compressor. On the spectral reconstructions made by the Wizzler (column 2), the spectral intensity is plotted in red whereas the phase is plotted in blue with a scale given in radians. The corresponding XPW spectra are shown on column 3. For the Dazzler settings 32400 fs^2, two XPW spectra are plotted (last column): the green one was obtained with a single crystal; the magenta one with two crystals.

We anyway tried to add a second similar BaF$_2$ crystal, which was located at 9 cm behind the
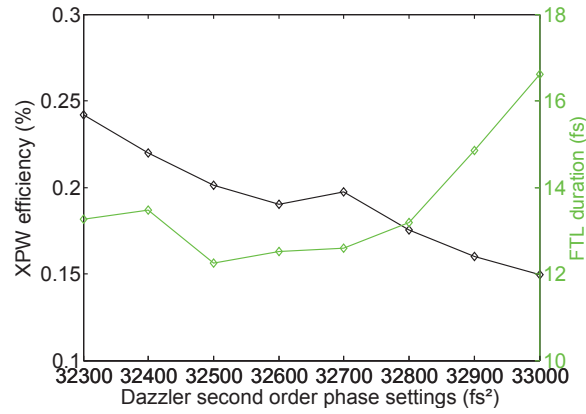
Figure 7.11 – XPW internal efficiency for a single 1.5 mm-thick crystal and corresponding FTL duration as a function of second order phase.
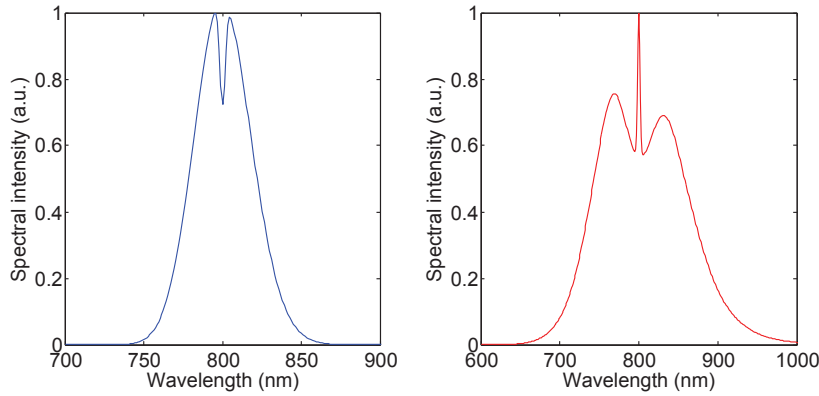
Figure 7.12 – MIRO simulations of the filling of a spectral hole via SPM. The blue curve corresponds to the spectrum of the initial 22 fs pulse spectrum shaped by a hole (amplitude 0.3). The red curve shows the spectrum of the pulse after propagation through a nonlinear medium (B = 4.2 rad).

first one. Its orientation is adjusted to maximize the efficiency. The XPW spectrum is plotted in magenta on Fig. 7.10 for a Dazzler second order phase setting of 32400 fs^2. The corresponding efficiency is 25 %. There is clearly no additional spectral broadening compared to the one obtained with a single crystal. However, the efficiency is improved, as the near-field beam profile (Fig. 7.13). The second crystal improves significantly the spatial profile of the XPW beam. This is probably due to the fundamental beam reshaping process during propagation between the two crystals, as previously observed at lower energy.
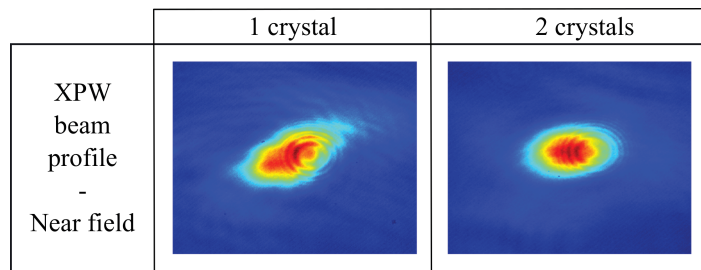
Figure 7.13 – Near field characterization of XPW beam profile in the case of 1 or 2 crystals.
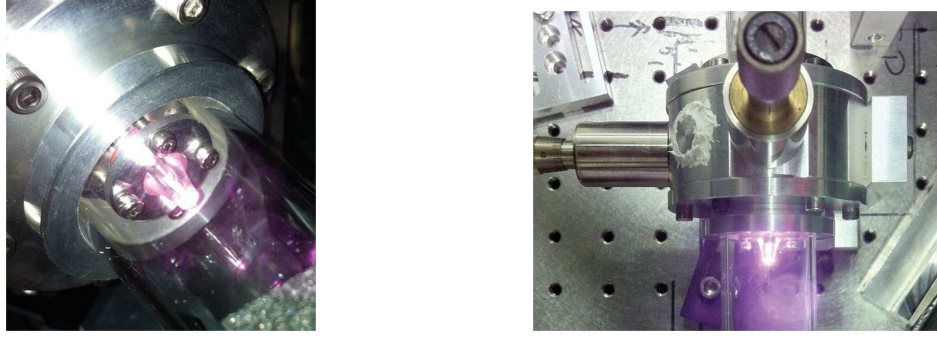
Figure 7.14 – Pictures of the glass-cone filter in the focus of the 10 mJ beam.

7.5   XPW generation with a glass-cone for spatial filtering

Because of the hollow-core fiber fragility at this average power, we turned to a more robust solution. To prevent irreversible damages, a conically-shaped hole might be used for spatial filtering. The surface area between the beam and the spatial filter is thus increased. It is particularly convenient when working with shouldered beam as the wings are progressively filtered so that thermal deposition is spread on the whole cone. Such taper filters (metallic or dielectric) were widely employed in high-energy lasers [122]. The use of a spatial pinhole for XPW filtering was also already reported [123]. Here, we tested and validated a conical-shaped glass filter. The exit hole diameter is around 270 µm, matching the focused beam dimension. The cone is mounted in a transparent tube with external x-y translation stages, as illustrated on Fig. 7.14.
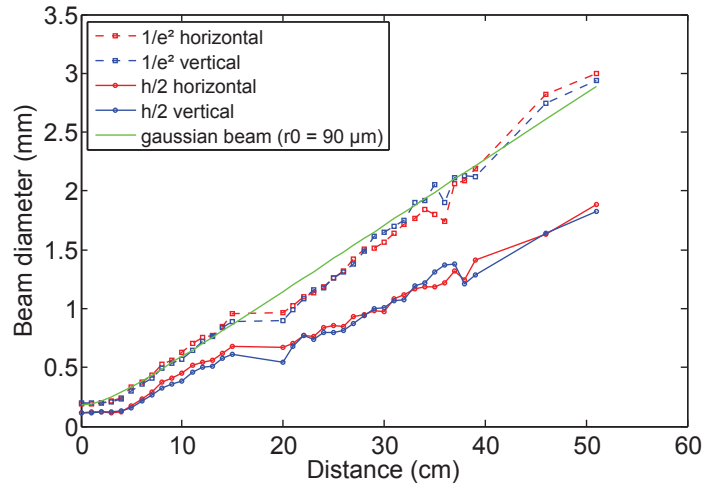
Figure 7.15 – Beam diameter ($1/e^2$ - dashed lines, $1/2$ - solid lines) as a function of the propagation distance after the cone output. The green line indicates the propagation of a Gaussian beam with an initial waist of 180 µm.

The cone-shaped filter is less sensitive to laser misalignments and imperfect beam profiles, compared to the hollow-core fiber. In addition to the setup robustness improvement, it allows a better overall transmission, as no modal filtering process happens. The maximum transmission reaches 70 % for 10 mJ input pulses with a 2000 fs^2 positive chirp. An additional difference between the two spatial filters is the divergence of the filtered beam. While the hollow-core fiber inner diameter fixes both divergence and beam shape of the filtered beam, the cone makes the amplitude distribution and divergence of the beam strongly dependent on the initial laser propagation. Therefore we performed measurements to characterize the beam propagation after the cone filter. To do so, a 4f imaging system with a focal length of 750 mm was installed. By shifting together the focusing mirror and the CCD camera, the beam spatial profile could be measured

from 1 cm to 50 cm from the cone output. No chirp was applied to the initial pulses. The input (resp. transmitted) energy was 9.2 mJ (resp. 5.6 mJ). Beam propagation is shown on Fig. 7.15. The beam diameter ($1/e^2$ and $1/2$) is given as a function of the propagation distance. I fitted the $1/e^2$ diameter evolution with one of a Gaussian beam (waist of 180 µm). The beam divergence is found to be 5.6 mrad, which is higher than the one measured after the 250 µm hollow-fiber (4 mrad). Otherwise, Fig. 7.16 highlights that high spatial frequencies are filtered after 46 cm of propagation. The Gaussian fits of the beam cross-sections indicate that the free propagation after the cone filter makes the beam shape evolve from a super-Gaussian beam to a Gaussian-shaped beam.
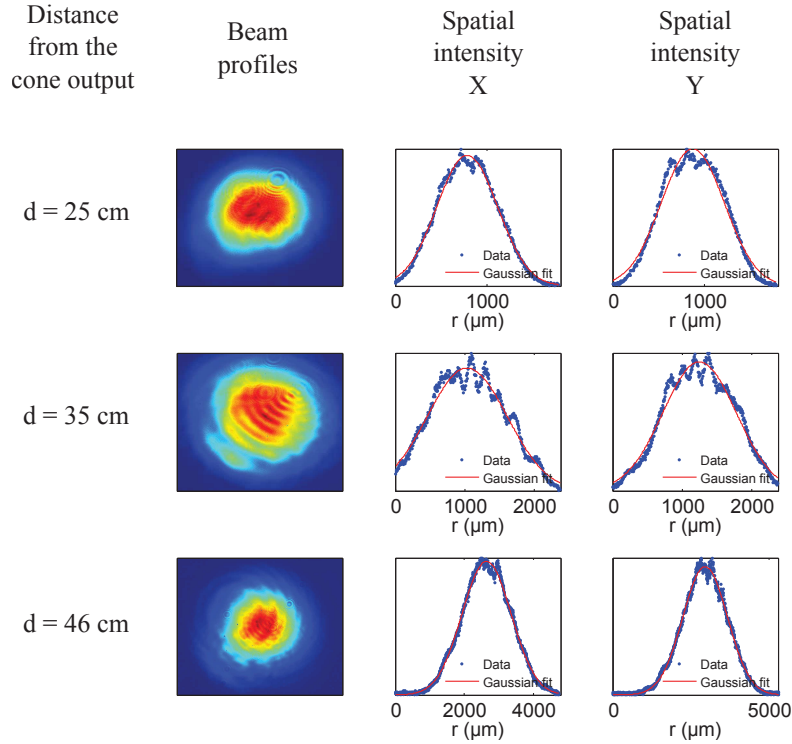
Figure 7.16 – Beam profiles and X-Y cross-sections for 3 propagation distances after the cone. The cross-sections are fitted with a Gaussian fit (dashed red line).

Obviously, the filter replacement does not solve the nonlinearities issues during propagation in air and in the windows setup. Again, the transmission of the setup was measured as a function of the input chirp when no XPW crystal is inserted (see Fig. 7.17). Pulse compression corresponds to a Dazzler setting of ≈ 32800 fs^2. The transmitted incident spectrum was recorded at the same time and is shown on Fig. 7.18. The transmission severely drops when the pulse is compressed because of amplitude and phase distortions. The filtered beam energy during the XPW process will be thus limited to 5.4 mJ for a compressed pulse (Dazzler setting to 32800 fs^2). Note that the transmission is lower for chirp values < 32800 fs^2 than for values > 32800 fs^2 because pulses are not chirped enough in the GRISM compressor. Besides, the transmitted incident spectra are significantly distorted (Fig. 7.18), as expected.

The Wizzler measurement performed after the filtering setup for an input energy of only 5 mJ confirmed the spectro-temporal distortions experienced by the transmitted incident pulse (Fig. 7.19). The spectral modulations are particularly pronounced because the temporal measurement is performed in the center of the beam, where the pulse intensity is the highest.

Nevertheless, XPW generation experiments were performed for two input energy levels: 5 mJ and 9.6 mJ. The crystal was located 46 cm (resp. 58 cm) from the cone filter for an input energy of 5 mJ (resp. 9.6 mJ). The results shown on Fig. 7.20 and Fig. 7.21 are similar in both cases: no significant spectral broadening can be achieved to reach sub-10 fs pulses because of the strong spatio-temporal distortions described above. Although the spectral quality is enhanced compared to the one of the transmitted incident spectrum, the XPW spectrum presents some remaining sharp
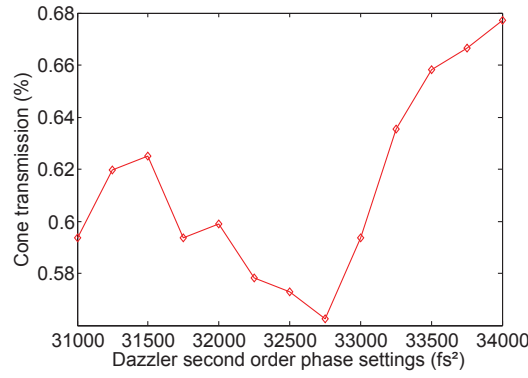
Figure 7.17 – Vacuum transmission of the glass-cone filter as a function of input chirp for 9.6 mJ input energy.
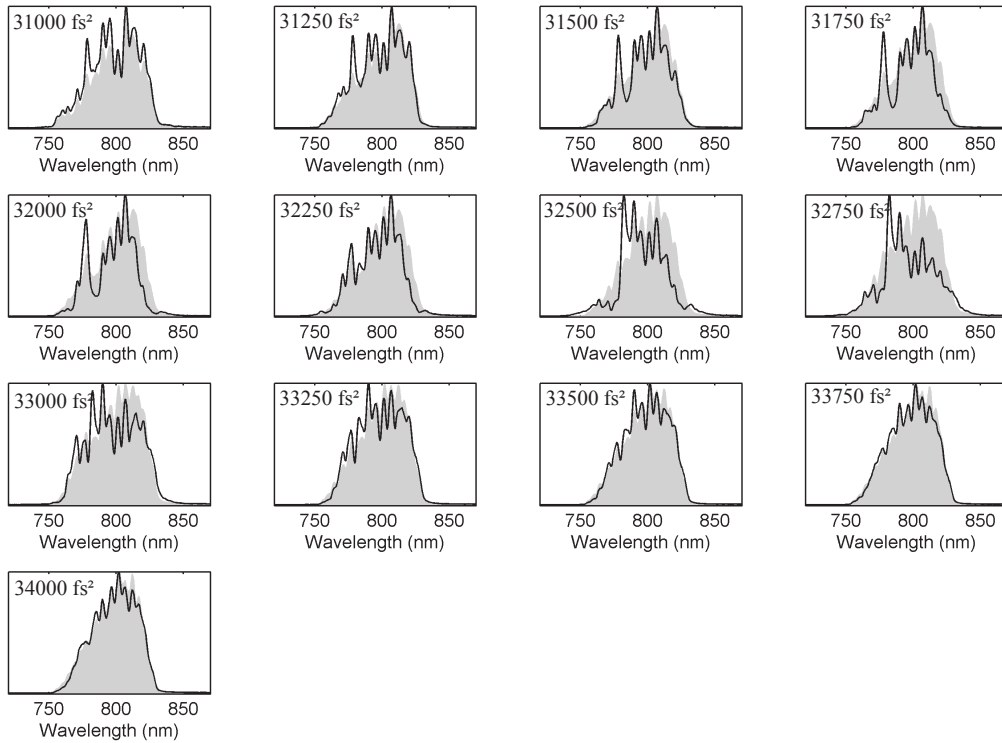
Figure 7.18 – Transmitted incident spectrum through the spatial filtering setup as a function of input chirp for 9.6 mJ input energy. The shaded are is the spectrum measured at the output of the GRISM compressor.

peaks due to initial phase modulations, as highlighted by the Wizzler measurement of the transmitted incident wave (Fig. 7.19). Because of the nonlinear nature of the deleterious process, the overall behavior is slightly better for an input energy of 5 mJ. The largest XPW spectral bandwidth corresponds to a FT-limited duration of 11 fs (see Fig 7.22 and Fig 7.23), which is shorter compared to the hollow-core fiber case (Fig 7.11) because of the higher XPW conversion.

This setup enabled an unexpected high XPW conversion for both input energies (see Fig. 7.22 and Fig. 7.23): it is > 30 % using a single thin 1.5 mm-thick crystal. No continuum generation or damage was noticed. For a similar thin nonlinear medium, such a high conversion level could not be achieved with the hollow-core fiber device, neither here nor in previous experiments. For instance, a XPW conversion about 30 % was obtained with a 2.5 mm-long crystal in [119]. In the present experiments, the high efficiency can be attributed to the optimal beam profile and curva-
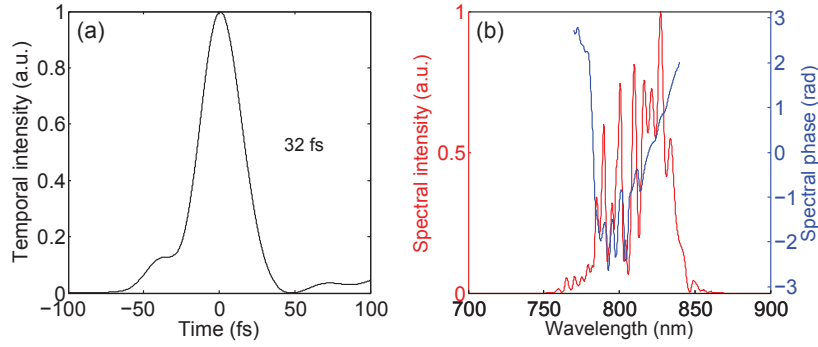
Figure 7.19 – Wizzler measurement of the transmitted incident pulse for an input energy of 5 mJ.
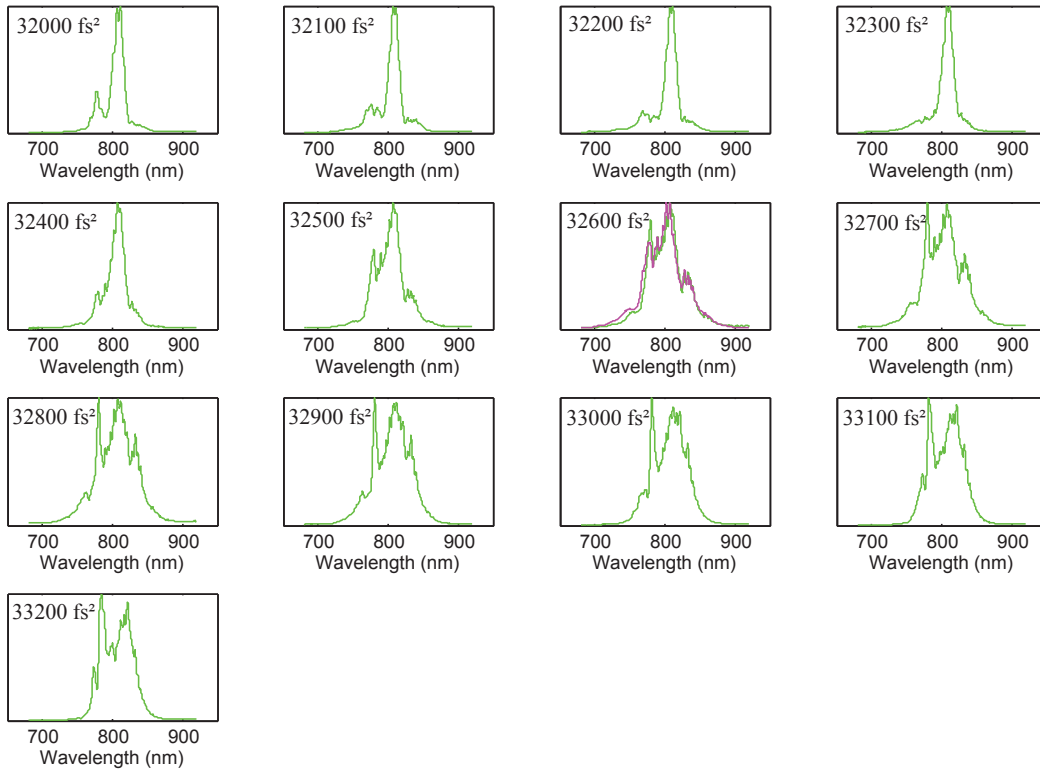
Figure 7.20 – XPW spectrum obtained with a single crystal as a function of input chirp for 9.6 mJ input energy. The magenta spectrum was obtained with two crystals.

ture for the XPW generation process. Indeed, the beam shape revealed to be smooth and Gaussian. Besides, the beam propagates differently after the cone filter compared to the HCF case. In particular, the beam divergence is higher after the cone than after the HCF, which might explain the discrepancy. A higher divergence would favor XPW conversion by mitigating Kerr-induced self-focusing in the crystal.

A two crystals configuration was tested for an input energy of 9.6 mJ and an input Dazzler setting of 32600 fs² (see the magenta spectrum on Fig. 7.20). No significant improvement of the conversion efficiency nor the spectral quality was noticed. However, the XPW beam quality was improved, as in the fiber case.

Conclusion

To conclude, the use of a cone filter and a single crystal enabled to generate 11 fs FTL XPW pulses with a unprecedented conversion efficiency, that is 32 % (resp. 39 %) for an input energy of 5 mJ (resp. 10 mJ). Again, the limited spectral broadening and the bad spectral quality of the XPW pulses
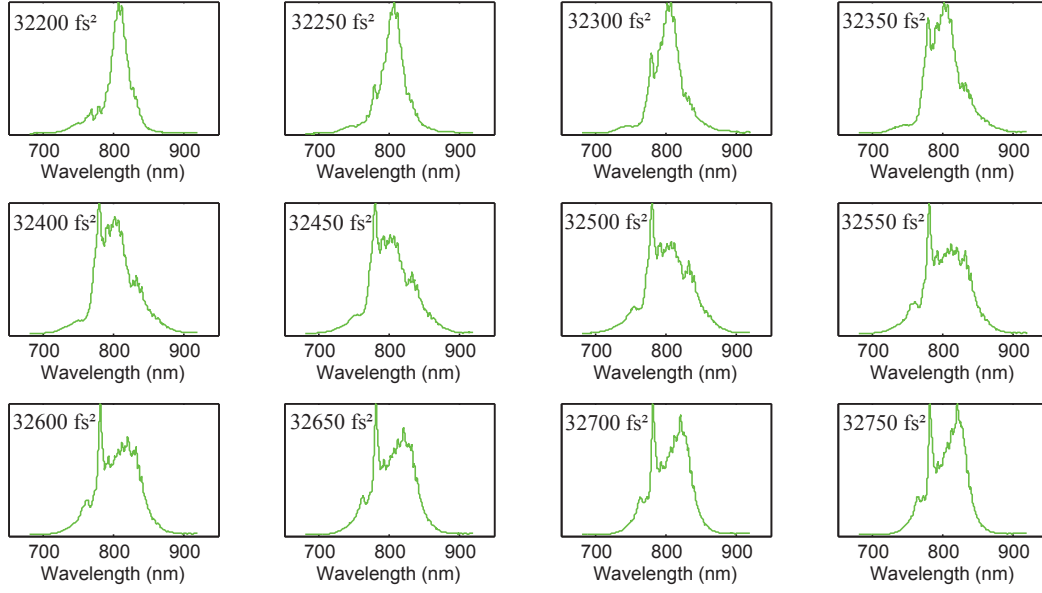
Figure 7.21 – XPW spectrum obtained with a single crystal as a function of input chirp for 5 mJ input energy.
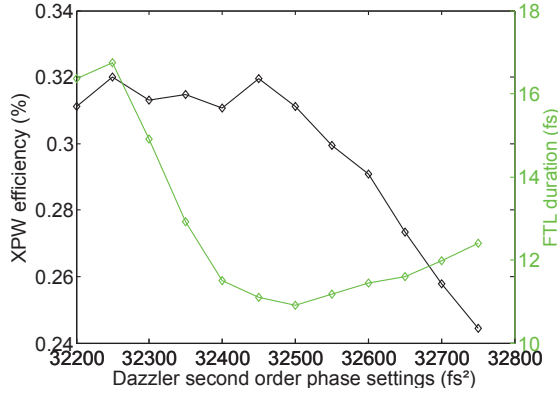
Figure 7.22 – XPW efficiency and FTL duration (1 single crystal) as a function of input chirp for 5 mJ input energy.
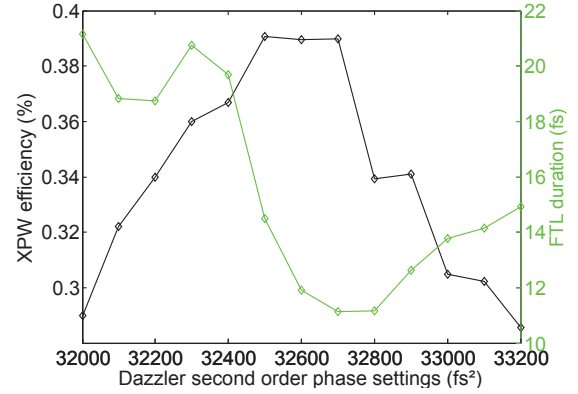
Figure 7.23 – XPW efficiency and FTL duration (1 single crystal) as a function of input chirp for 9.6 mJ input energy.

is related to the spectro-temporal phase and amplitude distortions in air and in the windows setup, as confirmed below with the numerical results.

7.6 Numerical results and comparison to the experimental ones

To validate the detrimental influence of the incident wave amplitude and phase distortions, I performed simulations with CommodPro. To define the initial light source, I used the Wizzler measurements of the incident wave transmitted through the spatial filtering setup when there is no XPW crystal. The distortions caused by the propagation in air and in the windows setup are thus taken into account in the initial simulated laser source. As the output window has no influence on XPW generation, being located after the nonlinear medium, the chirp introduced by this window was compensated in the simulation (the Wizzler measurements included indeed the chirp of this output window). The results are indicative as only time dimension is considered. Furthermore, the temporal measurements were performed into the central part of the beam and we know that there is a non negligible spatial chirp. Therefore, these measurements are not fully representative of the beam prior to the XPW crystal.

The S parameter was adjusted to match the measured XPW conversion efficiency.
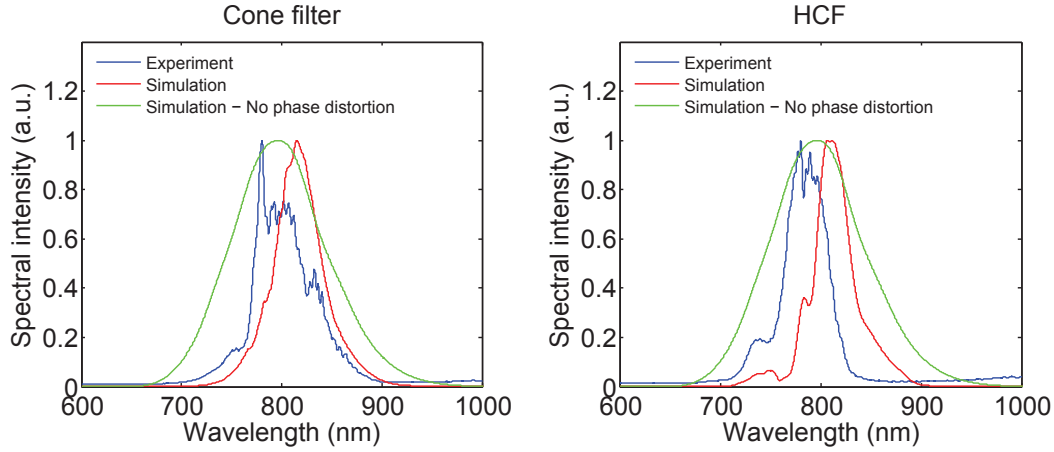
Figure 7.24 – Comparison between experiments (input energy: 5 mJ) and simulations for the two tested spatial filters. In the simulations, the incident pulse is defined by the Wizzler measurement of the transmitted pulses through the vacuum spatial filtering setup. The Dazzler setting was 32700 fs^2 (resp. 32450 fs^2) for the fiber case (resp. the cone filter). The green curve corresponds to the case where no distortions bother the XPW generation process. It was obtained performing the simulations with a laser source defined by the Wizzler measurement of the 10 mJ pulses, prior to the XPW vacuum setup.

The results are shown on Fig. 7.24. There is good agreement between experiments and simulations in terms of spectral bandwidth and overall shape. However, the central wavelengths are quite different in simulations and experiments. One reason is that the Wizzler measurement was performed at the center of the beam so that it includes only a part of the beam spectral components assuming that spatial chirp occurs. Another reason is that the code is not able to reproduce the blue-shift experienced by the XPW in the experiments.

The case where no phase and amplitude distortions bother the XPW generation process is exhibited (see the green curve on Fig. 7.24). It was obtained by performing simulations with a laser source defined by the Wizzler measurement of the 22 fs 10 mJ pulses (see Fig. 7.7), prior to the XPW vacuum setup. The chirp of the 1 mm-thick input window is taken into account and the S parameter is adjusted to 4.5 rad. The expected XPW spectrum is smooth and broad when no distortions occur. The corresponding FTL duration is 8.3 fs.

To conclude, these numerical results confirm pretty well that the amplitude and phase distortions occurring in air and in the vacuum windows setup are detrimental to the XPW generation process.

7.7   Assessment of the two experimental runs

As a general conclusion to this chapter, the performances are summarized in Tab. 7.2.

	HCF	**Cone filter**	
Input energy	5 mJ	5 mJ	10 mJ
Filter transmission	58 %	64 %	57 %
XPW FTL duration	12.6 fs	11 fs	11 fs
XPW efficiency	20 %	32 %	39 %

Table 7.2 – Assessment of the high energy post-compression experiments with the XPW technique. Only results obtained with a single crystal are presented here.

The XPW conversion efficiency is related to the incident spatial quality and requires thus the implementation of a filter prior to the nonlinear medium. Two spatial filtering techniques were

tested: spatial and modal filtering in a hollow-core fiber, and spatial filtering with a glass-cone filter. The later was definitely more robust at these average power levels and enabled higher transmission and higher XPW efficiency than the fiber. The filter transmission is limited by the spatial quality of the incident beam. As high energy lasers commonly present poor spatial quality, a reliable solution to prevent energy losses would be to implement an adaptive wavefront correction.

The question of the beam divergence influence on XPW generation was raised. The cone filter enabled an unprecedented high XPW conversion for both explored input energies and despite the use of a very thin nonlinear medium (1.5 mm long crystal). Such a high conversion could not be achieved with the hollow-core fiber device, neither here nor in previous experiments [119]. We have advanced the hypothesis that a higher divergence would favor XPW conversion by mitigating Kerr-induced self-focusing in the crystal.

Finally, the high sensitivity of the XPW generation process to the incident pulse quality is a strong constrain that has to be taken into account to design a XPW-based post-compressor at high energy. Efficient pulse shortening is conditioned to a flat input spectral phase and specific care is needed to eliminate sources of phase distortions. This requirement was difficult to achieve with our complex laser source. The high average power in the GRISM compressor induces a strong thermal lens and initiates spatio-temporal couplings in the laser beam. The 22 fs compressed pulses are very sensitive to the phase distortions inside the post-compressor setup windows. In these experiments, the chirp needed to preserve the spectral quality of the transmitted incident wave was about $1000\,\mathrm{fs}^2$. The corresponding decrease in peak intensity is about 10. To avoid non-linear effects during propagation in air and in the windows setup prior to the XPW crystals, it is thus necessary to implement a vacuum chamber after compression for beam focusing. However, such an implementation is costly and time consuming. Some other post-compression techniques can be more suited to high energy pulses, such as a gas-filled hollow-core fiber. Here, spectral broadening is a priori less sensitive to phase distortions prior to the nonlinear medium than XPW generation. However, the fiber issues related to the high average power remain with such a setup. A very promising approach to decrease the pulse intensity consists in implementing pulse dividing and combining in a hollow fiber compressor, as demonstrated in the next chapter.

Chapter 8

Pulse dividing and combining in a hollow fiber compressor

Contents

8.1 Principle of pulse dividing and coherent combining

The post-compression stages based on Self-Phase Modulation in a gas filled capillary enable to generate ultrashort pulses with a high spatial quality. However, when the input pulse energy approaches the mJ level, both the transmission and stability of hollow fiber compressors drop with the onset of self-focusing and ionization. The high order nonlinear effects in the setup windows and in the fiber cladding are also detrimental to the setup transmission. Finally, the CEP stability and temporal quality of the pulses are highly deteriorated. Several approaches have been successful in managing the peak power of multi-mJ pulses in hollow-core fiber (HCF) compressors, such as the use of pressure gradients [36], circular polarization [105] or large cross-section stretched waveguides [84].

However, despite the additional use of all these techniques, the post-compression of > 5 mJ pulses remains challenging. The post-compression experiments performed with 10 mJ, 23 fs pulses in Salle Noire 2.0 illustrate these words: it required the addition of two vacuum chambers on either side of the fiber to get free from the nonlinearities in the setup windows. Such an implementation is time consuming and very expensive. New tricks are needed to make the post-compression of intense pulses easier and successful.

Figure 8.1 – Principle of optical multiplexing.

Implementing pulse dividing and combining in gas-filled HCF post-compressors (see Fig. 8.1) is an attractive prospect for overcoming the encountered energy limitation. This technique consists in dividing the input pulse into several replicas which undergo Self-Phase Modulation in the capillary and are independently spectrally broadened. 5 fs pulses with high peak intensities can be then achieved by coherently combining the replicas before ending the compression with chirped mirrors. One of the main advantages of this technique compared to the previous ones is that it enables to considerably relax the nonlinear effects in the entrance setup window.

8.2 Overview of the pulse dividing and combining implementations

The energy related limits encountered in various applications like pulse amplification or nonlinear compression can be challenged thanks to optical multiplexing. Pulse division and combination can be achieved in time, in space or in spectral domain. In the last case, dividing a pulse spectrum into replicas with different spectral contents allows to overcome gain narrowing in ultrafast fiber amplifiers or to synthesize controlled sub-optical-cycle laser waveforms. A complete review dedicated to the coherent combining of femtosecond pulses is proposed in [124].

8.2.1 Pulse amplification

The pulse dividing and combining technique was initially applied to amplifiers in order to optimize the energy extraction, to overcome optical damage and to reduce undesirable nonlinear effects.

In this context, an optical multiplexing method based on Sagnac interferometers was implemented in excimer amplifiers to extract the stored energy efficiently [125]. This implies to make the delay between the replicas coincide with the recovery time of the gain. This concept was expanded to scale the performances of ultrafast fiber lasers. In this case, coherent beam combination architectures helped to decrease peak intensities, always maintaining a monomode opera-

tion with a moderate core diameter. The combination of two spatially-divided replicas previously amplified in two Ytterbium-doped fiber allowed the generation of 325 fs pulses thanks to an active feedback loop [126, 127]. Otherwise, the passive combination of two replicas from a Sagnac interferometer enabled the generation of 300 fs, 650 µJ pulses [128]. This setup was extended to manifold pulse division in temporal domain [129], always without active stabilization system.

As an alternative solution, multicore fibers setups have the benefit of a unique and common pump. Seven individual coupled cores were combined via supermode selection to achieve 110 fs pulses with a peak power about 150 MW [130]. An active scheme based on non-coupled cores is also attractive for power-scaling, as demonstrated in [131]. In this experiment, 860 fs pulses were achieved by combining 7 cores and controlling the individual phase of each beam with a common phase modulator. Otherwise, the coherent spectral combining technique proved to be relevant in a multicore fiber. The idea here is to amplify ultrashort laser pulses without any stretching device. This is how 228 fs lasers pulses were split in 12 spectral components and separately amplified in a 12 non-coupled cores fiber, before being coherently recombined [132].

The combination of optical parametric amplifiers (OPA) was also demonstrated: 50 µJ, 49 fs pulses were produced with 97% efficiency thanks to a two-loop active stabilization system [133]. More recently, the combination of two OPAs produced 23 fs relativistic-intensity laser pulses [134] with a similar but improved active stabilization system.

8.2.2 Pulse synthesis in spectral domain

The gain narrowing limitations in ultrafast fiber amplifiers can be solved using spectral multiplexing, as demonstrated in [135]. This technique is also attractive to combine different parametric sources with distinct spectral contents and synthesize thus several octaves broadband spectra [136].

8.2.3 Pulse nonlinear compression

Another application of beam combination is pulse nonlinear compression, whether with photonic crystal fibers, multicore fibers or hollow-core fibers. The idea is to overtake the energy limit encountered with these fibers, which is about the µJ level for fused-silica fibers because of self-focusing and about the mJ level for hollow-core fibers because of ionization. Optical multiplexing has largely been demonstrated with glass fibers. In this way, four temporally divided replicas were combined and lead to 100 fs, 1 µJ compressed pulses [137]. Such a passive approach has been then challenged with both spatial and temporal pulse division into 32 replicas, resulting in 71 fs, 7.5 µJ compressed pulses at 100 kHz repetition rate [138]. The two previously mentioned experiments have the benefit of using a single fiber, which guarantees an identical spectral broadening for each replica and stability. More recently, the combination of two spatially divided replicas with an active stabilization enabled the generation of 28 fs, 1.1 µJ compressed pulse at 2.1 MHz repetition rate with 75% efficiency [139]. Here, the use of two distinct fibers lead to replicas with different spatio-spectro-temporal properties, limiting thus the combination process.

Alternatively, the combination of a high number of sub-pulses using multicore fibers has been proposed. The specific feature of the combination process lies in occurring at a given fiber length and being self-managed by inter-cores couplings. Numerical simulations highlighted the nonlinear compression and combining of 20 [140] or even 100 [141] beams.

Finally, the technique can be used to overcome the ionization limitations in hollow-core gas-filled fibers. A theoretical study reported the feasibility of pulse compression beyond the mJ level in a temporally divided HCF compressor [142]. To our knowledge, the experimental implementation of coherent combining in such a compressor had never been explored before. Besides, the shortest pulse duration obtained with this technique in a post-compression setup using Kagome-type fibers is, to date, 70 fs [138].

In the following sections, I present the experimental implementation of optical multiplexing in a hollow fiber compressor to produce CEP-stable few-cycle pulses at the mJ level.

8.3 Implementing pulse division and combination in a hollow fiber post-compressor

Three setup can be considered to implement pulse division and combination.

8.3.1 Spatial pulse division
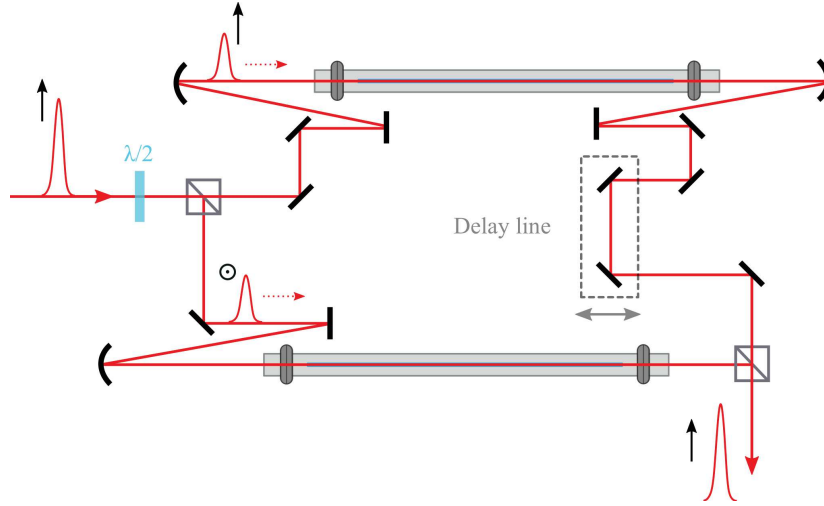
Figure 8.2 – Implementation of spatial pulse dividing with two independent fibers.

Spatial pulse division and combination can be achieved with a Mach-Zehnder interferometer using two independent hollow-core fibers, as illustrated on Fig. 8.2. A delay line is necessary to balance the beam paths of the replicas. An active feedback is here required because the two fibers are subject to different environmental conditions and the nonlinear media are not strictly identical within the two fibers. The capillary does not behave any more like a monomode waveguide when gas is added inside, meaning that the replicas may have different mode structures at the fibers output. As a result, the combining efficiency is reduced. Finally, coupling simultaneously and identically the replicas in two distinct fibers may be hard to manage, making this setup not suited to the passive coherent combining of few-cycle pulses.
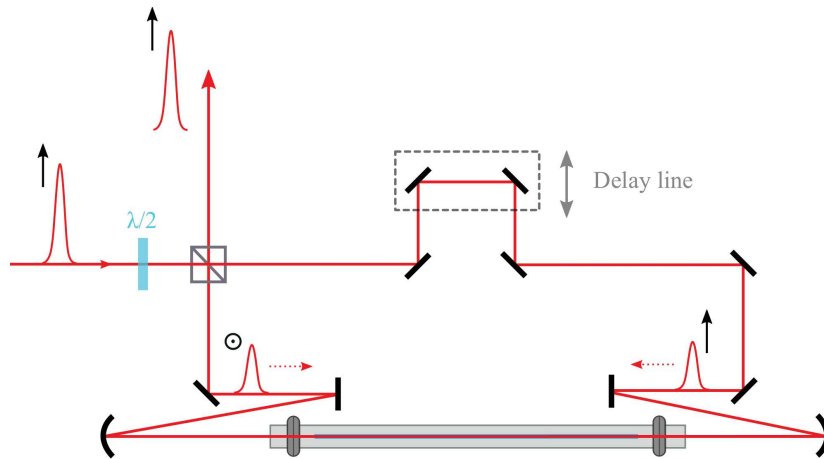
Figure 8.3 – Implementation of spatial pulse dividing in a Sagnac interferometer.

In a Sagnac interferometer, the beam is split in two spatially distinct beams, as seen on Fig. 8.3. This loop interferometer includes a single gas-filled hollow-core fiber so that both replicas undergo the same nonlinearities. This is crucial because an efficient combination will be achieved only if the spectrally broadened orthogonally polarized replicas have similar spectrum and phase.

Besides, the phase shift chances are minimized since the replicas experience the same beam path. However, the optical alignment of the interferometer is very sensitive and coupling simultaneously on either side of the fiber might be hard to manage. If beam coupling is not managed identically at each fiber edge, the peak intensity difference between the replicas will lead to different replica spectral broadening, affecting the combining efficiency and the final pulse duration. The polarizer is the most critical element of the setup. This component should feature a large enough aperture, broadband transmission and reflection coefficients, low GDD and a good surface quality. Furthermore, when the pulse hits back onto the polarizer, its finite extinction ratio creates a leakage going back to the laser amplifier. As our amplifier is highly sensitive to back reflection (some severe damage already happened because of the amplification of a back-reflection from an AR-coated plate), the implementation of a large aperture Faraday rotator before the interferometer is mandatory. Because of optical Kerr effect, it cannot be installed in the compressed beam (E> 1 mJ, 30 fs). This remains difficult before compression, as such a dispersive element adds constraints to our already borderline stretcher-compressor pair. This is then a highly restrictive aspect of the technique.
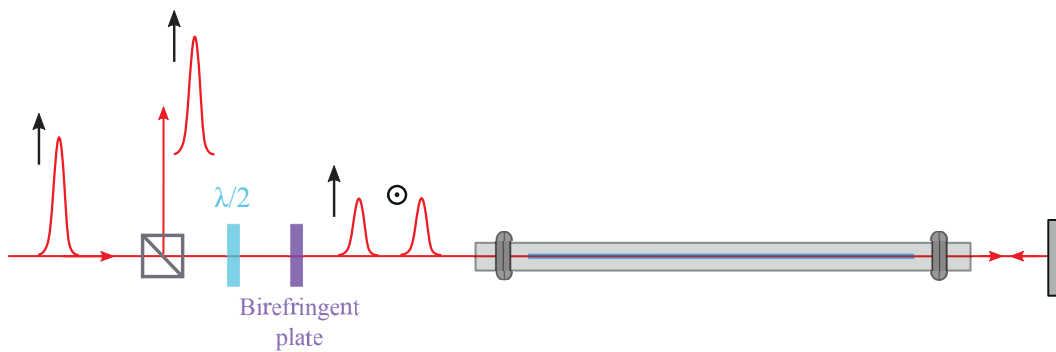
Figure 8.4 – Implementation of temporal pulse dividing in a 'One round trip configuration' with one birefringent plate.

8.3.2 Temporal pulse division

Another approach is based on temporal pulse division using a unique birefringent plate for pulse dividing and combining (Fig. 8.4). As in the Sagnac interferometer case, the phase shift chances are very low because both replicas experience the same beam path and pulse dividing and combining is achieved using the same plate. Again, coupling twice in the fiber makes the alignment hard and the losses high. Besides, the leakage due to the finite extinction ratio of the polarizer goes back in the amplifier.

Figure 8.5 – Implementation of temporal pulse dividing in a 'One trip configuration' with two similar birefringent plates.

The solution we developed consists in using two distinct birefringent plates and a fiber in a single pass configuration (Fig. 8.5). However, achieving a high combination efficiency in this configuration requires that the delays introduced by the different birefringent plates be strictly identical. One therefore needs to compensate for the eventual thickness difference between the two plates. Here, the crystallographic plate orientation choice is crucial and will be explained in more details

in the next section. Otherwise, in this last setup, the polarizer discriminates the combined pulse energy from that one of the uncombined pulse. The combining efficiency is defined as the ratio between the total energy measured before the polarizer and the energy of the combined beam measured after the polarizer.

8.4 Birefringent plate choice

Our setup is based on temporal pulse division into several replicas using birefringent plates. We first have to answer to the following issues:

- Which material to choose?

- What is the most adapted crystallographic orientation?

- How thick should be the crystal?

8.4.1 Material

Bulk material	$\Delta n = \lvert n_e\text{-}n_o \rvert$	$\Phi^{(2)}_{max}$(800 nm) (fs^2/mm)	$\Delta\Phi^{(2)}$(800 nm) (fs^2/mm)
CaCO$_3$	**0.166**	**75**	**36**
YVO$_4$	0.21	313	110
LibNO$_3$	0.08	430	62
TiO$_2$	0.27	1230	249
Al$_2$O$_3$	0.0079	60	2
TeO$_2$	0.1472	583	86

Table 8.1 – Non exhaustive list of birefringent materials with their characteristics: indices difference, maximum GDD and differential GDD, both calculated at 800 nm [50].

A list of birefringent materials is proposed in Tab. 8.1. The first criteria driving the material choice is that the difference between the ordinary and extraordinary indices must be high enough to avoid any temporal overlap between the 30 fs replicas considering thin plates (< 1 mm). In the cases of lithium niobate and aluminium oxide, the gap between the ordinary and extraordinary indices is too low to ensure a sufficient delay. For a 1 mm-thick Al$_2$O$_3$ or LibNO$_3$ crystal at normal incidence, the delay would be indeed about 26 fs. The second criteria is that the maximum GDD must be low enough to be easily compensated, keeping in mind the 12 chirped mirrors we have available (UltraFast Innovation, GmbH) exhibit a total GDD of -500 fs^2. This criteria excludes titanium dioxide and tellurium dioxide. The last requirement is that the differential GDD, ie the GDD difference between the two polarization components, is as low as possible. Finally, calcium carbonate (calcite) allows a good compromise between these 3 criteria and seems to be the best candidate to perform coherent combining in the few-cycle regime.

8.4.2 Crystallographic orientation

Usually, birefringent materials are used so that their crystallographic axes are parallel to their incident surface. However, for the application we aim for, the off-axis approach offers a degree of freedom to control the phase delay during the combination process. Θ_c defines the calcite orientation and is the angle between the extraordinary axis and the perpendicular axis to the plate plane (see Fig. 8.6). When the plate is placed at normal incidence, the refractive index experienced by the extraordinary ray can be expressed as:

$$n_e(\Theta_c) = \frac{1}{\sqrt{\frac{\cos\Theta_c^2}{n_o^2} + \frac{\sin\Theta_c^2}{n_e^2}}} \tag{8.1}$$
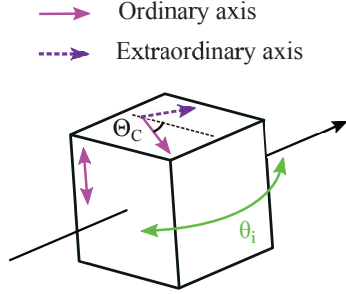
Figure 8.6 – Scheme of a birefringent plate. Extraordinary and ordinary axes are indicated respectively in purple and pink. θ_i is the plate tilt along the extraordinary direction.
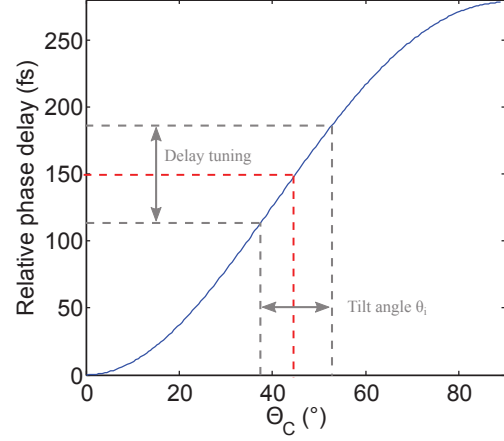
Figure 8.7 – Relative phase delay calculated at 800 nm and for a 500 μm thick calcite plate at normal incidence as a function of Θ_C, its crystallographic orientation.

Neglecting the walk-off angle, the relative phase delay for a plate at normal incidence is given by:

$$\tau = \frac{e}{c}\left(n_o - \frac{1}{\sqrt{\frac{(\cos\Theta_c)^2}{n_o^2} + \frac{(\sin\Theta_c)^2}{n_e^2}}} \right) \tag{8.2}$$

where e is the plate thickness, c is the light velocity in vacuum, n_o and n_e the phase indices. The relative phase delay is plotted on Fig. 8.7 as a function of Θ_c for a 500 μm-thick calcite crystal at normal incidence. A 45° oriented plate introduces a 150 fs delay between the two 30 fs replicas, and thus guarantees no temporal overlap between the replicas.

Looking at Fig. 8.8, the incidence angle on the plate belongs to the same plane as Θ_c (when $\Theta_c \neq 0°$). In this way, tilting the plate tunes the relative phase delay between the replicas and compensates any phase difference experienced by the replicas, as underlined by the dashed lines on Fig. 8.7. The extraordinary index is related to the incident angle according to:

$$n_e(\theta) = \frac{1}{\sqrt{\frac{\cos\theta^2}{n_o^2} + \frac{\sin\theta^2}{n_e^2}}} \tag{8.3}$$

where θ is the angle between the crystallographic axis and the extraordinary wave vector inside the crystal, as illustrated on Fig. 8.8. As calcite is a negative uniaxial medium, the extraordinary wave propagates along k_e, which is oriented by the angle $\theta = \Theta_c - \theta_{r,e}$, whereas the pulse energy propagates along the Poynting vector S_e. The angle between the wave vector and the Poynting vector is called the walk-off angle and named γ in the following.

8.4.3 Thickness

The plate thickness choice is driven by 3 criteria: the replicas must not be temporally overlapped, both the dispersion and differential dispersion must be as minimum as possible. In practice, the minimal thickness available at Eksma is 500 μm. A 45° oriented plate with such a thickness features a maximum GDD < 50 fs^2, a differential GDD < 10 fs^2 and delays the replicas by 150 fs.

To conclude, when working with off-axis crystals, θ is a very sensitive degree of freedom to tune the relative delay and correct for the eventual thickness difference between the two plates. If the
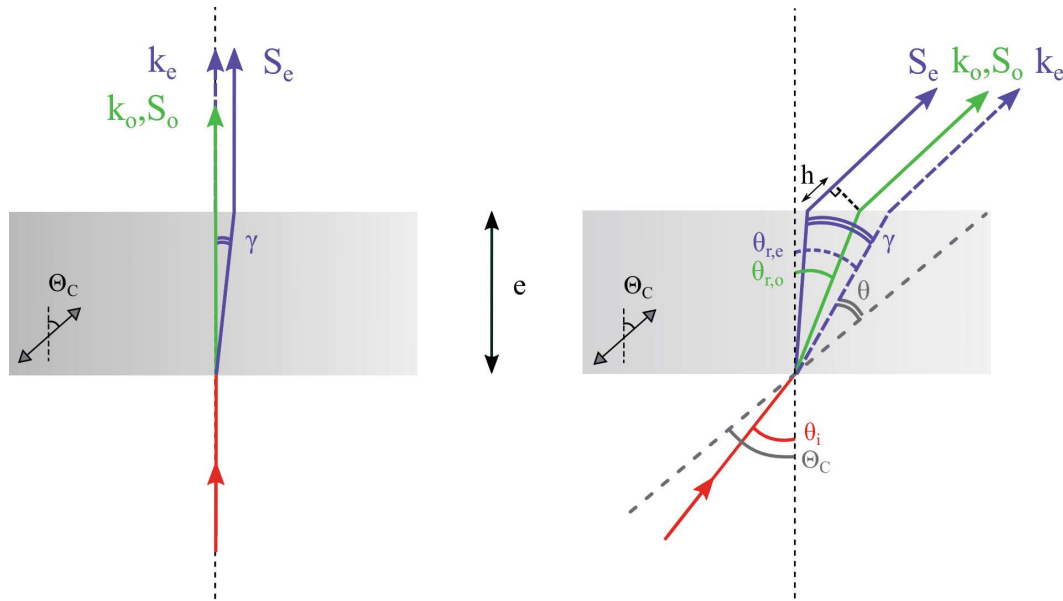
Figure 8.8 – Top view of a birefringent plate at normal incidence (left) and for a non zero incidence angle (right): ordinary (green) and extraordinary (purple) rays. θ_i is the incident angle on the plate. Θ_C is the crystallographic orientation of the plate. $\theta_{r,o}$ and $\theta_{r,e}$ are the refractive angle of respectively the ordinary and extraordinary ray. γ and h are relative to the walk-off and θ_i. θ is the angle between the extraordinary ray and the crystallographic axis. k_e and k_o (resp. S_e and S_o) are the wave vectors (resp. the Poynting vectors) of the extraordinary and ordinary waves.

dividing and combining plates are crossed, phase matching can therefore be achieved in the combining plate with a sub-fs precision. The phase delay corresponding to a rotation angle precision of 2' is indeed 100 as, which is small compared to the electric field period (2.7 fs at 800 nm).

However, it should be noticed that such oriented crystals present a non negligible walk-off angle γ because of double refraction. More precisely, the crystallographic orientation which maximizes the walk-off angle is given by [143]:

$$\tan(\Theta_{c,\gamma max}) = \frac{n_e}{n_o} \qquad (8.4)$$

In the case of a calcite crystal:

$$\Theta_{c,\gamma max} \approx 42° \qquad (8.5)$$

For the aimed application, the walk-off angle is not an issue for two reasons. First, the birefringent plates thickness is small enough (between 500 µm and 1 mm) so that the spatial shift between the ordinary and extraordinary rays is negligible compared to the beam size (>10 mm). Second, the replicas focusing in the fiber is not sensitive to the spatial shift induced by double refraction. To be safe, the walk-off angle has to be taken into account in our calculation.

8.5 Plates theoretical and experimental characterizations

8.5.1 Identification of the plates crystallographic axes

The calcite plate axes are oriented parallel to the horizontal and vertical directions. The half-waveplate turns the laser polarization from P to 45° from the plate axes so that two S and P polarized replicas with equal intensity are created in the calcite plate. The polarizer is then oriented to 45° to measure the spectral interferences between the two replicas, as shown on Fig. 8.9. The last step consists in tilting the calcite plate, simultaneously looking at the fringe spacing. If the fringe spacing changes with the plate tilt, the extraordinary axis is along the tilting direction.
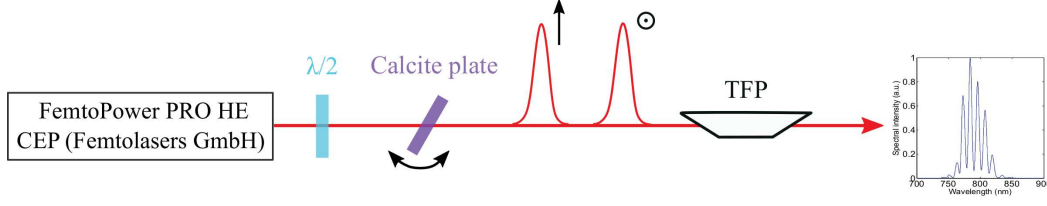
Figure 8.9 – Fringed spectrum measurement. TFP: Thin Film Polarizer.

8.5.2 Spectrometer requirement

A high spectral resolution is necessary to measure the spectral interferences with an acceptable fringe contrast, especially when the inter-replicas delay is long (typically > 350 fs). Besides, when the number of replicas is higher than 2, the optical adjustment of the setup is more critical and a high resolution is unavoidable: the spectrometer is indeed the key tool in the experiment to optimize both the Dividing and Combining Setups. For the same reasons, the spectrometer calibration must be good enough on the spectral bandwidth [500-1000]nm. The model 'AvaSpec-ULS2048XL-USB2' (Avantes) including a 300 lines/mm grating and featuring a 1.5 nm resolution answers to all these constraints.

8.5.3 Commercial specifications of the used calcite plates

In all the experiments, we used three pairs of calcite plates named (C1,C2), (C3,C4) and (C5,C6). Their specifications are given in Tab. 8.2.

	Θ_c	e (μm)
C1	45°	500 +/- 50
C2	45°	500 +/- 50
C3	60°	500 +/- 50
C4	60°	500 +/- 50
C5	60°	700 +/- 50
C6	60°	700 +/- 50

Table 8.2 – Commercial specifications of the calcite plates (crystallographic orientation and thickness), (EKSMA).

The theoretical group delay introduced by each plate can be calculated as a function as the plate tilt, as shown in the next section. The results of the calculation are then compared to the experimental data.

8.5.4 Theoretical calculation of the group delay introduced by the plates

The theoretical group delay has been calculated as a function of the incident angle on the plate, taking into account beam walk-off. Considering the extraordinary index along the Poynting vector direction (see Fig. 8.8), the group delay can be expressed as [144]:

$$\tau_g(\theta_i) = \frac{e}{c}\left[\frac{n_{g,o}}{\cos(\theta_{r,o})} - \frac{n_{g,e}(\Theta_c - \theta_{r,e})\cos(\gamma(\theta_{r,e}))}{\cos(\theta_{r,e} - \gamma(\theta_{r,e}))} \right] + \frac{h(\theta_i)}{c} \tag{8.6}$$

where $\theta_{r,o}$ and $\theta_{r,e}$ are the refracted angles for respectively the ordinary and extraordinary rays (see Fig. 8.8), γ is the walk-off angle and $n_{g,o}$ and $n_{g,e}$ are the group indices defined by:

$$n_{g,o} = n_o - \lambda\frac{dn_o}{d\lambda} \tag{8.7}$$

$$n_{g,e} = n_e - \lambda\frac{dn_e}{d\lambda} \tag{8.8}$$

The energy of the extraordinary wave propagates at the velocity $c/(n_{g,e}\cos\gamma)$ along S_e. The optical path difference, $h(\theta_i)$, experienced by the extraordinary and ordinary rays in air, as illustrated on Fig. 8.8, must also be taken into account:

$$h(\theta_i) = e\left[\sin(\theta_i)\left[\tan(\theta_{r,e} - \gamma(\theta_{r,e})) - \tan(\theta_{r,o})\right]\right] \tag{8.9}$$

The steps of the calculation are detailed below. The ordinary and extraordinary phase indices are first determined, before calculating the refracted angles inside the plate for both rays as well as the walk-off angle.

a) Calculation of the ordinary and extraordinary phase indices for calcite

The ordinary and extraordinary phase indices are calculated using the Sellmeier equations as follows:

$$n_o^2(\lambda) - 1 = A_o + \frac{B_{1,o}\lambda^2}{\lambda^2 - C_{1,o}} + \frac{B_{2,o}\lambda^2}{\lambda^2 - C_{2,o}} \tag{8.10}$$

$$n_e^2(\lambda) - 1 = A_e + \frac{B_{1,e}\lambda^2}{\lambda^2 - C_{1,e}} + \frac{B_{2,e}\lambda^2}{\lambda^2 - C_{2,e}} \tag{8.11}$$

The Sellmeier coefficients are given in Tab. 8.3 [50].

	o	e
A	0.73358749	0.35859695
B_1	0.96464345	0.82427830
B_2	1.82831454	0.14429128
C_1	0.0194325203 μm^2	0.0106689543 μm^2
C_2	120 μm^2	120 μm^2

Table 8.3 – Sellmeier coefficients for calcite.

b) Calculation of the refracted angles inside the calcite plate

The refracted angles are calculated using the Snell-Descartes relations:

$$\sin(\theta_i) = n_o(\lambda)\sin(\theta_{r,o}) \tag{8.12}$$

$$\sin(\theta_i) = n_e(\lambda, \theta)\sin(\theta_{r,e}) \tag{8.13}$$

where $\theta_{r,o}$ and $\theta_{r,e}$ are the refracted angles for respectively the ordinary and extraordinary rays (see Fig. 8.8). The extraordinary index is given by Eq. 8.3 with $\theta = \Theta_C - \theta_{r,e}$. Solving the below nonlinear equation enables to evaluate $\theta_{r,e}$:

$$\sin(\theta_i) = \frac{\sin(\theta_{r,e})}{\sqrt{\frac{\cos(\Theta_c - \theta_{r,e})^2}{n_o(\lambda)^2} + \frac{\sin(\Theta_c - \theta_{r,e})^2}{n_e(\lambda)^2}}} \tag{8.14}$$

c) Calculation of the walk-off angle

In an anisotropic medium, the pulse energy propagates in general in a different direction from the wave vector. The electric susceptibility and electric permittivity tensors of the medium, χ and ϵ, are indeed not reduced to scalars. As a consequence, the electric polarization **P** and the electric field **E** are not parallel each other (see Fig. 8.10). This also holds true for the electric displacement **D** and the electric field. Neglecting currents, the Maxwell equation are given by:

$$\mathbf{k} \cdot \mathbf{D} = 0 \qquad (8.15)$$

$$\mathbf{k} \wedge \mathbf{E} = \omega \mathbf{B} \qquad (8.16)$$

$$\mathbf{k} \cdot \mathbf{B} = 0 \qquad (8.17)$$

$$\mathbf{k} \wedge \mathbf{B} = -\omega \mathbf{D} \qquad (8.18)$$

where $\mathbf{k}$ is the wave vector, $\mathbf{B} = \mu \mathbf{H}$ the magnetic field, μ is the permeability of the medium. $\mathbf{D}$ can be expressed as:

$$\mathbf{D} = \frac{1}{\omega^2 \mu} \mathbf{k} \wedge (\mathbf{k} \wedge \mathbf{E}) \qquad (8.19)$$

$$\mathbf{D} = \frac{1}{\omega^2 \mu} \underbrace{[\mathbf{E} - \mathbf{k}(\mathbf{k} \cdot \mathbf{E})]}_{\mathbf{E}_\perp} \qquad (8.20)$$
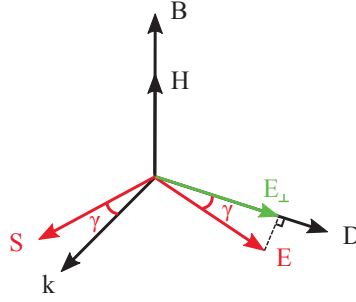
Figure 8.10 – Directions of the wave vector, the electric and magnetic fields in an anisotropic medium. γ is the walk-off angle and S the energy flow direction.

where $\mathbf{E}_\perp$ denotes the vector component of $\mathbf{E}$ perpendicular to $\mathbf{k}$ in the plane of $\mathbf{E}$ and $\mathbf{k}$. According to the equations 8.18, $\mathbf{D}$, $\mathbf{H}$ and $\mathbf{k}$ form an orthogonal coordinate system. Furthermore, it is clear that $\mathbf{k}$ belongs to the same plane than $\mathbf{D}$ and $\mathbf{E}$ but is not perpendicular to $\mathbf{E}$ according to Eq. 8.20. The angle between $\mathbf{E}$ and $\mathbf{D}$ is the walk-off angle that I call γ. The same angle is between $\mathbf{k}$ and the energy flow direction. The Poynting vector is indeed defined as:

$$\mathbf{S} = \frac{\mathbf{E} \wedge \mathbf{B}}{\mu} \qquad (8.21)$$

Therefore, the energy does not propagate in the wave vector direction. The walk-off angle γ can be calculated from the equation:

$$\tan \gamma = -\frac{1}{n_e(\theta)} \frac{\partial n_e(\theta)}{\partial \theta} \qquad (8.22)$$

where θ is the angle between the crystallographic axis $\hat{C}$ and $\mathbf{k}_e$ [145]. For a negative uniaxial crystal, n_e decreases when θ increases. Therefore, $\mathbf{k}_e$ lies between $\mathbf{S}_e$ and $\hat{C}$, as illustrated in Fig. 8.11.

Differenciating Eq. 8.3 leads to the walk-off expression:

$$\tan(\gamma(\lambda, \theta_{r,e})) = \frac{(n_o(\lambda)^2 - n_e(\lambda)^2) \sin(\Theta_c - \theta_{r,e}) \cos(\Theta_c - \theta_{r,e})}{n_e(\lambda)^2 \cos^2(\Theta_c - \theta_{r,e}) + n_o(\lambda)^2 \sin^2(\Theta_c - \theta_{r,e})} \qquad (8.23)$$

γ depends on the crystallographic orientation of the plate. Fig. 8.12 shows γ (calculated at 800 nm) as a function of θ_i, the plate tilt, for two different crystallographic orientations. In both cases, γ is barely higher than 6°.
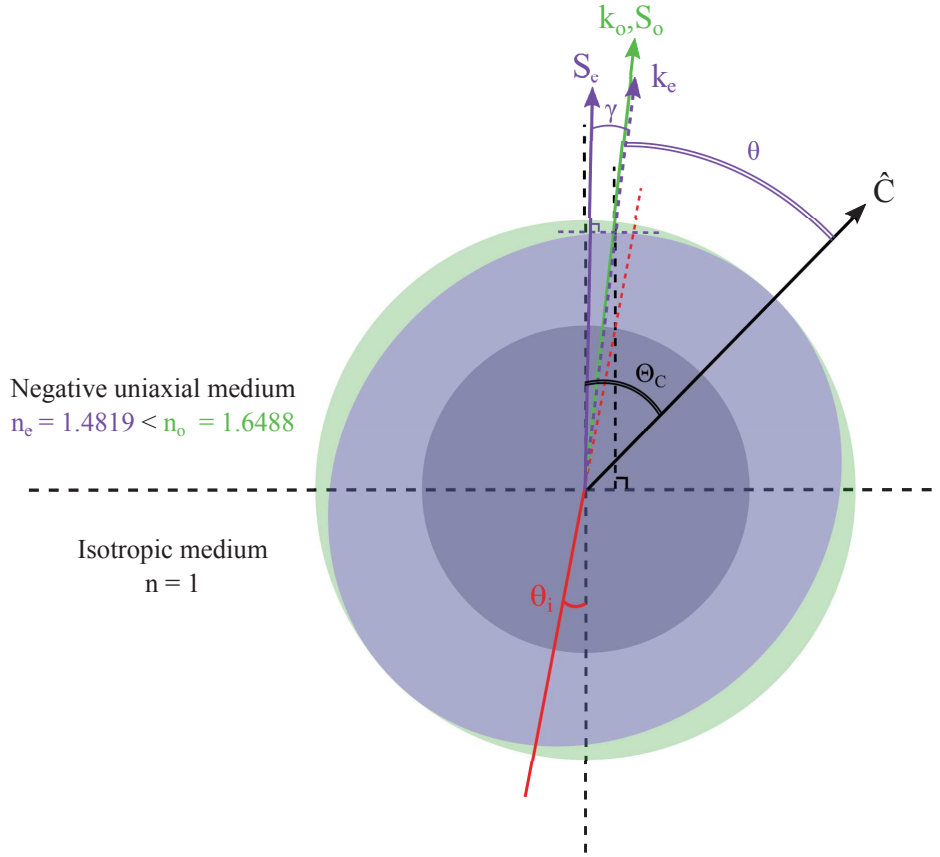
Figure 8.11 – Descartes diagram to scale for construction of refraction angles between an isotropic medium and a negative uniaxial medium. The S_e vector direction is normal to the tangent to the extraordinary indicatrix (purple) taken at the point of intersection with k_e

.
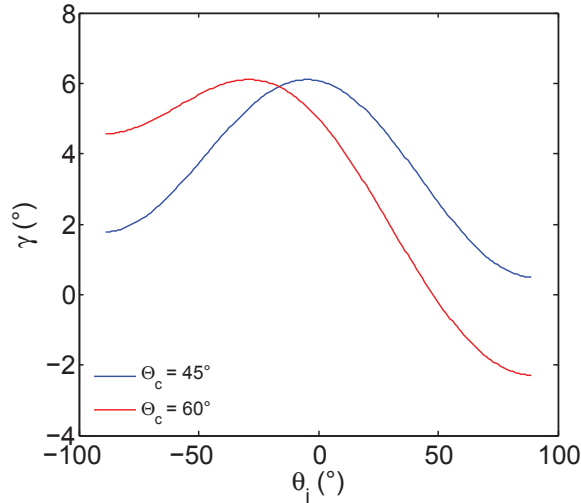
Figure 8.12 – Calculated walk-off angle at 800 nm for a 45° and a 60° oriented calcite plate as a function of the plate tilt.

8.5.5 Group delay versus θ_i - Comparison between experimental data and theoretical values

The experimental influence of the incident angle (θ_i, where i is the plate number) on the group delay is then investigated in the case of each plate. To do so, the fringed spectrum is recorded for each value of the tilt plate, as illustrated on Fig. 8.9. The group delay can be deduced performing a

Fourier Transform of the fringed spectrum, as shown on Fig. 8.13.
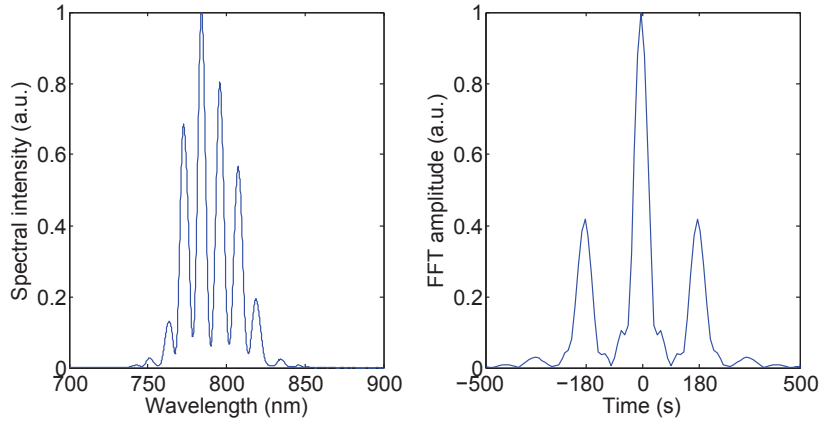
Figure 8.13 – Fringed spectrum and its Fourier transform in the case of the plate C1 at normal incidence.

Since the thickness specified by the supplier is given with an uncertainty of ± 50 μm, theory and experiments will be in good agreement only if we consider the actual thickness of the plate. Assuming that the plates crystallographic orientation is correct, the plate thickness is deduced from the experimental group delay measured at normal incidence according to:

$$e = \frac{c \times \tau_g(\theta_i = 0)}{n_{g,o} - n_{g,e}(\theta_i = 0)} \tag{8.24}$$

where $n_{g,o}$ and $n_{g,e}$ are the group indices defined previously.

The actual thicknesses of the plates are summed up in Tab. 8.4. All thickness values are in-

	Θ_c	e (μm)	$\tau_{g,exp}$ (fs)	e_{exp} (μm)
C1	45°	500 +/- 50	179	544
C2	45°	500 +/- 50	179	544
C3	60°	500 +/- 50	245	518
C4	60°	500 +/- 50	218	462
C5	60°	700 +/- 50	351	742
C6	60°	700 +/- 50	344	728

Table 8.4 – Commercial specifications of the calcite plates, experimental group delay deduced from the Fourier analysis of fringed spectra, and actual plates thicknesses.

cluded in the margin of error given by the supplier. Plates C1 and C2 are found to be identical, while the thickness difference between C3 and C4, as well as between C5 and C6, require some experimental adjustment to match both delays. The calculations were performed using these actual thicknesses values, and not the ones specified by the supplier.

The graph 8.14 shows the group delay as a function of the plate tilt and compares the experimental and theoretical results for each plate. As expected, θ_i is an accurate tool for tuning the delay. The measured tunability is indicated in Tab. 8.5 for all plates. A very good agreement is found with calculations, which confirms the correctness of the crystallographic orientation of the plates, as the delay dependence with θ_i is significantly affected by a change of Θ_c. To conclude this part, we found that both C1 and C2 can be used at normal incidence for efficient combining (a slight tilting of C2 might be necessary for exact phase matching), while C4 will need to be tilted by almost +10° relative to C3, and C6 by -1.8° relative to C5.
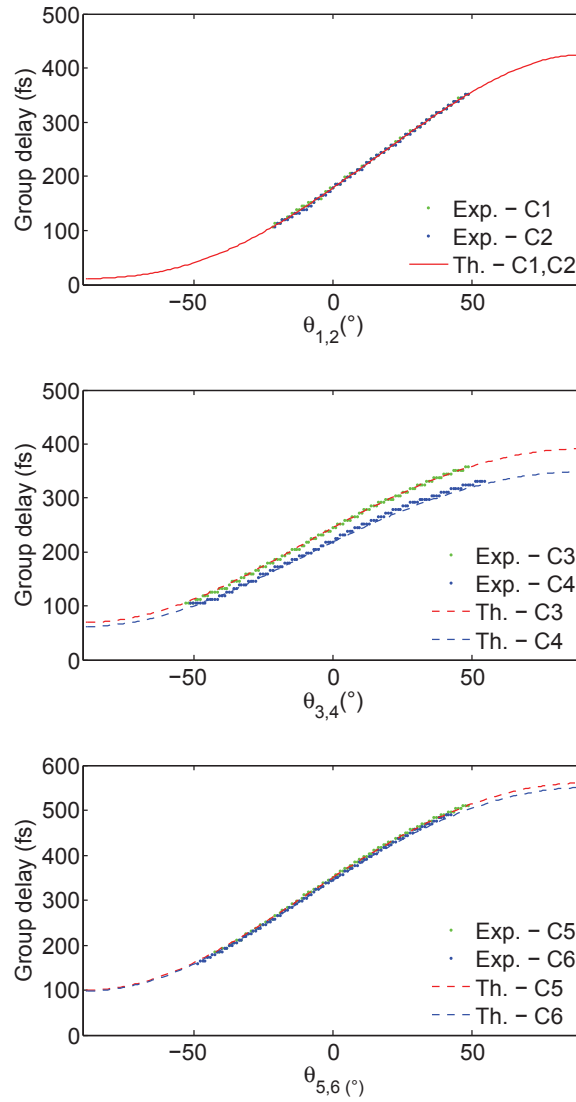
Figure 8.14 – Experimental and theoretical group delays for (C1,C2), (C3,C4) and (C5,C6) as a function of the incident angle on the plate θ_i. The actual thickness of the plate is deduced from the experimental delay measured at $\theta_i=0°$, assuming that the crystallographic orientation is correct.

	Θ_c	e (μm)	$\tau_{g,exp}$ (fs)	e_{exp} (μm)	δ_t (fs/°)
C1	45°	500 +/- 50	179	544	3.61
C2	45°	500 +/- 50	179	544	3.61
C3	60°	500 +/- 50	245	518	2.74
C4	60°	500 +/- 50	218	462	2.49
C5	60°	700 +/- 50	351	742	4.05
C6	60°	700 +/- 50	344	728	3.95

Table 8.5 – Commercial specifications of the calcite plates, experimental group delay deduced from the Fourier analysis of fringed spectra, actual plates thicknesses, and delay tunability with θ_i (tilt of the plate i).

8.5.6 Delay chromatism

Because the medium index is frequency dependant, group and phase velocity are different. It can be interesting to quantify the gap between group delay and phase delay, especially because

broadband pulses are considered. The phase delay is given by:

$$\tau(\theta_i) = \frac{e}{c}\left[\frac{n_o}{\cos(\theta_{r,o})} - \frac{n_e(\Theta_c - \theta_{r,e})\cos(\gamma(\theta_{r,e}))}{\cos(\theta_{r,e} - \gamma(\theta_{r,e}))}\right] + \frac{h(\theta_i)}{c} \tag{8.25}$$
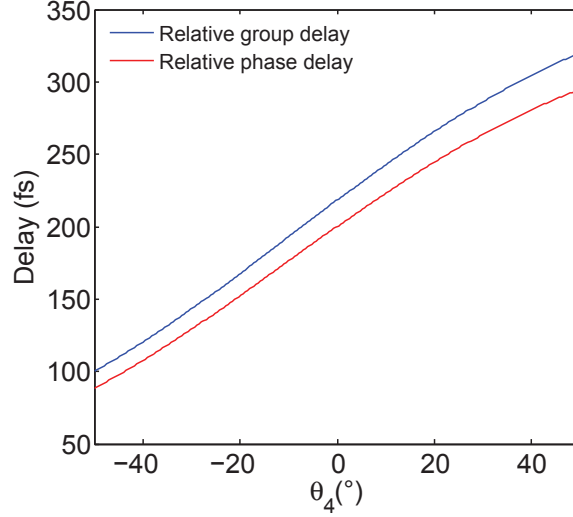
Figure 8.15 – Relative group and phase delays calculated at 800 nm, as a function of the C4 plate tilt.

In a first approach, both delays are calculated at 800 nm as a function of the plate tilt considering the plate C4 (Fig. 8.15). In the angle range where delays and tilt evolve linearly, the slopes are nearly identical in both cases: it is about 2.49 fs/° for the group delay and 2.32 fs/° for the phase delay.
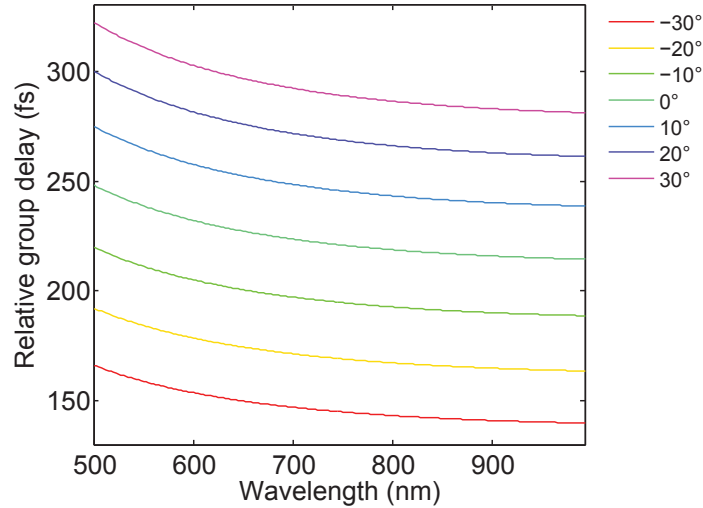
Figure 8.16 – Relative group delay in fs, calculated as a function of wavelength for different incidence angle on the plate C4.

The relative group delay chromatism is then investigated for various incidence angles in the case of the combining plate C4 (see Fig. 8.16). The curves highlight that the group delay is not constant with the wavelength. In other words, the combining plate tilt which maximizes the combining efficiency matches the delay for most of the wavelengths, except the blue ones. This limits the spectral bandwidth of the combined pulse. Besides, the positive incidence angles on the plate accentuate this phenomenon, meaning that the spectral bandwidth of the combined pulse will be larger for a negative incident angle. It is thus possible to pre-compensate the delay with the dividing plate to avoid a large positive tilt of the combining plate C4.

The residual second order phase can be finally quantified. This quantity is called differential GDD ($\Delta\phi^{(2)}$) because it corresponds to the GDD difference between the two polarization components. Note that the phase difference introduced by the first dividing plate only marginally affects the 30 fs pulse and is smeared during the spectral broadening process in the fiber. In the combining plate, however, the GDD difference might not allow phase matching of all the newly created wavelengths. $\Delta\phi^{(2)}$ is expressed as:

$$\Delta\phi^{(2)}(\omega, \theta_i) = \phi_o^{(2)}(\omega, \theta_i) - \phi_e^{(2)}(\omega, \theta_i) \tag{8.26}$$

$$\Delta\phi^{(2)}(\omega, \theta_i) = \frac{\partial \tau_g(\omega, \theta_i)}{\partial \omega} \tag{8.27}$$
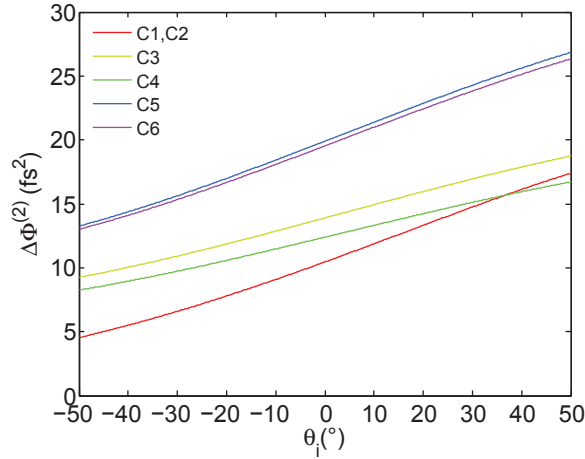
Figure 8.17 – Calculated differential GDD at 800 nm as a function of the plate tilt.

A linear fit of the group delay at 800 nm gives the differential GDD value at this wavelength. The results are shown on Fig. 8.17. The differential GDD evolves nearly linearly with the incident angle on the plate. As group delay and incidence angle are linked by a linear relation, it means that the differential GDD evolves linearly with the group delay. At normal incidence, the differential GDD is about 10 fs^2 for C1 and C2, 12 fs^2 for C4 and 19 fs^2 for C5 and C6. C1 and C2 are the most fitted plates in terms of $\Delta\phi^{(2)}$. A plate exhibiting a too high differential GDD will limit the final combined pulse duration. As explained in the next sections, we proposed an experimental method to measure this quantity.

8.6 Experimental implementation

The experiments were performed using the Femtolasers system described in Part. I. The experimental setup is described in Fig. 8.18. A commercial FemtoPower (Femtolasers GmbH), including a CEP-stabilized oscillator with external frequency shifting in a feed-forward scheme, delivers 1.6 mJ, 30 fs pulses at 800 nm with a 1 kHz repetition rate. The energy is tunable between 0.8 and 1.8 mJ by changing the seed energy in the last passes of the amplifier. The laser is linearly P-polarized. The beam is focused with a 1 m focal length mirror into a 1 m long HCF featuring an inner diameter of 250 μm. The evacuated fiber transmission is ≈70%. The fiber can be statically filled with noble gas (neon or argon). A 1 m focal length concave mirror collimates the output beam. Post-compression of the combined pulse is achieved using a pair of thin fused-silica wedges (70 fs^2) and a set of 12 double-angle chirped mirrors (500 fs^2, UltraFast Innovations GmbH). Finally, a Wizzler-USP device (Fastlite) is used to measure the temporal profile and spectral phase of the compressed few-cycle pulse, whereas a f-2f interferometer enables the CEP drift measurement.
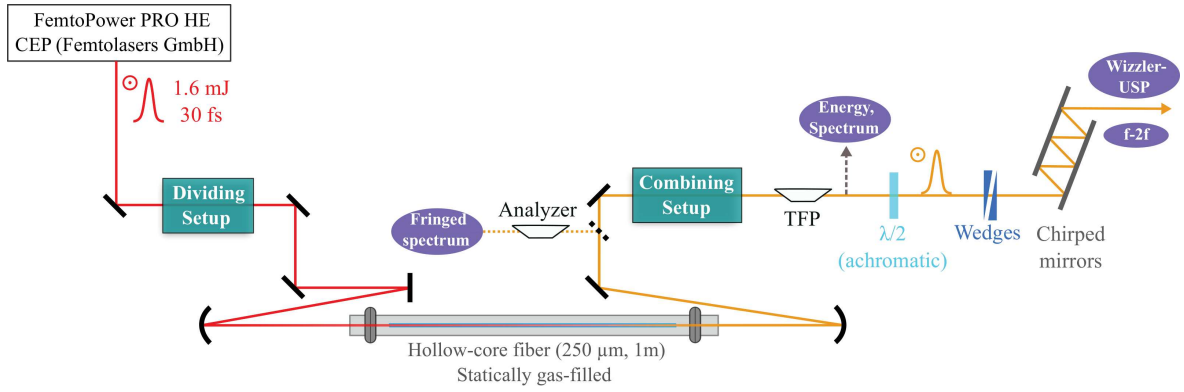
Figure 8.18 – Experimental setup (TFP, thin film polarizer).

Before and after the HCF, the pulse Dividing and Combining Setups are inserted in the colli-mated 10 mm sized beam. The Pulse Dividing Setup includes a half-wave plate and one or two calcite plates positioned at normal incidence. The first plate, with axis orientated at 45° from the laser polarization direction, creates two replicas with the same intensity and delayed by 179 fs (C1) or 245 fs (C3). A second calcite plate can either create two additional replicas or change the origi-nal delay if the neutral axes of both plates have the same orientation. The last plate of the Dividing Setup is orientated so that the generated replicas always propagate through the HCF setup with P and S polarizations. The initial half-wave plate (T>99%) adjusts the laser polarization direction to balance the replicas intensity.

The Combining Setup has a symmetric configuration with respect to the Dividing Setup, as illustrated in Tab. 8.6, where the different experimental implementations are summarized. The rainbow area represents the nonlinear medium, which is between the Dividing and Combining Setups. α_k is defined as the rotation angle in the plate plane and θ_k as the plate tilt angle in the extraordinary axis direction. The axis of each pair of plates (C1-C2 or C3-C4) are crossed so as to compensate the introduced group delay. As the angle $\theta_{k,k=2,4,6}$ of the combining plates is care-fully adjusted to optimize the combined pulse spectrum and energy, those plates are mounted on high-resolution manual rotation stages (better than 2 minutes of arc). The fringed spectrum cor-responding to the spectral interferences between the replicas is measured thanks to an analyzer. A thin film polarizer (Femtolasers GmbH) (T>98%) discriminates the combined pulse and enables the measurement of both the combining efficiency and combined pulse spectrum. A broadband half-wave plate is then used to recover P-polarization before propagation on the chirped mirrors if necessary.
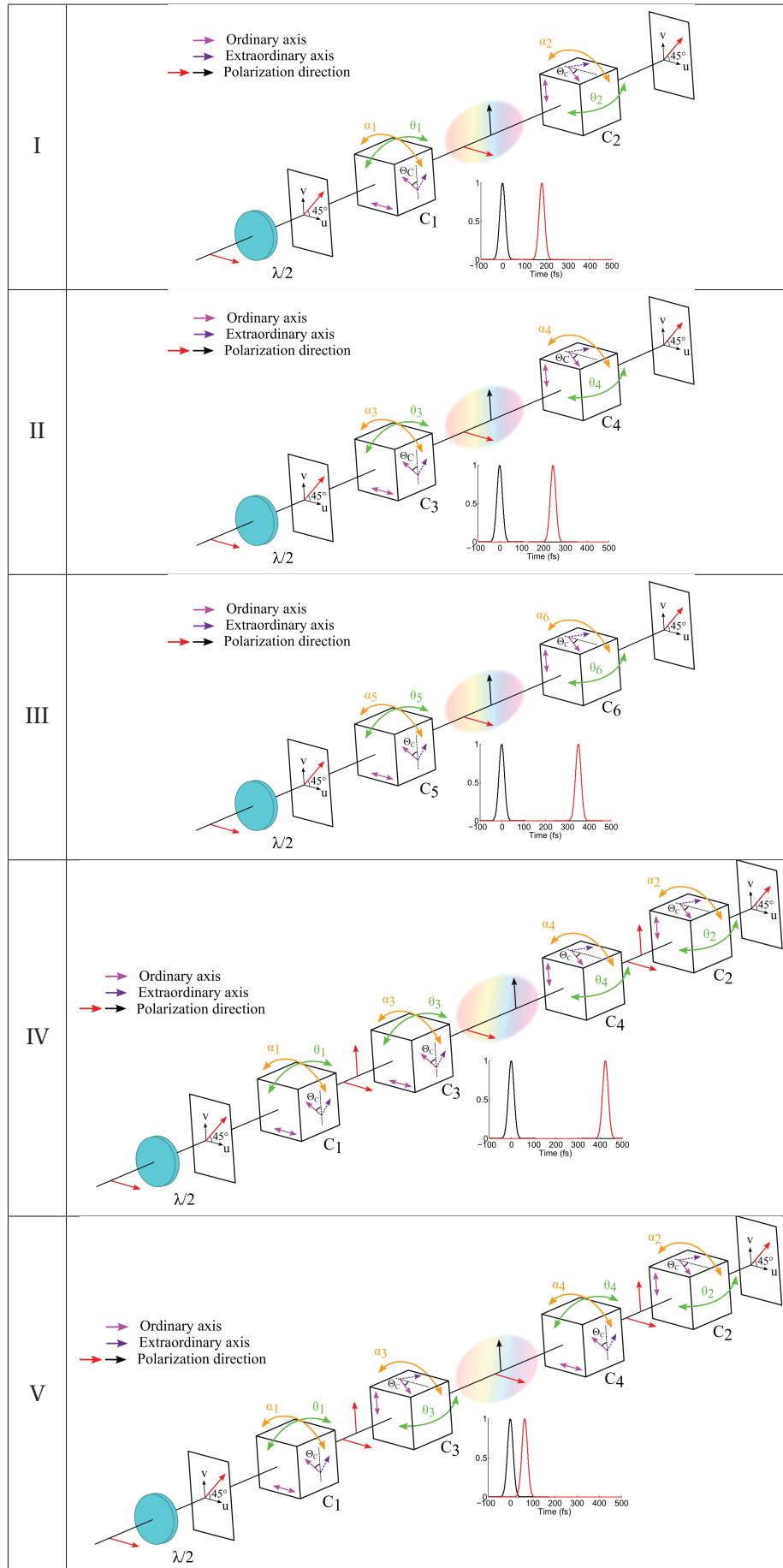
Table 8.6 – Implementation of pulse dividing and pulse combining in the case of two replicas: polarization direction (red), half-wave plate (blue). The nonlinear medium is represented with a rainbow area. Extraordinary and ordinary axes are indicated for each plate. The delayed replicas are also represented (black: S polarized, red: P polarized).

8.7   Numerical simulation tool
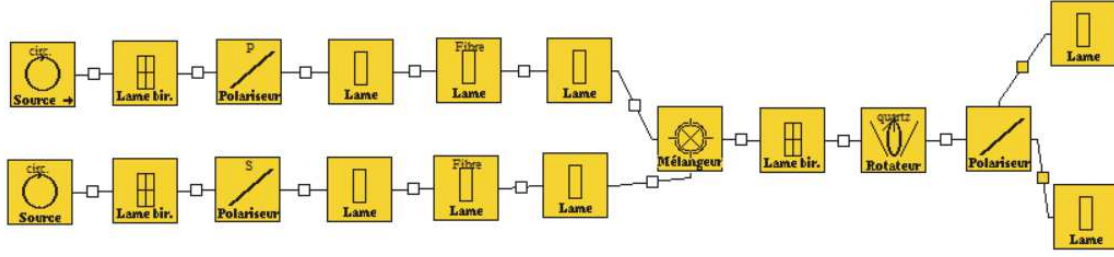
Figure 8.19 – Code architecture for coherent combination calculation with MIRO.

To strengthen our experimental results, numerical simulations were performed using the MIRO propagation code [53]. It solves the nonlinear Schr*ö*dinger equation and takes into account diffraction, optical Kerr effect, and material dispersion. The calculations are performed with the mode 'Broad spectrum' as pulses are not significantly stretched. In order to take into account differential dispersion, two independent and identical laser sources are defined. 1 mJ, 30 fs, 45°-polarized pulses are simulated. The beam diameter and the central wavelength are adjusted so that the nonlinear medium output spectrum is similar to the experimental one. The two light sources are followed each by a dividing birefringent plate which creates two orthogonally polarized replicas. Each line includes a polarizer to select a replica: the S-polarized replica in line 1 and the P-polarized replica in line 2. Then, the nonlinear medium is simulated with a 1 m-long bulk material featuring an index similar to the Neon one at a pressure of 2 bars ($n_2 = 15.10^{-25}$ m^2/m). Miro does not allow wave guide simulation. As Fresnel diffraction is taken into account in the 'Broad spectrum' mode and the nonlinear medium is quite long, the calculations are performed in only one dimension, meaning that the transverse spatial dependance is not taken into account. This makes sens as, in our setup, both replicas propagate through the same optical path and have thus similar spatial properties. Then, differential dispersion is simulated thanks to a plate located in only one of the lines. Its Group Velocity Dispersion (GVD) is adjusted to match the differential GDD of the considered combining plate. Finally, its thickness is adjusted to the aimed dispersion. For instance, a differential dispersion of 10 fs^2 corresponds to a plate thickness of 167 µm and a group velocity of 3.10^{-26} s^2/m. In Miro, the chirp $\phi^{(2)}$ introduced by a plate with a thickness e is indeed defined according to:

$$\phi^{(2)} = 2 \times e \times \text{GVD} \tag{8.28}$$

It should be noticed that Miro calculates dispersion at the specified central wavelength, that is fixed here to match the fiber output experimental spectra. Finally, a mixer gathers the replicas in the combining plate, which is identical to the dividing plate. A polarizer discriminates what is combined from what is not, exactly like in the experiment. The code architecture is illustrated on Fig. 8.19.

8.8   Experimental results with two replicas in the optimal conditions

First of all, we used the calcite pair (C1,C2) in the configuration I (Tab. 8.6). A half-wave plate turning the initial P-polarization at 45° is followed by the first calcite plate C1 (T≈97%) oriented at normal incidence ($\theta_1 = 0°$) with its ordinary axis oriented horizontally ($\alpha_1 = 90°$). The half-wave plate is adjusted so as to create two replicas with similar intensities. This adjustment is crucial since both pulses must undergo identical spectral broadening. A first rough tuning is achieved by minimizing the spectral broadening when gas is added into the fiber. A second more precise tuning consists in analyzing each replicas at the fiber output with a thin film Polarizer (TFP) and

making the two replicas spectra identical, slighlty orientating the half-wave plate iteratively with spectra recording. This tuning is essential as it influences directly the combining process. The accuracy on the orientation of the waveplate is $0.5°$, which corresponds to an intensity difference between the replicas of less than 3.5%. With α_2, the optical axis of the second crystal is adjusted parallel (perpendicular) to the polarization directions of the replicas, preventing further pulse division, which manifests itself by spectral modulations. With θ_2, the exact timing can be obtained. Finally, the polarization direction of the combined pulse is $45°$.
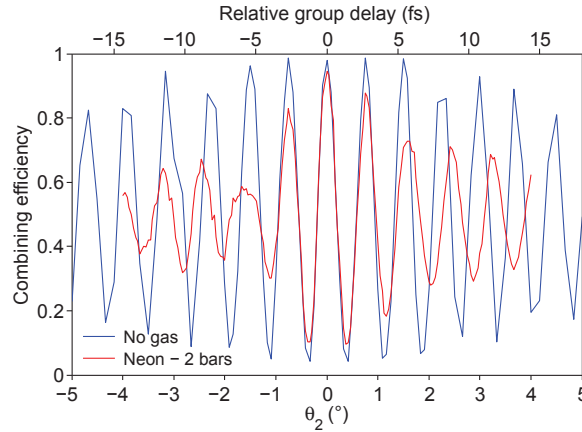
Figure 8.20 – Evolution of the combining efficiency as a function of θ_2 with (red) and without gas (blue).

The influence of the degree of freedom θ_2 was then investigated, by recording both the combining efficiency and combined pulse spectrum for many values of this parameter. This experimental protocol is named θscan. At this point, no gas is added in the fiber. The blue curve on Fig. 8.20 shows periodic constructive and destructive interferences between the two replicas, meaning that the combining process can be controlled with a high precision. The best combining efficiency is 98%, which corresponds to the nominal transmission of the TFP. The θ_2 value obtained for the best combining efficiency is very close to the auto-collimation position, as expected. The angular excursion is converted into relative group delay according to the previous calculations (Tab. 8.5), and the oscillation period is found to be $2.7\,fs$, that is the laser electric field period at $800\,nm$.

The Neon pressure influence inside the fiber is now explored, as illustrated on Fig. 8.21. The combined pulse spectrum broadens progressively with the increasing pressure (Fig. 8.21a). The systematic recording of the fringed spectra (Fig. 8.21b) shows that the increased nonlinear broadening of the pulse replicas inside the fiber does not affect their relative phase. Fig. 8.21c shows the combined pulse spectrum versus Neon pressure. It is clear that the spectral bandwidth of the fringed and combined spectra is similar, meaning that both replicas have very close spatio-temporal properties, what is crucial to achieve a high combining efficiency. Fig. 8.21a shows indeed that the combining efficiency stays above 90% for all pressures. The sudden recovery of efficiency at $1.75\,bar$ is due to the realignment of the setup with increasing gas pressure: when the gas pressure increases, the fiber might be slightly deviated so that the fiber output beam direction is changed. As a result, the combining efficiency can drop as the incidence angle on the plate is slightly different. At the optimum Neon pressure of $2\,bars$, a $166\,nm$ FWHM spectrum is obtained and the combining efficiency is 95%. The energy of the combined pulse is then $0.62\,mJ$ but could be even higher using a better AR-coating on the second calcite plate. The three main contributions to the overall losses are the inherent fiber transmission and coupling losses, the AR-coating of both plates, and the combination losses embedded in the overall transmission of the TFP. Note that the two last contributions are small compared to the first one.
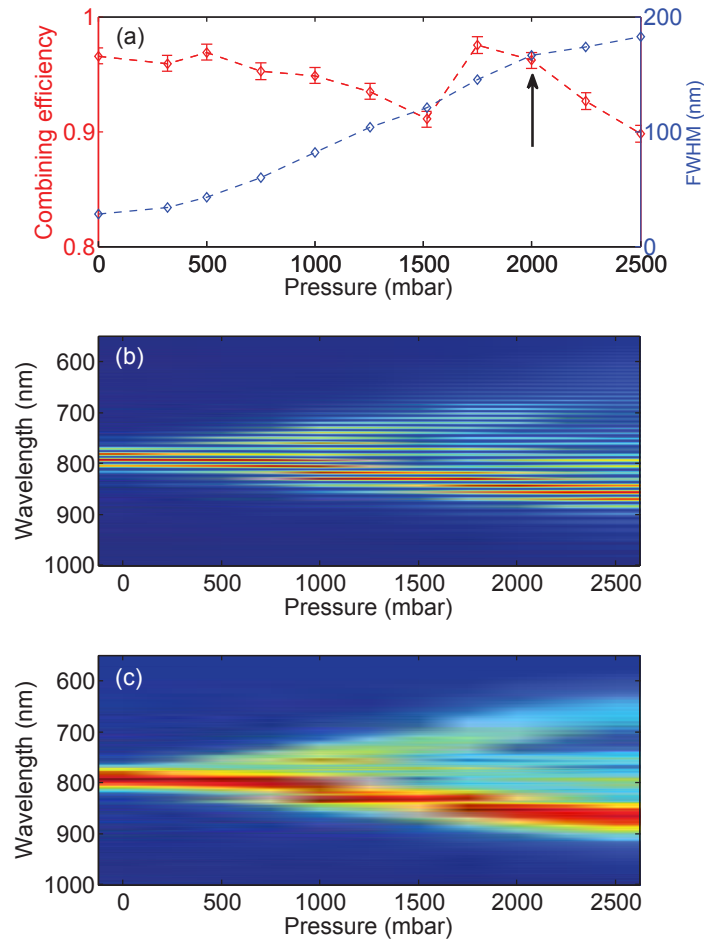
Figure 8.21 – (a) Evolution of the combining efficiency and spectral bandwidth of the combined pulse as a function of Ne pressure. The black arrow indicates to optimal regime. (b) Evolution of the fringed spectrum as a function of Ne pressure. (c) Evolution of the combined pulse spectrum as a function of Ne pressure.
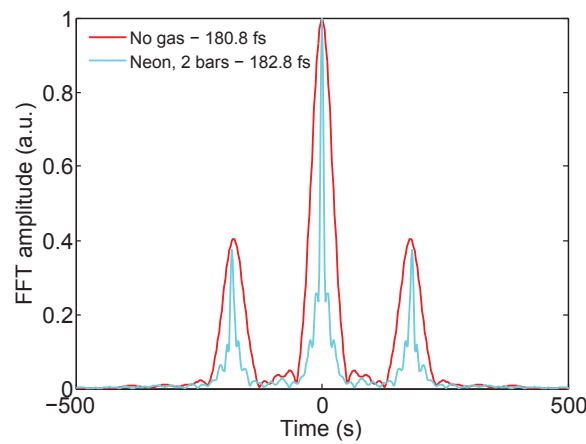
Figure 8.22 – Fourier transform of the fringed spectrum at the fiber output, with and without gas.

We can wonder if the delay between the replicas is shifted during the nonlinear process. This issue was investigating by recording the fringed spectrum at the fiber output with and without gas. Fig. 8.22 shows the Fourier transform of the fringed spectra. The relative group delay is almost not affected by the gas pressure, confirming that both replicas experience a similar index and that no ionization occurs.

We performed again a θscan, but this time at the optimum Neon pressure of 2 bars. The resulting combining efficiency curve is plotted in red on Fig. 8.20. The oscillation envelope is shorter than in the case of vacuum because of the much broader spectrum of the combined fields. The coherence time is indeed inversely proportional to the pulse spectral bandwidth and is not related to the chirp of the pulse. The oscillation period of the combining efficiency varies as the central wavelength of the pulse shifts due to the nonlinear spectral broadening process.
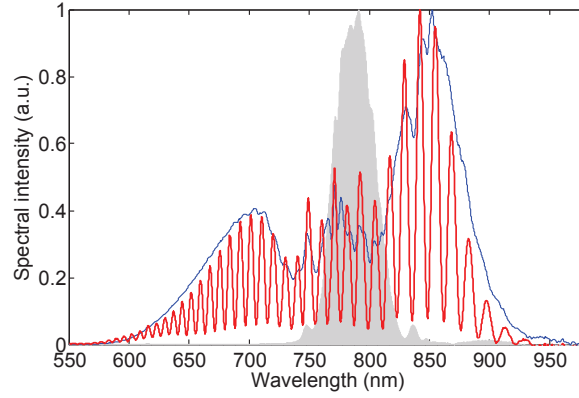
Figure 8.23 – Initial laser spectrum (shaded area). Combined pulse spectra (blue) and fringed spectrum (red) are registered for 2 bars Ne pressure.
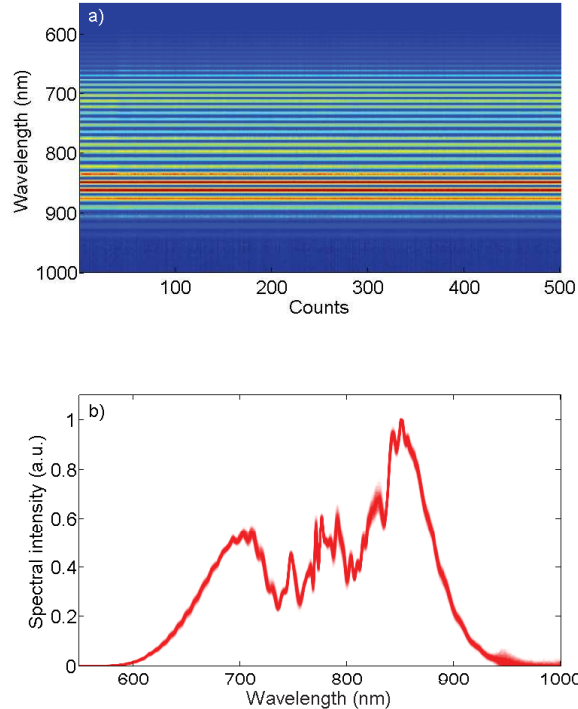
Figure 8.24 – Short-term stability study for a Neon pressure of 2 bars. a) 500 consecutive fringed spectra. b) 500 consecutive combined pulse spectra.

Fig. 8.23 shows the fringed spectrum together with the combined spectrum. The fringed spectrum is deeply contrasted over the whole bandwidth demonstrating that the two replicas undergo

similar nonlinear broadening in the fiber. A cumulative record of 500 consecutive combined spectra with 10 ms integration time demonstrates that the combining process in the calcite plate enables the phase-matching of the newly created wavelengths with a remarkable short-term stability (Fig. 8.24).
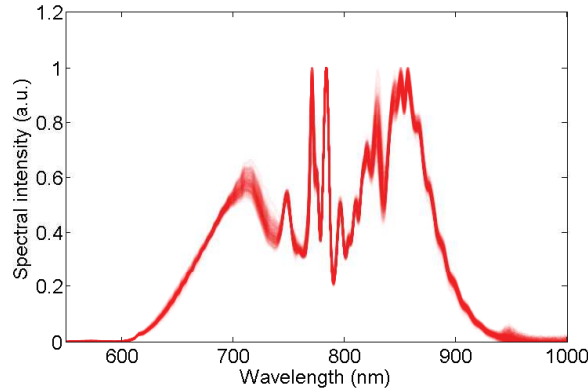
Figure 8.25 – Long-term stability record: 540 combined pulse spectra over more than 3 hours.

The long-term energy stability is then evaluated. 540 combined pulse spectra were recorded over more than 3 hours, always with 10 ms integration time. The results are shown on Fig. 8.25. The corresponding energy fluctuation of the combined pulse is 1.8 % RMS, which is directly related to the pump laser fluctuations inside the Femtopower.
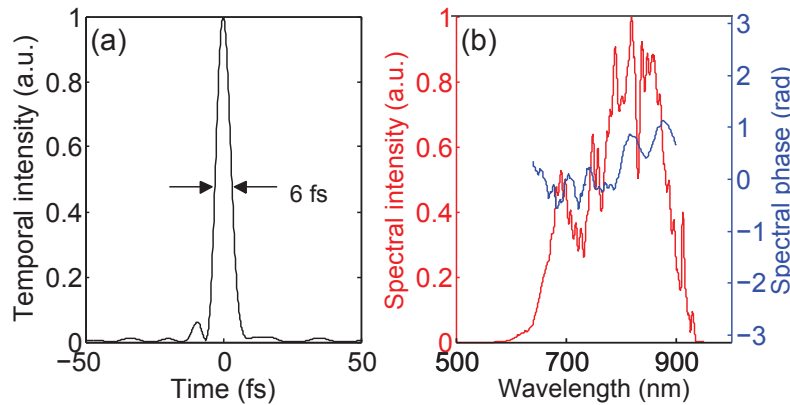
Figure 8.26 – Characterization of the combined pulse with a Wizzler-USP device: (a) temporal intensity and (b) spectral intensity and phase.

The compressed recombined pulse was temporally characterized with a Wizzler-USP measurement, as shown in Fig. 8.26. A 6 fs pulse was obtained for a Ne pressure of 2 bars. The spectral phase is globally flat with residual oscillations introduced by the chirped mirrors. The high dynamic range of the Wizzler-USP device allows the optimization of the temporal pulse shape by adjusting α_2. At the optimal α_2 value ($0°$), no pre-pulse at 178 fs is measured above 10^{-3} relative intensity (Fig. 8.27a), demonstrating the efficiency of the combining process. Away from this optimal value, the pre-pulse intensity increases. At 10^{-2} relative intensity, a weak residual modulation starts to become visible on the combined fringed spectrum (Fig. 8.27b).

Finally, it is necessary to confirm that the CEP stability of the combined pulse is preserved. The CEP was measured with a home-made f-to-2f interferometer interfaced with a spectrometer and analysis software from Menlo Systems. A 100 µm-thick BBO crystal was used. When performing CEP drift measurements with ultrashort pulses, no plate is needed for the continuum generation which is simultaneously generated with the second harmonic inside the BBO crystal. However, the CEP fringes are reachable towards 500 nm, meaning that the fundamental spectrum
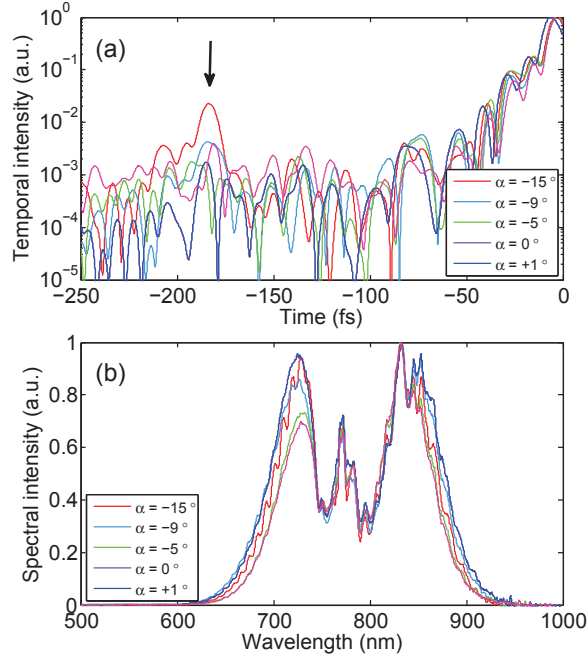
Figure 8.27 – Wizzler measurement of the combined pulse for various α_2 values: (a) temporal intensity profile (logarithmic scale), (b) corresponding spectra.
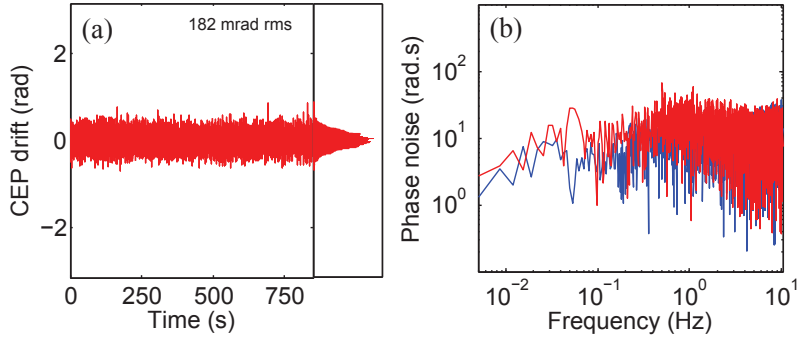
Figure 8.28 – (a) Relative CEP drift of the combined pulse after temporal post-compression with slow feedback on the stretcher. (b) Fourier analysis of the CEP noise registered for post-compressed single pulse (blue, 145 mrad RMS) and two combined replicas (red, 182 mrad RMS).

bandwidth upper limit must exceed 1000 nm. It can be thus helpful to use a sapphire plate ahead the BBO crystal to broaden the fundamental spectrum. The feedback drives the bulk stretcher mounted on a motorized translation stage inside the FemtoPower. The CEP noise of the 6 fs pulse was found about 180 mrad RMS for an integration time of 1 ms and a slow feedback period of 48 ms (Fig. 8.28a), which is comparable to that of the input pulses from the amplifier. Moreover, we measured the CEP of a single pulse propagating through the fiber and exhibiting the same broadened spectrum (Fig. 8.28b). Given the intrinsic noise of the f-to-2f device, the CEP drifts are of the same order of magnitude in both configurations, confirming that no measurable CEP noise is introduced by the recombination process.

The two additional pair of plates (C3-C4 and C5-C6) were also validated in the same experimental conditions. The results are summarized in Tab. 8.7. It was confirmed that an adequate tilt of the combining plate enables to compensate for the thickness difference between the two plates and to get a high combining efficiency. For the pair C5-C6, the overall efficiency is slightly lower (92%). This is explained by the longer group delay associated with a higher GDD difference ($19 \, \text{fs}^2$) between the two polarization components in the combining plate. As explained in the

next section, this limits the combined pulse spectral bandwidth and might affect to some extent the combined pulse energy.
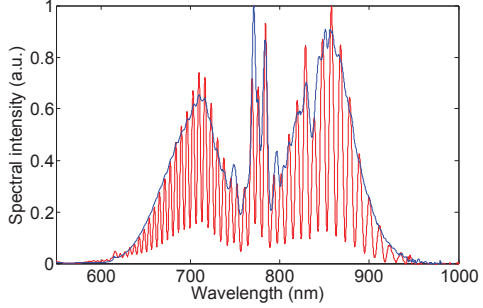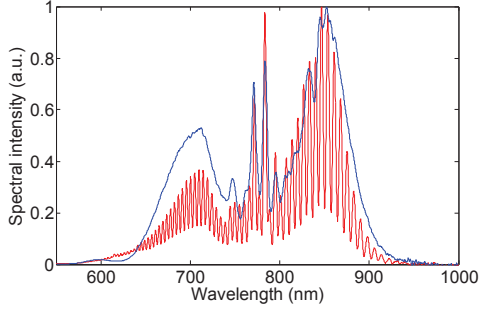
Pair of plates	Implementation	Combining efficiency	Fringed and combined spectra
C3-C4	II	95 %	
C5-C6	III	92 %	

Table 8.7 – Coherent combining of two replicas with two different pair of plates. The input energy is 1 mJ, the Neon pressure is 2 bars. The experimental implementation illustrated in Tab. 8.6 is indicated.

Conclusion on the experiments performed with two replicas in the optimal conditions

To conclude this part, we demonstrated for the first time the coherent combining of two replicas in the few-cycle regime. The proposed setup is not only simple as it requires no active feedback, but also very robust. The final combined pulses exhibit an excellent spectral and energy stability, and also a high temporal quality. Finally, it was confirmed that implementing optical multiplexing in a HCF compressor does not degrade the CEP stability of the final pulse. These results make this technique very promising for the post-compression of highly intense pulses as it meets the requirements of a demanding application like attosecond generation on solid target in terms of contrast, pulse duration and CEP stability. To go further, the limitations of the technique are explored more deeply to control the combination process with high fidelity. In the further experiments, the pulse energy and gas pressure were adapted to achieve similar spectral broadening at the HCF output (Fig. 8.23).

8.9 Measurement of the residual relative phase

To explore the setup limitations and optimize the process efficiency and fidelity, one needs a diagnostic to measure the residual phase between the replicas.

The θscan method

An elegant tool consists in analyzing the dependance of the combined pulse energy and spectrum as a function of θ, the combining plate tilt. The corresponding registered signal is given by:

$$I(\omega, \theta) = I_1(\omega) + I_2(\omega) + 2\sqrt{I_1(\omega)I_2(\omega)} \cos(\Delta\Phi(\omega, \theta) + \omega\tau) \tag{8.29}$$

where τ is the delay between the electric fields and $\Delta\Phi(\omega, \theta)$ their relative spectral phase. When tilting the combining plate, the delay is linearly tuned between the two electric fields and periodic constructive and destructive interferences can be thus observed. These data can be then Fourier-analyzed following methods used for pulse characterization relying on spectral interferometry [146, 147]. It gives access to the eventual phase-mismatch for each wavelength of the two electric fields, collected during the propagation in the HCF as well as in the combining plate itself. In a first approach, this method was applied to the measurement of the differential GDD introduced by the combining plate. Note that we are talking about measuring phase of the order of $10\,\text{fs}^2$, which is too low to be measured by a standard phase measurement device.

Application of the θscan method to the differential GDD determination - Simulations
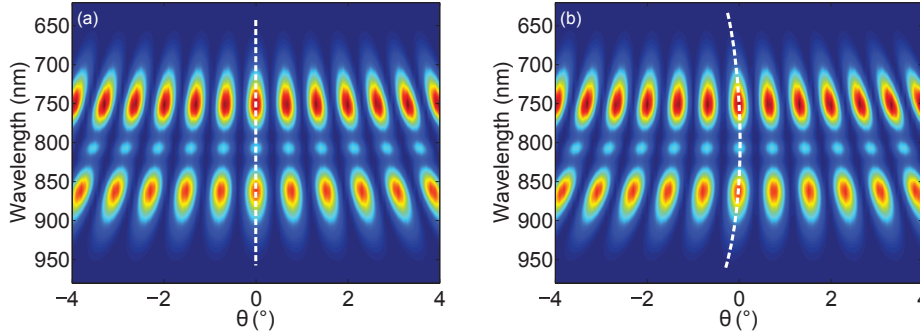
Figure 8.29 – MIRO simulation of the combined pulse spectral evolution with θ. θ = 0° corresponds to the maximum combining efficiency. (a) No differential GDD is taken into account. (b) $\Delta\Phi^{(2)}$ of the combining plate is set to $10\,\text{fs}^2$.

MIRO simulations were first performed with the code described in Fig. 8.19. The spectral bandwidth at the output of the nonlinear stage corresponds to an FT-limited 6 fs pulse. Two cases were considered for beam combining: (a) the two replicas undergo the same linear dispersion in the combining plate ($37\,\text{fs}^2$) and (b) a GDD difference of $10\,\text{fs}^2$ is applied between the two replicas. The combined pulse spectrum is then recorded as a function of θ in the range [-4°; +4°], as shown in Fig. 8.29. θ = 0° corresponds to the maximum combining efficiency. As expected, the interferogram shows regular combining of the two light fields, with a frequency-dependent periodicity. In case (a), the optimum θ = 0° value enables phase matching of all the newly created wavelengths. In case (b), around this optimal value, the exact delay differs at extreme wavelengths. This spectral curvature, underlined with a white dashed line in the figure, is the residual relative phase between the replicas due to the combining plate. Assuming that $\Delta\Phi$ is purely quadratic, the frequency dependence of the maximum energy around θ = 0° can be fitted with the following equation:

$$\frac{\Delta\Phi^{(2)}}{2}(\omega - \omega_0)^2 + \omega\tau = 0 \qquad (8.30)$$

In this theoretical case, the method enables to accurately recover $\Delta\Phi^{(2)}$.

Otherwise, the θscan method highlights that the maximum spectral bandwidth won't be obtained for the same incident angle than the maximum combining efficiency because of differential GDD. The spectral widths of the data shown on Fig. 8.29 can be calculated according to Eq. 7.2 and Eq. 7.3. When the differential GDD is not taken into account (Fig. 8.30a), the spectral bandwidth of the combined pulse is almost constant on the theta range where the maximum efficiency is reached. This is not the case when a differential GDD of $10\,\text{fs}^2$ is applied (Fig. 8.30b): tuning θ maximizes either the spectral bandwidth, either the efficiency. There is a gap of 1 fs between the maximum spectral bandwidth (θ ≈ −0,255°) and the spectral bandwidth achieved when the efficiency is maximal (θ = 0°). A compromise can be found between these two criteria. In all experiments presented here, we optimized the combining efficiency.
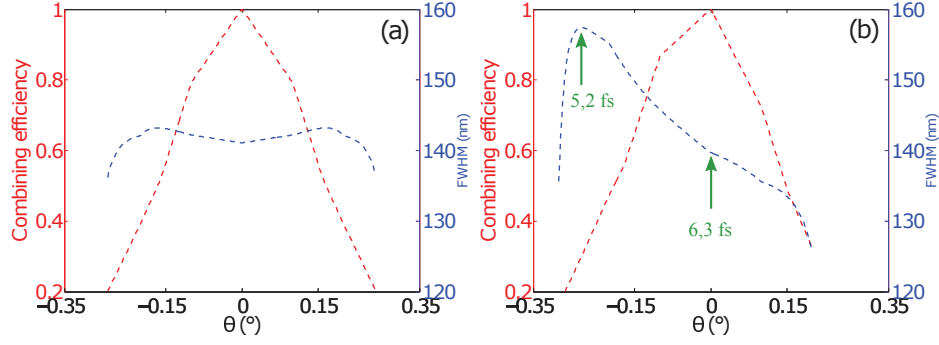
Figure 8.30 – MIRO simulation - Combining efficiency and spectral bandwidth (FWHM) of the combined pulse in two cases: (a) No differential GDD is taken into account. (b) $\Delta\Phi^{(2)}$ of the combining plate is set to $10\,\text{fs}^2$.

Application of the θscan method to the differential GDD determination - Experiments
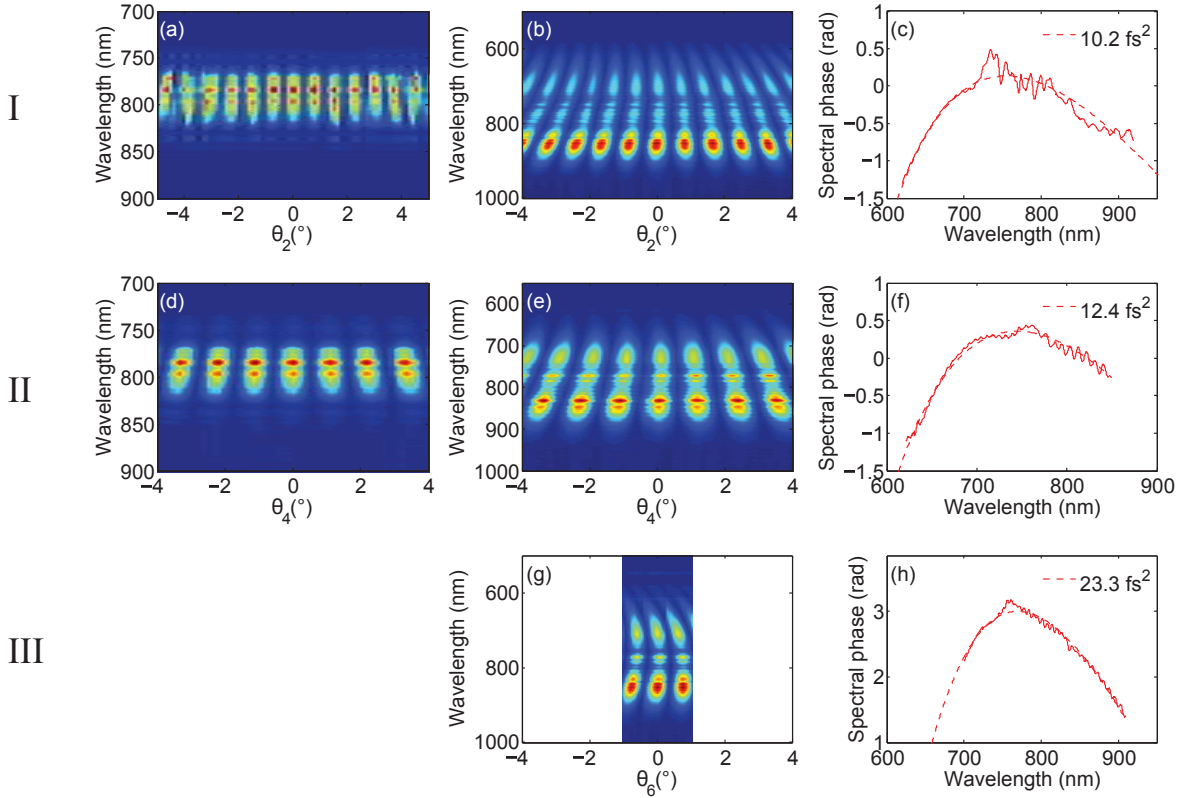
Figure 8.31 – (a,d) θscan with plates C2 (a) and C4 (d) without gas. (b,e,g) θscan with plates C2 (b), C4 (e) and C6 (g) with Neon. Gas pressure and input energy in HCF are respectively 2 bars-0.96 mJ, 1.6 bar-1.06 mJ and 1.6 bar-1.1 mJ. (c,f,h) Relative spectral phase deduced from the Fourier analysis of the interferogram. A second-order fit is indicated (dashed line). Roman numerals I, II and III indicate the corresponding experimental implementations (see Tab 8.6).

The corresponding experiments were then performed with and without gas for each combining plate (C2, C4 and C6) implemented according to the configurations I, II and III described in Tab. 8.6. We tried to achieve a similar spectral broadening in each case. The results are shown on Fig. 8.31. The θscan map are weighted with the factor Γ defined by:

$$\Gamma(\theta) = \frac{\eta(\theta)}{\int I(\lambda,\theta)d\lambda} \tag{8.31}$$

The combining efficiency η is indeed measured on the whole spectral bandwidth. Each wavelength of the interferogram must be thus weighted by an effective efficiency defined by Γ. When the fiber is under vacuum (Fig. 8.31(a,d)), the θscan maps exhibit straight lobes, meaning that all wavelengths are phase-matched in the combining plate. Otherwise, Fig. 8.31(a,d) illustrate the tunability difference between C2 and C4, as these two plates have a different crystallographic orientation (the lobe period is not the same). When gas is added in the fiber and spectral broadening occurs, the lobes curvature is the signature of a relative residual phase between the replicas. A Fourier analysis of the data enables to extract this residual relative phase in the case of each combining plate. If the differential GDD is assumed to be the only source of phase-mismatch between the wavelengths, it is possible to fit the extracted phase with a second order phase and deduce thus the value of the differential GDD according to Eq. 8.30. The results are summarized in Tab. 8.8 and compared to the theoretical values calculated at 800 nm for the combining plates at normal incidence. A good agreement is found between experiments and calculations for all plates, demonstrating that there is no other significant phase mismatch source between the replicas than differential GDD in the considered experimental conditions. Note that the phase recovered in the case of the plate C6 is only between 700 and 910 nm because of an experimental protocol error which added another contribution to that of differential GDD. The gap between experiment and theory is indeed higher for C6 than C2 or C4. Fitting the phase (C6) between 750 and 910 nm gives a differential GDD value of 19.8 fs^2.

Plate	$\Delta\Phi^{(2)}_{exp,\mathrm{TF}}$ (fs^2)	$\Delta\Phi^{(2)}_{th}$ (fs^2)
C2	10.2 ± 0.5	10.4
C4	12.4 ± 0.5	12.4
C6	23.3 ± 0.5	19.5

Table 8.8 – Differential GDD of the combining plates. Comparison between theory (800 nm, normal incidence) and values extracted from the θscan maps with a Fourier analysis.

There is another method to extract the residual relative phase from the interferogram: fitting the curvature around the optimum θ_2 value (which is 0°) yields a similar result. To do so, I first isolated the central lobe before calculating for each wavelength the gravity center of the considered lobe. The resulting residual phase can be then fitted with Eq. 8.30. The result is shown on Fig. 8.32 in the case of C2. The differential GDD is found to be 11 ± 0.5 fs^2, which is very close to the value obtained with a Fourier analysis.

Conclusion on the proposed θscan method for residual relative phase measurement

To conclude, an *in situ* technique was developed to recover accurately the value of $\Delta\Phi^{(2)}$, although quite low. More generally, this technique enables to extract the residual relative phase between the replicas and thus to quantify the phase mismatching issues that impact the combining process, as shown in the following section.
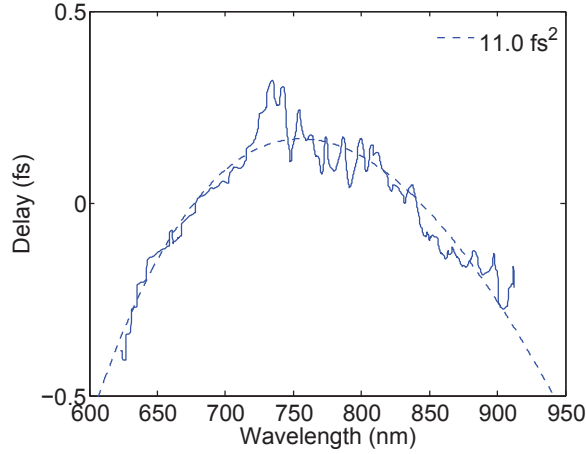
Figure 8.32 – Relative spectral phase deduced from the fit of the interferogram central lobe in the case of the experimental setup II (see Tab. 8.6). A second-order fit is indicated (dashed line).

8.10 Optimizing the process efficiency and the temporal fidelity of the combined pulse

Many phenomena can affect the final pulse quality and stability. First, the polarization quality of the replicas is of prime importance, requiring careful adjustment of the Dividing Setup and steering mirrors to couple the beam into the fiber. Second, in the Combining Setup, the differential GDD experienced by the replicas in the combining plate(s) limits the spectral bandwidth of the final pulse. Third, the nonlinear medium itself affects the combining process: spectral phase mismatching between the replicas can originate from gas ionization, or XPM between the replicas if the delay is too short. Finally, it is demonstrated how the finite coherent contrast of the laser causes crossed interactions between the replicas and the other replicas pedestals, strongly affecting the temporal quality of the final pulse. A method is proposed to minimize the deleterious effects of these interactions.

8.10.1 Polarization changes due to the mirrors before the fiber

In this section, the role of a polarization change occurring before the nonlinear process is highlighted. Indeed, the experimental arrangement described here has some constraints: the Dividing Setup must be inserted in the collimated beam and the incidence angle on the focusing optics has to be as small as possible to ensure efficient coupling in the fiber. As a consequence, once the replicas have been created, two 45° silver-coated mirrors are needed to seed the HCF (see Fig. 8.18). If the polarization orientations of the replicas are not exactly S and P, some modifications of the polarization states will occur, making their polarizations elliptical [144]. As a consequence, polarization rotation occurs during the nonlinear process [148]. In the following, the term depolarization is used to refer to the polarization changes undergone before the fiber.

A single linearly polarized pulse (one replica R1) with a polarization different from S or P is first considered. The angle α_{INI} defines its polarization orientation relative to P. Some silver-coated mirrors deteriorate the pulse polarization which becomes elliptical, as illustrated in Fig. 8.33(a). φ is defined as the phase-shift between the two P and S polarization components.

The orientation of the elliptical polarization after these silver mirrors (and before the fiber) is α_{SM}, defined according to:

$$\tan 2\alpha_{\mathrm{SM}} = \tan 2\alpha_{\mathrm{INI}} \cdot \cos\varphi \qquad (8.32)$$

α_{HCF} is defined as the elliptical polarization orientation after the fiber. The rotation angle experienced by the elliptical polarization after propagation through a nonlinear medium is given by:

a)   b)
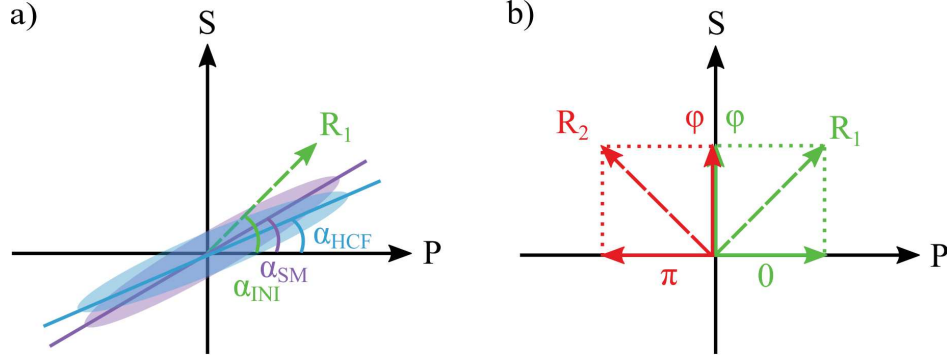
Figure 8.33 – a) Scheme of the polarization of one replica R1 before the silver mirrors (green), after the silver mirrors (purple) and after the fiber (blue). b) Schemes of the polarizations states of two replicas R1 and R2 with their S and P-polarized components. The phase of each component is indicated, relative to the P-polarized component of R1.

$$\Delta\alpha = \alpha_{\mathrm{HCF}} - \alpha_{\mathrm{SM}} \tag{8.33}$$

The electric field can be decomposed into a linear combination of left- and right-circular components or into two linear polarization components as:

$$\mathbf{E} = E_+\sigma_+ + E_-\sigma_- = E_x\mathbf{x} + E_y\mathbf{y} = E_{0x}\mathbf{x} + E_{0y}\exp(i\varphi)\mathbf{y} \tag{8.34}$$

where E_x and E_y are parallel to the S and P polarization directions. The circular-polarization vectors are defined by:

$$\sigma_\pm = \frac{\mathbf{x} \pm i\,\mathbf{y}}{\sqrt{2}} \tag{8.35}$$

According to [148], the rotation angle experienced by the electric field after propagation through a nonlinear medium is given by:

$$\Delta\alpha = \alpha_{\mathrm{HCF}} - \alpha_{\mathrm{SM}} = \frac{1}{2}\Delta n\,\frac{\omega}{c}\,z \tag{8.36}$$

where ω is the pulse angular frequency, z the length of the nonlinear medium, c the light velocity and Δn the difference between the refractive indices experienced by the left- and right-circular components σ_+ and σ_- of the laser beam:

$$\Delta n = n_+ - n_- = \frac{B}{2\,n_0}\left[\,|E_-|^2 - |E_+|^2\,\right] \tag{8.37}$$

$$\Delta n = \frac{B}{2\,n_0}\left[-2\,E_{0x}E_{0y}\sin\varphi\right] \tag{8.38}$$

E_{0x} and E_{0y} are the amplitude of the electric field components so that $E_{0y} = E_{0x}\tan\alpha_{\mathrm{INI}}$. n_0 is the linear index of the medium and B is given by :

$$B = 2\chi^{(3)} = \frac{8}{3}\,n_0^2\,\epsilon_0\,c\,n_2 \tag{8.39}$$

where n_2 is the Kerr index of the medium and ϵ_0 its dielectric constant. The pulse intensity is defined by:

$$I = 2\,c\,\epsilon_0\,n_0\,E_{0x}^2\left(1 + \tan^2\alpha_{\mathrm{INI}}\right) \tag{8.40}$$

Finally:

$$\boxed{\Delta\alpha = \frac{2}{3}\,n_2\,I\,\frac{\tan\alpha_{\mathrm{INI}}}{\left(1 + \tan^2\alpha_{\mathrm{INI}}\right)}\,\frac{\omega}{c}\,z\,\sin\varphi} \tag{8.41}$$

The major axis of the incident elliptical polarization is turned by $\Delta\alpha$ after propagation through the nonlinear medium. The rotation angle can also be expressed according to the ellipticity β:

$$\Delta\alpha = \frac{2}{3} n_2 I \frac{\tan\beta}{\left(1 + \tan^2\beta\right)} \frac{\omega}{c} z \tag{8.42}$$

where $\tan\beta$ is the ratio of the minor to the major axis of the ellipse described by the electric field of the replica.

Two orthogonally polarized replicas (R1, R2) are now considered. They propagate through the fiber and experience polarization rotation. The projection of each replica polarization and their relative phase-shift are illustrated in Fig. 8.33b. The P components of the replicas are phase-shifted by π, meaning that $\Delta\alpha$ will be positive for one replica and negative for the other one. As a consequence, the replicas will not be orthogonally polarized anymore at the fiber output. Finally, the angle between their polarization directions is $90° \pm 2\Delta\alpha$.

This issue was experimentally highlighted. Indeed, the experimental value of φ was determined measuring the polarization rotation of a single pulse propagating through the fiber. To do so, the pulse polarization orientation at the fiber output, α_{HCF}, was recorded as a function of the incident linear polarization orientation, α_{INI}, for various Neon pressures. The incident energy was limited to $700\,\mu J$ to be safe from ionization or higher-order nonlinearities. A half-waveplate sets the incident polarization and the two $45°$ mirrors ensuring beam coupling in the HCF deteriorate the initially linear polarization. A Thin Film Polarizer (TFP) and a spectrometer were used to accurately measure the beam extinction at the HCF output and thus determine the pulse polarization direction after the nonlinear medium. The results are shown on Fig. 8.34.
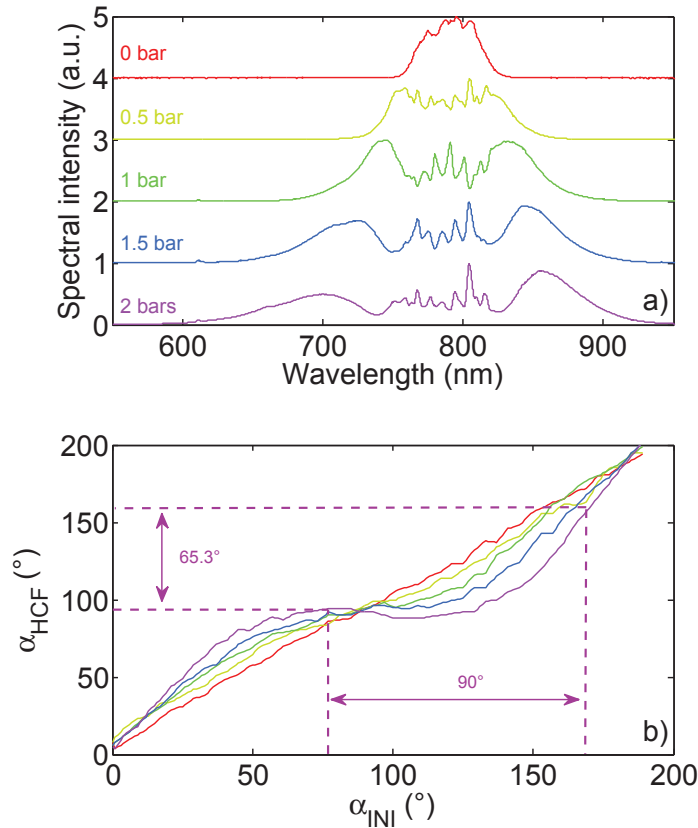
Figure 8.34 – (a) Evolution of the spectrum out of the hollow-fiber as a function of gas pressure. (b) Evolution of output versus input polarization direction with respect to gas pressure. Colors refer to gas pressure, as indicated in a). Polarizations P and S corresponds respectively to $0°$ and $90°$.

The curves show that an incident polarization different from P ($\alpha_{INI} = 0°$) or S ($\alpha_{INI} = 90°$) will be rotated during the nonlinear process, especially when the nonlinear index is high. Fitting the

curves with Eq. 8.32 and Eq. 8.41, φ is found to be equal to 0.2 rad. This phase-shift value is related to the two 45° silver coated mirrors ensuring beam coupling in the fiber.

Now φ is known, $\Delta\alpha$ can precisely calculated for each replica, using Eq. 8.41. As an example, if $\alpha_{INI} = 3°$, $2\Delta\alpha = 5°$ so that the angle between the two replicas polarizations is 85° or 95° according to the sign of φ. The phenomenon is illustrated in Fig. 8.34b. These two non orthogonally polarized replicas will not be fully recombined in the combining plate, resulting in the formation of pre or post pulses according to the orientation of the plate. The intensity of the pre or post pulse can be evaluated thanks to $\frac{1}{2}\sin^2(2\Delta\alpha)$, the $\frac{1}{2}$ factor corresponding to the polarization direction of the combined pulse (45°). In this example, the intensity ratio between the created parasitic pulse and the combined pulse is about 0.4 %. The temporal quality of the combined pulse will be thus highly affected by depolarization effects occurring prior to the fiber. In the spectral domain, these effects are translated into spectrum modulations. Therefore, the tuning of the axis orientation of the last plate of the Dividing Setup, α_B, is crucial as it adjusts the polarization orientations of the replicas parallel to S and P before the fiber. A bad adjustment of α_B results in the creation of pre or post pulses during the combining process. If we consider that the pre or post pulse energy should not exceed 0.01 % to preserve the initial laser contrast, the corresponding α_B absolute precision should be 0.5°.

This study can be generalized calculating the maximum ellipticity β_{max} to achieve a final coherent contrast of 10^{-N}. As explained above, the intensity of the pre- or post-pulses surrounding the combined pulse is given by:

$$\frac{1}{2}\sin^2(2\Delta\alpha) = 10^{-N} \tag{8.43}$$

Assuming that β and $\Delta\alpha$ are small:

$$1 + \tan^2\beta \approx 1 \tag{8.44}$$

$$\frac{1}{2}\sin^2(2\Delta\alpha) \approx 2\Delta\alpha^2 \tag{8.45}$$

The maximum ellipticity β_{max} to achieve a final coherent contrast of 10^{-N} can be deduced using Eq. 8.42:

$$\boxed{\tan\beta_{max} = \frac{3\sqrt{2}}{4}\frac{1}{\Phi_{NL}}10^{-N/2}} \tag{8.46}$$

$\Phi_{NL} = n_2\,I\,\omega\,z/c$ is the nonlinear phase accumulated in the fiber. For instance, an aimed coherent contrast of 10^{-4} implies that the ellipticity prior to the fiber is lower than 2.10^{-3} for a nonlinear phase of 6 rad.

Conclusion on the depolarization effects

To conclude, the quality of the linear polarizations at the fiber entrance is crucial to maintain the replicas polarizations orthogonal prior to the Combining Setup. We established the maximum tolerable ellipticity at the fiber entrance to achieve a given final coherent contrast. In practice, the number of mirrors between the last plate of the Dividing Setup and the entrance of the fiber should be minimal. The axis orientation of the last plate of the Dividing Setup, α_B, must be finely adjusted to make the polarization orientations of the replicas parallel to S and P before the fiber.

8.10.2 Differential GDD in the Combining Setup

In the combining plate, the GDD difference might not allow phase matching of all the newly created wavelengths. To highlight this phenomenon, four plates were used to create two replicas delayed by 424 fs (see Tab. 8.6-IV). The two sub-pulses suffer from the GDD difference in both plates C4 and C2. The calculated value is 24.9 fs^2 taking into account the tilt of 10° of the plate C4.
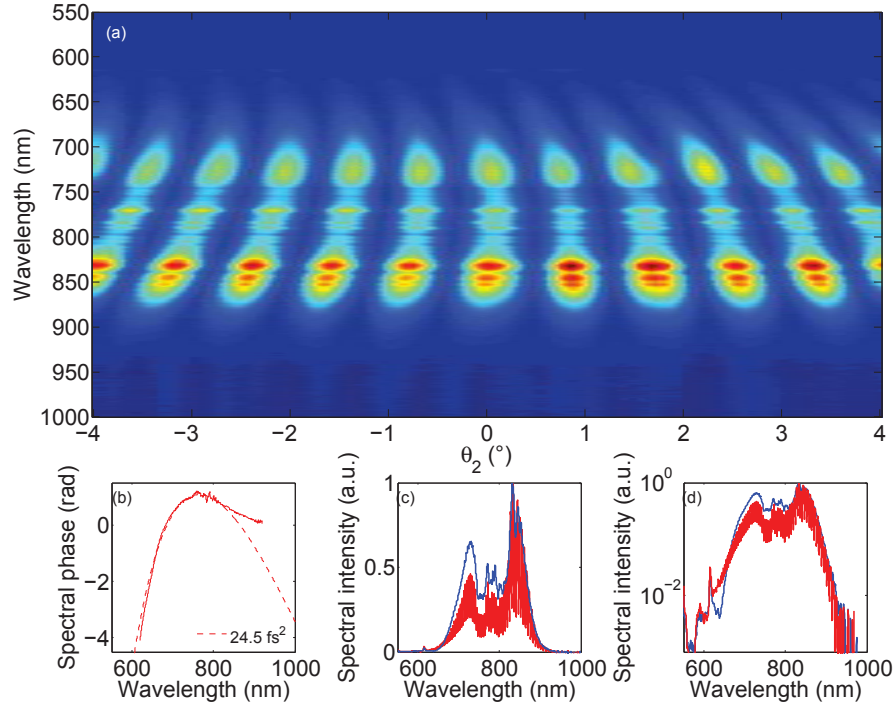
Figure 8.35 – Analysis of the experimental case IV for a gas pressure of 1.7 bar and an input energy of 1.1 mJ. The maximum combining efficiency is 94 %. (a) Spectral dependence of the combined pulse as a function of θ_2. $\theta_2 = 0°$ corresponds to the maximum combining efficiency. (b) Relative spectral phase deduced from the Fourier analysis of the interferogram. A second-order fit is indicated (dashed line). (c,d) Combined pulse (blue) and fringed (red) spectra measured for $\theta_2 = 0°$, in linear (c) and log (d) scale.

The input pulse energy is 1.1 mJ and the Neon pressure is fixed to 1.7 bar in order to get the same spectral bandwidth out of the nonlinear stage than in the case described in section 8.8. Effective combination is achieved in C2 through θ_2. Results are shown in Fig. 8.35. The visible stronger curvature is confirmed by the Fourier analysis, retrieving a second-order relative GDD of 24.5+/-0.5 fs^2. In this case, the larger GDD difference limits the spectral bandwidth of the combined pulse, slightly narrower than the fringed spectrum, as shown in Fig. 8.35(b,c).
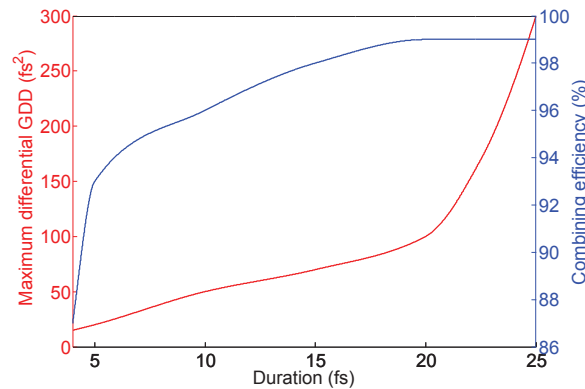
Figure 8.36 – $\Delta\phi^{(2)}$ of the combining plate leading to a 10% increase of the desired combined pulse duration (red). The corresponding combining efficiencies are given (blue). The calculations were performed with MIRO.

It is possible to define a critical value of differential GDD above which the effective combined pulse duration is 10 % higher than for $\Delta\phi^{(2)} = 0\,fs^2$. The dependence of this quantity with respect

to the desired output duration has been calculated using MIRO. The propagation code architecture was explained in section 8.7. The beam diameter and the central wavelength are adjusted respectively to 50 µm and 740 nm so that the nonlinear medium output spectrum is similar to the experimental one. The dividing birefringent plate creates two replicas delayed by 190 fs. Differential dispersion is simulated by adjusting the Group Velocity Dispersion (GVD) and the thickness of the combining plate.

The aimed FT-limited duration of the pulses at the fiber output is adjusted via the input energy. For each FT-limited duration, the combined pulse spectrum is shortened to increase the corresponding FT-limited duration of 10 %, playing with the plate thickness simulating differential dispersion. The final dispersion introduced by this plate is recorded for each aimed FT-limited duration. I should mention that the combining plate is at normal incidence so that no optimization of the combining process is performed.

The results are shown on Fig. 8.36 and underline that the differential GDD should be lower than 20 fs^2 for an intended 5 fs pulse. For such a pulse duration, the combining efficiency is about 93 %. 10 fs pulses will be achieved if the differential GDD is lower than 50 fs^2. These results show how carrying out coherent combining in the few-cycle regime is very constraining. Limiting differential dispersion means limiting the birefringent plates thickness and so the delay inter-replicas. A too short delay can induce nonlinear interactions between the replicas, as demonstrated in the following. The trade-off between these two parameters has to be determined for each experimental configuration.
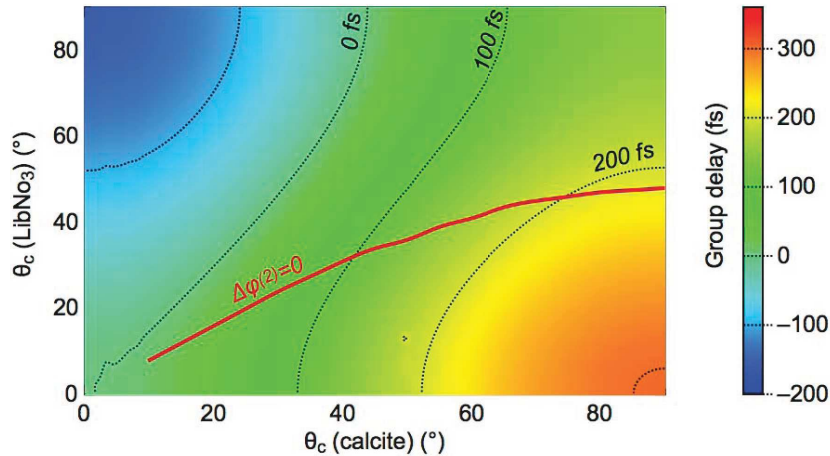
Figure 8.37 – Calculated group delay introduced by one 0.5 mm calcite and one 0.5 mm LiNbO$_3$ plates orientated with crossed-axis according to their crystallographic orientation. The red line indicates the combinations leading to $\Delta\phi^{(2)}$=0. LiNbO$_3$ index values are taken from [149].

Another solution consists in using compensation plates to counterbalance the GDD difference with little change of the group delay [142]. To do so, LiNbO$_3$ can be used together with calcite, in a configuration similar to IV, with C3 and C4 replaced by LiNbO$_3$. Feasibility is emphasized by calculating the group delay and $\Delta\Phi^{(2)}$ introduced by one calcite and one LiNbO$_3$ plates, placed at normal incidence, according to the crystallographic orientation of both plates (θ_c). The samples thickness is fixed to 0.5 mm, as thinner pieces are hardly achievable and thicker ones would lead to higher overall GDD. The group delay map is shown in Fig. 8.37. Solutions leading to a compensated GDD difference between the two polarizations are lined out in the same figure. However, such a scheme rises the number of plates, therefore increases the overall GDD that needs to be compensated for compression (250 fs^2 in that example).

Conclusion on the differential GDD study

The differential GDD experienced by the replicas in the combining plate(s) constrains the generation of ultra-short pulses. The associated borderline calculations were expounded. To overcome

this limitation, a solution is proposed and consists in using compensation plates with specific crystallographic orientation.

8.10.3 Ionization

Ionization is usually considered to be issue in a high-energy HCF post-compressor, generating uncompensated phase, instabilities and lower transmission because of excitation of high-order modes [105, 111]. The methods previously cited and demonstrated for post-compression of high-energy pulses all tend to decrease the influence of ionization to preserve the fidelity of the generated few-cycle pulses. This paragraph aims to underline the manifestations of ionization and to explain how that affects the combining process.

Figure 8.38 – Analysis of the experimental case II for a gas pressure of 2.6 bars and an input energy of 1.2 mJ. The maximum combining efficiency is 88 %. (a) Spectral dependence of the combined pulse as a function of θ_4. $\theta_4 = 0°$ corresponds to the maximum combining efficiency. (b) Combined pulse (blue) and fringed (red) spectra measured for $\theta_4 = 0°$. (c) Relative spectral phase deduced from the Fourier analysis of the interferogram.

When gas ionization occurs, the free electron density rapidly changes on the leading edge of the ionizing pulse, thus generating a fast temporal modification of the index of the medium. The associated temporal phase creates new frequencies on the blue side of the spectrum [99, 98]. Meanwhile, the group velocity is slightly decreased and the spatial modification of the index induces plasma defocusing. Coupled to SPM during propagation, ionization triggers a complex spatio-temporal dynamics of the fundamental and higher-order fiber propagation modes, which degrades the output pulse quality.

Increasing the gas pressure as done in the experiment might naturally raise the free electron density, but essentially strengthen the Kerr nonlinearities (SPM and self-focusing). Higher intensity then leads to higher ionization rates followed by plasma defocusing. The plasma lifetime is then on the ns timescale. The second sub-pulse thus propagates through an already ionized medium and the balance between nonlinearities (self-focusing and defocusing) might be strongly different than for the first pulse. This behavior cannot be easily predicted as calculations require in that case an accurate 3D propagation code. However, we expect a phase mismatch between the

replicas, most likely to the blue side of the spectrum as it is the most impacted by ionization.

Case II was then implemented with an input energy of 1.2 mJ. To drive the onset of ionization, the Neon pressure was increased to 2.6 bars. The combining efficiency then drops to 88 %. A phase mismatch between the replicas is experimentally visible in the fringed spectrum by Fourier analysis, and in the combined pulse spectrum (combining of the blue wavelengths is limited, see Fig. 8.38(b)).

The interferogram registered as a function of θ_4 (tilt angle of the combining plate) is shown in Fig. 8.38(a). The behavior differs from the other experimental cases. The phase-matching of the lower wavelengths deviates strongly, compared to the main part of the spectrum. The deduced relative spectral phase (Fig. 8.38(c)) shows an important phase shift over the 550-700 nm spectral range. It can be noticed that at 600 nm, the relative phase-shift is π, leading to destructive interference of the two components, as illustrated by the hole in the combined pulse spectrum in this wavelength region. Therefore, ionization limits the combined spectral bandwidth. Temporal characterization of the combined pulse shows a sharp spectral phase-shift around 650 nm (Fig. 8.39(b)). This is because of the relative phase that cannot be compensated. The temporal quality (Fig. 8.39(a)) is degraded.

Figure 8.39 – Wizzler measurement of the compressed combined pulse in configuration II with ionized medium: (a) Temporal intensity, (b) Spectral intensity and phase.

Conclusion on the ionization influence

To conclude, ionization is detrimental to the combining process. This is due to the strong phase difference from 500 to 700 nm between the replicas. It should be noticed that the combining process allows very sensitive measurement of the onset of ionization in the nonlinear stage, which is of fundamental interest.

8.10.4 Cross-phase modulation (XPM) between the replicas

In this section, the detrimental effect of cross-phase modulation between the replicas on the combined pulse quality is demonstrated. To do so, two pairs of plates enable to produce two temporally overlapping replicas. As illustrated in Tab. 8.6 (V), the plate C3 is orientated to reduce the delay between the two replicas created by C1, without further pulse splitting. The two 30 fs subpulses are delayed by about 60 fs when propagating through the HCF. The plates C4 and C2 compensate the overall group delay. Effective combination is achieved in C2 via adjustment of θ_2.

The input energy is 1.1 mJ. When no nonlinear effect occurs in the hollow fiber, the combining process is as efficient as in cases I and II. Fourier treatment of the fringed spectrum (Fig. 8.40(b)) confirms a temporal spacing of 62 +/- 0.5 fs. However, adding gas induces cross-phase modulation between the replicas, thereby modifying their relative phase. As a result, for a Neon pressure of 1.4 bar, the spectrum of the combined pulse is modulated (Fig. 8.40(b)) and the combining efficiency drops to 85 %.
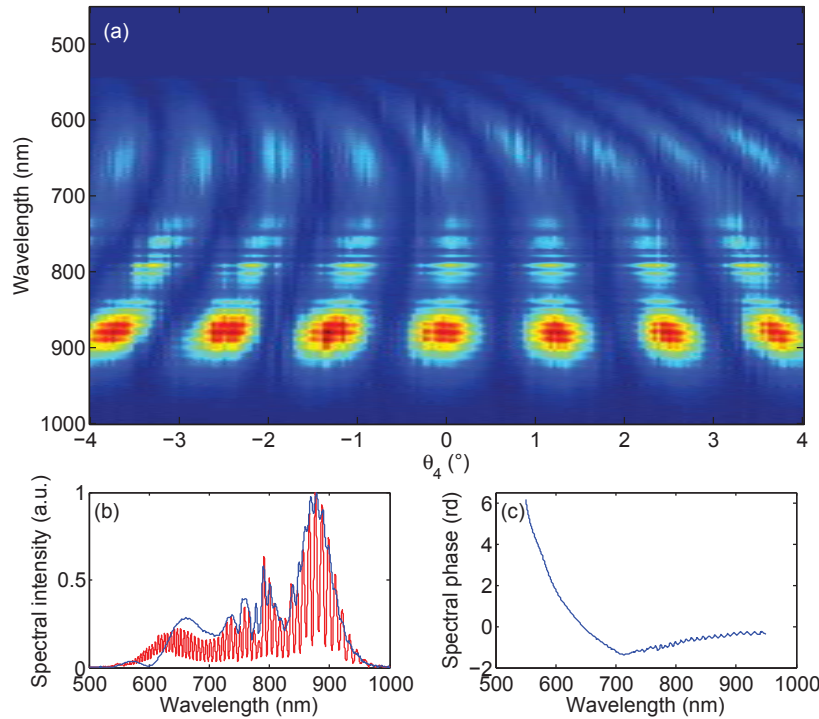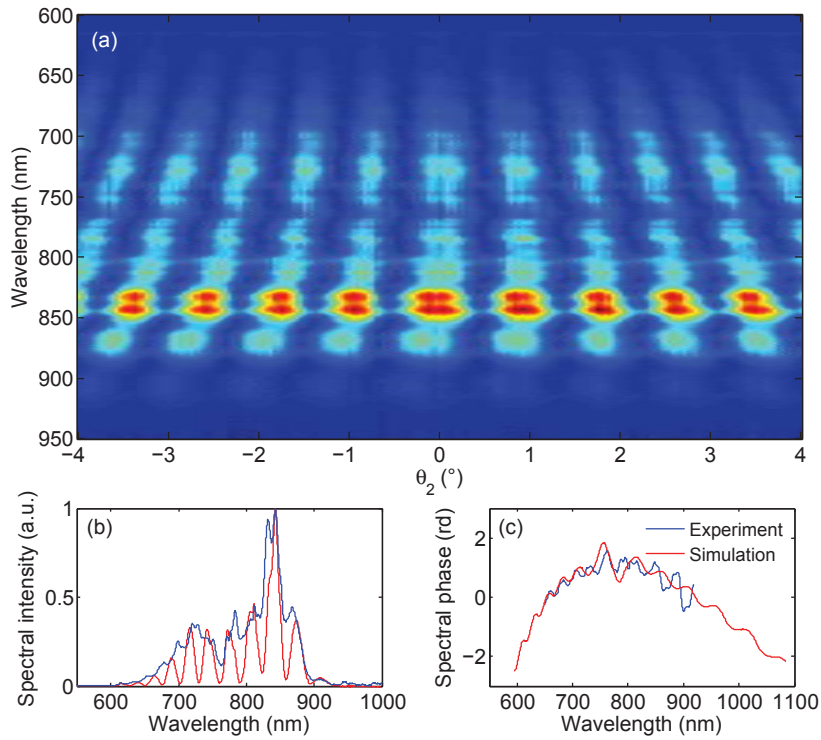
Figure 8.40 – Analysis of the experimental case V for a gas pressure of 1.4 bar and an input energy of 1.1 mJ. The maximum combining efficiency is 85 %. (a) Spectral dependence of the combined pulse as a function of θ_2. $\theta_2 = 0°$ corresponds to the maximum combining efficiency. (b) Combined pulse (blue) and fringed (red) spectra measured for $\theta_2 = 0°$. (c) Relative spectral phase deduced from the Fourier analysis of the interferogram.

The spectrum of the combined pulse as a function of θ_2 is shown in Fig. 8.40(a). The result of the interferogram analysis is shown in Fig. 8.40(c). It highlights the phase mismatch between the replicas because of the nonlinear interaction between the two sub-pulses. The phase modulations cannot be compensated by the combining plate, and the remaining phase defects are mapped onto the spectrum of the combined pulse. As a result, the combining efficiency is lower. A Wizzler measurement of the compressed combined pulse confirms the strongly modulated uncompensated spectral phase (Fig. 8.41). This degraded temporal quality can be compared to the measurements previously set out (Fig. 8.26 and 8.27), where no XPM occurs. It emphasizes the necessity of avoiding any temporal overlap between the replicas.
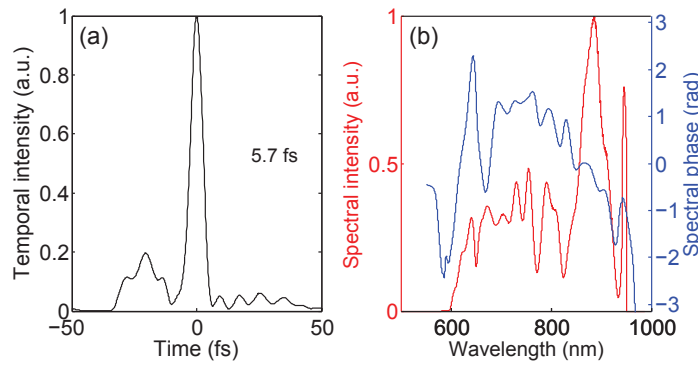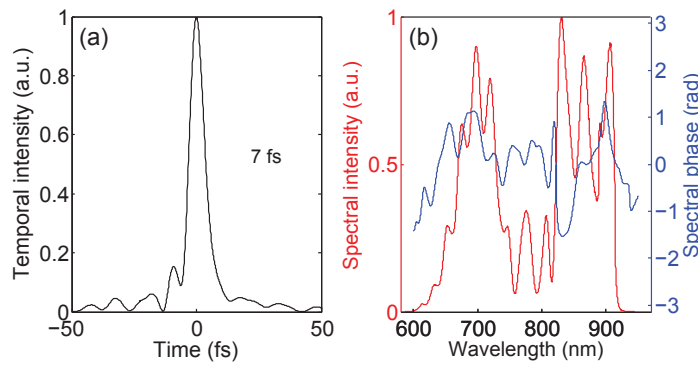

Figure 8.41 – Wizzler measurement of the compressed combined pulse in configuration V: (a) Temporal intensity, (b) Spectral intensity and phase.

Again, numerical simulations were performed with MIRO under the same conditions. The cal-

culations confirm that the temporal overlap of the trailing edge of the first sub-pulse and leading edge of the second one, both chirped by SPM, leads to spectral phase modulations. The modulated relative spectral phase is found in good agreement with the experimental data (Fig. 8.40(c)). The combined pulse exhibits modulated spectral amplitude and phase, with a slight decrease in the combining efficiency. Assuming perfect Gaussian 30 fs pulses with no pedestal, increasing the delay between the replicas smoothens these modulations. For delays higher than 90 fs, the phenomenon becomes negligible.

Conclusion on the cross-phase modulation influence

To conclude, temporal overlapping between the replicas leads to lower combining efficiency and poor spectro-temporal quality of the combined pulse. It is recommended to introduce a minimum temporal spacing of three times the FWHM of the initial pulse duration to inhibit XPM. However, such a recommendation is not sufficient to guarantee high coherent contrast and combining efficiency, as the pedestals of the replicas can influence each other via XPM process too.

8.10.5 Nonlinear interactions between the replicas pedestals

Although the replicas are delayed by more than three times the pulse width, the finite coherent contrast of the laser (10^{-3} relative intensity, Fig. 8.42) causes nonlinear interactions between the replicas. The parasitic pulses inside the replicas pedestals can indeed temporally coincide with any other replica. As efficient combination relies on adequate phase compensation in the combining plate(s), any nonlinear interaction between the replicas have to be minimized as much as possible, or then at least precisely controlled.

A diagnostic to analyze the nonlinear interaction between the replicas inside the fiber consists in measuring the spectrum at the fiber output, before the Combining Setup. The HCF output spectrum corresponds to the spectral interferences between the replicas. If the replicas remain perpendicularly polarized after propagation through the nonlinear medium, the HCF output spectrum should be smooth. A modulated HCF output spectrum indicates that polarization rotation and/or nonlinear interaction inter-replicas could have occurred during the nonlinear process. Such modulations may also result from non equally intense replicas when working with more than two replicas. Analyzing this spectrum enables to optimize the plates included in the Dividing Setup, independently of the combining plates. Indeed, the Combining Setup cannot compensate defaults due to the nonlinear crossed interactions between the replicas.
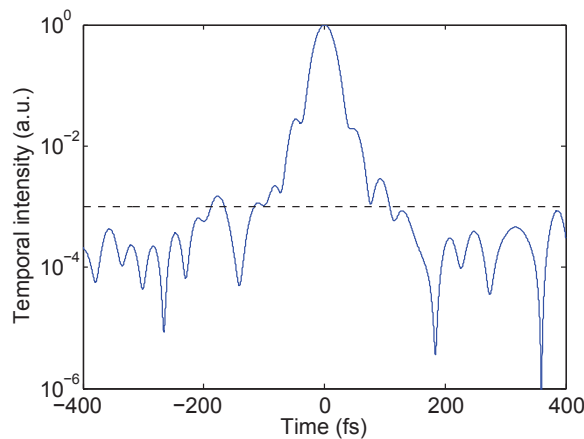
Figure 8.42 – Typical temporal profile of the laser (Wizzler measurement).

The first case to be considered is the one where a parasitic pulse matches temporally a replica and is crossed-polarized with this replica (see figures in Tab. 8.9). Depending on their relative phase, the replicas polarization might be turned to elliptical and so undergo rotation in the nonlinear medium. As a consequence, replicas are not cross-polarized anymore and spectral modula-

tions appear on the HCF output spectrum. This effect can be minimized by controlling the relative phase between the replicas, as shown below.

Numerical simulations with an analytical light source deteriorated by a pre-pulse
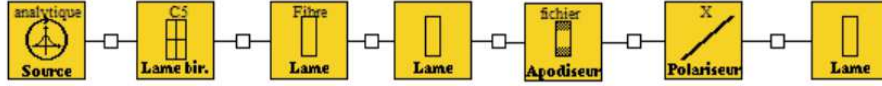
Figure 8.43 – Code architecture for pedestal influence study with an analytical laser source (pulse + pre-pulse).
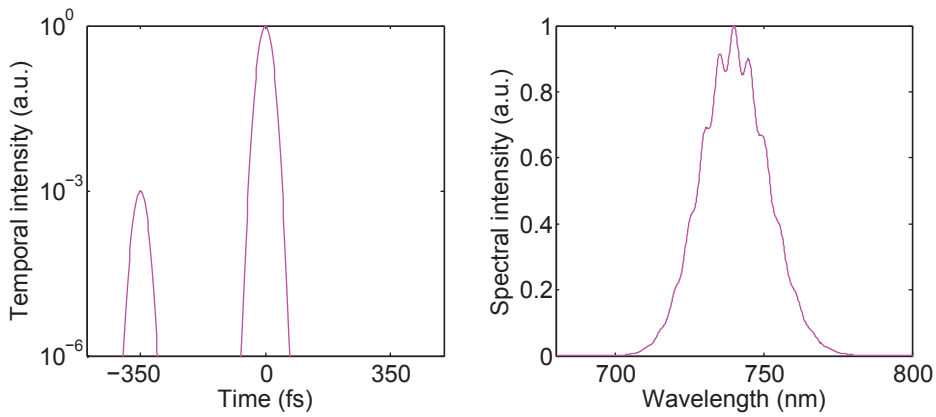
Figure 8.44 – Simulated source temporal profile and spectrum. The prepulse is delayed from the main pulse of 350 fs and has a relative intensity of 10^{-3}.

To illustrate this phenomenon, MIRO simulations were performed as follows. The code architecture is given on Fig. 8.43 and the simulated setups are illustrated in Tab. 8.9. An analytic light source is simulated and generates a 45°-polarized pulse with a pre-pulse at 10^{-3} relative intensity delayed by 350 fs. The source spectrum is shown on Fig. 8.44 and presents spectral modulations because of the parasitic pre-pulse. The simulated dividing plate corresponds to C5 and delays the replicas by 350 fs, which corresponds to the delay between initial pulse and pre-pulse (see figures in Tab. 8.9). In this way, the S-polarized parasitic pulse replica [PP-R(S)] is in temporal coincidence with the P-polarized replica [R(P)]. By tilting the plate C5, it is possible to adjust the phase between these two pulses so that the resulting pulse polarization is linear or elliptical.

Three cases are explored: [A]-the S-polarized Pre-Pulse Replica and the P-polarized replica are phase-matched (Fig. 8.46, column 1). [B]-the phase between the S-polarized Pre-Pulse Replica and the P-polarized replica is adjusted so that the HCF output spectrum features modulations with a maximum contrast (Fig. 8.46, column 2). [C]-the phase between the S-polarized Pre-Pulse Replica and the P-polarized replica is adjusted so that the HCF output spectrum features no modulations (Fig. 8.46, column 3). In each case, the phase, spectrum and temporal intensity of the resulting S and P polarized components at t = 350 fs is plotted. To do so, a temporal apodizer and a polarizer were used to isolate the pulses of interest, as shown in Fig. 8.43. Besides, the HCF output spectrum is given and corresponds to the spectral interferences of all replicas and pre-pulse replicas after the nonlinear medium (it is recorded prior to the apodizer).

The parameters are defined in MIRO to fit the experimental data. Doing so, calculations were performed with an intensity per replica of 6.10^{17} W.m^{-2}, a 1 m-long nonlinear medium, a Kerr index of $12.8.10^{-25}$ m^2.W^{-1} and a central wavelength of 740 nm.

In case [A] (see (Fig. 8.46, column 1), R(P) and PP-R(S) are phase-matched, making their resulting polarization linear. Negligible energy transfer occurs between the two components: their

Case	Phase relation	Simulated setup
A	Pre-pulse and replica are phase-matched	
B,C	Pre-pulse and replica are phase-shifted	

Table 8.9 – Setup simulated with MIRO to explore the interaction between the S-polarized pre-pulse replica (green) and the P-polarized replica (red).
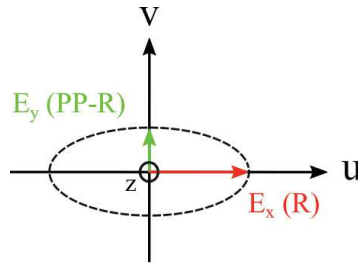
Figure 8.45 – Coordinate system in the case of an elliptically polarized electric field. PP-R: pre-pulse replica; R: replica. z is the propagation axis.

phase and spectra after propagation through the nonlinear medium are similar to that ones prior to the nonlinear medium. However, the PP-R(S) intensity is 20 % higher than before the fiber, meaning that there is even though an interaction between R(P) and PP-R(S). It is probably related to the not perfect adjustment of the phase between the two considered pulses, making the resulting polarization not strictly linear. In this way, PP-R(S) and R(P) may form an elliptical polarization with a very small ellipticity and allow polarization rotation effects. However, the following reasoning is carried out considering that the polarization is linear because the temporal phase of R(P) and PP-R(S) are identical. The resulting polarization formed by R(P) and PP-R(S) is not crossed polarized with R(S). As a consequence, the HCF output spectrum (purple) exhibits modulations.

In case [B] (see (Fig. 8.46, column 2), the phase between R(P) and PP-R(S) is adjusted to maximize the fringes contrast on the HCF output spectrum. The resulting temporal phase and spectra along the P and S polarization directions are not similar each other after propagation through the fiber, meaning that crossed interactions occurred. In this case, it is clear that the energy transfer is
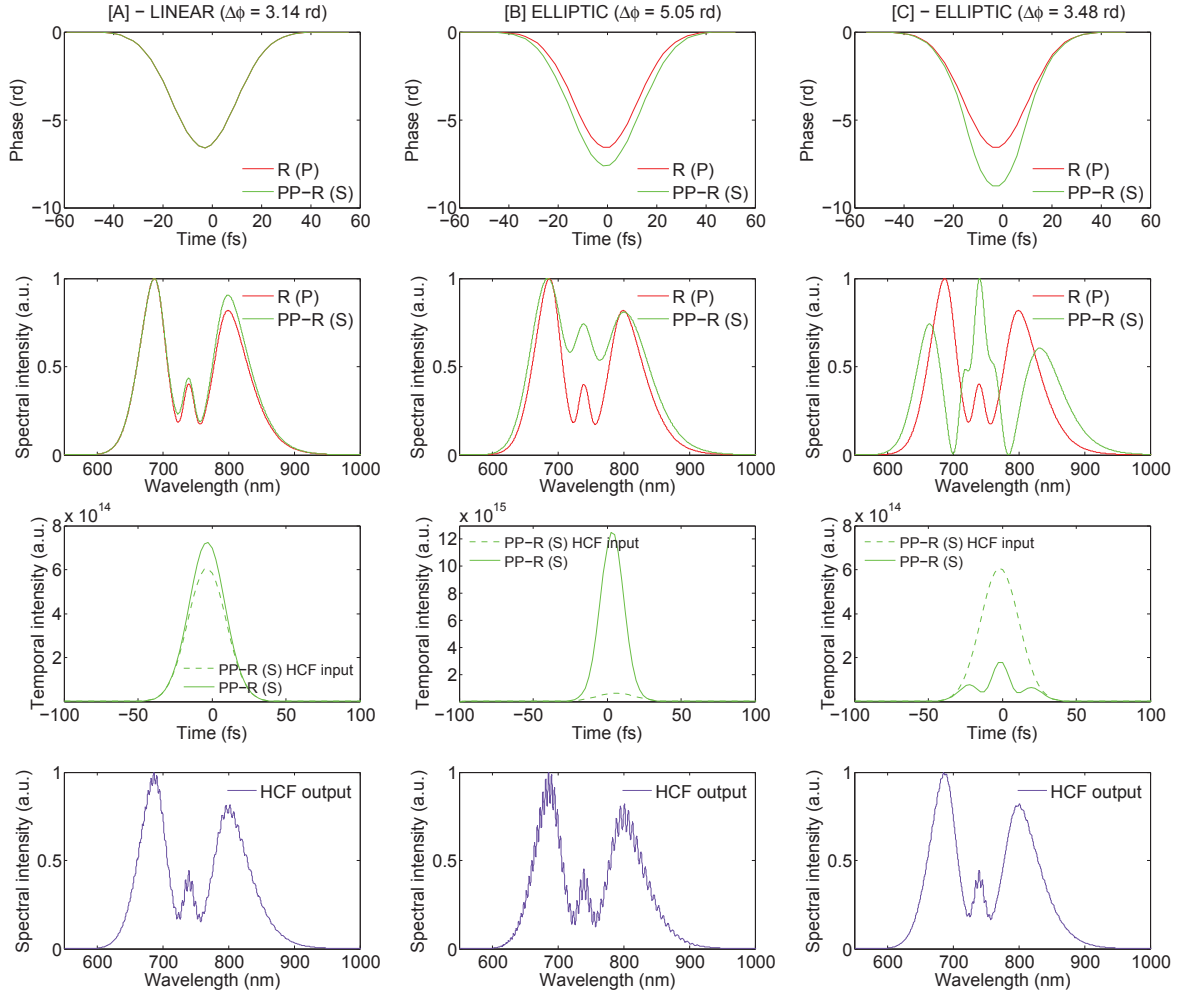
Figure 8.46 – MIRO simulation of a pre-pulse influence when implementing optical multiplexing with two replicas. The prepulse is delayed from the main pulse by 350 fs and has a relative intensity of 10^{-3}. Three cases are explored: [A]-the phase-shift between the S-polarized Pre-Pulse Replica (PP-R, green) and the P-polarized replica (R, red) is π before HCF. [B]-the phase-shift between the S-polarized Pre-Pulse Replica and the P-polarized replica is 5.05 rad before HCF. [C]-the phase between the S-polarized Pre-Pulse Replica and the P-polarized replica is adjusted so that the HCF output spectrum (purple) presents no modulations. The resulting phase-shift before HCF is 3.48 rad. [A,B,C] In each case, the phase, spectra and temporal intensity (before the fiber (dashed line) and after (solid line)) of the two considered polarizations components at t=350 fs is plotted. The HCF output spectrum is also given (purple).

favorable to PP-R (S), because the resulting S-polarized component at the considered delay (350 fs) is more intense after the nonlinear medium ($1.2.10^{16}$ W.m^{-2}) than before ($6.0.10^{14}$ W.m^{-2}). This corresponds to an increasing factor of 20. For comprehension, an illustration is given on Fig. 8.47: the ellipse turns so that the new S-polarized component is added coherently to PP-R (S). Therefore, spectral interferences between the resulting PP-R(S) at t = 350 fs and the R(S) at t = 0 result in fringes with a higher contrast than in case [A]. This situation should be avoided.

To overcome these deleterious effects, a solution is to induce deliberately crossed interactions so that the ellipse is rotated and the newly created resulting S-polarized component interferes destructively with PP-R(S), as demonstrated in case [C] (see (Fig. 8.46, column 3) and illustrated on Fig. 8.47. Here, the resulting temporal phase and spectra along the P and S polarization directions are not similar each other after propagation through the fiber, confirming that polariza-
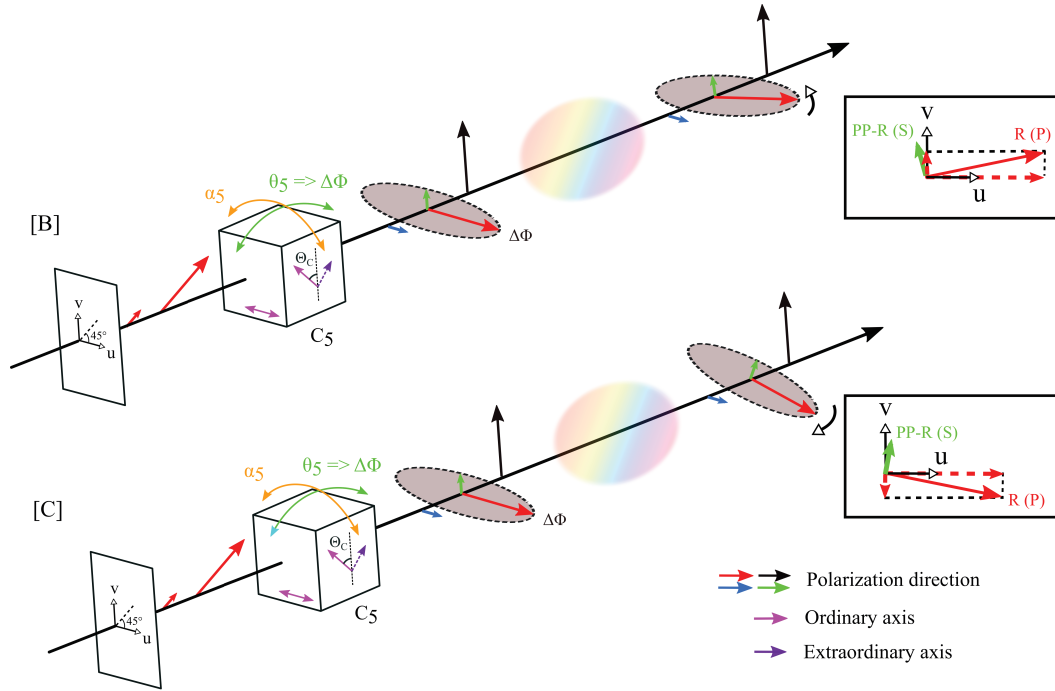
Figure 8.47 – Sketch of cases [B] and [C], when polarization rotation occurs.

tion rotation phenomena occurred. However, these interactions make the resulting S-polarized component intensity 70 % lower after the fiber ($1.8.10^{14}$ W.m^{-2}) than before ($6.0.10^{14}$ W.m^{-2}). The destructive spectral interferences between the new S-polarized component of the rotated P-polarized replica and PP-R(S) are highlighted by the shape of the spectrum of the S-polarized resulting component: the HCF output spectrum exhibits a minimal fringes contrast. There is still very weak fringes on the whole bandwidth. This is related to the fact that the elliptic polarization formed by R(P) and PP-R(S) turns, meaning that both replica and parasite experience polarization rotation (see Fig. 8.47[C]). Therefore, the destructive interferences happen between the S component of the initially P-polarized replica and the parasite which is not any more S-polarized. This explains why the fringes are still slightly visible at the fiber output. Finally, some visible fringes remain between 720 nm and 760 nm because PP-R(P) (drawn in blue on schemes included in Tab. 8.9) is not broadened contrary to PP-R(S).

To summarize, when a replica [R(P)] temporally matches the parasitic pulse of another replica [PP-R(S)], their relative phase enables to optimize the HCF output spectrum. If [R(P)] and [PP-R(S)] are phase-matched, the resulting polarization is linear slightly away from P direction. The two main replicas are consequently not cross-polarized anymore and fringes appear on the HCF output spectrum. Otherwise, the resulting polarization is elliptical and undergoes nonlinear rotation. A new component along S direction is created, enabling constructive or destructive interferences with [PP-R(S)] according to the initial relative phase between [R(P)] and [R(S)]. Adjusting this value enables to decrease the intensity of the parasitic pulse and produce a smooth HCF output spectrum. The phase between [R(P)] and [PP-R(S)] can be adjusted playing with the tilt θ_i of the dividing plate. This is, of course, possible only if the dividing plate is mounted on a high precision rotation stage (typically with a precision better than 2 minutes of arc). This optimization is performed prior to the combining process and is crucial for the temporal quality of the final combined pulse.

Finally, a θscan was performed with MIRO, recording the HCF output spectrum for each tilt value of the dividing plate. The step is chosen 0.09 fs to see the progressive apparition and extinction of fringes. A reference spectrum is calculated when the light source features no pre-pulse.

This reference spectrum is then subtracted to each recorded spectrum, so that fringes apparition and extinction is highlighted (see Fig. 8.48). The regular apparition of fringes can be observed with the scanned delay. The periodicity is 1.4 fs, that is half of the electric field period. This map shows that a wise tuning of θ_5 enables to eliminate the fringe pattern. However, the delay range for fringes suppression is very restrained (it is less than 0.1 fs in terms of relative phase delay). The rotation mount of the birefringent plates must be thus precise enough to achieve such a tiny delay range.
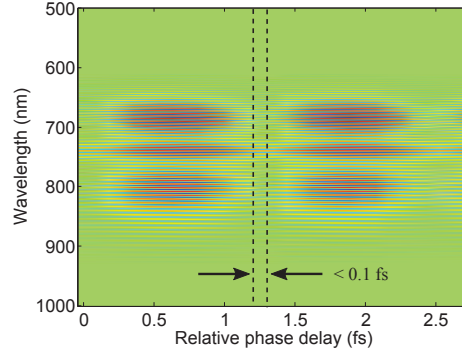
Figure 8.48 – θscan performed with MIRO: Spectral evolution of the HCF output spectrum with the tilt of the dividing plate. A reference spectrum, calculated when the source has no pre-pulse, is systematically subtracted.

I underline that these simulations were performed with a well defined pre-pulse at 10^{-3} relative intensity. In real life, the whole laser pedestal is involved in these nonlinear interactions and make the optimization previously described more difficult. Furthermore, these crossed interactions can be affected by the initial polarization of the replicas, as demonstrated below.

Theoretical approach of the polarization rotation process

The numerical simulations performed with MIRO highlighted that the tilt of the dividing plate should be adjusted to minimize the fringes at the HCF output. The S-polarized component at t=350 fs is thus minimal. The optimal phase-shift was found to be 3.48 rad (case [B]), which is very close to the phase-shift in the linear case (3.14 rad - case [A]). However, it is hard to extract precisely the required phase-shift value in the simulation. The idea in this paragraph is to calculate theoretically the required phase-shift to achieve an optimal HCF output spectrum.

To do so, the theoretical model related to the polarization changes induced by an isotropic nonlinear medium is considered [117]. In the case of a nonlinear isotropic medium where only Kerr effect is taken into account, the evolution of the electric field components, E_x and E_y (see Fig. 8.45), is described by:

$$\frac{dE_x}{dz} = i \frac{6\pi}{8\lambda n_0} \chi_{xxxx}^{(3)} \left\{ |E_x|^2 E_x + \frac{1}{3} \left[2|E_y|^2 E_x + E_y^2 E_x^* \right] \right\} \tag{8.47}$$

$$\frac{dE_y}{dz} = i \frac{6\pi}{8\lambda n_0} \chi_{xxxx}^{(3)} \left\{ |E_y|^2 E_y + \frac{1}{3} \left[2|E_x|^2 E_y + E_x^2 E_y^* \right] \right\} \tag{8.48}$$

Terms $|E_x|^2 E_x$ and $|E_y|^2 E_y$ correspond to self-phase modulation whereas terms $|E_y|^2 E_x$ and $|E_x|^2 E_y$ correspond to cross-phase modulation. These equations show that a linear polarization (E_y=0) experiences no modification during propagation through a nonlinear isotropic medium. The same applies to a circular polarization (E_y=iE_x). However, an elliptical polarization will be rotated because of Kerr effect-induced birefringence. The rotation angle was already calculated in section 8.10.1. This calculation is performed again with an incident electric field defined as:

$$\mathbf{E} = E_{0x}\mathbf{x} + E_{0y} \exp i\phi \mathbf{y} \tag{8.49}$$

The incident elliptical polarization is defined by ϕ, the phase between the two polarization components, and ξ, the angle defined according to the axes X and Y (and not according to the ellipse axes) (see Fig. 8.49):

$$\tan\xi = \frac{E_{0y}}{E_{0x}} \tag{8.50}$$

Performing a similar calculation to the one presented in section 8.10.1 allows to express the rotation angle of the incident elliptical polarization:

$$\Delta\alpha = -\frac{2}{3}n_2 I \frac{\tan\xi}{(1+\tan^2\xi)}\frac{\omega}{c}z\sin\phi \tag{8.51}$$

$$\Delta\alpha = -\frac{2}{3}\Phi_{\mathrm{NL}}\frac{\tan\xi}{(1+\tan^2\xi)}\sin\phi \tag{8.52}$$
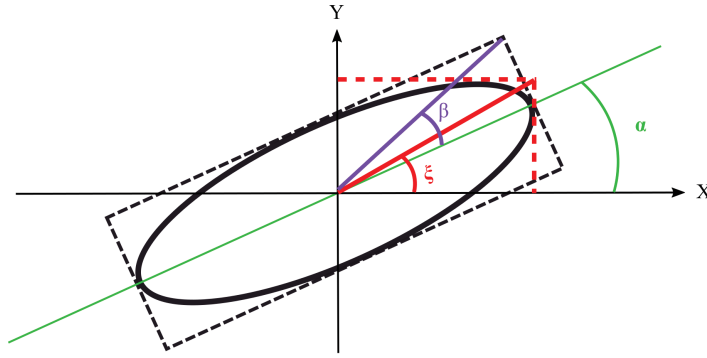
Figure 8.49 – Scheme of the ellipse. α is the orientation of the ellipse axes, β its ellipticity and ξ is the ratio between the ellipse projections on the axes X and Y.

where $\Phi_{\mathrm{NL}} = n_2 I \omega z/c$ is the nonlinear phase accumulated in the fiber. In the simulation performed previously, the pre-pulse had a relative intensity of 10^{-3}. Thereafter, ξ is fixed as follows:

$$\tan\xi = \sqrt{10^{-3}} \approx 0{,}0316 \tag{8.53}$$

The idea is now to determine the optimal value of ϕ. To do so, intensities along the X and Y directions (corresponding respectively to the polarization states P and S) are calculated at the fiber output as a function of ϕ. The phase ϕ is optimal when the Y intensity is minimal.

According to [148], the electric field components after the nonlinear medium can be expressed as:

$$E_x = \frac{1}{2}\left[\left(E_{0x} + \frac{E_{0y}}{i}e^{i\phi}\right)e^{i\Delta\alpha} + \left(E_{0x} - \frac{E_{0y}}{i}e^{i\phi}\right)e^{-i\Delta\alpha}\right]e^{ik_m z} \tag{8.54}$$

$$E_y = \frac{i}{2}\left[\left(E_{0x} + \frac{E_{0y}}{i}e^{i\phi}\right)e^{i\Delta\alpha} - \left(E_{0x} - \frac{E_{0y}}{i}e^{i\phi}\right)e^{-i\Delta\alpha}\right]e^{ik_m z} \tag{8.55}$$

where k_m is the mean propagation constant. The corresponding intensity can be calculated according to:

$$I_x = |E_x|^2 = E_{0x}^2\cos^2\Delta\alpha + E_{0y}^2\sin^2\Delta\alpha + 2E_{0x}E_{0y}\cos\Delta\alpha\cdot\sin\Delta\alpha\cdot\cos\phi \tag{8.56}$$

$$I_y = |E_y|^2 = E_{0x}^2\sin^2\Delta\alpha + E_{0y}^2\cos^2\Delta\alpha - 2E_{0x}E_{0y}\cos\Delta\alpha\cdot\sin\Delta\alpha\cdot\cos\phi \tag{8.57}$$

Fig. 8.50 shows the evolution of $\Delta\alpha$ as a function of ϕ. The calculations were performed with the same parameters than the ones used in the numerical simulations (intensity, nonlinear

medium characteristics). When $\phi = \pi$, $\Delta\alpha = 0°$ (see the solid black line on Fig. 8.50), because a linear polarization does not experience rotation.
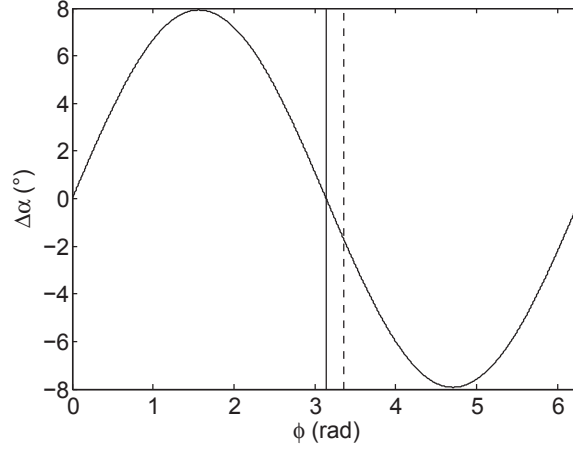
Figure 8.50 – Rotation angle $\Delta\alpha$ as a function of ϕ, the phase-shift between PP-R (S) and R-(P), after propagation through the nonlinear medium. The relative intensity of the pre-pulse is 10^{-3}. The solid black line corresponds to $\phi = \pi$ whereas the dashed black line is the ϕ value which minimizes I_y (see Fig. 8.51).
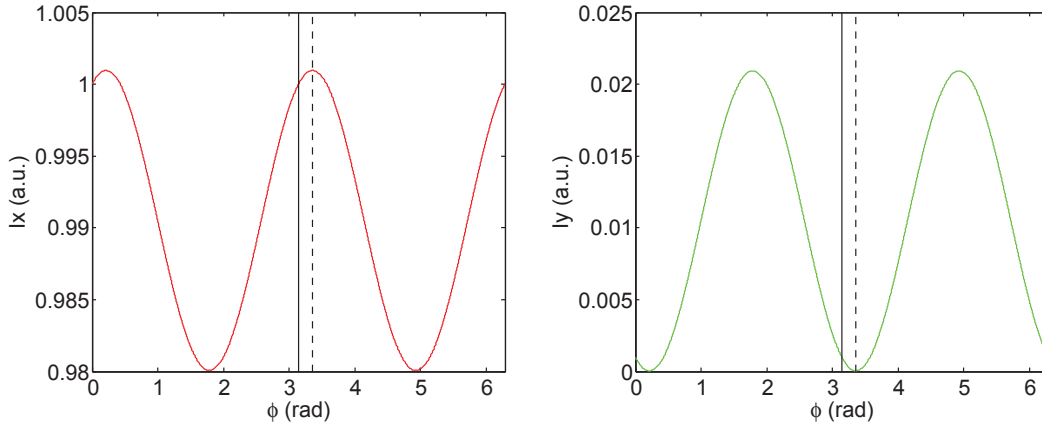
Figure 8.51 – Intensity along X (red - P polarization direction) and intensity along Y (green - S polarization direction) as a function of ϕ, the phase-shift between PP-R (S) and R-(P), after propagation through the nonlinear medium. The relative intensity of the pre-pulse is 10^{-3}. The solid black line corresponds to $\phi = \pi$ whereas the dashed black line is the ϕ value which minimizes I_y.

Fig. 8.51 shows I_x (red) and I_y (green) as a function of ϕ. A minimal value of I_y will lead to a smooth output HCF spectrum. When $\phi = \pi$, I_x is not maximal and I_y is not minimal. To reach the I_y minimum (and so the I_x maximum), ϕ must be equal to 3.356 rad. This result is not intuitive. One might have expected that the resulting polarization formed by the replica and the pre-pulse replica at t=350 fs should be linear ($\phi = \pi$). When creating deliberately an elliptical polarization before propagation through the fiber, the P-polarized replica polarization is turned by $\Delta\alpha \approx$ -1.7°. In this way, its resulting S component interferes destructively with the S polarized pre-pulse replica. The temporal quality of the final pulse will be thus optimal.

To conclude, the theoretical calculations enabled to determine the optimal phase-shift between PP-R (S) and R-(P) to minimize the HCF output spectrum fringes. $\Delta\phi$ is the difference between the optimal phase-shift and π and is equal to:

$$\Delta\phi_{\text{MIRO}} = \phi_{opt,\text{MIRO}} - \pi = 3.48 - \pi = 0.34\,\text{rad} \tag{8.58}$$

$$\Delta\phi_{\text{THEORY}} = \phi_{opt,\text{THEORY}} - \pi = 3.356 - \pi = 0.21\,\text{rad} \tag{8.59}$$

It should be noticed that the theoretical value was calculated for the central wavelength and maximum intensity, whereas MIRO performs a complete temporal calculation. This can explain the difference between the results of two methods.

To conclude, these data are essential to design the mechanical mount of the dividing birefringent plates. The phase-shift adjustment is indeed achieved tuning the tilt of the plate in its extraordinary direction. The theoretical phase-shift of 0.21 rad can be translated into a fraction of the electric field period and then into an angle $\delta\theta$ using the tunability factor of the birefringent plates, as summed up in Tab. 8.10. This angle corresponds to the required precision on the rotation mount of the birefringent plate. It should better than 2 minutes of arc to achieve such a small phase-shift. Here, mechanical mounts with a precision of 2 minutes of arc were used and it was noticed that it was barely enough to perform the fringes optimization at the fiber output when working with four replicas.

	Θ_c	$\tau_{g,exp}$ (fs)	δ_t (fs/°)	$\delta\theta$ (°)	$\delta\theta$ (')
C1	45°	179	3.61	0.0250	1.50'
C3	60°	245	2.74	0.0329	1.97'
C5	60°	351	4.05	0.0223	1.34'

Table 8.10 – Required mechanical precision $\delta\theta$ for the rotation mount of the dividing birefringent plates. I remind the crystallographic orientation, the experimental group delay deduced from the Fourier analysis of fringed spectra and the delay tunability with θ_i (tilt of the plate i).

Experimental demonstration of the pedestals interactions and corresponding numerical simulations using a Wizzler measurement as a laser source

To go further, experiments are performed to recover the numerical trends for the fringes management at the HCF output. One plate (C5) is used to create only two replicas delayed by 351 fs propagating through the fiber with crossed polarizations (replicas and potential parasitic pulses are cross-polarized as well). The gas pressure is 1.4 bar and the pulse energy is 600 µJ. Slight tilting of C5 in the extraordinary direction (θ_5) enables to tune the phase delay between the replicas. Doing so, the phase between one replica and a potential time-matched parasitic pulse is controlled. The polarization orientation of the replicas is measured at the output of the fiber as a function of θ_5 (Fig. 8.52(line 1)). The spectrum at the output of the fiber is simultaneously recorded for each value of the tilt θ_5 (Fig. 8.52 (line 2)). The spectral evolution result is a 2D map with the regular apparition of fringes with the scanned delay. Two cases were considered : $\alpha_5 \approx 0°$ (Fig. 8.52 (column 1)) and $\alpha_5 \approx 3°$ (Fig. 8.52 (column 2)).

Fig. 8.52 (line 1) shows the measured angle (Ψ) between the replicas polarization directions at the output of the fiber, as a function of the phase delay. $\Psi = 90°$ indicates that the polarization direction of the replicas are orthogonal after the nonlinear process. According to Fig. 8.52 (line 1), Ψ changes with the delay, meaning that polarization rotation occurs during the nonlinear process: its value evolves periodically with the delay. Indeed, polarization rotation originates from crossed interactions between replicas and parasitic pulses, thus depending on their relative phase. When the relative phase is $0 \pm k\pi$, the resulting polarization of the replica and its parasitic pulse is linear, no polarization rotation occurs and Ψ is kept before and after the fiber. Because of the pre-pulse replica, the resulting polarization direction is not strictly P. As a consequence, the replicas are not orthogonally polarized at the fiber output, that means $\Psi \neq 90°$. When the relative phase is different from $k\pi$, the resulting polarization is elliptic and polarization rotation occurs. There is an optimal phase-shift for which the replicas are orthogonally polarized at the fiber output ($\Psi = 90°$), as demonstrated before in the MIRO simulations. This optimal phase-shift is found to be very close to $0 \pm k\pi$, but it is not visible on these experimental data. This process could be understood only thanks to the simulations and theoretical calculations. Note that the periodicity of the process is 2.7 fs (electric field period at 800 nm), independently of the α tuning (Fig 8.52a and e).
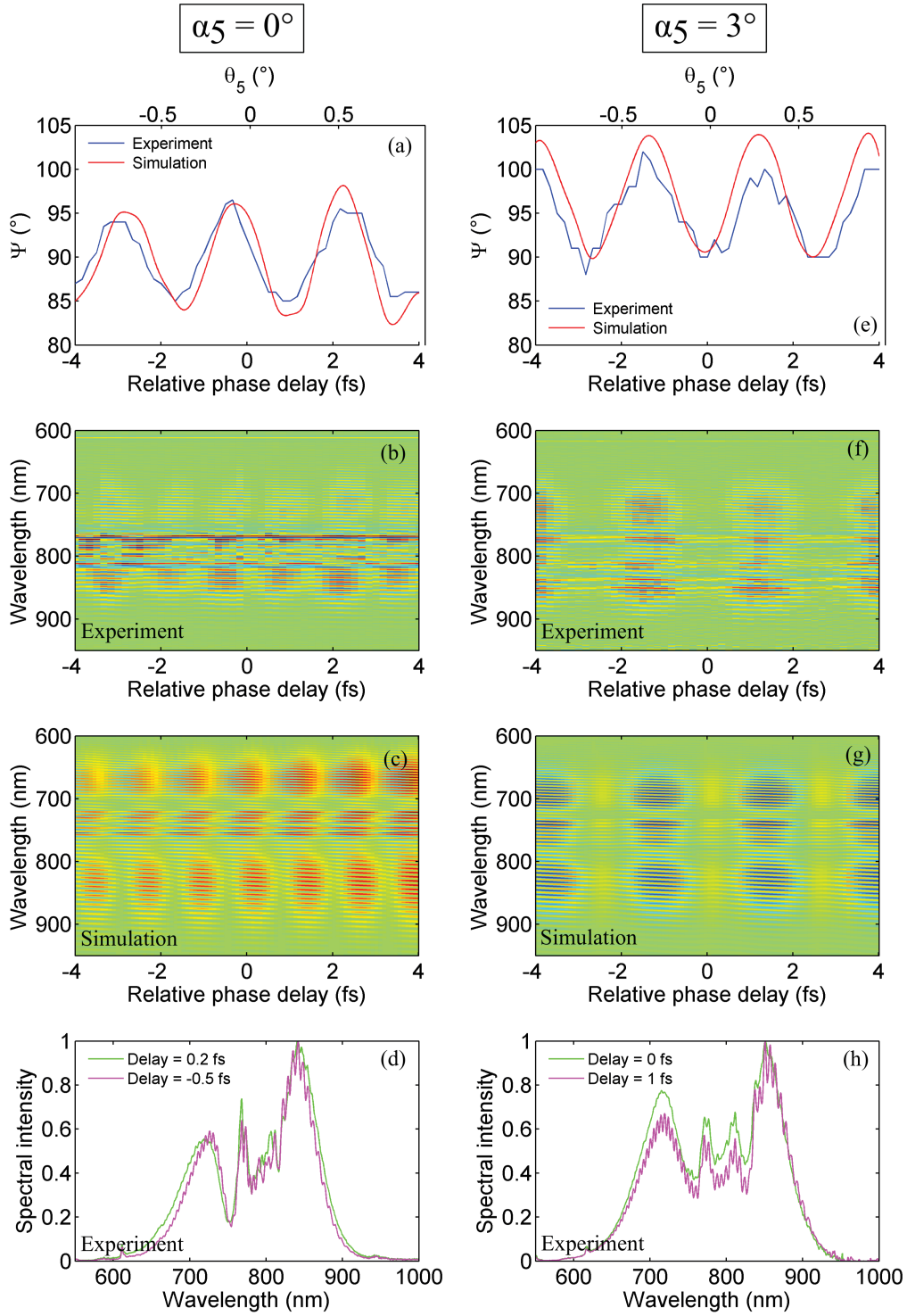
Figure 8.52 – Two cases are explored: $\alpha_5 \approx 0°$ (column 1) and $\alpha_5 \approx 3°$ (column 2). In each case are first given the evolution of the angle between the polarization states of the replicas after propagation through the fiber, as a function of the tilt of the plate C5 converted into relative phase delay (line 1). Then, the experimental θscan are given and represent the spectral evolution of the HCF output spectrum as a function of the relative phase delay between the replicas (line 2). The corresponding θscan performed with MIRO are given on line 3. Finally, a selection of two HCF output experimental spectra is shown on line 4.

The mean value of the recorded oscillation is the signature of polarization rotation due to depolarization before the fiber. As explained in part. 8.10.1, depolarization effects between the Dividing Setup and the fiber entrance do not depend on the relative phase between the replicas but

induces the same defect ($\Psi \neq 90°$), visible as an "offset" of the oscillation of Ψ with θ_5. If the oscillation is centered on 90° (Fig. 8.52a), it means that the replicas are S and P polarized before the fiber, without taking into account here the replicas pedestals influence. The axis orientation of the dividing plate α_5 is correctly adjusted. In the case where α_5 is badly tuned ($\alpha_5 \approx 3°$), the oscillation is not centered on 90° (Fig. 8.52e) and the replicas polarizations are elliptical before the fiber. It should be noticed that crossed interactions between the replicas can compensate, to some extent, an initial depolarization issue. In practice, tuning θ_5 enables to achieve $\Psi = 90°$, as seen on Fig. 8.52e.

Experimental θscans were performed in both cases $\alpha_5 \approx 0°$ (Fig. 8.52b) and $\alpha_5 \approx 3°$ (Fig. 8.52f). To observe easily the fringes apparition and extinction, it is necessary to process the data as follows. A smooth spectrum is calculated for each recorded spectrum thanks to a sliding window average. This smooth spectrum is retrieved to the fringed ones, highlighting thus the fringes apparition or extinction. The periodicity of fringes apparition is related to the angle between the polarization states of the replicas at the HCF output. When α_5 is well tuned, the fringes periodicity is π and when it is badly tuned, the periodicity of fringes apparition is different from π. In this way, the periodicity of fringes apparition at the HCF output is a very useful diagnostic to tune α_5 correctly. Note that in case (b), some strong fringes remains at roughly 770 nm for all the delay values. As explained previously, these fringes come from the parasitic pulses which are not broadened and interfere with the identically polarized replicas. In case (f), these fringes are weaker probably because the two runs of experiments ($\alpha_5 \approx 0°$ and $\alpha_5 \approx 3°$) were not performed the same day and the laser pedestal is not always similar from day to day.

Whether rotation polarization is due to depolarization before the fiber or crossed interactions between the replicas during propagation through the fiber, the HCF output spectrum is modulated as soon as the replicas polarizations are not orthogonal. Fig. 8.52(d,h) shows for the two considered α_5 values some typical fringed and smooth spectra measured at the output of the fiber. This simple measurement is consequently a useful diagnostic for α_5 adjustment.
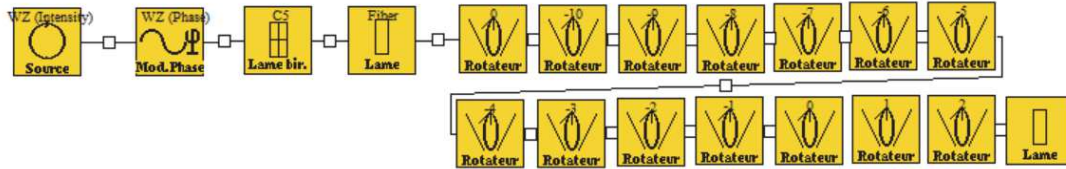
Figure 8.53 – Code architecture for pedestal influence study with a Wizzler measurement of the laser as a source.

To strengthen the experimental results, numerical simulations were performed using the MIRO propagation code (see Fig. 8.53). The Wizzler measurements of the laser are used to define the temporal phase and intensity of the simulated laser pulse. Parameters of the birefringent plate and the nonlinear medium are defined to fit the experimental conditions. A succession of 1° Faraday rotators is used to determine the rotation angle of the polarization components. More precisely, the rotation angle of a component is given by the Faraday rotator exhibiting an output pulse with a minimal intensity.

Looking at Fig. 8.52(a,c), simulations and experiments are in good agreement. For $\alpha_5 = 0°$, the ideal case of an input pulse with no pedestal is considered (Fig. 8.52a). Under that condition, Ψ does not oscillate with the introduced delay and the replicas remain cross-polarized after the nonlinear process. θscans were also performed using the corresponding Wizzler measurements of the laser as a source (Fig. 8.52c,g). The reference spectrum is calculated at the fiber output, dividing the laser source energy by a factor 2 and removing the dividing plate. The periodicity of fringes apparition is similar to the one found with the experiment. The good agreement between simulations and experiments confirm that the laser coherent contrast influence, as well as the depolarization effects are well understood and highlighted. Furthermore, a simple experimental method

was proposed to detect nonlinear interactions between the replicas due to the laser pedestal.

In a general way, the coherent contrast of the combined pulse can be analytically predicted using Eq. 8.52. $\tan\xi$ is the electric field amplitude ratio of the parasitic pulse to the replica before the fiber and is related to the contrast N of the incident pulse intensity:

$$\tan\xi = \frac{E_{0y}}{E_{0x}} = 10^{-N/2} \tag{8.60}$$

During propagation in the fiber, the field amplitude of the initial parasitic pulse and of the parasitic pulse induced by polarization rotation are coherently added, depending on their relative phase:

$$E_{0y} = E_{0x}\, 10^{-N/2} + E_{0x}\, \sin(\Delta\alpha) \approx E_{0x}\, 10^{-N/2} + E_{0x}\, \Delta\alpha \tag{8.61}$$

$$E_{0y} \approx E_{0x}\, 10^{-N/2} + E_{0x}\, \frac{2}{3}\varPhi_{NL}\, \frac{\tan\xi}{\left(1 + \tan^2\xi\right)}\, \sin\phi \tag{8.62}$$

$$E_{0y} \approx E_{0x}\, 10^{-N/2} \left[1 + \frac{2}{3}\varPhi_{NL}\sin\phi\right] \tag{8.63}$$

Finally, the contrast of the combined pulse is given by:

$$C \approx 10^{-N} \left[1 + \frac{2}{3}\varPhi_{NL}\sin\varphi\right]^2 \tag{8.64}$$

where 10^{-N} is the coherent contrast before the fiber. A more rigorous calculation can be performed using equations Eq. 8.56 and Eq. 8.57 and considering that $E_{0y} \ll E_{0x}$ and $\Delta\alpha \ll 1$. The result is given below:

$$C \approx \frac{10^{-N}}{2} \left[2 + \left(\frac{2}{3}\varPhi_{NL}\sin\varphi\right)^2 - \frac{4}{3}\varPhi_{NL}\sin\varphi\cos\varphi\right] \tag{8.65}$$

In the worst case ($\sin\varphi = 1$), the contrast is degraded by nearly one order of magnitude ($\varPhi_{NL}$ = 6 rad). However, the phase-shift φ is linearly dependent on the tilt of the dividing plate. In this way, as demonstrated above, tuning the tilt of the plates of the Dividing setup enables to optimize the coherent contrast of the combined pulse.

An additional contribution to nonlinear interactions between the replicas pedestals when working with 4 replicas

In the previous paragraphs, the case where a parasitic pulse temporally matches a replica and is crossed-polarized, was analyzed in details. However, an additional case can occur when dividing the pulse into 4 sub-pulses: the parasitic pulse can temporally match another replica with the same polarization. In this case, the replica intensity will be increased if parasitic pulse and replica are in phase, or decreased if they are out of phase. As a result, the nonlinear broadening experienced by the replicas will be different for each sub-pulses and the spectral bandwidth of the final combined pulse will be thus affected. Besides, this intensity imbalance between the replicas modifies the inter-replicas phase difference. In other words, the spectral interference pattern from each couples of identically polarized replicas are not any more in opposition and have different amplitudes. As a result, their addition is a modulated spectrum at the output of the fiber. To minimize the relative replicas intensity imbalance, the phase difference between the parasitic pulse and the replica should be a quarter of the electric field period. This tuning might not be compatible with the previous ones minimizing the polarization rotation effects. A compromise has to be reached by adjusting successively θ_A and θ_B.

Conclusion on the nonlinear interactions between the replicas

To conclude, the coherent pedestal of a typical femtosecond laser is already intense enough to induce nonlinear interaction between the replicas, and thus fiber output spectral modulations. Such modulations can also be the signature of depolarization issues before the fiber. This pattern will persist on the combined pulse spectrum and degrade the temporal quality. Accurate adjustment of the dividing plates enables to minimize these deleterious effects.

General conclusion on the combining process limitation and optimization

It was demonstrated that controlled tilting of the combining plate provides a simple and sensitive *in situ* measurement of the spectral phase mismatch between the replicas. This technique was successfully applied to the measurement of the residual phase shift between the replicas, as well as the relative dispersion introduced by the combining plate. An optimized regime is described, highlighting how high-fidelity few-cycle pulses can be efficiently produced. Limitations were particularly quantified, by defining a lower limit to the temporal delay according to the input pulse duration, and a maximum GDD difference in the combining plate according to the expected final duration.

Furthermore, although this result was unexpected, it was demonstrated that the coherent pedestal of a typical femtosecond laser may be already intense enough to induce nonlinear interactions between the replicas, and thus fiber output spectral modulations. Depolarization effects prior to the fiber input result also in spectral modulations at the fiber output. This pattern will persist on the combined pulse spectrum and degrade the temporal quality. To get free from the laser pedestal influence, a solution would be to increase the delay between the replicas. However, this option is not suitable here, as it would increase the total amount of dispersion that then needs to be compensated. Furthermore, it would also increase the differential GDD experienced by the replicas in the Combining Setup and limit thus the output spectral bandwidth. As a result, the laser pedestal influence must be controlled. If not, the contrast can be degraded by one order of magnitude for an accumulated nonlinear phase of 6 rad. An *in-situ* procedure is proposed to minimize the deleterious effects related to the laser pedestal influence as well as to the polarization changes of the replicas prior to to the fiber: the coherent contrast of the combined pulse can be optimized by accurate adjustment of the dividing plates.

All these considerations must be taken into account before further increasing the input energy. The feasibility of further pulse splitting (> 2 sub-pulses) is now examined.

8.11   Extending the experiment to 4 replicas

To generate 4 replicas delayed by similar quantities, a new pair of calcite plates was acquired. The delay inter-replica should be indeed at least 3 times the FWHM pulse duration. Combined with the plates (C1-C2), this pair enables to generate 4 almost equidistant replicas, delayed by 170 fs or 180 fs. In the following, these new plates are named C5 and C6.

8.11.1   Plates tuning and polarization of the combined pulse in an ideal configuration

In a first step, pulse division into 4 replicas and combination are investigated with pulses involving ultra broad spectrum, in the ideal configuration where no nonlinear effect occurs between the Dividing Setup and Combining Setup. Doing so, the polarization and spectral properties of the combined pulse are established as a function of the plates tilt.

The experimental setup is shown in Fig. 8.54. The Neon pressure is fixed to 1 bar for a pulse energy of 1.3 mJ. Out of the fiber, the spectral bandwidth is 170 nm (FWMH). The Dividing and Combining Setups are inserted after the fiber in the collimated beam. The four considered plates are named A, B (Dividing plates), C, D (Combining plates), as illustrated on Fig. 8.55. Pulse Division includes two calcite plates positioned at normal incidence. The first plate (A ie C1), with
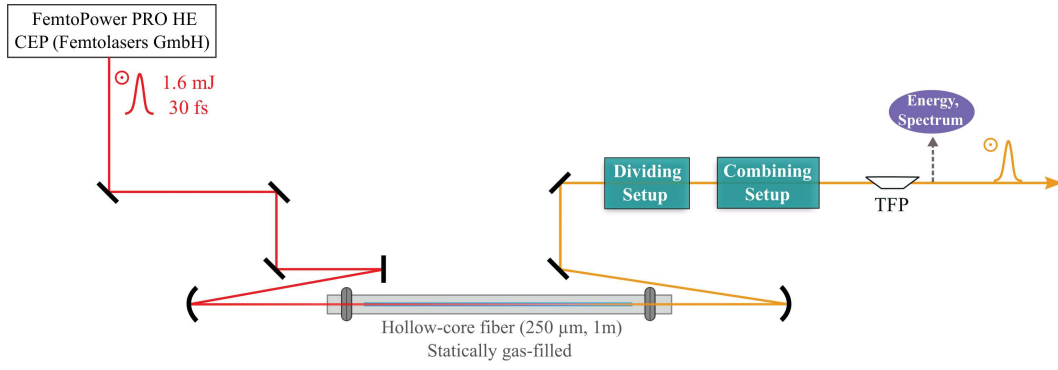
Figure 8.54 – Experimental implementation of pulse dividing and combining with broadband pulses when the nonlinear stage is before the Dividing Setup.
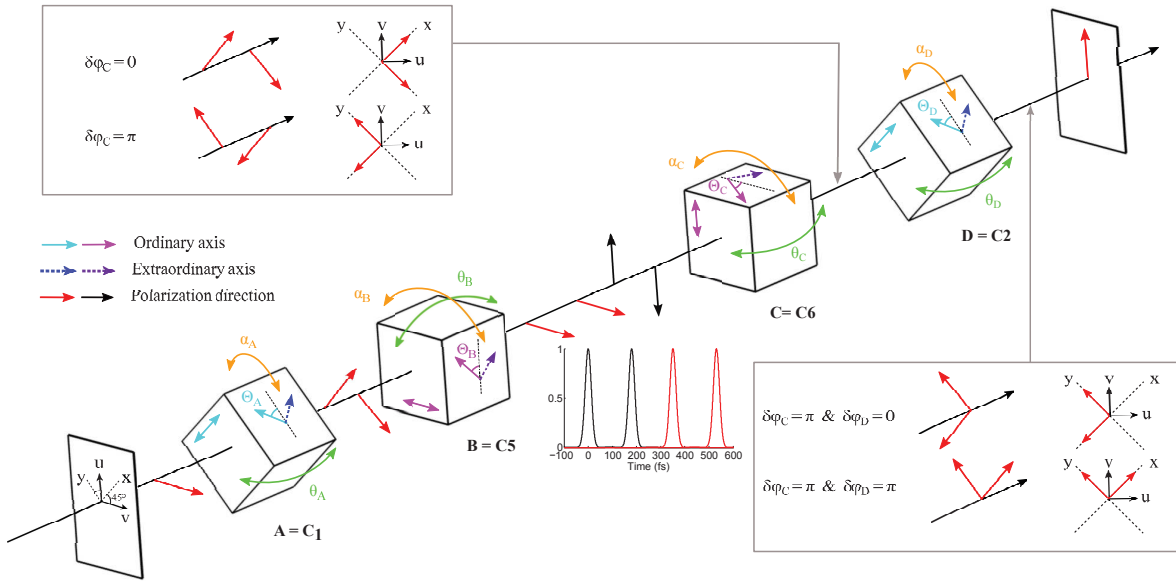
Figure 8.55 – Schematic of the dividing and combining pulse setup with the detailed orientation of the plates.

extraordinary and ordinary axes oriented at 45° from the incident polarization of the laser, creates two equally intense replicas delayed by 179 fs. A second calcite plate (B ie C5), with axis oriented at 45° from the axis of the first plate, divides each replica into two additional sub-pulses delayed by 351 fs. All the plates are mounted on high-resolution manual rotation stages (better than 2 minutes of arc) to achieve a high precision orientation of the plates in the extraordinary direction.

The extraordinary axes of the plates B and C are crossed, whereas the extraordinary axes of A and D can be either parallel, or crossed to each other. In a general way, two orthogonally polarized sub-pulses can be recombined along two crossed polarization directions, depending on their relative phase. After the plate C, the two remaining replicas polarization directions are adjusted with θ_C, the tilt of the plate C in the extraordinary direction. If the phase shift introduced by the plate C ($\delta\varphi_C$) is 0, the fast (resp. slow) replica is polarized along y (resp. x) where $\{\mathbf{x}, \mathbf{y}\}$ form an orthonormal coordinate system oriented at 45° from the system $\{\mathbf{u}, \mathbf{v}\}$, as shown on Fig. 8.55. In this case, the plate D should be crossed with the plate A to make the two remaining replicas in temporal coincidence. If $\delta\varphi_C = \pi$, the fast (resp. slow) replica is polarized along x (resp. y), so the plates A and D should be parallel. The two configurations (A and D parallel, A and D crossed) lead to roughly the same combining efficiency. Theoretically, when A and D are parallel, the combining efficiency is 1 % lower than in the other case because of the small temporal mismatch related to the π phase-shift in plate C.

Once the plates are oriented, the polarization direction of the final combined pulse must be

chosen P or S. The degree of freedom leading to this polarization swap is θ_D. If the phase shift introduced by the plate D is 0 (resp. π), the combined pulse is P-polarized (resp. S-polarized). As previously, a S-polarized combined pulse leads to a the combining efficiency 1 % lower than a P-polarized pulse. This polarization switch ability is very useful to choose the final polarization state with no need of an additional plate, which would introduce more dispersion.
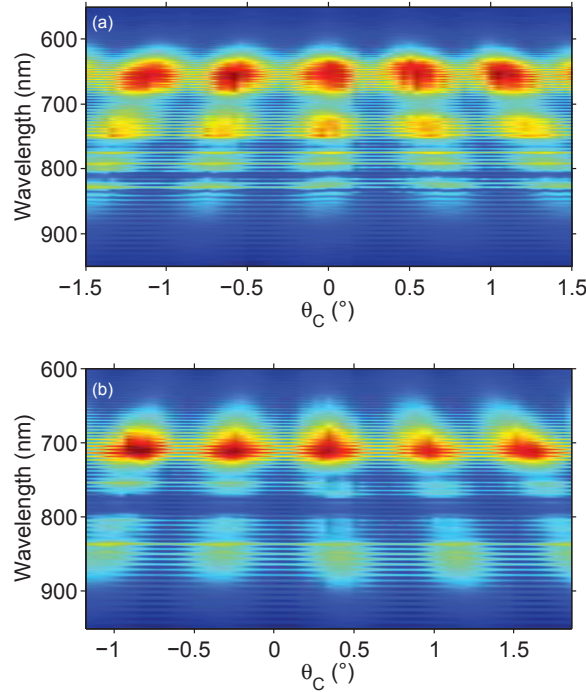
Figure 8.56 – Experimental spectral evolution of the combined pulse with θ_C (a) when C1 and C2 axis are crossed. (b) when C1 and C2 axis are parallel.

As explained in section 8.9, scanning the delay between the replicas by tilting the combining plate is a simple interferometric method to measure the relative spectral phase between the replicas, as well as the phase-mismatch originating from the combining plate. This measurement was performed: Fig. 8.56 shows the experimental spectral evolution of the combined pulse with θ_C, respectively in the case where the axis of A, D are crossed and parallel. Combination occurs regularly with a period of 2π, regardless of the orientation of the last plate with respect to the first plate, as explained before. The fringed spectra are related to the spectral interferences between the two last replicas when they are not combined but further delayed after plate D. When fringes appear, the orientation of plate D does not match the current value of θ_C. This illustrates the critical alignment required on the combining plate C. If θ_C is far from its optimal value, fringes appear on the blue or the red part of the combined pulse spectrum. This criteria, consisting in minimizing the fringes on the whole combined pulse spectrum, is useful to correctly adjust θ_C.

Besides, the corresponding combined pulse spectra are shown on Fig. 8.57. When the axis of A and D are parallel, the combining efficiency if 93.4 % whereas it is 95 % when A and D are crossed. In both cases, the differential group delay dispersion is fully compensated for each replica despite a very broad spectral bandwidth. More precisely, as A (ie C1) and D (ie C2) have the same thickness, the only source of differential group dispersion comes from the thickness difference between B (ie C5) and C (ie C6) and is theoretically about $0.4\ \text{fs}^2$. The relative spectral phase between each couple of replicas was extracted from the θscan with a Fourier analysis and is flat, as expected (Fig. 8.57).

However, when new wavelengths are created between the Dividing Setup and the Combining Setup, the delay won't be fully compensated on the whole bandwidth because of the differential GDD, limiting the combined pulse duration.
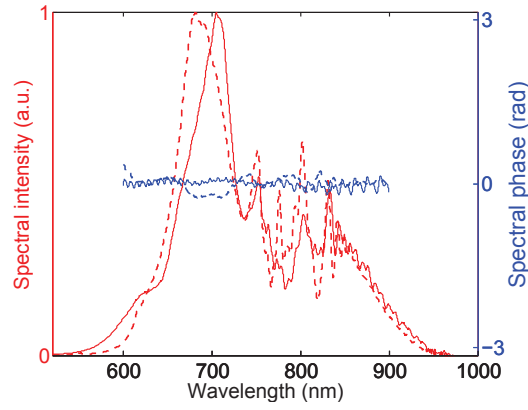
Figure 8.57 – Combined pulses spectra and corresponding relative spectral phase between the 2 last replicas to be combined in two cases: A and D axis are parallel (solid lines); A and D axis are crossed (dashed lines). Spectral phase were extracted from the θscan with a Fourier analysis.

Conclusion on plates and polarization tuning of the combined pulse

To conclude, in the simple implementation presented in this section, combining of 4 broadband replica is achieved with high efficiency. The polarization direction of the final combined pulse can be chosen P or S, without affecting its other properties. When displacing the Dividing Setup before the fiber, experimental conditions are different because the 4 sub-pulses propagate through the fiber and acquire significant temporal phase. Efficient combination is then strongly dependent on the relative spectrum, phase and polarization state of all replicas.

8.11.2 Plates tuning when nonlinear interactions occur between the replicas

The nonlinear stage is now inserted between the Dividing Setup and the Combining Setup (see Fig. 8.18). The plates scheme is given in Fig. 8.58.
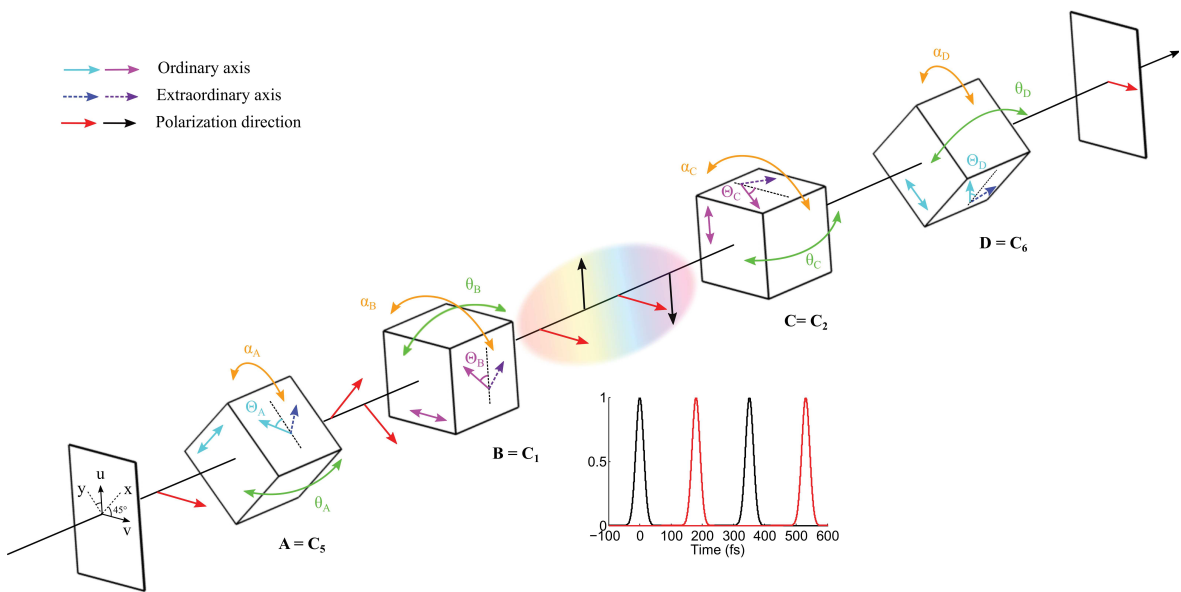
Figure 8.58 – Schematic of the dividing and combining pulse setup with the detailed orientation of the plates.

Initial experiments

At the beginning, we were not aware of all the effects involved in the post-compression of several 170 fs-delayed replicas. In this paragraph, I show a case where the optimization of the Dividing Setup was not carefully achieved. The results shown on Fig. 8.59 and 8.60 were obtained with a Neon pressure of 2 bars, four 300 μJ replicas, (C1,C5) as Dividing Setup and (C6,C2) as Combining Setup.
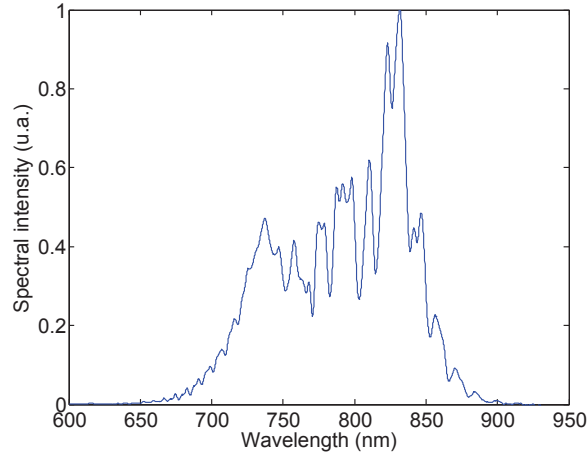
Figure 8.59 – Combined pulse spectrum after combination of 4 replicas with the calcite pairs (C1, C2) and (C5, C6).
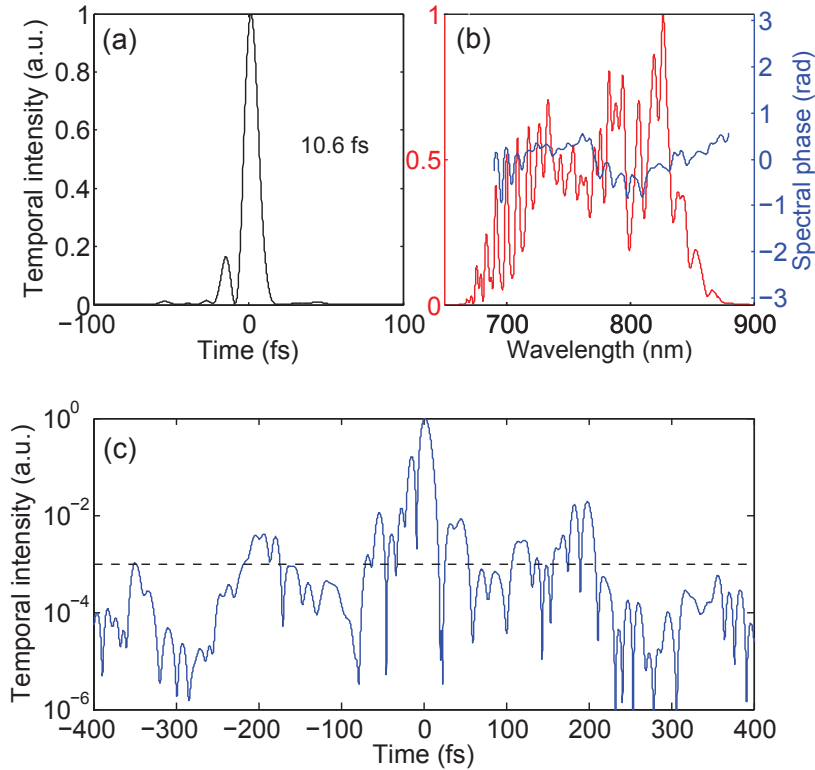
Figure 8.60 – Wizzler-USP measurement of a pulse resulting from the combination of 4 replicas.

The energy per replicas is twice lower than in the case of the combination of two replicas (see section 8.8). The nonlinear interactions between the replicas pedestals could be thus considered as being minimal and with no impact on the combination process. However, the modulations on the combined pulse spectrum (Fig. 8.59) and the bad coherent contrast of the compressed pulse (<

10^2) (Fig. 8.60) prove that this is not correct. Tuning the plates tilts included in the Dividing Setup is crucial to optimize the temporal quality of the final pulse. The physical process involved in this tuning was deeply described in section 8.10.5. Note that nonlinear interactions are accumulated when working with four replicas so that the setup adjustment is considerably more difficult than when working with only two replicas.

Plates tuning for contrast enhancement

The first step is to optimize the Dividing Setup. To do so, only the plate B is placed in the beam and tuned to make the replicas polarizations parallel to P and S. α_B is adjusted looking at the fiber output spectrum to get a fringes periodicity of half of the electric field period when scanning θ_B, according to section 8.10.5. This tuning guarantees that there are θ_B values for which the replicas polarization states are 90° spaced after the nonlinear process. Then, θ_B is fixed to a value leading to a smooth spectrum measured at the output of the fiber. Replicas and pedestals interactions during the nonlinear process are thus limited as far as possible.

Then, the plate A is added. α_A is adjusted to balance the intensity of the four replicas. A good combination will be indeed achieved if the replicas spectra have the same spectral bandwidth. θ_A is then tuned to attenuate the spectral modulations on the fiber output spectrum. Tuning iteratively θ_A and α_A allows to obtain a smooth spectrum at the fiber output. If some modulations remain, θ_A and θ_B can be tuned on a large range to avoid as much as possible the temporal-match between parasite pulses and replicas. However, if the plate is wedged or if the plate is not maintained perfectly in a vertical plane, a large tilt can deteriorate the α tuning performed previously. In this case, an iteration between all the tuning described above is necessary.

The second step consists in adjusting the Combining setup. The four degrees of freedom (α_C, θ_C, α_D, θ_D) are tuned to achieve the same spectrum that the one measured at the output of the fiber, and the maximal combining efficiency.

8.11.3 Differential GDD issues

A last point to mention is that the order of the plates becomes an important parameter when combining four replicas.
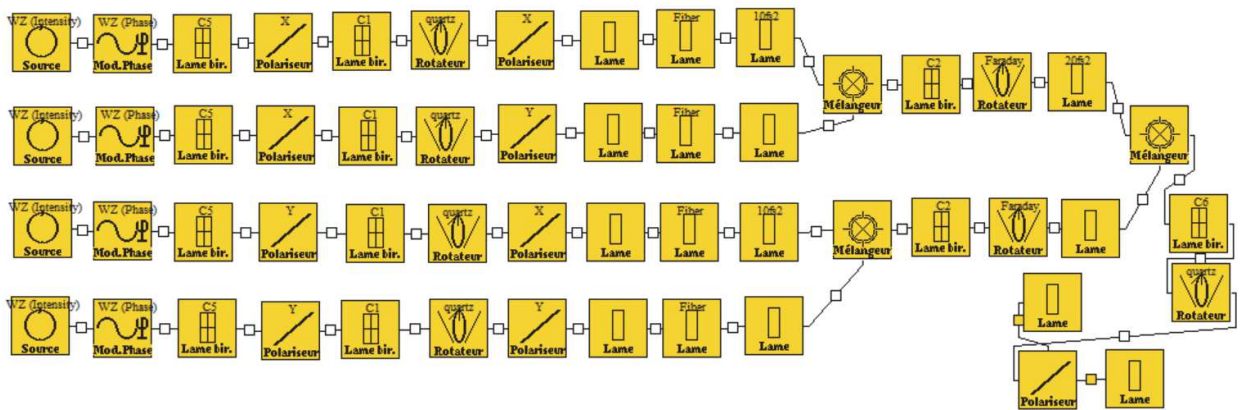
Figure 8.61 – Code architecture (MIRO) for simulating the influence of plates order on the final coherent contrast when working with 4 replicas.

It has been demonstrated that differential GDD ($\Delta\Phi^{(2)}$) limits the spectral bandwidth of the final combined pulse and has to be minimized as far as possible. After the plate C, the edges of the involved spectrum might not be recombined properly if the differential GDD is too high, creating some 'parasitic pulses' perpendicularly polarized to the two remaining replicas. These 'parasitic' replicas are then further delayed in plate D and deteriorate the temporal quality of the

final combined pulse, as pre- and post-pulses. As a result, weak fringes on the spectral edges of the combined pulse might be visible. The amplitude of these pre- and post-pulses depends on the differential GDD of the plate C. On the contrary, differential GDD in the last plate D only limits the spectral bandwidth of the combined pulse. As a consequence, the plate with the lowest differential GDD should be placed first in the Combining Setup.
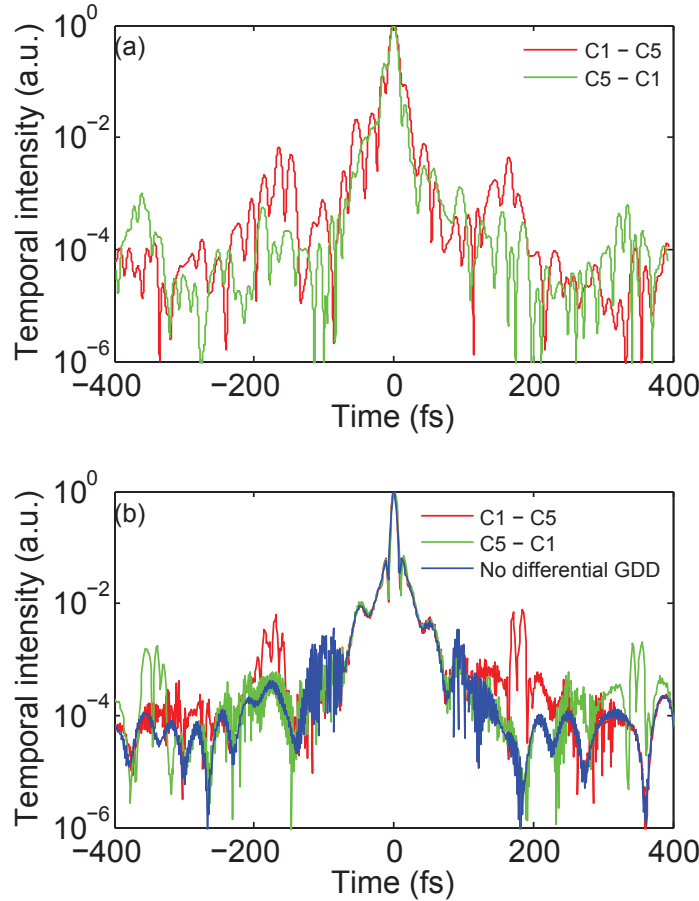
Figure 8.62 – Wizzler-USP measurement (a) and Miro simulation (b) of the combined pulse in two cases: the dividing setup is made of C1 then C5, or the dividing setup is made of C5 then C1.

To illustrate this purpose, experimental temporal characterizations of the combined pulse after compression were performed in two cases: the Combining Setup is composed of C2 (plate C) then C6 (plate D); or C6 (plate C) then C2 (plate D). The Dividing Setup is set accordingly: "'C5 then C1 "' and "'C1 then C5"'. According to Tab. 8.8, the differential GDD for C1-C2 is almost two times lower than for C5-C6. The experiment was optimized with a similar protocol in both cases. As shown in Fig. 8.62(a), the configuration "'C5 then C1"' is advantageous in terms of coherent contrast: parasitic pulses are one order of magnitude below, compared to the other configuration.

Fig. 8.62(b) shows the corresponding simulations performed with MIRO and the ideal case where no differential GDD is applied during combination. The code architecture is given on Fig. 8.61. The three cases were calculated using the same laser source, that is the measured temporal profile of the laser with a Wizzler device. When the differential GDD is not taken into account, the coherent contrast of the compressed combined pulse is better than in the two other cases. Simulations are in good agreement with the experiment and demonstrate the differential GDD influence.

Conclusion on the GDD differential influence

When working with more than two replicas, differential GDD experienced by pulses in the combining plates has a strong influence on the temporal quality of the final pulse. Optimization of the temporal quality of the combined pulse dictates the plates order in the Dividing Setup and thus in the Combining Setup.

8.11.4   Experimental results with 4 replicas

Taking all the precautions described above, the coherent combining of 4 post-compressed replicas was demonstrated in the few-cycle regime. The order of the plates is chosen to optimize the contrast of the final combined pulse, as explained previously. The Neon pressure was fixed to 2.5 bars and the fiber input energy was 1.4 mJ.

Figure 8.63 – HCF output and combined pulse spectra.
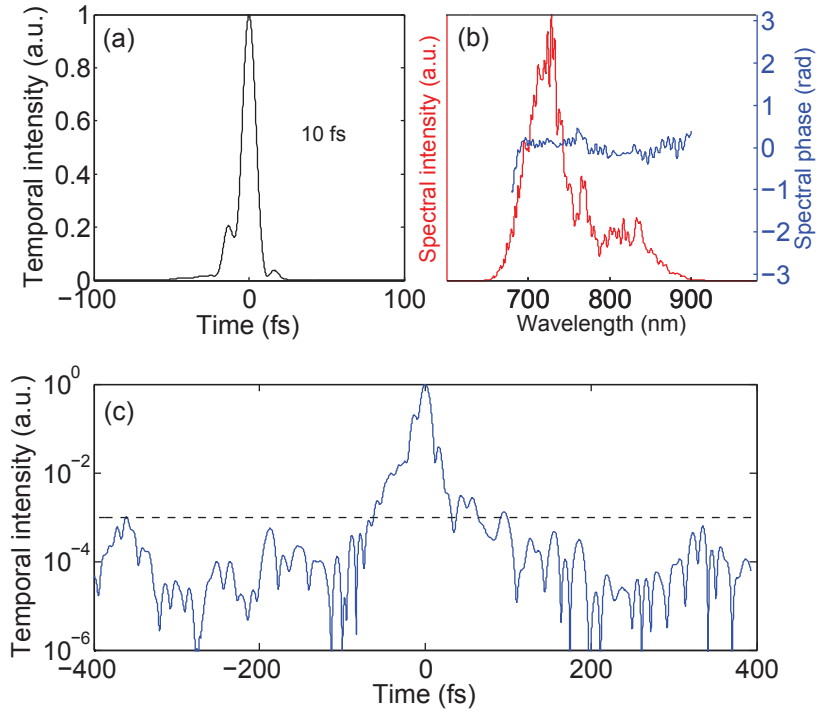
Figure 8.64 – Wizzler-USP measurement of the combined pulse after compression.

The final combined pulse spectrum is shown on Fig. 8.63 together with the HCF output spec-

trum. Both spectra exhibit nearly the same bandwidth, which is limited by the relatively low energy per replica (350 μJ). A slight difference can still be observed at the spectrum edges because of differential GDD, which limits the available spectral bandwidth. The HCF output spectrum is smooth, demonstrati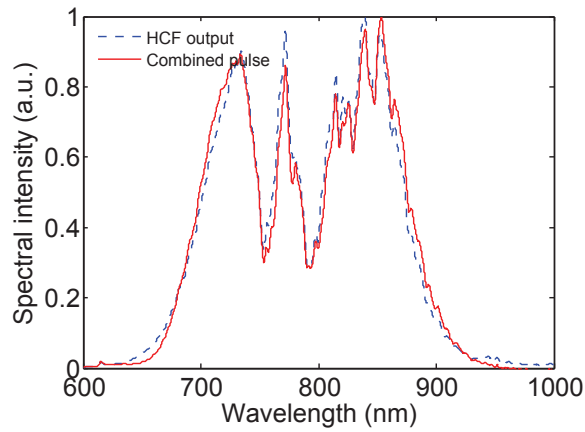ng that the laser pedestal influence is controlled. Differential GDD causes very weak modulations at the long wavelengths of the combined pulse spectrum. The coherent combining efficiency is 92 %. The short and long-term energy stability of the combined pulse is directly related to the pump laser fluctuations inside the FemtoPower. The full width at half maximum duration of the Fourier Transform of the combined pulse spectrum is 6 fs. The Wizzler measurement of the compressed combined pulse is shown on Fig. 8.64. The spectral phase is globally flat with residual oscillations lower than 0.3 rad. The corresponding duration of the 540 μJ pulses is 10 fs. Fig. 8.64c demonstrates that the proposed optimization procedure is successful, as the coherent contrast is hardly above 10^{-3}.

8.12   Conclusion

The study proposed here proved for the feasibility of implementing pulse dividing and combining in a mJ-class hollow-fiber post-compressor. This technique enables to decrease the peak intensity by a factor 2 to 4 according to the replicas number, and to overcome the energy limitation encountered with such post-compressors.

For the first time, the passive coherent combining of two and even four replicas was performed successfully in the few-cycle regime. Broadband pulse dividing and combining was achieved without major difficulty. However, when a nonlinear stage is inserted between the Dividing and the Combining Setups, the temporal quality of the combined pulse can be affected by polarization changes prior to the fiber input, as well as nonlinear interactions between the replicas. A detailed analysis was performed to study the effects of depolarization before the fiber, the laser pedestals influence and the differential GDD impact in the Combining Setup. Solutions are proposed to overcome these deleterious effects and generate high temporal quality combined pulses with significant combining efficiency. Regarding the duration, contrast, energy and CEP stability performances we obtained, the coherent combining technique is very promising for the post-compression of highly intense pulses in the framework of demanding applications like attosecond generation.

Chapter 9

Application of pulse dividing and combining to N_2^+ air lasing experiments

This chapter aims to demonstrate the robustness of the pulse dividing and combining technique, which was implemented during an experiments campaign. During the last weeks of my phD, I had indeed the opportunity to perform laser filamentation experiments with the ILM group. Over the past few years, they intensively studied the N_2^+ lasing generation from an air filament. However, physical mechanisms involved in the air lasing process remain not well understood. A way to discriminate the various hypotheses about the air lasing effect mechanism is to use ultra-short pulses and in particular their CEP-dependance properties. In this context, air lasing experiments were performed with sub-5 fs pulses from the pulse dividing and combining setup I implemented during my PhD.

9.1   Introduction

Laser filaments can be generated as far as few kilometers thanks to the nonlinear propagation of powerful femtosecond lasers in air. A filament results from a dynamic competition between self-focusing due to the refractive index change by Kerr effect, ionization and diffraction. Intensity is kept high and constant along the entire filament, which creates a plasma column.

   Filamentation induces side secondary radiations, in particular a white light cone source in the laser propagation direction that can be used for broadband spectroscopy applications [150]. More recently, it was shown that the plasma column acts as an amplifier medium when pumped by short and intense mid-infrared pulses. Strong forward stimulated emissions were observed at, among others, 391 nm and 428 nm. These wavelengths correspond to the line emission of ionized nitrogen molecules [151]. Such emissions can be observed with a single 800 nm femtosecond laser source, without any external seeding pulse [152]. Seeding is actually provided by the second harmonic generated around 400 nm (responsible for the 391 nm radiation) and the super-continuum white light (responsible for the 428 nm radiation), all generated during the filamentation process of the incident laser pulses. Note that the 428 nm radiation can be observed if the laser spectrum is broadened enough via SPM during propagation through the filament to cover the corresponding transition of the N_2^+ ions.

   There are several theories to explain the physical mechanism involved in the air lasing effect.

   One theory suggests that the air lasing effect results from the amplification of a weak harmonic pulse in the presence of population inversion [151, 153]. This population inversion mechanism was attributed to many controversial process [154, 151, 155, 156, 157, 158, 159, 160, 161] that I won't detail here. In a very recent publication [162], performing the air lasing experiment with ultra short pulse (sub-5 fs) enlightened that the mechanism involved in the population inversion of ions N_2^+ could be related to the strong field-induced post-ionization coupling of the three first electronic states of N_2^+, the first excited state acting as a population reservoir. In other words, the first excited state would allow at the same time the population transfer to the second excited state and the

ground state depletion. Although this theory is not entirely satisfying because strong hypotheses were made on the initial wave function, this paper demonstrates that air lasing could be achieved with sub-5 fs pulses, meaning that only 4 to 5 fs are necessary to achieve the population inversion.

The ILM group proposed another theory: air lasing would be induced by multiple electrons recollisions [163], as illustrated on Fig. 9.1. When a neutral nitrogen molecule is placed in a intense laser field, an electron from the outer orbital is removed, accelerated and then driven back by the electric field to the parent molecular ion, where it collides inelastically with an inner orbital electron. Such a population transfer is characterized by a strong dependance upon the laser polarization, as demonstrated in [163]. Besides, CEP should play a prominent role in the process, as in the case of the recollision-controlled fragmentation of polyatomic molecules [164].
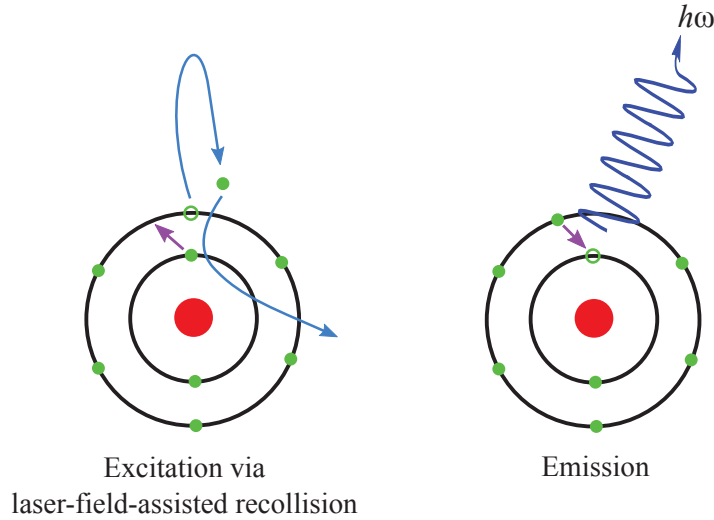
Figure 9.1 – Scenario to explain the air lasing effect which would originate in multiple electrons recollisions.

As ultra-short laser pulses were demonstrated to be relevant for air lasing generation [162], it can be interesting to explore the laser parameters influence when performing air lasing experiments in the few-cycle regime. In a first step, the chirp influence on the air lasing signal was investigated with 5 fs pulses. Previous experiments were indeed performed with another laser source at LOA (Salle Orange) and a chirp scan highlighted that the maximum air lasing signal was obtained for a non zero incident chirp, whereas harmonics 13, 15 and 17 were optimal for a zero incident chirp. This behavior was not really expected so that another experiment run was required to confirm or not this result. In a second step, the CEP influence is investigated. A CEP dependance of the air lasing signal would make the ILM group theory the most plausible.

9.2 Experimental setup

The experimental setup is illustrated on Fig. 9.2 and is similar to the one presented in section 8.6. The plate C1 allows pulse dividing into two replicas and combination occurs in the plate C2, located after the Neon filled fiber. The fiber transmission at 2 bars is about 61 %. The Thin Film Polarizer (TFP) allows discrimination of the combined energy. Compression is achieved using a bench of 12 chirped mirrors and thin wedges. The pulse energy after these wedges was between 500 and 600 μJ on a daily basis. To know the pulse duration at the filament position, the distance from the wedges to the XPW crystal of the Wizzler-USP must be the same than the distance from the wedges to the filament (≈ 70 cm here). A ≈ 2 cm long filament is produced by using a 25 cm focal length parabola, as illustrated on Fig. 9.3. The white light cone emission propagates through filters before being focused in a fiber spectrometer with a 10 cm or 2 cm focal length lens. The choice of the filters is crucial to observe properly the emission of interest. The 428 nm emission was observed with a pass-band filter (FGB25M, Thorlabs) and 2 BG40 filters.
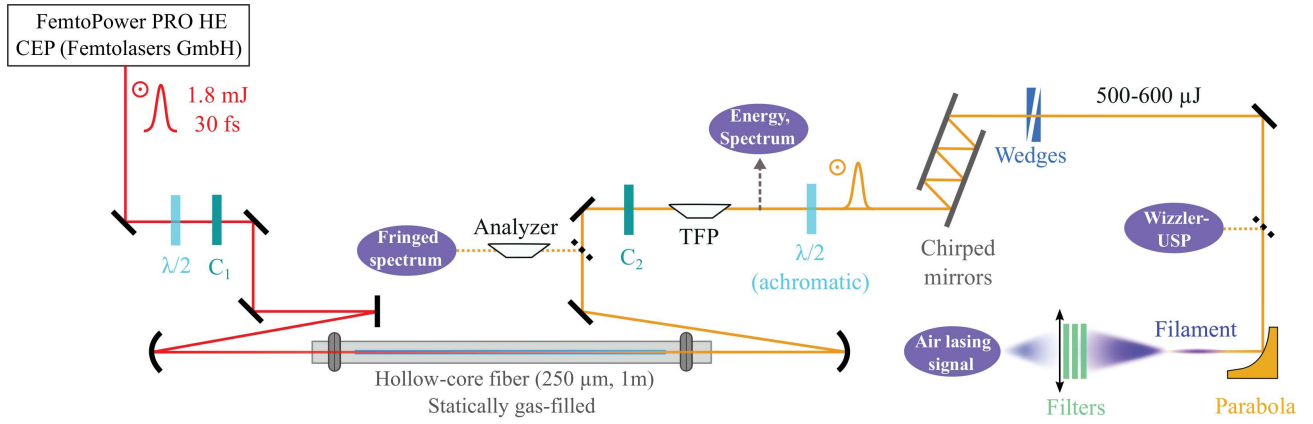
Figure 9.2 – Setup of the air lasing experiment. The calcite plate C1 (resp. C2) allows pulse dividing (resp. pulse combining).
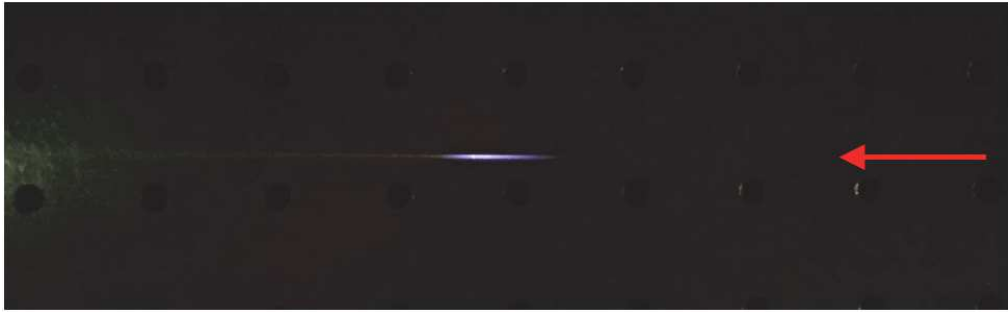
Figure 9.3 – Picture of the ≈ 2 cm long filament. The direction of the incident laser pulses is indicated in red.
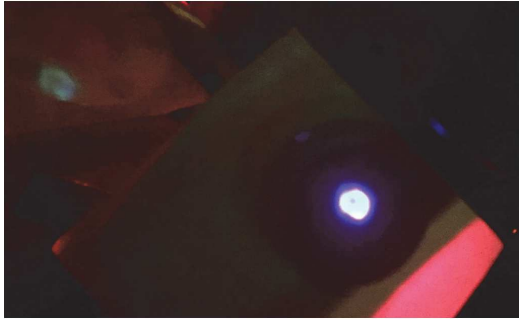
Figure 9.4 – Doughnut shape of the blue lasing emission beyond the filters.
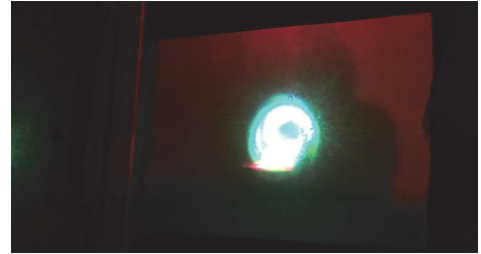
Figure 9.5 – Doughnut shape of emission reflected by the filter BG40.

Fig. 9.4 and Fig. 9.5 exhibit the doughnut pattern of the 428 nm lasing radiation (pictures quality is quite bad as no performing camera was available). It is not clear on the picture because of the non adapted exposure time but we obtained a very clean doughnut shape, meaning that the spatial distribution of the pump laser was optimal. It was suggested in [160] that this doughnut pattern of the 428 nm single pass lasing emission originates in the spatial distribution of the white-light seeding pulse.

9.3   Experimental results

9.3.1   Air lasing when optimizing the combining efficiency

The C2 plate tilt is tuned to maximize the combining efficiency. A Wizzler measurement of the combined compressed pulse was performed in this configuration (see Fig. 9.6). The pulse exhibits

a duration of 4.9 fs (Fig. 9.6a) and an excellent temporal quality: the contrast is better than 10^{-3} (Fig. 9.6c). The spectral phase (Fig. 9.6b) is globally flat with residual oscillation due to the chirped mirrors.
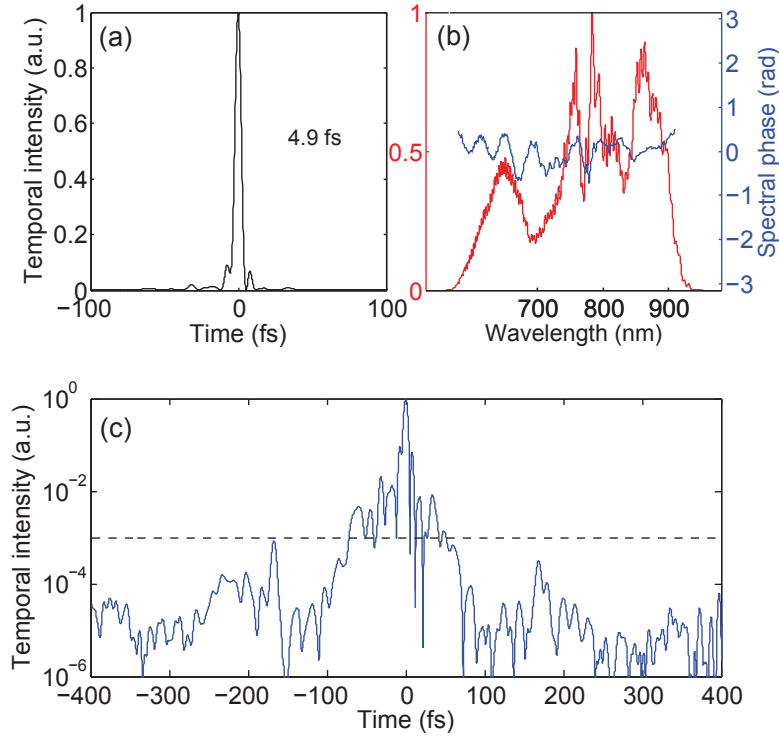
Figure 9.6 – Wizzler-USP measurement of the combined pulse after compression.

Using a 10 cm focal length lens to couple the lasing radiation in the spectrometer, three main peaks are observed at 357 nm, 391 nm and 428 nm in the forward direction (Fig. 9.8). These emissions correspond to specific transitions in the N$_2^+$ molecules, as illustrated in Fig. 9.7. Note that experiments performed with few-cycle laser pulses in [162] allowed only the generation of a lasing emission at 391 nm. An radiation at 357 nm was observed in [151], but it was obtained with a specific pump wavelength and not in a self-seeded configuration. Here, when optimizing the fiber spectrometer to maximize the 391 nm lasing emission, the intensity radiation was more than seven times larger than the one of the white light laser signal taken around 410 nm. Because of the spatial chirp, the lasing radiations are not all maximal for a similar position of the spectrometer fiber. We chose to optimize the 428 nm radiation, playing with the focusing conditions (2 cm focal lens) and the fiber alignment. The resulting signal is shown on Fig. 9.9.

9.3.2   Air lasing when optimizing the combined pulse duration

As explained in section 8.9, it is possible to optimize either the combining efficiency, either the combined pulse duration. When performing the air lasing experiments, it was noticed once that the filament emitted a stronger acoustic wave when the C2 plate tilt was tuned to maximize the combined pulse duration at the cost of the combined pulse energy. This phenomenon was not observed systematically probably because of the interweaving of many parameters for filament optimization as pulse energy, spatial distribution, central wavelength and spectral chirp. However, it highlights how the combining plate offers a degree of freedom to optimize the filamentation process, especially when the other parameters are borderline. A Wizzler measurement was performed in these conditions (see Fig 9.10). The spectral hole around 600 nm is related to the differential GDD experienced by the replicas in the combining plate, resulting in a modulated spectral phase at this wavelength. Coherent contrast is therefore slightly deteriorated.

B$^2\Sigma_u^+$

X$^2\Sigma_g^+$

$v' = 2$
$v' = 1$
$v' = 0$

X$^1\Sigma_g^+$

$v = 1$
$v = 0$

1 => 0 : 357 nm
0 => 0 : 391 nm
0 => 1 : 428 nm

Energy

Internuclear distance
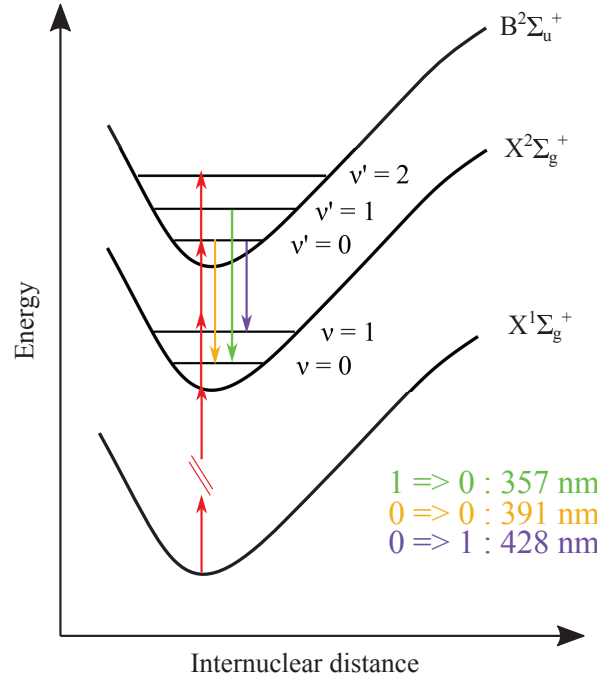
Figure 9.7 – Energy-level diagram of ionized and neutral nitrogen molecules. The wavelengths correspond-ing to the lasing signals observed in the experiment are indicated.
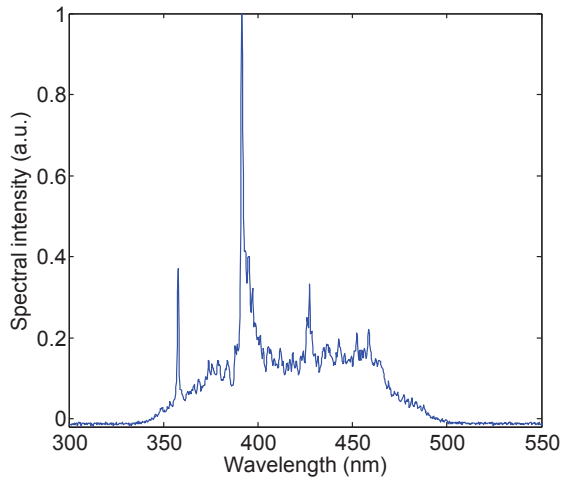
Figure 9.8 – Forward spectrum of air lasing recorded with a 10 cm focal length lens as a coupling optics in the spectrometer. One can observe laser emission at 391 nm, 428 nm and 358 nm.
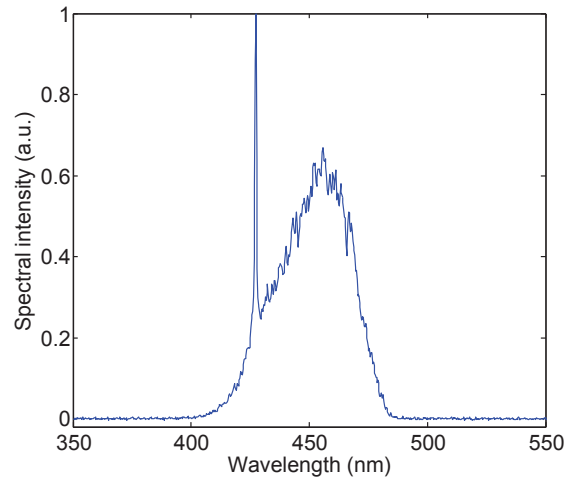
Figure 9.9 – Forward spectrum of air lasing recorded with a 2 cm focal length lens as a coupling optics in the spectrometer. A strong laser emission is noticed at 428 nm.

In these conditions, a chirp scan was performed, reducing or increasing the glass quantity with the thin wedges in a range of $\approx 20\,\text{fs}^2$. The implicit issue is indeed to know if the air lasing signal is optimal for a non zero incident chirp. To do so, the 428 nm lasing emission was systematically recorded, as shown on Fig. 9.11. The air-generated third harmonic signal was also recorded, us-ing a single UG11 filter (see Fig. 9.12). The third harmonic signal is taken as a reference, with its maximum intensity for a zero incident chirp. The results show that pulses air lasing signal is optimal for a slightly negative chirp (-3,6 fs^2). Furthermore, the lasing spectra maxima were extracted and corrected from the white light level signal at 438 nm. These data are shown on Fig. 9.13 and com-pared to the third harmonic signal maxima. Both signals evolves similarly with the incident chirp and seem to be maximum for a close to zero incident chirp.
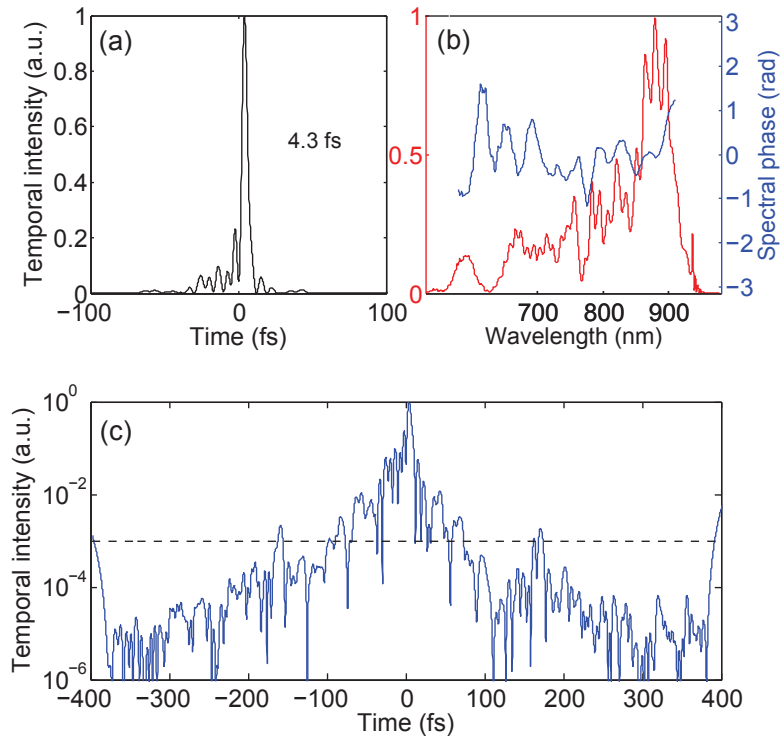
Figure 9.10 – Wizzler-USP measurement of the combined pulse after compression when optimizing the combined pulse duration.
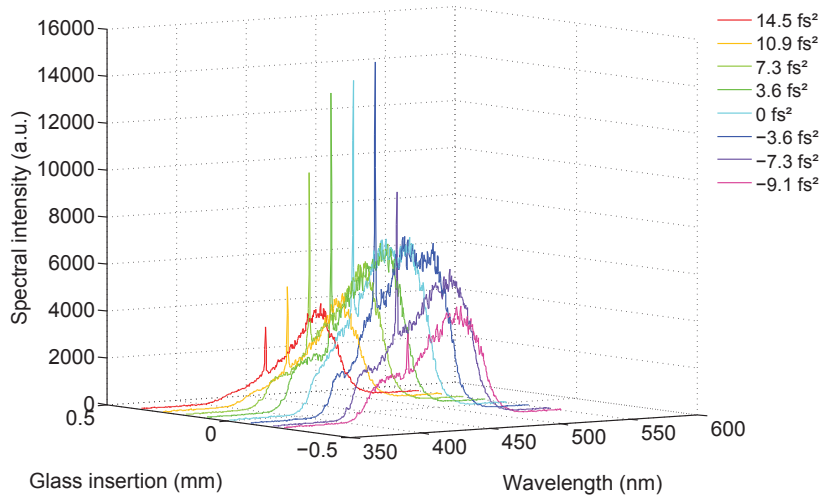
Figure 9.11 – Chirp scan - 428 nm lasing emission as a function of the glass quantity insertion. The corresponding chirp values are given in the legend.

9.3.3   Chirp scan coupled with Wizzler measurements

The comparison of the air lasing signal to the third harmonic one did not allow to conclude clearly. To clarify if the air lasing signal is optimal for a non zero incident chirp, another chirp scan was performed but with systematic Wizzler-USP measurements (see Fig. 9.14 and 9.15). Note that this device is not able to characterize 5 fs pulses featuring a chirp above 20 fs^2, which is not a problem here as it corresponds to the considered chirp range. The curves shown on Fig. 9.15 enable to conclude that the lasing emission is optimal for the minimum incident pulse duration.
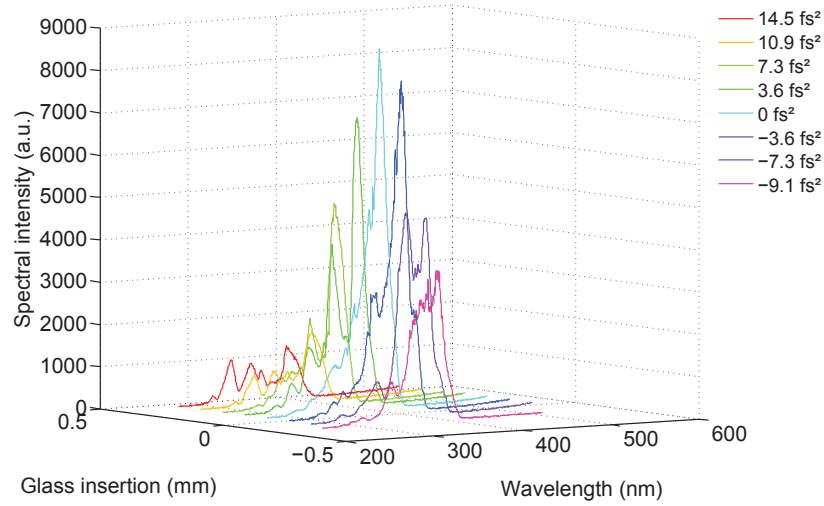
Figure 9.12 – Chirp scan - Third harmonic generation in air as a function of the glass quantity insertion. The corresponding chirp values are given in the legend.
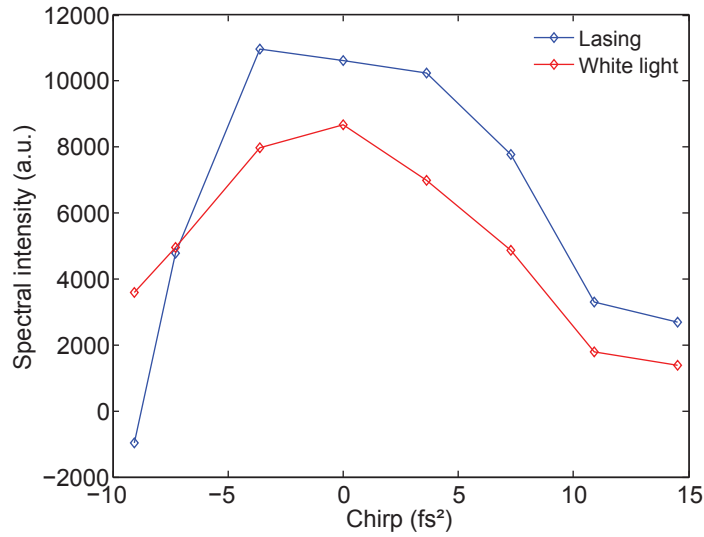
Figure 9.13

9.3.4 CEP dependance of the air lasing signal: preliminary results

Finally, the CEP dependance of the air lasing signal was investigated. To do so, the CEP drift was measured using a f-2f interferometer interfaced with a software from Menlo Systems performing a slow feedback on the stretcher inside the FemtoPower. The CEP noise was about 300 mrad because of a strong and fast instability of the pump laser. CEP variation is achieved using thin wedges. Two scans are shown on Fig. 9.16. The laser fluctuation is measured at the FemtoPower output prior to the post-compression setup and is about 3.5 % in both cases. It is hard to discriminate the CEP contribution to the air lasing signal from the laser instability one. However, it seems that the air lasing signal intensity varies periodically with CEP (period $\approx$ 3 rad). These preliminary results must be confirmed by other runs of experiments in better conditions, especially after a maintenance operation by the pump laser supplier. If the CEP dependance of the air lasing signal is confirmed by further experiments, the theory of multiple electrons recollisions proposed by the ILM group will be consistent.
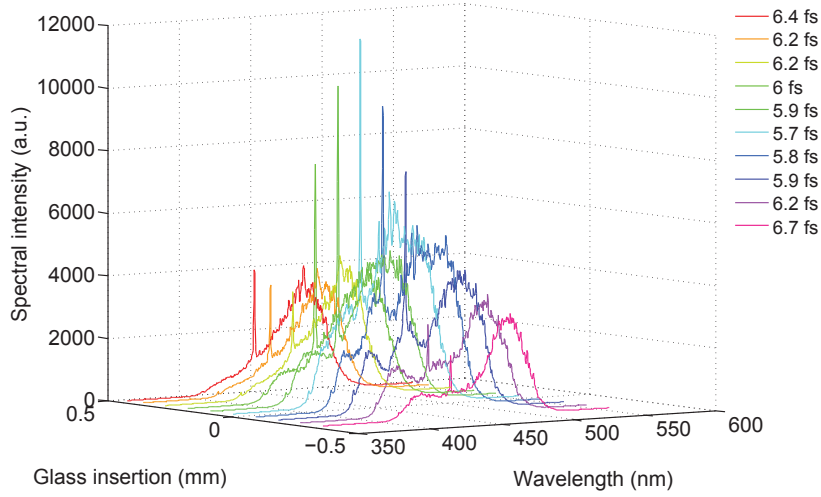
Figure 9.14 – Chirp scan coupled with systematic Wizzler measurements - 428 nm lasing emission as a function of the incident chirp. Durations given by the device are indicated in the figure legend.
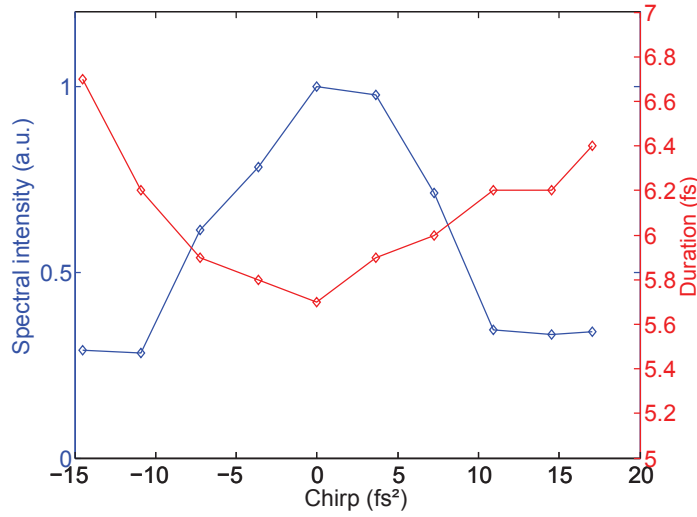
Figure 9.15 – Air lasing emission maximum and incident pulse duration as a function of chirp.

CEP-scan 1

CEP-scan 2
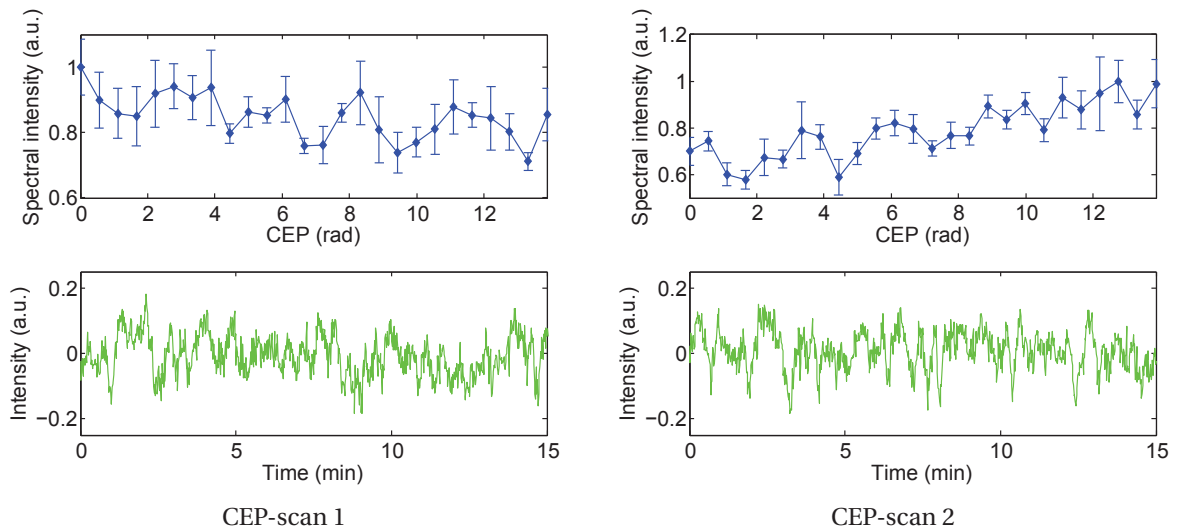
Figure 9.16 – The intensity of the air lasing signal is plotted in blue as a function of CEP. The green curve corresponds to the laser fluctuations during the scan.

9.4 Conclusion

These experiments demonstrate the robustness of the pulse dividing and combining-based post-compressor. A strong air lasing signal was obtained, meaning that the seed pulses had optimal temporal and spatial quality. I underlined how it is possible to maximize the air lasing signal, optimizing either pulse duration or pulse energy with the tilt of the combining plate. It is possible to overcome the differential GDD limitation inherent to the combining plate and to achieved pulse durations down to 4 fs, keeping the seed pulse coherence.

The chirp scan study enables to conclude that the air lasing signal is maximum for a zero incident chirp. This conclusion disproves results obtained previously in Salle Orange with 40 fs pulses. Otherwise, some preliminary results about the CEP dependance of the air lasing signal are shown. The interpretation of these results is limited by the strong instability of the laser. Much work remains thus to be done to decide which physical mechanism is involved in the air lasing effect.

General conclusion

This thesis was carried out within the framework of the development of a unique few-cycle laser source with an increased energy on target compared to the current Salle Noire 2.0. This new high contrast few-cycle CEP-stabilized Terawatt-class 1 kHz laser should help exploring attosecond pulse generation in the relativistic regime. In this context, the beginning of my PhD was dedicated to dimensioning calculations for the design of the entire laser chain. This involved the optical design of the key optical systems (stretcher and compressor), the amplification process simulations and a preliminary study on thermal issues. The selected configuration for the pulse stretching and compression design is an Öffner-type stretcher and a Transmission Gratings Compressor. The optical aberrations and spectral transmission of the stretcher were experimentally validated. The stretcher capability to preserve CEP stability still remains to characterize when a Dazzler will be available to perform pulse compression prior to the CEP measurement device. The results of the amplification simulations highlighted that 25 mJ, 20 fs compressed pulses can be achieved at the second CPA output with a two-passes home-made power amplifier pumped by a 100 W laser and seeded by a commercial amplifier (FemtoLasers). Today, 100 W pump lasers are commercially available (Photonics Industries) and are not a limit to the Salle Noire 3.0 development. The main topical issue is the control of thermal effects in the power amplifiers. The thermal study proposed in this thesis should help in the future characterization of the cryogenic cooling system used in the last power amplifier. These theoretical considerations were completed by the experimental characterization of the front-end through temporal measurements, CEP noise measurements and a spatio-temporal coupling estimation. The effect of nonlinear temporal diffraction on the laser contrast was particularly highlighted by both experiments and simulations.

There are many work prospects for the development of the Salle Noire 3.0 laser. To date, the knowledge about the control of thermal effects in Ti:Sa crystals is limited. The behavior of the layer between the crystal and its mount is not well understood, especially at low temperatures. The lack of data on the optical and mechanical properties of the considered materials for various temperatures set a limit to this study. This is why a solid knowledge about thermal issues can be developed in a first step rather via experimental tests than numerical simulations. The use of a deformable mirror could be also considered to correct the optical aberrations induced by thermal effects in the second CPA. Another critical point is the presence of pre- and post-pulses that are all the more so intense because of nonlinear temporal diffraction, occurring even for low B integral values. Spatial pulse division and combination could be considered to further decrease the B integral in the power amplifier and in the compressor. However, an active combination scheme could be required in these cases. Concerning the CEP stabilization issues, a scheme based on several loops at different stages of the laser system would prevent from a too strong noise that cannot be corrected at the laser back-end, as observed in Salle Noire 2.0. Finally, the development of a TERMITES software that reconstructs the spatio-temporal profile of the laser beam in real time would help to correct directly the eventual misalignment of the compressor. However, the data volume produced by a TERMITES measurement is so huge that we can wonder if the development of another technique would be more suited to instantaneous data processing, as required for laser alignment.

The novelty and originality of this thesis work come from the study of different options to post-compress multi-mJ pulses down to the few-cycle regime (< 10 fs). Two post-compression campaigns were performed. One consisted in implementing a XPW setup (Cross-polarized wave gen-

eration) as a post-compressor of a 10 mJ, 25 fs, 1 kHz laser source (Salle Noire 2.0). 11 fs pulses were produced, but with spectro-temporal deformations because of the nonlinear effects in the GRISM compressor and in the entrance window of the vacuum setup. Although the result is mitigated with the considered laser source (the Salle Noire 2.0 laser is strongly constrained by its stretcher-compressor design for CEP stability issues), this post-compression technique may be promising for sources with reduced non-linearities in the compression stage. In any case, an unprecedented conversion efficiency about 40 % was achieved with a single crystal and remains unexplained.

The other option consisted in implementing a pulse dividing and combining setup in a hollow-core fiber post-compressor. For the first time, coherent combining was achieved with few cycle pulses. In these experiments, temporal pulse division and recombination were passively achieved using carefully oriented calcite plates. The setup proved its robustness, producing in a routinely way 6 fs, CEP-stable pulses with high efficiency, stability and temporal quality. Regarding the duration, contrast, energy and CEP stability performances we obtained, the coherent combining technique is very promising for the post-compression of highly intense pulses in the framework of demanding applications like attosecond generation.

A simple interferometric method for measuring the relative spectral phase between two replicas was demonstrated. This method enabled the measurement of the phase mismatch in the combining plate, as well as that induced by eventual cross-phase-modulation or ionization processes during propagation in the fiber. This method is also of fundamental interest because it enables to study the non-linearities within the gas-filled capillary, using the second replica as a probe. The establishment of ionization could be thus accurately studied.

A detailed analysis of the limitations to the combining process was proposed. The impact of the ionization process, the polarization changes within and prior to the fiber, the nonlinear interactions between the pulse replicas and the differential GDD experienced by the replicas in the combining plate, was deeply investigated. This study helped to extend the setup to fourfold coherent combining. 10 fs pulses were produced with a high efficiency and a contrast similar to that one of the initial laser source.

Because of the limitations mentioned above, a number of four replicas is the limit in the few-cycle regime with a setup based on temporal pulse division and combination. To increase the number of replicas, spatial pulse division via a Sagnac interferometer together with temporal division should be considered. Although this setup requires caution to protect the laser source from the polarizer leakage which directly goes back in the amplifier, it would decrease the peak intensity on the fiber entrance by a factor 8. Increasing the number of replicas is not the only line of work. The experiments were indeed performed with the front-end of the new laser chain, delivering 30 fs pulses with an energy of 1 to 2 mJ. A validation at higher energy levels still needs to be done. In this case, the plates design should be carefully calculated. The aperture of the plates should be large enough to limit the nonlinear effects. This constrains the thickness of the plates and consequently their crystallographic orientation: the differential GDD in the combining plates should be minimized, always maintaining a sufficient inter-replicas delay to limit the nonlinear interactions between the replicas. To overcome this last issue, the passive pulse division and combination technique could be combined with the use of a gradient pressure and circular polarizations.

Appendix A

Dispersion influence on a Gaussian pulse

This appendix aims to calculate changes experienced by a light pulse during propagation through a z-long dispersive medium. The frequency-dependence of the medium refractive index affects the temporal amplitude, spectral phase and CEP of a light pulse. I introduce the parameter Γ, as defined in Tab. A.1.

Physical quantity	Definition	FTL pulse	Dispersed pulse
Electric field	$E(t) = E_0 \exp\left[-\Gamma t^2 + j\omega_0 t\right]$	$\Gamma_0 \in \mathbb{R}$	$\Gamma \in \mathbb{C}$
			$\Gamma(z) = a - jb$
Temporal intensity	$I(t) = |E(t)^2| = |E_0^2| \exp\left[\frac{-t^2}{2\sigma_t^2}\right]$	$\sigma_{t0} = \frac{1}{\sqrt{4\Gamma_0}}$	$\sigma_t = \frac{1}{\sqrt{4\operatorname{Re}\Gamma}}$
	Temporal FWHM	$\Delta t_0 = 2\sqrt{2\ln 2}\,\sigma_{t0}$	$\Delta t = 2\sqrt{2\ln 2}\,\sigma_t$

Table A.1 – Expression of the electric field and intensity of a Gaussian pulse. The pulse parameters are defined when it is Fourier Transform Limited (FTL) and after linear propagation through a dispersive medium. The Gaussian pulse intensity distribution is described by σ_{t0} and σ_t, which are the standard deviations when the pulse is respectively FTL and dispersed. The Full Width at Half Maximum (FWHM) are defined in the temporal domain.

Incident electric field

An initial FTL pulse with a CEP set to 0 is considered. Its electric field can be expressed according to Γ_0 and ω_0 as follows:

$$E_0(t) = E_0 \exp\left[-\Gamma_0 t^2 + j\omega_0 t\right] \tag{A.1}$$

The spectral amplitude of the initial electric field is defined as the Fourier Transform (FT) of its temporal amplitude:

$$\widetilde{E_0}(\omega) = TF\left[E_0(t)\right] = E_0' \exp\left[\frac{-(\omega - \omega_0)^2}{4\Gamma_0}\right] \tag{A.2}$$

Calculation of electric field after the dispersive medium

When propagating in a dispersive medium, the incident electric field accumulates a phase Φ. The resulting electric field can be expressed as:

$$\widetilde{E}(z, \omega) = \widetilde{E_0}(\omega) \exp\left[-j\phi(z, \omega)\right] \tag{A.3}$$

170

Considering only the second order phase, the electric field can be written as:

$$\widetilde{E}(z,\omega) = \widetilde{E_0}(\omega) \exp\left[-j\frac{1}{2}\phi^{(2)}(\omega_0)(\omega-\omega_0)^2\right] \tag{A.4}$$

The electric field is then expressed in the temporal domain via an inverse FT as follows:

$$E(z,t) = \int_{-\infty}^{+\infty} \widetilde{E}(z,\omega) \exp(j\omega t)\, d\omega \tag{A.5}$$

$$E(z,t) = \int_{-\infty}^{+\infty} E_0' \exp\left[\frac{-(\omega-\omega_0)^2}{4\Gamma_0}\right] \exp\left[-j\frac{1}{2}\phi^{(2)}(\omega_0)(\omega-\omega_0)^2\right] \exp(j\omega t)\, d\omega \tag{A.6}$$

One can define the parameter Γ for the resulting chirped pulse according to:

$$\frac{1}{\Gamma(z)} = \frac{1}{\Gamma_0} + 2j\phi^{(2)}(\omega_0) \tag{A.7}$$

$$E(z,t) = E_0' \exp(j\omega_0 t) \int_{-\infty}^{+\infty} \exp\left[\frac{-(\omega-\omega_0)^2}{4\Gamma(z)}\right] . \exp\left[j(\omega-\omega_0)t\right]\, d(\omega-\omega_0) \tag{A.8}$$

The integral calculation is performed at the light of:

$$\int_{-\infty}^{+\infty} \exp(-Ay^2 - 2By)\, dy = \sqrt{\frac{\pi}{A}} \exp\left[\frac{B^2}{A}\right] \tag{A.9}$$

The electric field can be then written as:

$$\boxed{E(z,t) = \sqrt{4\pi|\Gamma(z)|}\, E_0'\, \exp(j\omega_0 t) \exp\left[-\Gamma(z)t^2\right]} \tag{A.10}$$

where

$$\boxed{\Gamma(z) = \frac{\Gamma_0\left[1 - 2j\Gamma_0\phi^{(2)}(\omega_0)\right]}{1 + 4\Gamma_0^2\phi^{(2)}(\omega_0)^2} = a - jb \ \text{ avec } \ a = \frac{\Gamma_0}{1 + 4\Gamma_0^2\phi^{(2)}(\omega_0)^2} \ \text{ and } \ b = \frac{2\Gamma_0^2\phi^{(2)}(\omega_0)}{1 + 4\Gamma_0^2\phi^{(2)}(\omega_0)^2}} \tag{A.11}$$

Finally:

$$E(z,t) = \sqrt{4\pi}\,(a^2 + b^2)^{1/4}\, E_0'\, \exp\left[-j\phi_{\text{CEP}}/2\right] \exp(j\omega_0 t) \exp\left[-at^2\right] \exp\left[jbt^2\right] \tag{A.12}$$

$$\boxed{E(z,t) = \mathscr{A} \exp\left[-j\phi_{\text{CEP}}/2\right] \exp(j\omega_0 t) \exp\left[-at^2\right] \exp\left[jbt^2\right]} \tag{A.13}$$

where:

$$\begin{cases} \mathscr{A} = \dfrac{\sqrt{4\pi}}{16\,\sigma_{t0}^4} \dfrac{E_0'}{1 + \left[\dfrac{\phi^{(2)}(\omega_0)}{2\,\sigma_{t0}^2}\right]^2} \\[4ex] \phi_{\text{CEP}} = -\arctan\left[\dfrac{\phi^{(2)}(\omega_0)}{2\,\sigma_{t0}^2}\right] \end{cases} \tag{A.14}$$

$\mathscr{A}$ and ϕ_{CEP} are respectively the amplitude and CEP of the electric field after propagation through the dispersive medium. The pulse stretching ratio is related to $\phi^{(2)}(\omega_0)$. The higher $\phi^{(2)}(\omega_0)$ is, the lower the pulse amplitude is and the higher the CEP shift is.

Chirped pulse duration

With notations of Eq. A.13, the pulse intensity is given by:

$$I(t) \propto \exp\left[-2\,a\,t^2\right] = \exp\left[-\frac{t^2}{2\sigma_t^2}\right] \tag{A.15}$$

By identification:

$$\sigma_t = \frac{1}{2\sqrt{a}} \tag{A.16}$$

According to Eq. A.11 and the definition of Γ_0 (Tab. A.1):

$$\sigma_t = \sigma_{t0}\sqrt{1 + \frac{\phi^{(2)}(\omega_0)^2}{4\sigma_{t0}^4}} \geq \sigma_{t0} \tag{A.17}$$

The FWHM of the chirped pulse can be deduced:

$$\boxed{\Delta t = \Delta t_0\,\sqrt{1 + \frac{16\,(\ln 2)^2\,\phi^{(2)}(\omega_0)^2}{\Delta t_0^4}}} \tag{A.18}$$

As an example, a 5 fs FWHM pulse propagating through a 500 μm fused silica plate is considered. The group velocity dispersion for this material is 36 fs.^{2}mm^{-1} at 800 nm [50] so that the final pulse duration is about 20.7 fs and the CEP shift is 1.3 rad. Accurate spectral phase and CEP control is thus crucial when working with ultrashort pulses.

In these calculations, I considered only the second order term of the spectral phase, which affects the pulse duration. The third order term makes the pulse shape asymmetrical, without affecting significantly the pulse duration. It also degrades the temporal coherent contrast, creating parasitic pulses. Higher order terms are also detrimental to the temporal coherent contrast.

Temporal chirp parameter

The b parameter, as defined in Eq. A.11, is the temporal chirp parameter:

$$b = \frac{1}{2\sigma_{t0}^2}\frac{\dfrac{\phi^{(2)}(\omega_0)}{\sigma_{t0}^2}}{1 + \left[\dfrac{\phi^{(2)}(\omega_0)}{\sigma_{t0}^2}\right]^2} \tag{A.19}$$

For a significant stretching ratio, $\phi''(\omega_0) \gg \sigma_{t0}^2$ and b can approximated according to:

$$\boxed{b \approx \frac{1}{2\phi^{(2)}(\omega_0)}} \tag{A.20}$$

The b factor is widely used in the numerical simulations performed in this thesis. b can be also expressed according the spectral and temporal FWHM of the pulse intensity, respectively written $\Delta\omega$ and Δt, as:

$$\widetilde{E}(z,\omega) \propto \exp\left[-\frac{(\omega - \omega_0)^2}{4\Gamma(z)}\right] = \exp\left[-\frac{(\omega - \omega_0)^2}{2}\frac{a}{2(a^2 + b^2)}\right] \tag{A.21}$$

For a Gaussian pulse:

$$\left|\widetilde{E}(z,\omega)\right|^2 = \exp\left[-4\,\ln 2\left[\frac{\omega - \omega_0}{\Delta\omega}\right]^2\right] \tag{A.22}$$

Finally:

$$\Delta\omega = 2\sqrt{2\ln 2}\,\sqrt{a\left[1+\left[\frac{b}{a}\right]^2\right]} \tag{A.23}$$

According to Eq. A.16:

$$b^2 = \frac{\Delta\omega^2}{4\,\Delta t^2} - \frac{4\,(\ln 2)^2}{\Delta t^4} \tag{A.24}$$

For a significant stretching ratio, the second term is negligible compared to the first one so that:

$$\boxed{b \approx \frac{\Delta\omega}{2\,\Delta t} = \frac{\pi\,c\,\Delta\lambda}{\lambda^2\,\Delta t}} \tag{A.25}$$

$\Delta\lambda$ is the spectral width (FWHM) of the spectral pulse intensity. In practice, I used this expression to calculate the b factor in the numerical simulations performed with MIRO [165].

Appendix B

Layout of the FemtoPower
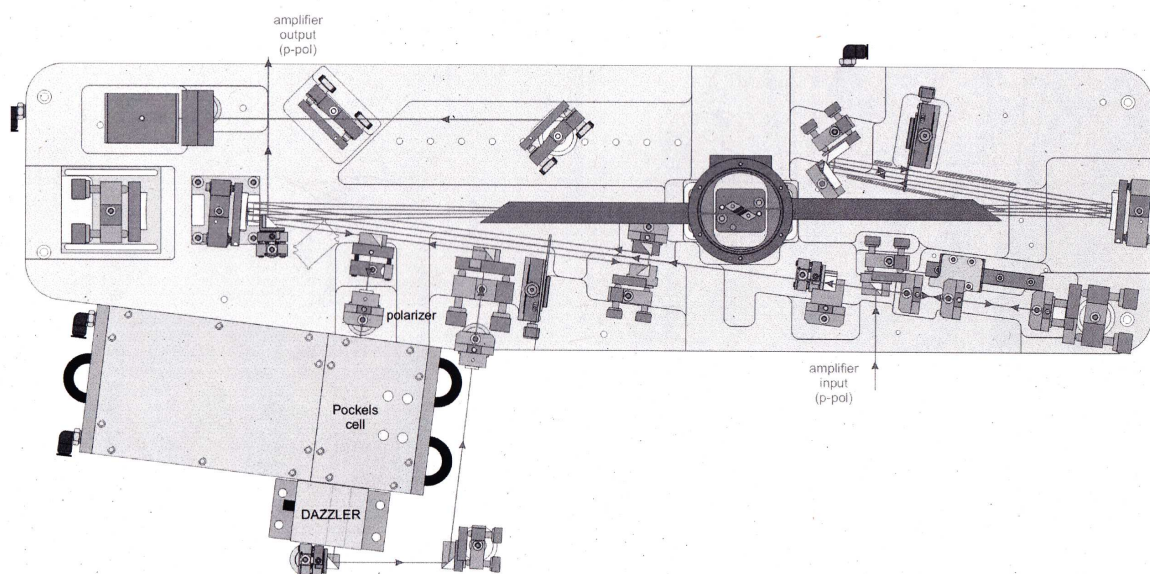
Figure B.1 – Scheme of the FemtoPower (Femtolasers GmbH).
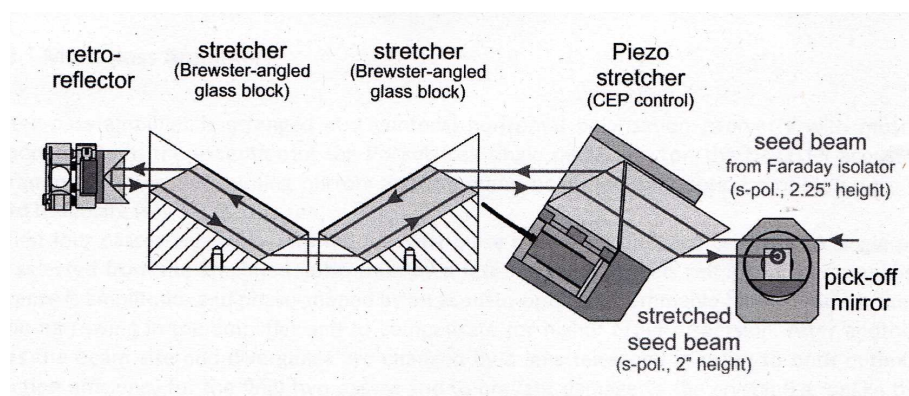
Figure B.2 – Scheme of the bulk stretcher included in CPA 1 (Femtolasers GmbH).

Appendix C

Experimental analysis of the main CEP noise sources in Salle Noire 2.0

To achieve a better understanding of the CEP noise sources, systematic CEP stabilization and measurements were performed at various stage of the laser system in Salle Noire 2.0. This laser source is described in details in [9].
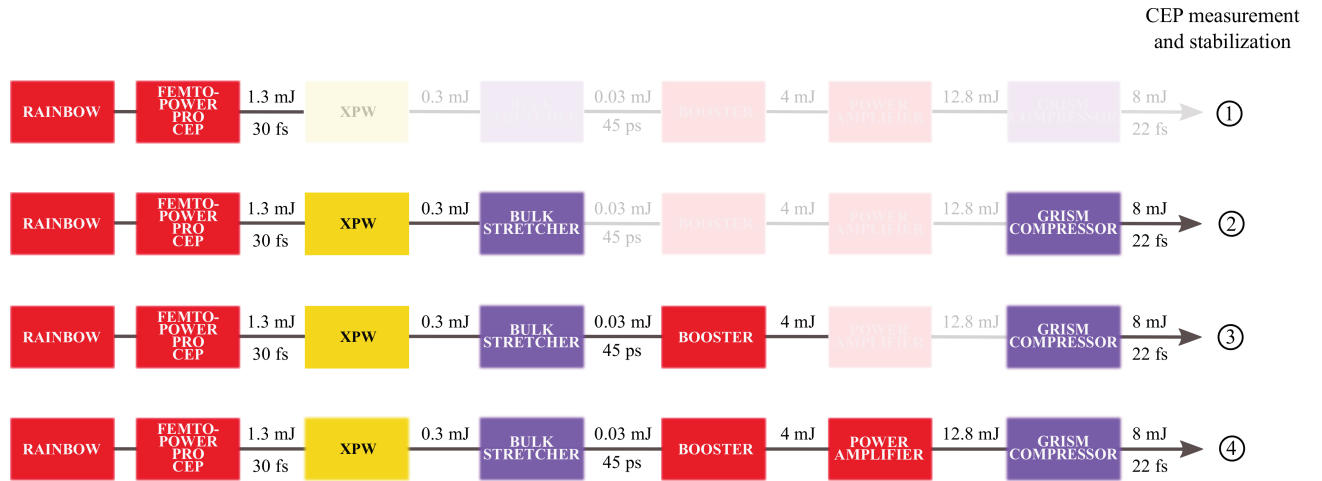
Figure C.1 – Scheme of the different setup of CEP measurement and stabilization performed in Salle Noire 2.0. The bypassed modules are almost transparent.

CEP was measured and stabilized at four different levels of the laser chain, as illustrated on Fig. C.1:

- Measurement 1: CEP is stabilized at the Femtopower output.

- Measurement 2: The beam path is enlarged to the stretcher and compressor.

- Measurement 3: The booster is added in the beam path.

- Measurement 4: the entire laser chain is CEP characterized.

In measurements 2, 3 and 4, pulse compression is achieved adjusting the Grism compressor and the settings of the Dazzler, which is located after the bulk stretcher. The results are shown on Fig. C.2. The power amplifier adds a strong CEP noise that could not be compensated by the slow loop acting on the pump power of the oscillator.

To go further about the noise contribution of the power amplifier, CEP measurements were performed for various seed energy, adjusting the high voltage of the Pockels Cell located between the Booster and the power amplifier. In the amplifier stages, phase noise is indeed related to thermal effects in the crystal, mechanical vibrations induced by the vacuum pump, intensity variations

of the pump laser or nonlinear effects in the amplification medium. A variation of the seed energy of the power amplifier highlights the nonlinear effects contribution, as the vacuum pump and pump power parameters are identical for each measurement. The results are shown on Fig. C.3. For a voltage between 1 kV and 5 kV, the CEP noise is similar whereas when the Pockels Cell voltage is maximum, it becomes almost one order of magnitude higher.

The nonlinear effects in any material can be quantified by the B integral, defined as:

$$B = \frac{2\pi}{\lambda_0} \int_0^L n_2 \max\left[I(z)\right] dz \qquad (C.1)$$

where λ_0 is the central wavelength of the laser, n_2 the nonlinear index of the medium, L the length of the medium and I the pulse intensity. To avoid temporal and spatial distortions in the amplifiers, the cumulative B integral should be lower than 3 to 5 rad [166].

I performed numerical simulation with CommodPro, a MIRO-based code developed by CEA [53] for 3D laser pulse propagation. The B integral is estimated to be about 4.4 rad after three passes in the amplification medium for a pump power of 30 W and a seed energy of 3.5 mJ. The B integral is significant in this amplifier because the stretched pulse duration is limited to 45 ps. Note that the limited stretching ratio is specific to CEP-stable lasers.
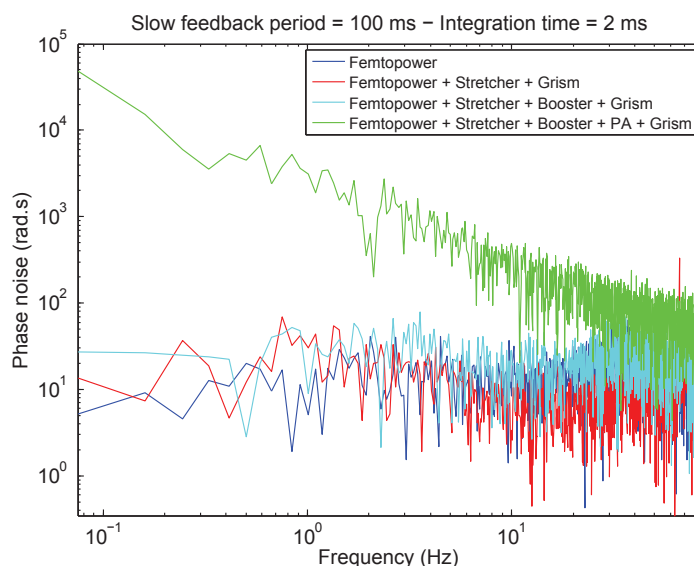
Figure C.2 – CEP measurement and stabilization at various stages of the laser in Salle Noire 2.0.

To conclude, this campaign of CEP measurements in Salle Noire 2.0 demonstrated that CEP stabilization is compatible with a laser architecture 'double CPA' including nonlinear filtering. After the energy upgrade of the Salle Noire 2.0 up to 8 mJ after compression, CEP stabilization was demonstrated [9]. However, the oscillator and the first CPA have to introduce a very low phase noise because the retro-action scheme cannot manage a too strong phase noise. Feedback is indeed performed exclusively on the pump power of the oscillator. When strong phase noise related to nonlinear and thermal effects in the power amplification stages becomes significant, one needs to decouple the fast loop controlling the oscillator from the slow loop controlling the whole laser chain. The CEP stabilization scheme of the Salle Noire 3.0 meets such a constrain, performing a fast stabilization on an AOFS and a slow stabilization on the glass quantity in the pre-amplifier. Experiments performed in Salle Noire 2.0 underlined that the nonlinear and thermal effects in the amplification and compression stages must be minimized as far as possible, keeping in mind that CEP stability of the entire laser chain results of a balance between stretching ratio and B integral.
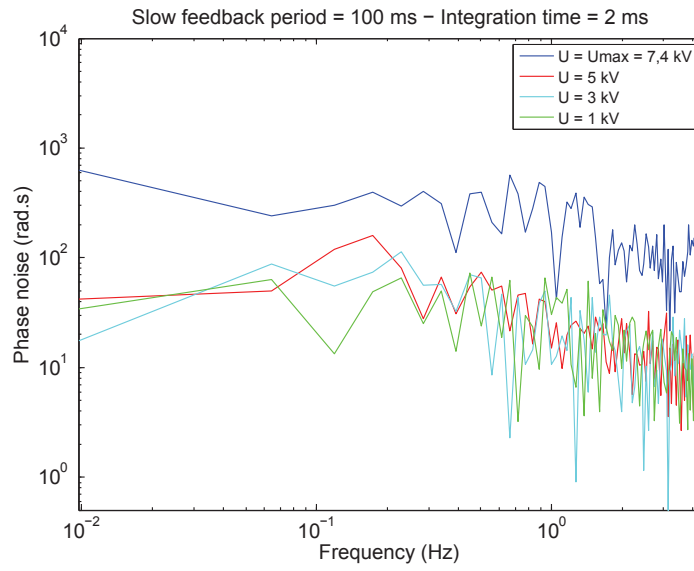
Figure C.3 – CEP measurement and stabilization of the whole laser chain for various seed energies of the power amplifier. The Pockels Cell voltage prior to the power amplifier is indicated in each case.

Appendix D

Laser implementation in Salle Azzurra
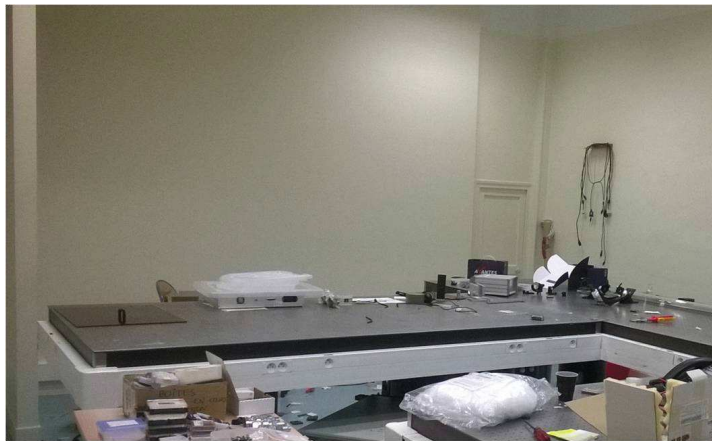
Salle Azzurra at the beginning of my PhD.

Salle Azzurra once the front end of the Salle Noire 3.0 laser and the post-compression stage are installed.
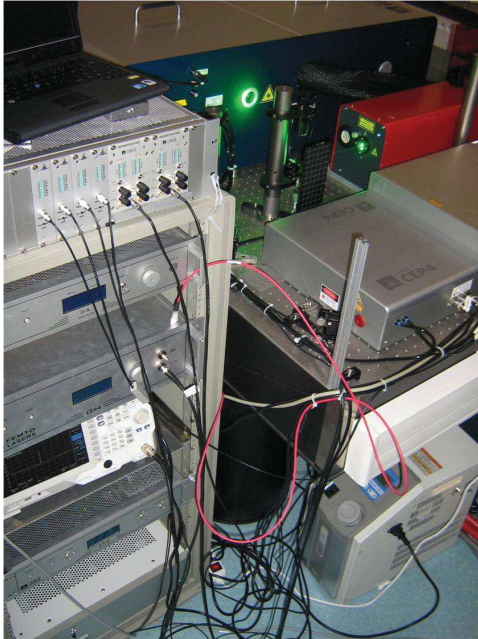
Front-end and its electronics.
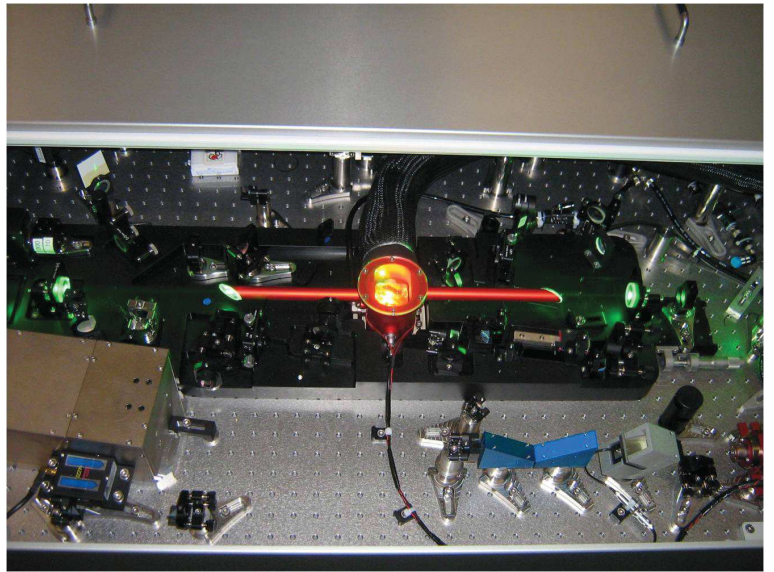
FemtoPower inside.
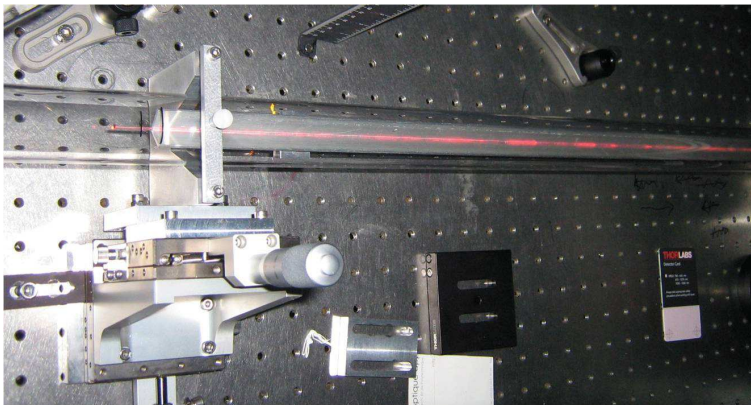
Gas-filled hollow-core fiber used in the pulse dividing and combining post-compressor.

Appendix E

Publications

1. *Carrier-envelope-phase stable, high-contrast, double chirped-pulse-amplification laser system*, A. Jullien, A. Ricci, F. Böhle, J-P. Rousseau, S. Grabielle, N. Forget, **H. Jacqmin**, B. Mercier, and R. Lopez-Martens, **Opt. Lett.** 39, 3774-3777 (2014)

2. *Passive coherent combining of CEP-stable few-cycle pulses from a temporally divided hollow fiber compressor*, **H. Jacqmin**, A. Jullien, B. Mercier, M. Hanna, F. Druon, D. Papadopoulos and R. Lopez-Martens, **Opt. Lett.** 40, 709-712 (2015)

3. *Temporal pulse division in hollow fiber compressors*, **H. Jacqmin**, A. Jullien, B. Mercier and R. Lopez-Martens, **J. Opt. Soc. Am. B** 32, 1901-1909 (2015)

4. *Manifold coherent combining of few-cycle pulses in hollow-fiber compressors*, **H. Jacqmin**, B. Mercier , A. Jullien and R. Lopez-Martens, *Accepted in **Applied Physics B***

Bibliography

[1] P. M. Paul, E. S. Toma, P. Breger, G. Mullot, F. Auge, P. Balcou, H. G. Muller, and P. Agostini, "Observation of a Train of Attosecond Pulses from High Harmonic Generation," *Science*, vol. 292, pp. 1689–1692, June 2001.

[2] M. Hentschel, R. Kienberger, C. Spielmann, G. a. Reider, N. Milosevic, T. Brabec, P. Corkum, U. Heinzmann, M. Drescher, and F. Krausz, "Attosecond metrology.," *Nature*, vol. 414, no. 6863, pp. 509–513, 2001.

[3] F. Krausz, "Attosecond physics," *Reviews of Modern Physics*, vol. 81, pp. 163–234, feb 2009.

[4] L. Gallmann, C. Cirelli, and U. Keller, "Attosecond science: recent highlights and future trends.," *Annual review of physical chemistry*, vol. 63, pp. 447–69, jan 2012.

[5] A. Borot, A. Malvache, X. Chen, A. Jullien, J.-P. Geindre, P. Audebert, G. Mourou, F. Quere, and R. Lopez-Martens, "Attosecond control of collective electron motion in plasmas," *Nat Phys*, vol. 8, no. 4, pp. 416–421, 2012.

[6] F. Quere, "Ultrafast science: Attosecond plasma optics," *Nat Phys*, vol. 5, pp. 1745–2473, June 2009.

[7] R. Loch, P. Martin, T. Ceccotti, P. Monot, F. Quéré, H. George, M. Bougeard, F. Réau, P. DâĂŹO-liveira, and K. Boller, "High-order harmonic and fast ion generation in high intensity laser-solid interactions," in *Laser-Driven Relativistic Plasmas Applied to Science, Industry and Medicine: 2nd International Symposium*, vol. 1153, pp. 94–102, AIP Publishing, 2009.

[8] J. A. Wheeler, A. Borot, S. Monchoce, H. Vincenti, A. Ricci, A. Malvache, R. Lopez-Martens, and F. Quere, "Attosecond lighthouses from plasma mirrors," *Nat Photon*, vol. 6, no. 4, pp. 829–833, 2012.

[9] A. Jullien, A. Ricci, F. Böhle, J.-P. Rousseau, S. Grabielle, N. Forget, H. Jacqmin, B. Mercier, and R. Lopez-Martens, "Carrier-envelope-phase stable, high-contrast, double chirped-pulse-amplification laser system," *Opt. Lett.*, vol. 39, pp. 3774–3777, Jul 2014.

[10] M. Bocoum, M. Thévenet, F. Böhle, B. Beaurepaire, A. Vernier, A. Jullien, J. Faure, and R. Lopez-Martens, "Anticorrelated emission of high harmonics and fast electron beams from plasma mirrors," *Phys. Rev. Lett.*, vol. 116, p. 185001, May 2016.

[11] B. Beaurepaire, A. Vernier, M. Bocoum, F. Böhle, A. Jullien, J.-P. Rousseau, T. Lefrou, D. Douillet, G. Iaquaniello, R. Lopez-Martens, A. Lifschitz, and J. Faure, "Effect of the laser wave front in a laser-plasma accelerator," *Phys. Rev. X*, vol. 5, p. 031012, Jul 2015.

[12] E. Ippen, C. Shank, and A. Dienes, "Passive mode locking of the cw dye laser," *Applied Physics Letters*, vol. 21, no. 8, pp. 348–350, 1972.

[13] R. L. Fork, B. I. Greene, and C. V. Shank, "Generation of optical pulses shorter than 0.1 psec by colliding pulse mode-locking," in *Conference on Lasers and Electro-Optics*, p. WL1, Optical Society of America, 1981.

[14] J. A. Valdmanis, R. L. Fork, and J. P. Gordon, "Generation of optical pulses as short as 27 femtoseconds directly from a laser balancing self-phase modulation, group-velocity dispersion, saturable absorption, and saturable gain," *Opt. Lett.*, vol. 10, pp. 131–133, Mar 1985.

[15] R. L. Fork, C. H. B. Cruz, P. C. Becker, and C. V. Shank, "Compression of optical pulses to six femtoseconds by using cubic phase compensation," *Opt. Lett.*, vol. 12, pp. 483–485, Jul 1987.

[16] C. Rolland and P. Corkum, "Amplification of 70 fs pulses in a high repetition rate xecl pumped dye laser amplifier," *Optics Communications*, vol. 59, no. 1, pp. 64 – 68, 1986.

[17] P. F. Moulton, "Spectroscopic and laser characteristics of ti:al2o3," *J. Opt. Soc. Am. B*, vol. 3, pp. 125–133, Jan 1986.

[18] D. E. Spence, P. N. Kean, and W. Sibbett, "60-fsec pulse generation from a self-mode-locked ti:sapphire laser," *Opt. Lett.*, vol. 16, pp. 42–44, Jan 1991.

[19] U. Keller, G. W. 'tHooft, W. H. Knox, and J. E. Cunningham, "Femtosecond pulses from a continuously self-starting passively mode-locked ti:sapphire laser," *Opt. Lett.*, vol. 16, pp. 1022–1024, Jul 1991.

[20] R. Szipöcs, C. Spielmann, F. Krausz, and K. Ferencz, "Chirped multilayer coatings for broadband dispersion control in femtosecond lasers," *Opt. Lett.*, vol. 19, pp. 201–203, Feb 1994.

[21] R. Szipocs, A. Stingl, C. Spielmann, and F. Krausz, "Chirped dielectric mirrors for dispersion control in femtosecond laser systems," *Proc. SPIE*, vol. 2377, pp. 11–22, 1995.

[22] A. Stingl, R. Szipöcs, M. Lenzner, C. Spielmann, and F. Krausz, "Sub-10-fs mirror-dispersion-controlled ti:sapphire laser," *Opt. Lett.*, vol. 20, pp. 602–604, Mar 1995.

[23] D. Strickland and G. Mourou, "Compression of amplified chirped optical pulses," *Optics Communications*, vol. 55, no. 6, pp. 447 – 449, 1985.

[24] P. Maine, D. Strickland, P. Bado, M. Pessot, and G. Mourou, "Generation of ultrahigh peak power pulses by chirped pulse amplification," *IEEE Journal of Quantum Electronics*, vol. 24, pp. 398–403, Feb 1988.

[25] J. V. Rudd, P. Bado, G. Korn, S. Kane, J. Squier, and G. Mourou, "Chirped-pulse amplification of 55-fs pulses at a 1-khz repetitionrate in a ti:al2o3 regenerative amplifier," *Opt. Lett.*, vol. 18, pp. 2044–2046, Dec 1993.

[26] H. Fattahi, H. G. Barros, M. Gorjan, T. Nubbemeyer, B. Alsaif, C. Y. Teisset, M. Schultze, S. Prinz, M. Haefner, M. Ueffing, A. Alismail, L. Vámos, A. Schwarz, O. Pronin, J. Brons, X. T. Geng, G. Arisholm, M. Ciappina, V. S. Yakovlev, D.-E. Kim, A. M. Azzeer, N. Karpowicz, D. Sutter, Z. Major, T. Metzger, and F. Krausz, "Third-generation femtosecond technology," *Optica*, vol. 1, pp. 45–63, Jul 2014.

[27] S. Backus, C. G. Durfee, G. Mourou, H. C. Kapteyn, and M. M. Murnane, "0.2-tw laser system at 1 khz," *Opt. Lett.*, vol. 22, pp. 1256–1258, Aug 1997.

[28] Y. Nabekawa, Y. Kuramoto, T. Togashi, T. Sekikawa, and S. Watanabe, "Generation of 0.66-tw pulses at 1-khz by a ti:sapphire laser," *Opt. Lett.*, vol. 23, pp. 1384–1386, Sep 1998.

[29] M. Hentschel, Z. Cheng, F. Krausz, and C. Spielmann, "Generation of 0.1-tw optical pulses with a single-stage ti:sapphire amplifier at a 1-khz repetition rate," *Applied Physics B*, vol. 70, no. 1, pp. S161–S164, 2000.

[30] V. Bagnoud and F. Salin, "Amplifying laser pulses to the terawatt level at a 1-kilohertz repetition rate," *Applied Physics B*, vol. 70, no. 1, pp. S165–S170, 2000.

[31] J. Z. H. Yang and B. C. Walker, "0.09-terawatt pulses with a 31% efficient, kilohertz repetition-rate ti:sapphire regenerative amplifier," *Opt. Lett.*, vol. 26, pp. 453–455, Apr 2001.

[32] S. Backus, R. Bartels, S. Thompson, R. Dollinger, H. C. Kapteyn, and M. M. Murnane, "High-efficiency, single-stage 7-khz high-average-power ultrafast laser system," *Opt. Lett.*, vol. 26, pp. 465–467, Apr 2001.

[33] D. M. Gaudiosi, A. L. Lytle, P. Kohl, M. M. Murnane, H. C. Kapteyn, and S. Backus, "11-w average power ti:sapphire amplifier system using downchirped pulse amplification," *Opt. Lett.*, vol. 29, pp. 2665–2667, Nov 2004.

[34] I. Matsushima, H. Yashiro, and T. Tomie, "10 khz 40 w ti:sapphire regenerative ring amplifier," *Opt. Lett.*, vol. 31, pp. 2066–2068, Jul 2006.

[35] S. Chen, M. Chini, H. Wang, C. Yun, H. Mashiko, Y. Wu, and Z. Chang, "Carrier-envelope phase stabilization and control of 1 khz, 6 mj, 30 fs laser pulses from a ti:sapphire regenerative amplifier," *Appl. Opt.*, vol. 48, pp. 5692–5695, Oct 2009.

[36] S. Bohman, A. Suda, T. Kanai, S. Yamaguchi, and K. Midorikawa, "Generation of 5 fs, 5 mJ pulses at 1 kHz using hollow-fiber pulse compression," *Optics Letters*, vol. 35, pp. 1887–1889, Jun 2010.

[37] J.-F. Hergott, O. Tcherbakoff, P.-M. Paul, P. Demengeot, M. Perdrix, F. Lepetit, D. Garzella, D. Guillaumet, M. Comte, P. D. Oliveira, and O. Gobert, "Carrier-envelope phase stabilization of a 20 w, grating based, chirped-pulse amplified laser, using electro-optic effect in a linbo3 crystal," *Opt. Express*, vol. 19, pp. 19935–19941, Oct 2011.

[38] C. Feng, J.-F. Hergott, P.-M. Paul, X. Chen, O. Tcherbakoff, M. Comte, O. Gobert, M. Reduzzi, F. Calegari, C. Manzoni, M. Nisoli, and G. Sansone, "Complete analog control of the carrier-envelope-phase of a high-power laser amplifier," *Opt. Express*, vol. 21, pp. 25248–25256, Oct 2013.

[39] M. Nisoli, S. De Silvestri, and O. Svelto, "Generation of high energy 10 fs pulses by a new pulse compression technique," *Applied Physics Letters*, vol. 68, no. 20, pp. 2793–2795, 1996.

[40] L. Xu, T. W. Hänsch, C. Spielmann, A. Poppe, T. Brabec, and F. Krausz, "Route to phase control of ultrashort light pulses," *Opt. Lett.*, vol. 21, pp. 2008–2010, Dec 1996.

[41] M. Kalashnikov, E. Risse, H. Schonnagel, and W. Sandner, "Ase-temporal contrast of 1010 with a double cpa laser," in *2005 Quantum Electronics and Laser Science Conference*, vol. 3, pp. 2018–2020 vol. 3, May 2005.

[42] A. Jullien, O. Albert, F. Burgy, G. Hamoniaux, J.-P. Rousseau, J.-P. Chambaret, F. Augé-Rochereau, G. Chériaux, J. Etchepare, N. Minkovski, and S. M. Saltiel, "10(-10) Temporal Contrast for Femtosecond Ultraintense Lasers By Cross-Polarized Wave Generation.," *Optics letters*, vol. 30, pp. 920–2, apr 2005.

[43] A. Offner, "Unit power imaging catoptric anastigmat," July 24 1973. US Patent 3,748,015.

[44] A. Poppe, R. Holzwarth, A. Apolonski, G. Tempea, C. Spielmann, T. Hänsch, and F. Krausz, "Few-cycle optical waveform synthesis," *Applied Physics B*, vol. 72, no. 3, pp. 373–376, 1999.

[45] T. Fuji, J. Rauschenberger, A. Apolonski, V. S. Yakovlev, G. Tempea, T. Udem, C. Gohle, T. W. Hänsch, W. Lehnert, M. Scherer, and F. Krausz, "Monolithic carrier-envelope phase-stabilization scheme.," *Optics letters*, vol. 30, pp. 332–4, feb 2005.

[46] A. Poppe, R. Holzwarth, A. Apolonski, G. Tempea, C. Spielmann, T. Hänsch, and F. Krausz, "Few-cycle optical waveform synthesis," *Applied Physics B*, vol. 72, no. 3, pp. 373–376, 2001.

[47] F. Lücking, A. Assion, A. Apolonski, F. Krausz, and G. Steinmeyer, "Long-term carrier-envelope-phase-stable few-cycle pulses by use of the feed-forward method.," *Optics letters*, vol. 37, pp. 2076–8, jun 2012.

[48] S. Koke, C. Grebing, H. Frei, A. Anderson, A. Assion, and G. Steinmeyer, "Direct frequency comb synthesis with arbitrary offset and shot-noise-limited phase noise," *Nature Photonics*, vol. 4, pp. 462 – 465, May 2010.

[49] I. H. Malitson and M. J. Dodge, "Refractive index and birefringence of synthetic sapphire," *J. Opt. Soc. Am.*, vol. 62, p. 1405, 1972.

[50] M. N. Polyanskiy, "Refractive index database," *http://refractiveindex.info*, 2016.

[51] D. E. McCumber, "Einstein relations connecting broadband emission and absorption spectra," *Phys. Rev.*, vol. 136, pp. A954–A957, Nov 1964.

[52] X. Liu, R. Wagner, a. Maksimchuk, E. Goodman, J. Workman, D. Umstadter, and a. Migus, "Nonlinear temporal diffraction and frequency shifts resulting from pulse shaping in chirped-pulse amplification systems.," *Optics letters*, vol. 20, pp. 1163–5, may 1995.

[53] O. Morice, "Mirò: Complete modeling and software for pulse amplification and propagation in high-power laser systems," *Optical Engineering*, vol. 42, no. 6, pp. 1530–1541, 2003.

[54] C. Bourassin-Bouchet, M. Stephens, S. de Rossi, F. Delmotte, and P. Chavel, "Duration of ultrashort pulses in the presence of spatio-temporal coupling," *Opt. Express*, vol. 19, pp. 17357–17371, Aug 2011.

[55] G. Pretzler, A. Kasper, and K. Witte, "Angular chirp and tilted light pulses in cpa lasers," *Applied Physics B*, vol. 70, no. 1, pp. 1–9, 2000.

[56] S. Akturk, X. Gu, P. Bowlan, and R. Trebino, "Spatio-temporal couplings in ultrashort laser pulses," *Journal of Optics*, vol. 12, no. 9, p. 093001, 2010.

[57] V. Gallet, F. Qéré, and G. Pariente, "Dispositifs de caractérisation spatio-temporelle du champ électrique d'un système laser."

[58] V. Gallet, *Experimental devices for the spatiotemporal characterization of femtosecond high-power laser chains.* Theses, Université Paris Sud - Paris XI, Sept. 2014.

[59] A. Ricci, A. Jullien, J.-P. Rousseau, and R. Lopez-Martens, "Front-End Light Source for aWaveform-Controlled High-Contrast Few-Cycle Laser System for High-Repetition Rate Relativistic Optics," *Applied Sciences*, vol. 3, no. 1, pp. 314–324, 2013.

[60] A. Ricci, A. Jullien, J.-P. Rousseau, Y. Liu, A. Houard, P. Ramirez, D. Papadopoulos, A. Pellegrina, P. Georges, F. Druon, N. Forget, and R. Lopez-Martens, "Energy-scalable temporal cleaning device for femtosecond laser pulses based on cross-polarized wave generation.," *The Review of scientific instruments*, vol. 84, p. 043106, apr 2013.

[61] L. Canova, X. Chen, A. Trisorio, A. Jullien, A. Assion, G. Tempea, N. Forget, T. Oksenhendler, and R. Lopez-Martens, "Carrier-envelope phase stabilization and control using a transmission grating compressor and an aopdf," *Opt. Lett.*, vol. 34, pp. 1333–1335, May 2009.

[62] P. Tournois, "Sur un interféromètre de phase à variation linéaire du temps de retard en fonction de la fréuence," *C.R. Acad. Sc. Paris*, pp. 455–458, 1969.

[63] A. Ricci, A. Jullien, N. Forget, V. Crozatier, P. Tournois, and R. Lopez-Martens, "Grism compressor for carrier-envelope phase-stable millijoule-energy chirped pulse amplifier lasers featuring bulk material stretcher," *Opt. Lett.*, vol. 37, pp. 1196–1198, Apr 2012.

[64] Z. Chang, "Carrier-envelope phase shift caused by grating-based stretchers and compressors," *Appl. Opt.*, vol. 45, pp. 8350–8353, Nov 2006.

[65] T. Fordell, M. Miranda, A. Persson, and A. L'Huillier, "Carrier-envelope phase stabilization of a multi-millijoule, regenerative-amplifier-based chirped-pulse amplifier system," *Opt. Express*, vol. 17, pp. 21091–21097, Nov 2009.

[66] G. Cheriaux, B. Walker, L. F. Dimauro, P. Rousseau, F. Salin, and J. P. Chambaret, "Aberration-free stretcher design for ultrashort-pulse amplification," *Opt. Lett.*, vol. 21, pp. 414–416, Mar 1996.

[67] N. Forget, V. Crozatier, and P. Tournois, "Transmission bragg-grating grisms for pulse compression," *Applied Physics B*, vol. 109, no. 1, pp. 121–125, 2012.

[68] A. Cotel, *Réseaux de diffraction à multicouches diélectriques pour la compression d'impulsions petawatt par mosaïques de réseaux.* PhD thesis, Ecole polytechnique, Palaiseau, 2007. Thèse de doctorat dirigée par Le Blanc, Catherine - Spécialité: Optique et physique des lasers.

[69] V. Bagnoud and F. Salin, "Influence of optical quality on chirped-pulse amplification: characterization of a 150-nm-bandwidth stretcher," *J. Opt. Soc. Am. B*, vol. 16, pp. 188–193, Jan 1999.

[70] S. Chénais, F. Balembois, F. Druon, G. Lucas-leclin, and P. Georges, "Thermal Lensing in Diode-Pumped Ytterbium Lasers - Part I : Theoretical Analysis and Wavefront Measurements," *IEEE Journal of Quantum Electronics*, vol. 40, no. 9, pp. 1217–1234, 2004.

[71] P. Albers, E. Stark, and G. Huber, "Continuous-wave laser operation and quantum efficiency of titanium-doped sapphire," *J. Opt. Soc. Am. B*, vol. 3, pp. 134–139, Jan 1986.

[72] R. C. Powell, G. E. Venikouas, L. Xi, J. K. Tyminski, and M. R. Kokta, "Thermal effects on the optical spectra of al2o3:ti3+," *The Journal of Chemical Physics*, vol. 84, no. 2, pp. 662–665, 1986.

[73] S. Ferré, *Caractérisation expérimentale et simulation des effets thermiques d'une chaîne laser ultra-intense à base de saphir dopé au titane.* PhD thesis, Ecole polytechnique, Palaiseau, 2002. Thèse de doctorat dirigée par Chambaret, Jean-Paul - Spécialité: Optique et physique des lasers.

[74] J. Didierjean, *Thermal study of laser crystals, design of single-crystal-fiber lasers.* Theses, Université Paris Sud - Paris XI, Dec. 2007.

[75] Y. F. Chen, T. M. Huang, C. F. Kao, C. L. Wang, and S. C. Wang, "Optimization in scaling fiber-coupled laser-diode end-pumped lasers to higher power: influence of thermal effect," *IEEE Journal of Quantum Electronics*, vol. 33, pp. 1424–1429, Aug 1997.

[76] F. Sanchez, M. Brunel, and K. Aït-Ameur, "Pump-saturation effects in end-pumped solid-state lasers," *Journal of the Optical Society of America B*, vol. 15, p. 2390, sep 1998.

[77] S. Chenais, *New ytterbium-doped laser materials : diode-pumped operation and investigation of thermal effects.* Theses, Université Paris Sud - Paris XI, Dec. 2002.

[78] C. Pfistner, R. Weber, H. Weber, S. Merazzi, and R. Gruber, "Thermal beam distortions in end-pumped Nd:YAG, Nd:GSGG, and Nd:YLF rods," *IEEE Journal of Quantum Electronics*, vol. 30, pp. 1605–1615, jul 1994.

[79] A. C. DeFranzo and B. G. Pazol, "Index of refraction measurement on sapphire at low temperatures and visible wavelengths," *Appl. Opt.*, vol. 32, pp. 2224–2234, May 1993.

[80] Wagner, "Theoretical analysis and design of high-performance frequency converters for LI-DAR systems," *PhD thesis*, 2009.

[81] M. A. Herráez, D. R. Burton, M. J. Lalor, and M. a. Gdeisat, "Fast two-dimensional phase-unwrapping algorithm based on sorting by reliability following a noncontinuous path.," *Applied optics*, vol. 41, no. 35, pp. 7437–7444, 2002.

[82] R. M. Goldstein, H. A. Zebker, and C. L. Werner, "Satellite radar interferometry: Two-dimensional phase unwrapping," *Radio Science*, vol. 23, no. 4, pp. 713–720, 1988.

[83] C. Torrence and G. P. Compo, "A practical guide to wavelet analysis," *Bulletin of the American Meteorological Society*, vol. 79, no. 1, pp. 61–78, 1998.

[84] F. Boehle, M. Kretschmar, A. Jullien, M. Kovacs, M. Miranda, R. Romero, H. Crespo, U. Morgner, P. Simon, R. Lopez-Martens, and T. Nagy, "Compression of cep-stable multi-mj laser pulses down to 4 fs in long hollow fibers," *Laser Physics Letters*, vol. 11, no. 9, 2014.

[85] I. a. Walmsley and C. Dorrer, "Characterization of ultrashort electromagnetic pulses," *Advances in Optics and Photonics*, vol. 1, no. 2, p. 308, 2009.

[86] A. Moulet, S. Grabielle, C. Cornaggia, N. Forget, and T. Oksenhendler, "Single-shot, high-dynamic-range measurement of sub-15 fs pulses by self-referenced spectral interferometry," *Opt. Lett.*, vol. 35, pp. 3856–3858, Nov 2010.

[87] L. Lepetit, G. Chériaux, and M. Joffre, "Linear techniques of phase measurement by femtosecond spectral interferometry for applications in spectroscopy," *J. Opt. Soc. Am. B*, vol. 12, pp. 2467–2474, Dec 1995.

[88] M. Miranda, T. Fordell, C. Arnold, A. LâĂŹHuillier, and H. Crespo, "Simultaneous compression and characterization of ultrashort laser pulses using chirped mirrors and glass wedges," *Optics Express*, vol. 20, no. 1, p. 688, 2012.

[89] C. Hauri, a. Guandalini, P. Eckle, W. Kornelis, J. Biegert, and U. Keller, "Generation of intense few-cycle laser pulses through filamentation - parameter dependence.," *Optics express*, vol. 13, no. 19, pp. 7541–7547, 2005.

[90] L. Gallmann, T. Pfeifer, P. M. Nagel, M. J. Abel, D. M. Neumark, and S. R. Leone, "Comparison of the filamentation and the hollow-core fiber characteristics for pulse compression into the few-cycle regime," *Applied Physics B: Lasers and Optics*, vol. 86, no. 4, pp. 561–566, 2007.

[91] X. Chen, X. Li, J. Liu, P. Wei, X. Ge, R. Li, and Z. Xu, "Generation of 5 fs, 0.7 mJ pulses at 1 kHz through cascade filamentation.," *Optics letters*, vol. 32, no. 16, pp. 2402–2404, 2007.

[92] G. Stibenz, N. Zhavoronkov, and G. Steinmeyer, "Self-compression of millijoule pulses to 7.8 fs duration in a white-light filament," *Conference on Lasers and Electro-Optics and 2006 Quantum Electronics and Laser Science Conference, CLEO/QELS 2006*, vol. 31, no. 2, pp. 274–276, 2006.

[93] M. Nurhuda, A. Suda, S. Bohman, S. Yamaguchi, and K. Midorikawa, "Optical pulse compression of ultrashort laser pulses in an argon-filled planar waveguide," *Phys. Rev. Lett.*, vol. 97, p. 153902, Oct 2006.

[94] C. L. Arnold, B. Zhou, S. Akturk, S. Chen, A. Couairon, and A. Mysyrowicz, "Pulse compression with planar hollow waveguides: A pathway towards relativistic intensity with table-top lasers," *New Journal of Physics*, vol. 12, 2010.

[95] J. Chen, A. Suda, E. J. Takahashi, M. Nurhuda, and K. Midorikawa, "Compression of intense ultrashort laser pulses in a gas-filled planar waveguide," *Opt. Lett.*, vol. 33, pp. 2992–2994, Dec 2008.

[96] S. Akturk, C. L. Arnold, B. Zhou, and A. Mysyrowicz, "High-energy ultrashort laser pulse compression in hollow planar waveguides.," *Optics letters*, vol. 34, no. 9, pp. 1462–1464, 2009.

[97] A. Jarnac, F. Brizuela, C. M. Heyl, P. Rudawski, F. Campi, B. Kim, L. Rading, P. Johnsson, A. Mysyrowicz, A. L'Huillier, A. Houard, and C. L. Arnold, "Compression of TW class laser pulses in a planar hollow waveguide for applications in strong-field physics," *European Physical Journal D*, vol. 68, no. 12, 2014.

[98] T. Auguste, C. Fourcade Dutin, A. Dubrouil, O. Gobert, O. Hort, E. Mével, S. Petit, E. Constant, and D. Descamps, "High-energy femtosecond laser pulse compression in single- and multi-ionization regime of rare gases: experiment versus theory," *Applied Physics B*, vol. 111, pp. 75–87, jan 2013.

[99] C. F. Dutin, A. Dubrouil, S. Petit, E. Mével, E. Constant, and D. Descamps, "Post-compression of high-energy femtosecond pulses using gas ionization," *Opt. Lett.*, vol. 35, pp. 253–255, Jan 2010.

[100] O. Hort, A. Dubrouil, A. Cabasse, S. Petit, E. Mével, D. Descamps, and E. Constant, "Postcompression of high-energy terawatt-level femtosecond pulses and application to high-order harmonic generation," *Journal of the Optical Society of America B*, vol. 32, no. 6, p. 1055, 2015.

[101] M. Nisoli, S. Stagira, S. De Silvestri, O. Svelto, S. Sartania, Z. Cheng, M. Lenzner, C. Spielmann, and F. Krausz, "A novel-high energy pulse compression system: generation of multi-gigawatt sub-5-fs pulses," *Applied Physics B: Lasers and Optics*, vol. 65, no. 2, pp. 189–196, 1997.

[102] W. Schweinberger, A. Sommer, and E. Bothschafter, "Waveform-controlled near-single-cycle milli-joule laser pulses generate sub-10 nm extreme ultraviolet continua," *Optics letters*, vol. 37, no. 17, pp. 3573–5, 2012.

[103] S. Ghimire, B. Shan, C. Wang, and Z. Chang, "High-energy 6.2-fs pulses for attosecond pulse generation," *Laser physics*, vol. 15, no. 6, pp. 838–842, 2005.

[104] X. Chen, A. Jullien, A. Malvache, L. Canova, A. Borot, A. Trisorio, C. G. Durfee, and R. Lopez-Martens, "Generation of 4.3 fs, 1 mJ laser pulses via compression of circularly polarized pulses in a gas-filled hollow-core fiber.," *Optics letters*, vol. 34, no. 10, pp. 1588–1590, 2009.

[105] A. Malvache, X. Chen, C. G. Durfee, a. Jullien, and R. Lopez-Martens, "Multi-mJ pulse compression in hollow fibers using circular polarization," *Applied Physics B*, vol. 104, pp. 5–9, jul 2011.

[106] M. Nurhuda, A. Suda, K. Midorikawa, M. Hatayama, and K. Nagasaka, "Propagation dynamics of femtosecond laser pulses in a hollow fiber filled with argon: constant gas pressure versus differential gas pressure," *J. Opt. Soc. Am. B*, vol. 20, pp. 2002–2011, Sep 2003.

[107] J. H. Sung, J. Y. Park, T. Imran, Y. S. Lee, and C. H. Nam, "Generation of 0.2-TW 5.5-fs optical pulses at 1 kHz using a differentially pumped hollow-fiber chirped-mirror compressor," *Applied Physics B: Lasers and Optics*, vol. 82, no. 1, pp. 5–8, 2006.

[108] S. Bohman, A. Suda, M. Kaku, M. Nurhuda, T. Kanai, S. Yamaguchi, and K. Midorikawa, "Generation of 5 fs, 0.5 tw pulses focusable to relativistic intensities at 1 khz," *Opt. Express*, vol. 16, pp. 10684–10689, Jul 2008.

[109] J. Park, J.-H. Lee, and C. H. Nam, "Generation of 1.5 cycle 0.3 TW laser pulses using a hollow-fiber pulse compressor.," *Optics letters*, vol. 34, no. 15, pp. 2342–2344, 2009.

[110] T. Nagy, M. Forster, and P. Simon, "Flexible hollow fiber for pulse compressors," *Appl. Opt.*, vol. 47, pp. 3264–3268, Jun 2008.

[111] T. Nagy, V. Pervak, and P. Simon, "Optimal pulse compression in long hollow fibers," *Optics Letters*, vol. 36, no. 22, p. 4422, 2011.

[112] L. P. Ramirez, D. Papadopoulos, M. Hanna, A. Pellegrina, F. Friebel, P. Georges, and F. Druon, "Compact, simple, and robust cross polarized wave generation source of few-cycle, high-contrast pulses for seeding petawatt-class laser systems," *J. Opt. Soc. Am. B*, vol. 30, pp. 2607–2614, Oct 2013.

[113] A. Ricci, A. Jullien, J.-P. Rousseau, Y. Liu, A. Houard, P. Ramirez, D. Papadopoulos, A. Pellegrina, P. Georges, F. Druon, N. Forget, and R. Lopez-Martens, "Energy-scalable temporal cleaning device for femtosecond laser pulses based on cross-polarized wave generation.," *The Review of scientific instruments*, vol. 84, p. 043106, apr 2013.

[114] L. Canova, O. Albert, N. Forget, B. Mercier, S. Kourtev, N. Minkovski, S. M. Saltiel, and R. Lopez Martens, "Influence of spectral phase on cross-polarized wave generation with short femtosecond pulses," *Applied Physics B*, vol. 93, no. 2, pp. 443–453, 2008.

[115] A. J. Ricci, *Développement d'une source laser ultra-brève, stabilisée en phase et à haut contraste pour l'optique relativiste haute cadence*. PhD thesis, 2013. Thése de doctorat dirigée par Lopez-Martens, Rodrigo Physique Palaiseau, Ecole polytechnique 2013.

[116] R. DeSalvo, A. A. Said, D. J. Hagan, E. W. V. Stryland, and M. Sheik-Bahae, "Infrared to ultraviolet measurements of two-photon absorption and n 2 in wide bandgap solids," *IEEE Journal of Quantum Electronics*, vol. 32, pp. 1324–1333, Aug 1996.

[117] A. Jullien, *Generation of ultra-intense and ultra-short laser pulses with high temporal contrast.* Theses, Ecole Polytechnique X, Mar. 2006.

[118] L. Canova, S. Kourtev, N. Minkovski, A. Jullien, R. Lopez-Martens, O. Albert, and S. M. Saltiel, "Efficient generation of cross-polarized femtosecond pulses in cubic crystals with holographic cut orientation," *Applied Physics Letters*, vol. 92, no. 23, 2008.

[119] L. P. Ramirez, D. N. Papadopoulos, a. Pellegrina, P. Georges, F. Druon, P. Monot, a. Ricci, a. Jullien, X. Chen, J. P. Rousseau, and R. Lopez-Martens, "Efficient cross polarized wave generation for compact, energy-scalable, ultrashort laser sources.," *Optics express*, vol. 19, pp. 93–8, jan 2011.

[120] B. Mahieu, D. Gauthier, M. Perdrix, X. Ge, W. Boutu, F. Lepetit, F. Wang, B. Carré, T. Auguste, H. Merdji, D. Garzella, and O. Gobert, "Spatial quality improvement of a ti:sapphire laser beam by modal filtering," *Applied Physics B*, vol. 118, no. 1, pp. 47–60, 2014.

[121] a. Präkelt, M. Wollenhaupt, C. Sarpe-Tudoran, a. Assion, and T. Baumert, "Filling a spectral hole via self-phase modulation," *Applied Physics Letters*, vol. 87, no. 12, p. 121113, 2005.

[122] P. M. Celliers, K. G. Estabrook, R. J. Wallace, J. E. Murray, L. B. D. Silva, B. J. MacGowan, B. M. V. Wonterghem, and K. R. Manes, "Spatial filter pinhole for high-energy pulsed lasers," *Appl. Opt.*, vol. 37, pp. 2371–2378, Apr 1998.

[123] A. Jullien, J.-P. Rousseau, B. Mercier, L. Antonucci, O. Albert, G. Chériaux, S. Kourtev, N. Minkovski, and S. M. Saltiel, "Highly efficient nonlinear filter for femtosecond pulse contrast enhancement and pulse shortening," *Opt. Lett.*, vol. 33, pp. 2353–2355, Oct 2008.

[124] M. Hanna, F. Guichard, Y. Zaouter, D. N. Papadopoulos, F. Druon, and P. Georges, "Coherent combination of ultrafast fiber amplifiers," *Journal of Physics B: Atomic, Molecular and Optical Physics*, vol. 49, no. 6, p. 062004, 2016.

[125] S. Szatmari and P. Simon, "Interferometric multiplexing scheme for excimer amplifiers," *Optics Communications*, vol. 98, no. 1-3, pp. 181–192, 1993.

[126] L. Daniault, M. Hanna, L. Lombard, Y. Zaouter, E. Mottay, D. Goular, P. Bourdon, F. Druon, and P. Georges, "Coherent beam combining of two femtosecond fiber chirped-pulse amplifiers.," *Optics letters*, vol. 36, no. 5, pp. 621–623, 2011.

[127] L. Daniault, M. Hanna, L. Lombard, Y. Zaouter, E. Mottay, D. Goular, P. Bourdon, F. Druon, and P. Georges, "Impact of spectral phase mismatch on femtosecond coherent beam combining systems.," *Optics letters*, vol. 37, pp. 650–2, feb 2012.

[128] Y. Zaouter, L. Daniault, M. Hanna, D. N. Papadopoulos, F. Morin, C. Hönninger, F. Druon, E. Mottay, and P. Georges, "Passive coherent combination of two ultrafast rod type fiber chirped pulse amplifiers," *Optics Letters*, vol. 37, no. 9, p. 1460, 2012.

[129] F. Guichard, Y. Zaouter, M. Hanna, K.-L. Mai, F. Morin, C. Hönninger, E. Mottay, and P. Georges, "High-energy chirped- and divided-pulse Sagnac femtosecond fiber amplifier," *Opt. Lett.*, vol. 40, pp. 89–92, Jan 2015.

[130] X.-H. Fang, M.-L. Hu, B.-W. Liu, L. Chai, C.-Y. Wang, and A. M. Zheltikov, "Generation of 150 MW, 110 fs pulses by phase-locked amplification in multicore photonic crystal fiber.," *Optics letters*, vol. 35, no. 14, pp. 2326–2328, 2010.

[131] L. P. Ramirez, M. Hanna, G. Bouwmans, H. El Hamzaoui, M. Bouazaoui, D. Labat, K. Delplace, J. Pouysegur, F. Guichard, P. Rigaud, V. Kermène, A. Desfarges-Berthelemot, A. Barthélémy, F. Prévost, L. Lombard, Y. Zaouter, F. Druon, and P. Georges, "Coherent beam combining with an ultrafast multicore Yb-doped fiber amplifier," *Optics Express*, vol. 23, p. 5406, feb 2015.

[132] P. Rigaud, V. Kermene, G. Bouwmans, L. Bigot, a. Desfarges-Berthelemot, D. Labat, a. Le Rouge, T. Mansuryan, and a. Barthélémy, "Spatially dispersive amplification in a 12-core fiber and femtosecond pulse synthesis by coherent spectral combining," *Optics Express*, vol. 21, no. 11, p. 13555, 2013.

[133] S. N. Bagayev, V. E. Leshchenko, V. I. Trunov, E. V. Pestryakov, and S. a. Frolov, "Coherent combining of femtosecond pulses parametrically amplified in BBO crystals.," *Optics letters*, vol. 39, pp. 1517–20, mar 2014.

[134] V. E. Leshchenko, V. A. Vasiliev, N. L. Kvashnin, and E. V. Pestryakov, "Coherent combining of relativistic-intensity femtosecond laser pulses," *Applied Physics B: Lasers and Optics*, vol. 118, no. 4, pp. 511–516, 2015.

[135] F. Guichard, M. Hanna, L. Lombard, Y. Zaouter, C. Hönninger, F. Morin, F. Druon, E. Mottay, and P. Georges, "Two-channel pulse synthesis to overcome gain narrowing in femtosecond fiber amplifiers," *Opt. Lett.*, vol. 38, pp. 5430–5433, Dec 2013.

[136] C. Manzoni, O. Muecke, G. Cirmi, S. Fang, J. Moses, S.-W. Huang, K.-H. Hong, G. Cerullo, and F. X. KÃd'rtner, "Coherent pulse synthesis: towards sub-cycle optical waveforms," *Laser & photonics reviews*, vol. 9, no. 2, pp. 129 – 171, 2015.

[137] A. Klenke, M. Kienel, T. Eidam, S. Hädrich, J. Limpert, and A. Tünnermann, "Divided-pulse nonlinear compression.," *Optics letters*, vol. 38, pp. 4593–6, nov 2013.

[138] F. Guichard, Y. Zaouter, M. Hanna, F. Morin, C. Hönninger, E. Mottay, F. Druon, and P. Georges, "Energy scaling of a nonlinear compression setup using passive coherent combining.," *Optics letters*, vol. 38, pp. 4437–40, nov 2013.

[139] A. Klenke, S. Hädrich, M. Kienel, T. Eidam, J. Limpert, and A. Tünnermann, "Coherent combination of spectrally broadened femtosecond pulses for nonlinear compression.," *Optics letters*, vol. 39, no. 12, pp. 3520–2, 2014.

[140] A. M. Rubenchik, I. S. Chekhovskoy, M. P. Fedoruk, O. V. Shtyrina, and S. K. Turitsyn, "Nonlinear pulse combining and pulse compression in multi-core fibers," *Optics Letters*, vol. 40, no. 5, pp. 721–724, 2015.

[141] W. a. Okell, T. Witting, D. Fabris, D. Austin, M. Bocoum, F. Frank, A. Ricci, A. Jullien, D. Walke, J. P. Marangos, R. Lopez-Martens, and J. W. G. Tisch, "Carrier-envelope phase stability of hollow fibers used for high-energy few-cycle pulse generation.," *Optics letters*, vol. 38, pp. 3918–21, jun 2013.

[142] D. Wang, Y. Leng, and Z. Huang, "Divided-pulse compression with gas-filled hollow-core fiber for generation of high-energy few-cycle pulses," *J. Opt. Soc. Am. B*, vol. 31, pp. 1248–1254, Jun 2014.

[143] J. N. Damask, "Polarization Optics in Telecommunications," *Springer-Verlag New York*, 2005.

[144] M. Born and E. Wolf, "Principle of Optics," *Pergamon*, 1970.

[145] R. Paschotta, "Article on 'spatial walk-off'," *Encyclopedia of Laser Physics and Technology*, accessed on 2016-02-15.

[146] K. O'Brien, N. D. Lanzillotti-Kimura, H. Suchowski, B. Kante, Y. Park, X. Yin, and X. Zhang, "Reflective interferometry for optical metamaterial phase measurements," *Opt. Lett.*, vol. 37, pp. 4089–4091, Oct 2012.

[147] J. Cohen, P. Bowlan, V. Chauhan, and R. Trebino, "Measuring temporally complex ultrashort pulses using multiple-delay crossed-beam spectral interferometry," *Opt. Express*, vol. 18, pp. 6583–6597, Mar 2010.

[148] R. W. Boyd, "Nonlinear Optics," 2007.

[149] D. E. Zelmon, D. L. Small, and D. Jundt, "Infrared corrected sellmeier coefficients for congruently grown lithium niobate and 5 mol.% magnesium oxide –doped lithium niobate," *J. Opt. Soc. Am. B*, vol. 14, pp. 3319–3322, Dec 1997.

[150] R. Alfano, "The supercontinuum laser source," *Springer*, 2006.

[151] J. Yao, B. Zeng, H. Xu, G. Li, W. Chu, J. Ni, H. Zhang, S. L. Chin, Y. Cheng, and Z. Xu, "High-brightness switchable multiwavelength remote laser in air," *Phys. Rev. A*, vol. 84, p. 051802, Nov 2011.

[152] Y. Liu, Y. Brelet, G. Point, A. Houard, and A. Mysyrowicz, "Self-seeded lasing in ionized air pumped by 800 nm femtosecond laser pulses," *Optics express*, vol. 21, no. 19, pp. 22791–22798, 2013.

[153] J. Ni, W. Chu, H. Zhang, C. Jing, J. Yao, H. Xu, B. Zeng, G. Li, C. Zhang, S. L. Chin, Y. Cheng, and Z. Xu, "Harmonic-seeded remote laser emissions in n2-ar, n2-xe and n2-ne mixtures: a comparative study," *Opt. Express*, vol. 20, pp. 20970–20979, Sep 2012.

[154] Q. Luo, W. Liu, and S. Chin, "Lasing action in air induced by ultra-fast laser filamentation," *Applied Physics B*, vol. 76, no. 3, pp. 337–340, 2003.

[155] J. Yao, G. Li, C. Jing, B. Zeng, W. Chu, J. Ni, H. Zhang, H. Xie, C. Zhang, H. Li, H. Xu, S. L. Chin, Y. Cheng, and Z. Xu, "Remote creation of coherent emissions in air with two-color ultrafast laser pulses," *New Journal of Physics*, vol. 15, 2013.

[156] J. Ni, W. Chu, C. Jing, H. Zhang, B. Zeng, J. Yao, G. Li, H. Xie, C. Zhang, H. Xu, S.-L. Chin, Y. Cheng, and Z. Xu, "Identification of the physical mechanism of generation of coherent N2(+) emissions in air by femtosecond laser excitation.," *Optics express*, vol. 21, no. 7, pp. 8746–52, 2013.

[157] S. Mitryukovskiy, Y. Liu, P. Ding, A. Houard, and A. Mysyrowicz, "Backward stimulated radiation from filaments in nitrogen gas and air pumped by circularly polarized 800 nm femtosecond laser pulses," *Opt. Express*, vol. 22, pp. 12750–12759, Jun 2014.

[158] J. Yao, H. Xie, B. Zeng, W. Chu, G. Li, J. Ni, H. Zhang, C. Jing, C. Zhang, H. Xu, Y. Cheng, and Z. Xu, "Gain dynamics of a free-space nitrogen laser pumped by circularly polarized femtosecond laser pulses," *Optics Express*, vol. 22, no. 16, p. 19005, 2014.

[159] H. Zhang, C. Jing, J. Yao, G. Li, B. Zeng, W. Chu, J. Ni, H. Xie, H. Xu, S. L. Chin, K. Yamanouchi, Y. Cheng, and Z. Xu, "Rotational coherence encoded in an "Air-Laser" spectrum of nitrogen molecular ions in an intense laser field," *Physical Review X*, vol. 3, no. 4, pp. 1–6, 2014.

[160] G. Point, Y. Liu, Y. Brelet, S. Mitryukovskiy, P. Ding, A. Houard, and A. Mysyrowicz, "Lasing of ambient air with microjoule pulse energy pumped by a multi-terawatt infrared femtosecond laser.," *Optics letters*, vol. 39, no. 7, pp. 1725–8, 2014.

[161] Y. Liu, P. Ding, G. Lambert, A. Houard, V. Tikhonchuk, and A. Mysyrowicz, "Recollision-Induced Superradiance of Ionized Nitrogen Molecules," *Physical Review Letters*, vol. 115, no. 3, pp. 1–5, 2015.

[162] H. Xu, E. Lötstedt, A. Iwasaki, and K. Yamanouchi, "Sub-10-fs population inversion in N2+ in air lasing through multiple state coupling," *Nature Communications*, vol. 6, p. 8347, 2015.

[163] Y. Liu, P. Ding, G. Lambert, A. Houard, V. Tikhonchuk, and A. Mysyrowicz, "Recollision-Induced Superradiance of Ionized Nitrogen Molecules," *Physical Review Letters*, vol. 115, no. 3, pp. 1–5, 2015.

[164] X. Xie, K. Doblhoff-Dier, S. Roither, M. S. Schöffler, D. Kartashov, H. Xu, T. Rathje, G. G. Paulus, A. Baltuška, S. Gräfe, and M. Kitzler, "Attosecond-recollision-controlled selective fragmentation of polyatomic molecules," *Phys. Rev. Lett.*, vol. 109, p. 243001, Dec 2012.

[165] P. Donnat, G. Gallice, N. L'hullier, O. Morice, D. Nassiet, T. Porcher, X. Ribeyre, V. Rivoire, and C. Treimany, "Mirò V5," *Manuel de rÃl'fÃl'rence*, p. 167, 2009.

[166] A. Siegman, "Lasers," *University Science Books*, p. Chapter 10, 1986.

Titre : Combinaison cohérente d'impulsions de quelques cycles optiques dans le cadre du développement de futures sources laser Terawatt dédiées à la physique attoseconde

Mots clés : Optique non linéaire, Compression d'impulsions, Combinaison cohérente, Biréfringence

Résumé : Cette thèse s'inscrit dans le cadre du développement d'une source laser TW, de cadence élevée, stabilisée en phase, et délivrant des impulsions de quelques cycles optiques pour explorer la physique attoseconde. De telles impulsions ne sont pas directement disponibles à la sortie d'une source laser femtoseconde classique. Une technique de post-compression efficace pour obtenir de telles impulsions consiste à élargir le spectre des impulsions laser par automodulation de phase dans une fibre creuse remplie de gaz, puis à compenser la phase spectrale introduite avec des miroirs chirpés. Cette technique convient à des impulsions dont l'énergie est inférieure au millijoule. Au-delà, la transmission et la stabilité du compresseur chutent fortement à cause d'effets non linéaires tels que l'autofocalisation et l'ionisation. Pour comprimer des impulsions énergétiques et dont la phase de l'enveloppe est stabilisée par rapport à la porteuse, il est possible de diviser l'impulsion initiale en plusieurs répliques d'énergie moindre et de réduire ainsi l'intensité crête en entrée de fibre.

Dans le cadre de cette thèse, la combinaison cohérente passive d'impulsions de quelques cycles optiques issues d'une fibre creuse remplie de gaz est démontrée pour la première fois. L'utilisation de lames biréfringentes dont l'orientation est soigneusement déterminée permet de générer et combiner des répliques avec une efficacité élevée. L'étude détaillée de cette technique, aussi bien théorique qu'expérimentale, a permis de mettre en évidence les conditions requises pour générer des impulsions de quelques cycles optiques et présentant un bon contraste temporel. Plus précisément, la phase spectrale relative entre les répliques peut être mesurée à l'aide d'une méthode interférométrique permettant de quantifier les déphasages résiduels. Les effets qui affectent le processus de combinaison des répliques, tels que les modifications des états de polarisation des répliques ou bien les interactions non linéaires entre les répliques, sont analysés en détail. Une méthode est proposée pour minimiser ces effets, même dans le cas plus critique de la division et combinaison d'impulsions à quatre répliques.

Title : Coherent combining of few-cycle pulses for the next generation of Terawatt-class laser sources devoted to attosecond physics

Keywords : Ultrafast nonlinear optics, Pulse compression, Coherent combining, Birefringence

Abstract : The framework of this thesis is the design and development of a TW-class, high-repetition rate, CEP-stabilized, few-cycle laser system devoted to attosecond physics. Few-cycle pulses are not directly available at the output of typical femtosecond sources. A way to produce such pulses with high spatial quality is nonlinear spectral broadening in a gas-filled hollow-core fiber followed by temporal compression with chirped mirrors. However, as the input pulse energy approaches the milliJoule level, both the transmission and stability of hollow fiber compressors rapidly drop with the onset of self-focusing and ionization. A way of overcoming this limitation is to divide the input pulse into several lower energy replicas that can be subsequently recombined after independent spectral broadening in the fiber. In this thesis, the passive coherent combining of millijoule energy laser pulses down to few-cycle duration in a gas-filled hollow fiber is

demonstrated for the first time. High combining efficiency is achieved by using carefully oriented calcite plates for temporal pulse division and recombination. A detailed theoretical and experimental analysis of this temporal multiplexing technique is proposed to explain the conditions required for producing few-cycle pulses with high fidelity. In particular, an interferometric method for measuring the relative spectral phase between two replicas is demonstrated. This gives a measure of the phase mismatch in the combining plate, as well as that induced by eventual cross-phase modulation or ionization during propagation in the fiber. The effects degrading the combining process, as polarization change or nonlinear interactions between pulse replicas are analyzed in details. A method is proposed to overcome these limitations, even in the critical case of fourfold pulse division and combination.